ABSTRACT

Title of dissertation: INVESTIGATION OF TUNNELING IN SUPERCONDUCTORS USING A MILLIKELVIN SCANNING TUNNELING MICROSCOPE

Wan-Ting Liao, Doctor of Philosophy, 2019

Dissertation directed by: Professor Christopher J. Lobb
Department of Physics

In this thesis, I discuss my use of a millikelvin scanning tunneling microscope (STM) to investigate tunneling phenomena in superconductors. As part of an effort to construct an STM to measure the superconducting phase difference, I first describe how I modified a dual-tip scanning tunneling microscope by electrically connecting the two tips together with a short (3 mm) strip of flexible 25 μm thick Nb foil. I also discuss the technique I developed for keeping each tip in feedback when only the total tunnel current through both tips can be measured. I then describe simultaneous room-temperature imaging with both tips on samples of Au/mica and highly oriented pyrolytic graphite (HOPG).

Next, I report single-tip results from scanning tunneling microscopy of 25 nm and 50 nm thick films of superconducting TiN at 0.5 K. I found large variations

in the tip-sample conductance-voltage characteristics in these samples. At some locations the characteristics showed a clear superconducting gap, as expected for superconductor-normal (S-I-N) tunneling through a high barrier height. At other locations there was a distinct zero-voltage conductance peak, as expected for S-N Andreev tunneling through a low barrier height. I compare the data to the Blonder-Tinkham-Klapwijk (BTK) theory and the Dynes model of tunneling into a superconductor with broadened density of states. I find that the BTK model provides better fits and reveals a remarkable correlation between the superconducting gap Δ, the temperature T and the barrier height Z. Possible causes for this correlation, including local heating and surface contamination, are discussed.

Finally, I describe measurements of I(V) characteristics of a Josephson junction formed by a scanning tunneling microscope with a Nb sample and a Nb tip at 50 mK and 1.5 K. To better understand the physics of this system, I generalized the multiple Andreev reflection (MAR) theory of Averin and Bardas to describe junctions having electrodes with different superconducting gaps. For tunneling resistance R_n between 10 MΩ and 100 kΩ, there was no observable supercurrent at 50 mK or 1.5 K. For R_n between 100 kΩ and about 10 kΩ, the junctions showed hysteretic behavior, with the forward-sweep switching current I_s larger than the reverse-sweep retrapping current I_r. In this regime, the critical current I_0 was suppressed and the current-voltage characteristics showed a relatively small non-zero resistance R_0 at $V = 0$ that scaled with R_n^2. For R_n less than the quantum resistance (~ 12 kΩ), the I-V characteristics deviate from single channel MAR theory. In this limit, the tip makes contact with the sample, as revealed by the dependence of the junction conductance curves on

the tip-sample separation. By fitting my two-gap MAR theory to the I(V) data, I obtain superconducting gaps of the tip and sample as a function of the tunnel resistance R_n. I find the sample has nearly the full gap of bulk Nb ($\Delta \sim 1.5$ meV), but the tip gap is only about 0.67 meV, and decreases for $R_n \leq 10$ kΩ.

INVESTIGATION OF TUNNELING IN SUPERCONDUCTORS USING A MILLIKELVIN SCANNING TUNNELING MICROSCOPE

by

Wan-Ting Liao

Dissertation submitted to the Faculty of the Graduate School of the
University of Maryland, College Park in partial fulfillment
of the requirements for the degree of
Doctor of Philosophy
2019

Advisory Committee:
Professor Christopher J. Lobb, Chair/Advisor
Professor Frederick C. Wellstood, Co-Advisor
Dr. Michael Dreyer, Co-Advisor
Professor John Cumings
Dr. Kevin D. Osborn

Dedication

Dedicated to my father, my mother, my brothers, my aunts

and

my Fiancé Karl

Acknowledgments

As a student at University of Maryland (UMD) and the Laboratory for Physical Sciences (LPS), the last few years have been the best time of my academic life. None of the work in this thesis would have been possible without the help of many people and I humbly thank them all.

I thank my advisors, Prof. Christopher Lobb, Prof. Fred Wellstood and Dr. Michael Dreyer. In particular, I thank Dr. Lobb for being such a great mentor and scientist. There were many times when I was working on the Multiple Andreev Reflection (MAR) research where he often came to LPS to brainstorm the theoretical problem with me and cheered me up (he always told me that the problem will be solved by Monday). I thank Dr. Wellstood for being such a great scientist whom I can always consult to discuss about physics. He can always figure out where I am stuck in the problem and work our way on how to proceed next. His ability of looking at a simple problem from different angles is amazing and this always inspires me in my research. I thank Dr. Dreyer who is a real expert in scanning tunneling microscopy (STM), low temperature techniques and the UHV system. I learned most of the experimental skills that I needed during my graduate work from him. There were times when I wanted to speed up the experiment and I skipped some important steps. He warned me that, if something went wrong, then I would have to spend even more time to fix the problem. There was also an incident where I was totally stuck in my research. He just smiled and told me that one day you will run out of the problems that you need to solve.

I am grateful to Dr. Kevin Osborn for providing the TiN samples for the work I describe in Chapter 6. He was always willing to discuss physics and the TiN project, and agreed to be one of the committee members for my dissertation. I also want to thank Prof. John cumings for agreeing to serve as the Dean's representative for my committee at the last minute.

I thank Dr. Butera, the STM group manager at LPS. He always gave me full freedom to execute the projects and was very supportive when I needed help at LPS or in my academic life. I am thankful to Dr. Sudeep Dutta, a great scientist who is very detailed and could always spot any small flaws in my research that I had ignored. At the same time he is a heart-warming person who helped me hang on during dark times. I am grateful to my colleagues who worked on parts of this project and shared their experiences with me, notably Drs. Anita Roychowdhury and Rami Dana.

I thank the LPS cleanroom people, namely Toby Olver, Steve Brown, Jim Fogleboch, Paul Hannah, Dan Hinkel, Doug Ketchum, Warren Berk, Debtanu Basu, Curt Walsh, David Gutierrez, who were very knowledgeable and always helpful when I had any issues related to the cleanroom. I thank the machinists in the LPS machine shop, namely Donald Crouse, Ruben Brun, John Sugrue, and Bill Donaldson, who fabricated many different parts for my research and were always very fast and responsive after I submitted my requests. I am grateful to the administrative staff at LPS including Jonas Wood, Niquinn Fowler, Althia Kirlew, Cynthia Evans, Greg Latini, Charla Pryor, Anthony Littlefield and Mark Thornton.

I am thankful for the support I received from Bruce Kane, Ben Palmer and

Chris Richardson. I thank Ramesh Bhandari for being such a wonderful theoretical physicist who gave me significant insight during my theoretical work on the MAR problem described in Chapter 7. I thank Prof. Dmitri Averin, for guiding me through generalizing the MAR problem and for providing the Fortran code that I modified and then used in this thesis.

I am grateful to my friends from LPS, Luke Robertson, Joyce Coppock, Shavi Premaratne, Neda Forouzani, Chih-Chiao Hung, Liuqi Yu, Tim Kohler, Joseph Murray, Ashish Alexander, Chomani Gaspe, Margaret Samuels, Jennifer DeMell, Kevin Dwyer, Siddharth Tyagi, Rui Zhang, Jen-Hao Yeh, Tamin Tai, Yizhou Huang, and Philip Li for discussions of research, as well as trivial day-to-day greetings and chatting with me every time we met in the LPS hallway.

I am thankful to the members of the running group at LPS, including Victor Yun, Donghun Park, Alan I, Yuan Gu, Chenglin Yi. The daily jog at 11:30 AM made me feel vibrant after half a day of work and this routine kept me both mentally and physically healthy during my graduate study. I thank Charlie Kraft for inviting me sailing several times during the summer, with his sister Amy and brother Hank, who I enjoyed meeting.

Several friends who I met at UMD gave me support when I really needed it, including Xiaoxiao Ge, I-Lin Liu, Michelle Lin, Yiran Li, Chih-Yuan Su, Ayan Mallik and Sabyasachi Barik. I am grateful to my housemates Alice Rogers and Sarah Cochrane. I would never forget those three wonderful years that we lived together, shared our lives with each other and watched so many fun TV shows after dinner. There are many other friends who I met outside of school who have become

my best friends. I thank them all and apologize for leaving them out here.

I would like to acknowledge financial support from the Laboratory for Physical sciences and NSF DMR-1409925 for the work described in this thesis.

I am extremely grateful for my parents, my two brothers, and my aunts for their love and support throughout graduate life. I especially thank my friend Yu-Chun Wei, who shared many years of friendship and supported me during the first two years at Maryland when I had a hard time adapting to life in the US.

Finally, I thank my Fiancé Karl, a wonderful person who I met in my graduate life, who has gone through multiple ups and downs with me, who has traveled and done many fun activities with me, and who I decided to spend the rest of my life with.

Table of Contents

Dedication ii

Acknowledgements iii

List of Tables x

List of Figures xi

List of Abbreviations xiv

Chapter 1 Introduction 1

Chapter 2 Scanning Tunneling Microscopy 6
- 2.1 Introduction . . . 6
- 2.2 Theory of 1-D tunneling and principle of STM . . . 7
- 2.3 Topographic imaging . . . 14
  - 2.3.1 Constant current mode . . . 14
  - 2.3.2 Constant height mode . . . 15
- 2.4 Spectroscopy . . . 16
  - 2.4.1 N-I-N tunneling . . . 18
  - 2.4.2 N-I-S tunneling . . . 23
  - 2.4.3 S-I-S tunneling . . . 28
- 2.5 Cryogenic STM's . . . 29

Chapter 3 Experimental Setup of the Millikelvin STM 33
- 3.1 Dilution refrigerator . . . 34
- 3.2 Overall experimental setup of the millikelvin STM . . . 39
- 3.3 Dual-tip STM . . . 41
- 3.4 Wiring . . . 43
- 3.5 Damage to the heat exchanger and partial repair . . . 52
- 3.6 Ultra high vacuum (UHV) system . . . 55
- 3.7 Control electronics and measurement circuit . . . 56
- 3.8 STM niobium and vanadium tip preparation . . . 60
- 3.9 Conclusion . . . 61

Chapter 4 Simultaneously Scanning Two Connected Tips in a Dual-tip STM 62
- 4.1 Introduction . . . 62
- 4.2 Room temperature system setup . . . 65
- 4.3 Scanning two tips independently . . . 67

4.4 Simultaneously scanning two STM tips on test samples 75
4.5 Conclusions 86

Chapter 5 Superconductivity and BTK Theory 87
5.1 Introduction to superconductivity 88
5.1.1 Density of states 97
5.2 Andreev reflection 99
5.2.1 BTK theory 102
5.2.2 Calculation of I-V Characteristics for S-I-N junction from the BTK model 110

Chapter 6 Scanning Andreev Tunneling Microscopy of Titanium Nitride Thin Films 116
6.1 Introduction 116
6.2 TiN film growth and basic characteristics 118
6.3 STM measurements and Andreev effects 120
6.4 Δ, Z, T, h correlations in the 50 nm and 25 nm films 128
6.5 Physical mechanism causing correlations between Δ, T, Z and h . . . 139
6.6 Conclusions 144

Chapter 7 Theory of the I-V characteristics in S-I-S Junctions with Multiple Andreev Reflection 146
7.1 Introduction 146
7.2 MAR in symmetrical junction with transparency $D = 1$ 148
7.2.1 Averin-Bardas model 148
7.2.2 Finding the expression for the current when the gaps are the same 155
7.3 MAR in symmetrical junction with $D \neq 1$ 172
7.4 MAR in Asymmetrical junctions 176
7.5 The Josephson effect 200
7.6 Critical current in Asymmetrical junctions with MAR 205
7.7 Conclusion 210

Chapter 8 Ultra-small Josephson Junction Formed Using a Nb STM Tip and Nb Sample 213
8.1 Introduction 213
8.2 Sample preparation and experimental setup 214
8.3 $I - V$ characteristics from a Nb tip and a Nb sample 218
8.4 Dissipation analysis from the retrapping current 233
8.5 Conclusion 240

Chapter 9 Conclusions 242
9.1 Summary of main results 242
9.2 Some suggestions for further research 246
9.2.1 Low temperature requirement 246

9.2.2 Smaller SQUID loop 247
9.2.3 Better shielding 247
9.2.4 Intrinsic system constraint 248

Appendix A χ^2 fit for the TiN film **250**

Appendix B 50 nm TiN film showing S-I-S junction with a vanadium tip **253**

Appendix C Fortran code for symmetrical S-I-S junction with MAR effect **256**

Appendix D Fortran code for Asymmetrical S-I-S junction with MAR effect **262**

Bibliography **271**

List of Tables

Table 5.1 BTK coefficients 108

Table 6.1 Extracted parameters (Δ, T, Z) from fitting conductance curves to the BTK model 126

Table 6.2 General properties of the 50 nm and 25 nm TiN films 130

Table 8.1 Extracted parameters $R_n, \Delta_{\text{tip}}, \Delta_{\text{sample}}, \Delta_{\text{sum}}, D, Z$ from fitting the $I-V$ characteristics in Fig. 8.3 (a)-(c) to the asymmetrical MAR model at $T = 0$. 221

List of Figures

Fig. 2.1 Particle incident on a barrier . . . 9
Fig. 2.2 Principle of STM . . . 12
Fig. 2.3 voltage-bias and current-bias circuits . . . 19
Fig. 2.4 N-I-N tunneling . . . 22
Fig. 2.5 N-I-S tunneling . . . 25
Fig. 2.6 Conductance and voltage plot of N-I-S tunneling . . . 27
Fig. 2.7 S-I-S tunneling . . . 30
Fig. 2.8 $I - V$ characteristic of S-I-S tunneling . . . 31

Fig. 3.1 Phase diagram for ^{3}He/^{4}He mixture . . . 35
Fig. 3.2 Schematic diagram of dilution refrigerator . . . 37
Fig. 3.3 Schematic of mK-STM setup . . . 40
Fig. 3.4 Schematic of the dual tip mK-STM . . . 42
Fig. 3.5 Wiring and signal lines at 1 K pot stage . . . 44
Fig. 3.6 Wiring and signal lines at the still stage . . . 45
Fig. 3.7 Wiring and signal lines at the cold plate stage . . . 46
Fig. 3.8 Wiring and signal lines at the mixing chamber stage . . . 47
Fig. 3.9 Wiring and signal lines below the mixing chamber stage . . . 48
Fig. 3.10 Wiring and signal lines at the STM stage . . . 49
Fig. 3.11 Wiring of the drive lines at different stages . . . 51
Fig. 3.12 Photographs of the broken heat exchanger . . . 53
Fig. 3.13 Photographs of the re-sealed heat exchanger . . . 54
Fig. 3.14 Photograph of our mK-STM system . . . 57
Fig. 3.15 Schematic diagram of voltage-bias and current-bias modes . . . 59

Fig. 4.1 Bow-tie connectors . . . 66
Fig. 4.2 Two tips connected . . . 68
Fig. 4.3 Electronics setup for controlling two tips . . . 70
Fig. 4.4 I-z curve . . . 72
Fig. 4.5 $|\mathrm{d}I/\mathrm{d}z|$-$z$ curve . . . 73
Fig. 4.6 Electronic circuit of safety box . . . 76
Fig. 4.7 Topographic image of Au on Mica in current mode . . . 78
Fig. 4.8 Topographic image of Au on Mica in $\mathrm{d}I/\mathrm{d}z$ mode . . . 79
Fig. 4.9 Atomic image of HOPG in current mode . . . 80
Fig. 4.10 Atomic image of HOPG in $\mathrm{d}I/\mathrm{d}z$ mode . . . 81
Fig. 4.11 Simultaneous scans of Au on Mica using two connected tips . . . 83

Fig. 4.12 Stability test on HOPG 84
Fig. 4.13 Stability test on HOPG showing dragging of the inner tip by the outer tip 85

Fig. 5.1 Superconducting gap as a function of temperature 98
Fig. 5.2 Density of states of a superconductor 100
Fig. 5.3 Normal reflection and Andreev reflection amplitude *vs.* energy . 109
Fig. 5.4 Conductance as a function of energy for different Z at 75 mK . 112
Fig. 5.5 Conductance as a function of energy for different Z at 500 mK . 114
Fig. 5.6 Conductance as a function of energy for different Z at 500 and 75 mK 115

Fig. 6.1 Topographic image of the 50 nm TiN film and selected conductance curves 121
Fig. 6.2 Topographic image of the 50 nm TiN film and fine scale view of grains 125
Fig. 6.3 Fine scale topographic image maps of Δ, T, Z and line section for the 50 nm TiN film 127
Fig. 6.4 False color plot of conductance versus position and voltage along the line cut 129
Fig. 6.5 Large scale topographic image and line section of 50 nm and 25 nm TiN films 131
Fig. 6.6 Large scale topographic image, maps of Δ, T, Z and line section for the 50 nm TiN films 133
Fig. 6.7 Large scale topographic image, maps of Δ, T, Z and line section for the 50 nm TiN films 134
Fig. 6.8 Large scale topographic image, maps of Δ, T, Z and line section for the 25 nm TiN film 135
Fig. 6.9 Large scale topographic image, maps of Δ, T, Z and line section for the 25 nm TiN film 136
Fig. 6.10 Gap histograms for 50 nm and 25 nm TiN films 138
Fig. 6.11 Temperature dependent conductance curves for 25 nm TiN film taken at a fixed location. 140
Fig. 6.12 Histograms of the gap and averaged height versus gap. 141
Fig. 6.13 Correlations in the 50 nm and 25 nm TiN films 143
Fig. 6.14 Thermal model describing ion milling process which leads to higher barrier height and lower gap 145

Fig. 7.1 Schematic showing MAR reflection in S-I-S junction 149
Fig. 7.2 Electron-like quasiparticle incident from the left superconducting electrode and doing MAR. 156
Fig. 7.3 Electron-like quasiparticle incident from the right superconducting electrode and doing MAR. 163
Fig. 7.4 $I-V$ characteristics of a symmetrical S-I-S junction with MAR 177

Fig. 7.5 Hole-like quasiparticle incident from the left superconducting electrode and doing MAR. 183
Fig. 7.6 Hole-like quasiparticle incident from the right superconducting electrode and doing MAR. 185
Fig. 7.7 $I-V$ characteristics of an asymmetrical S-I-S junction with MAR effect 197
Fig. 7.8 Temperature effect on $I-V$ characteristics 198
Fig. 7.9 Temperature effect on $I-V$ characteristics showing sensitivity to the smaller superconducting gap 201
Fig. 7.10 AC current (first Fourier component) of the $I-V$ characteristics. 208
Fig. 7.11 Temperature dependence of the critical current 211

Fig. 8.1 Relay box for voltage-biased and current-biased setup 216
Fig. 8.2 Nb surface topography 217
Fig. 8.3 Superconducting Nb-Nb $I-V$ characteristics at different junction resistances 219
Fig. 8.4 Detailed view of the $I-V$ curves from Fig. 8.3 220
Fig. 8.5 Normalized conductance G/G_0 *vs.* distance z for different starting normal resistance R_n 225
Fig. 8.6 Temperature effect on the sub-gap bump at $V = \Delta/e$ 226
Fig. 8.7 Detailed view of subgap regions in Fig. 8.6 227
Fig. 8.8 Superconducting gap Δ and transparency parameter D as a function of junction resistance 229
Fig. 8.9 Critical current, switching current and retrapping current as a function of normal junction resistance R_n. 232
Fig. 8.10 Stewart-McCumber number β_c and the capacitance C between the tip and the sample as a function of normal resistance R_n . . 234
Fig. 8.11 Josephson energy E_J (black), charging energy E_C (red), plasma energy $\hbar\omega_p$ (blue) and MQT escape temperature *vs* normal resistance R_n of the junction 237
Fig. 8.12 Finite resistance $R_0 - R_c$ of the supercurrent branch versus normal resistance R_n of the junction 239

Fig. 9.1 Configuration for an STM-SQUID measurement 245

Fig. A.1 Histograms of χ^2 for the 50 nm thick and 25 nm thick TiN films. 252

Fig. B.1 Topography, superconducting gap map, gap histogram and sample curve of the S-I-S data taken from the 50 nm thick TiN film. 255

List of Abbreviations

BTK	Blonder, Tinkham and Klapwijk
BCS	Bardeen, Cooper and Schrieffer
DOS	Density of states
LDOS	Local density of states
N-I-N	Normal-Insulator-Normal
N-I-S	Normal-Insulator-Superconductor
S-I-N	Superconductor-Insulator-Normal
S-I-S	Superconductor-Insulator-Superconductor
IVC	Inner Vacuum Can
UHV	Ultra-High Vacuum
HOPG	Highly Ordered Pryolitic Graphite
TiN	Titanium nitride
MAR	Multiple Andreev Reflection
AB	Averin and Bardas
STM	Scanning Tunneling Microscopy
JSTM	Josephson Scanning Tunneling Microscopy
STS	Scanning Tunneling Spectroscopy
NSF	National Science Foundation

CHAPTER 1

Introduction

High transition temperature superconductors [1–7] were discovered more than 30 years ago. Despite theoretical advances and experimental discoveries, many basic questions remain unresolved; the most important being what is the mechanism causing pairing [8–10]. Many interesting phenomena have been observed in high T_c materials, including the existence of competing charge ordering phenomena [11, 12], the possible existence of different superconducting order parameters [13–17] and the occurrence of rapid variations in superconducting properties at atomic length scales [18, 19]. Such phenomena have naturally been examined at the atomic scale using low-temperature scanning tunneling microscopes (STM) [20]. Using normal metal tips, STMs allow sensitive measurements of the superconducting gap and energy level spectrum via quasiparticle tunneling [21–29], as I discuss in Chapter 2.

An STM with a superconducting tip and a superconducting sample can form a Josephson junction. Josephson junctions allow current to flow from one electrode to the other electrode with no voltage drop [30, 31]. Interestingly, STMs with superconducting tips are not very common. Hamidian *et al.* [32] reported the use

of an STM with a superconducting tip to investigate variations in the Cooper pair density around zinc impurities in $Bi_2Sr_2CaCu_2O_{8+x}$. Although in this case both the tip and sample were superconducting, the relatively large tunneling resistance (>1 MΩ) and the small tip-sample capacitance made it impossible to obtain a true Josephson supercurrent due to phase diffusion [33]. Instead one finds a dissipative current flow that peaks at a non-zero voltage [32–38] due to incoherent tunneling of Cooper pairs [39].

Previously in our lab at LPS, Anita Roychowdhury *et al.* [39–41] built a dual-tip mK STM as part of a project to operate an STM that showed a real Josephson supercurrent [42]. They demonstrated that each Nb-STM tip could independently scan the surface of a sample [40, 41] and observed photon-assisted tunneling of incoherent Cooper pairs in a single Josephson junction [39].

In this thesis, I first report further progress on the developement of a mK Josephson STM with two independent tips [43]. I describe the technique I used to simultaneously scan two connected STM tips when only the total current through both tips can be measured. To do this I had to connect the two tips together and develop a novel feedback system.

The second project I discuss involved using our STM system to measure 50 nm thick and 25 nm thick superconducting TiN films. I was surprised to observe features in the superconductor-insulator-normal (S-I-N) tunneling characteristics that were clearly due to Andreev reflection effects. This required me to analyze the data by fitting it to the Blonder-Tinkham-Klapwijk (BTK) theory of Andreev tunneling [44, 45].

TiN has been the subject of much research in recent years due to its potential applications in superconducting quantum computation [46–50] and its high kinetic inductance, which is potentially interesting for constructing superconducting microwave kinetic inductance detectors for x-ray spectroscopy and sub-millimeter-wave astronomy telescopes [51–55]. The final project I discuss involves observation of multiple Andreev reflection effects in Nb-Nb S-I-S tunneling.

In Chapter 2, I discuss two fundamental elements which form the basis for the rest of the thesis. I first discuss scanning tunneling microscopy (STM) and describe the two imaging methods I used, constant current and constant height. I then discuss scanning tunneling spectroscopy (STS), which I used for investigating the electronic density of states of samples. In particular, I describe the two operating modes I used, voltage biased mode and current biased mode, and why I needed to use the current-biased mode for Josephson tunneling experiments. In addition I describe the three basic tunneling situations I encountered: tunneling from a normal tip to a normal sample (N-I-N), tunneling from a normal tip to a superconducting sample (N-I-S), and tunneling from a superconducting tip to a superconducting sample (S-I-S). Finally, I briefly discuss STM measurements at millikelvin temperatures.

In Chapter 3, I describe the mK STM setup that I used. I begin with a discussion of the principles of operation of a dilution refrigerator and the operating procedure. I move on to describe the dual-tip mK STM apparatus and the wiring of the STM at each stage of the dilution refrigerator. I also discuss a difficulty I encountered, when the heat exchanger exploded during mixture removal, and the subsequent repairs to bring the system partially back into service. Finally, I discuss

the UHV chamber used for sample preparation, the control electronics for operating the STM, and the superconducting STM tips that I used.

In Chapter 4, I describe an important step towards constructing a true Josephson STM based on forming an asymmetric SQUID [42]. In particular, I first describe how I connected the two STM tips in our dual-tip system with a short flexible link made from thin Nb foil. I then discuss another challenge of this approach, which is how to implement feedback to control both tips when they share the same current lead. I present a new feedback technique that separates the current signal for each tip and then show results from simultaneously scanning two connected tips at room temperature. I finish by examining the electrical performance of the system and the mechanical compliance of the link.

Chapters 5 and 6 cover the second main topic I worked on. In Chapter 5, I discuss the Bardeen-Tinkham-Klapwijk (BTK) theory of Andreev reflection and their expression for the I(V) characteristics of S-N junctions with different transparencies. In Chapter 6, I discuss my STM measurements of 50 nm and 25 nm thick superconducting TiN samples in the mK-STM. While at first sight most of the I(V) characteristics appeared to show standard N-I-S tunneling, we eventually realized we were seeing obvious Andreev reflection effects, including zero bias conductance peaks at some locations. This is expected from Andreev reflection effects for a highly transparent barrier. Using BTK theory, as opposed to a standard tunneling approach to fit the data, I extracted spatial maps of the superconducting gap Δ, temperature T and barrier height Z which showed large spatial variations. I found striking spatially-dependent correlations between these parameters, as well

as differences between the two films, and I conclude with a discussion of a simple model which may explain this surprising aspect of the data.

Chapter 7 and Chapter 8 describe the final major topic that I worked on. In Chapter 7, I extend Averin and Bardas's theory of Multiple Andreev Reflection (MAR) in S-I-S junctions to the case where the electrodes can have different gaps. I use this theory to obtain current-voltage characteristics for a single superconducting channel with arbitrary transparency at temperature T. Using this theory I also work out the critical current of a Josephson junction for arbitrary transparency. Although this chapter includes a lot of mathematical detail, it is based on the simple and physically appealing scattering matrix approach of Averin and Bardas. In Chapter 8 I present measurements at 50 mK and 1.5 K of the current-voltage characteristics of S-I-S junctions formed by a Nb STM tip and a Nb(100) sample. The characteristics show clear features due to MAR and I apply my two-gap MAR theory from Chapter 7 to extract key parameters such as the superconducting gaps of the sample and tip.

In Chapter 9, I conclude with a summary of my main findings and discuss some possible future work to complete a dual-tip Josephson STM.

CHAPTER 2

Scanning Tunneling Microscopy

2.1 Introduction

The first scanning tunneling microscope was described by G. Binning and H. Rohrer [56–58] in 1981. The ability to resolve individual atoms stimulated considerable research world-wide and they were awarded the Nobel Prize in Physics in 1986. The invention of the STM opened up atomic scale imaging in real space and allowed researchers to manipulate single atoms and molecules. Moreover, spectroscopic techniques were developed to reveal the electronic properties of samples, such as the local density of states (LDOS). Unlike classical transport mechanisms such as diffusion and drift, the underlying principle of operation of an STM is quantum mechanical tunneling of electrons through a vacuum barrier, which cannot be explained using a classical picture.

In Section 2.2 I first discuss quantum mechanical tunneling in one dimension and give a brief overview of scanning tunneling microscopy. Next, in Section 2.3 I discuss two modes that are often used in imaging the surface of samples for STM,

constant current mode and constant height mode. I then discuss a powerful spectroscopy tool for investigating the electronic states of the samples in Section 2.4. I discuss voltage-biased spectroscopy in normal-insulator-normal (N-I-N) tunneling, normal-insulator-superconductor (N-I-S) tunneling and superconductor-insulator-superconductor (S-I-S) tunneling. I go on to describe current-biased spectroscopy for use in Josephson STM tunneling. Finally, in Section 2.5 I briefly discuss a mK cryogenic system is needed for conducting my STM experiments.

2.2 Theory of 1-D tunneling and principle of STM

Tunneling phenomena can be treated using a time-independent approach, which involves finding the wavefunctions inside and outside of a barrier and matching them at the boundaries, or using Fermi's golden rule, which arises from first order time-dependent perturbation theory [59–61]. Typical introductory discussions consider simple one-dimensional barriers and this is a good approximation for planar metal-oxide-metal junctions. On the other hand an STM tip and planer sample have a 3D geometry and a more complicated analysis is required to accurately describe the behavior.

Nevertheless, let me first review simple 1-D tunneling. To proceed, I consider an electron with energy E and mass m that is in region A and is incident from the left onto barrier B (see Fig. 2.1). The barrier in region B has a uniform height u. Classically, the particle can only get over the barrier if its energy E is greater

than the barrier height ($E > u$). In quantum mechanics, due to the wave nature of matter, there is some probability to penetrate through the barrier even if $E < u$. I can write Schrödinger's equation and find the wave function in each of the three regions (Fig. 2.1). In region A, Schrödinger's equation is

$$-\frac{\hbar^2}{2m}\frac{\mathrm{d}^2\Psi_1}{\mathrm{d}x^2} = E\Psi_1 \tag{2.1}$$

and the wavefunction is,

$$\Psi_1 = e^{ikx} + Ae^{-ikx} \tag{2.2}$$

where

$$k^2 = \frac{2mE}{\hbar^2}. \tag{2.3}$$

For region B, Schrödinger's equation is

$$-\frac{\hbar^2}{2m}\frac{\mathrm{d}^2\Psi_2}{\mathrm{d}x^2} + u\Psi_2 = E\Psi_2 \tag{2.4}$$

and we can write

$$\Psi_2 = Be^{\chi x} + Ce^{-\chi x} \tag{2.5}$$

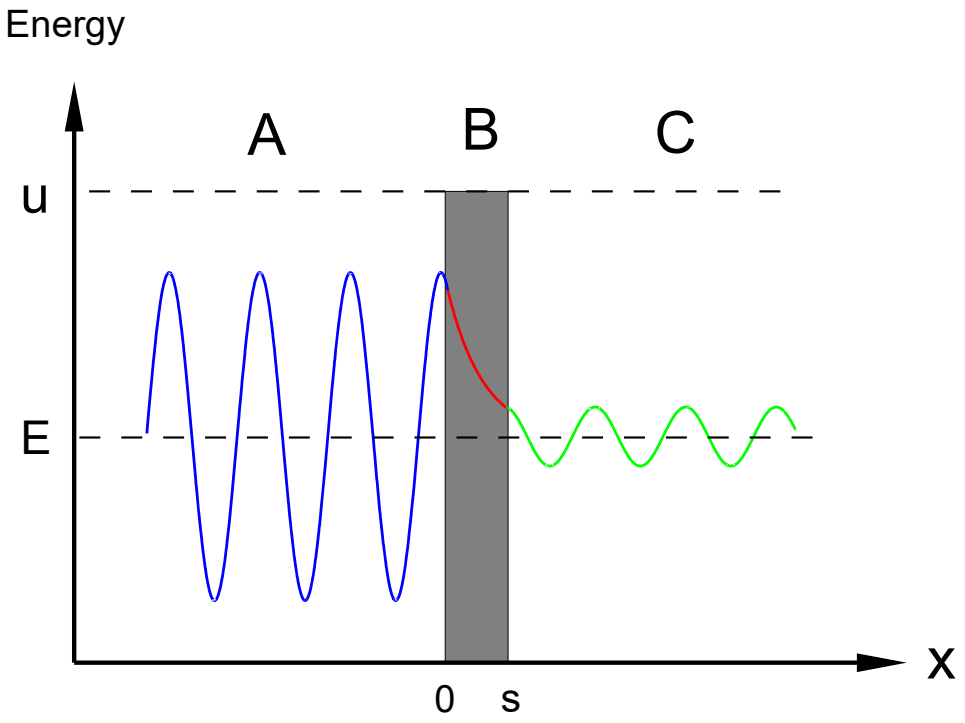

Figure 2.1: A particle with energy E is incident from the left in region A. In region B, the potential barrier u is larger than the energy E, but there is some probability for the particle to penetrate through the barrier into C.

where

$$\chi^2 = \frac{2m(u-E)}{\hbar^2}. \tag{2.6}$$

For region C, Schrödinger's equation is

$$-\frac{\hbar^2}{2m}\frac{\mathrm{d}^2\Psi_3}{\mathrm{d}x^2} = E\Psi_3 \tag{2.7}$$

and

$$\Psi_3 = De^{ikx} \tag{2.8}$$

where

$$k^2 = \frac{2mE}{\hbar^2}. \tag{2.9}$$

The rate at which electrons go through the barrier determines the tunnel current. This is calculated from the ratio of the transmitted current density j_t to the incident current density j_i; *i.e.* the transmission coefficient is $T{=}j_t/j_i{=}(\hbar k/m)|D|^2/(\hbar k/m){=}|D|^2$. By matching the wave function and the first derivative of the wave function at the boundary $x = 0$ and $x = s$, one finds [62]

$$T = \frac{1}{1 + (k^2+\chi^2)/(4k^2\chi^2)\sinh^2(\chi s)} = |D|^2. \tag{2.10}$$

Assuming a relatively high and wide barrier, so that the wave function in the barrier is strongly attenuated,

$$T \approx \frac{16k^2\chi^2}{(k^2+\chi^2)^2} e^{-2\chi s} \tag{2.11}$$

where from Eq. (2.6) χ is given by

$$\chi = \frac{\sqrt{2m(u-E)}}{\hbar}. \tag{2.12}$$

The factor $e^{-2\chi s}$ in Eq. (2.11) is crucial for STM tunneling because it indicates that the current depends exponentially on the barrier width s. Assuming a barrier width of $s = 5$ Å and effective vacuum barrier height of $u - E = 4$ eV gives $T \sim 10^{-5}$. For these parameters, changing the barrier width by 1 Å will change the barrier transmission by an order of magnitude.

Figure 2.2 shows a schematic of the setup of an STM, including an atomically sharp conducting tip, a vacuum tunnel barrier and the surface of a conducting sample. To control the x, y and z motion of the tip, the tip is attached to a piezoelectric scanner that has five electrode plates (x^+, x^-, y^+, y^-, z) insulated from each other. Applying voltage to specific electrodes causes the tip to move in x, y or z due to the piezo shrinking or expanding, depending on the voltage applied. When the tip is brought very close to the sample and a voltage is applied between the sample and the tip (typically mV to a few volts), a small current (typically in nA range) tunnels through the vacuum gap between the tip and sample. The tunneling

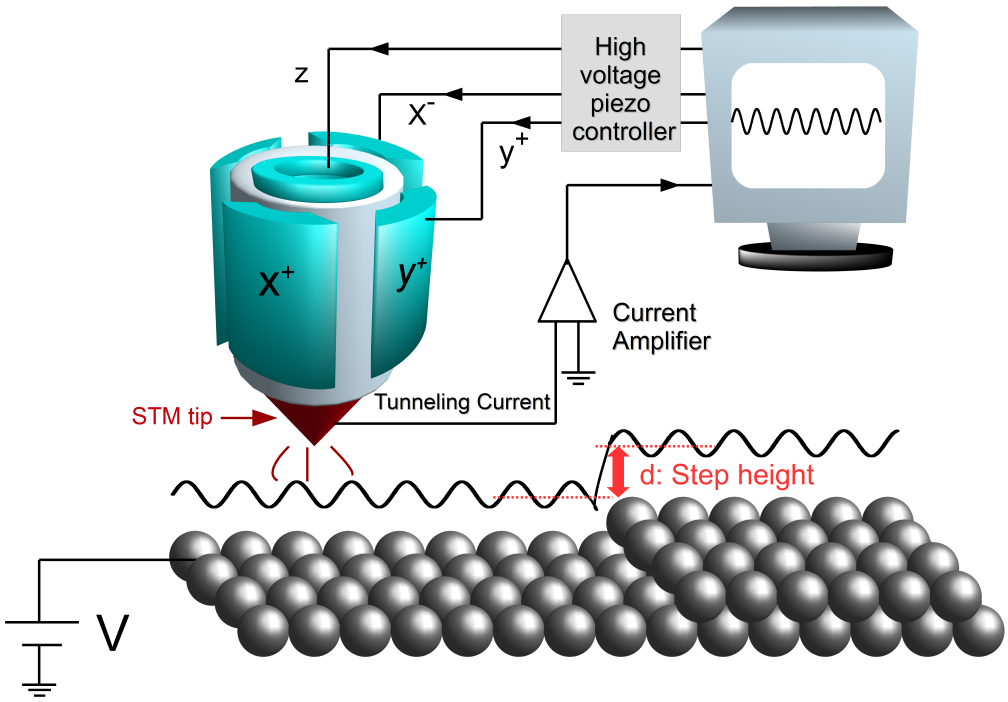

Figure 2.2: Schematic diagram of STM setup. The tip position is controlled by applying voltages to the x^+, x^-, y^+, y^-, z electrodes on the scan piezo. The tunneling current from the tip is detected when the sample is voltage biased and the tip is close to the sample. For topographic imaging, the voltage applied to the z electrode is adjusted to keep the tunneling current constant.

current is amplified and converted to a voltage which is fed to the control electronics. This voltage is compared to a set point and the difference is used to generate an error signal that is fed back to the z-piezo to keep the tip–sample separation constant. Because the tunnel current is extremely sensitive to the distance between the tip and the sample, the feedback forces the vertical motion of the tip to precisely follow the surface topography if the tip is moved laterally.

For a measureable tunneling current to be present, the tip has to be brought very close to the sample. This is done using a coarse approach mechanism, in our case a Pan-Style walker [63]. During the coarse approach, a dc bias voltage is applied to the sample and the tip is effectively grounded. For each step of the walker the tip typically moves forward a few 10s of nm. The z-piezo is then extended up to full range to see if the tunneling current increases. If no current signal is found, the z piezo is retracted, the walker moves one step closer toward the sample. This process is repeated until the tip is close enough to the sample that a tunneling current is detected.

Once the tip is in tunnel range, it is moved to an (x, y, z) position defined by the user. To raster scan an area, the lateral (x, y) motion is controlled by applying voltages to the x^+, x^-, y^+ and y^- electrodes. The vertical z-motion is controlled by the z-piezo feedback control electronics. Recording the voltage applied to the z-piezo as a function of the position (x, y) gives us the surface topography of the scan area.

2.3 Topographic imaging

As mentioned earlier, an STM tip has a 3D geometry and the 1D time-independent Schrödinger equation does not accurately model the situation. Tersoff and Hamann [60, 61] used time-dependent perturbation theory to model the 3-dimensional tip structure and calculate the corresponding current and conductance. Their theory also produced an exponential dependence of the current on the tip-sample separation, which is used in constant current mode of imaging. Moreover, they showed that the conductance is proportional to the density of states of the sample. This is particularly useful for spectroscopy and understanding images taken in the constant current mode. The other imaging mode I discuss in this section is the constant height mode. This mode is not used as much as the constant current mode, but it has some advantages in certain situations.

2.3.1 Constant current mode

In Section 2.2, I examined tunneling in one dimension and found the transmission through the barrier depended exponentially on the barrier thickness. Thus we expect that the tunneling current will obey

$$I \propto e^{-2\chi s}. \tag{2.13}$$

where χ is given roughly by Eq. (2.12) and s denotes the distance between the sample surface and the front of the tip. The useful feature for imaging is that the current is exponentially sensitive to the separation s.

A feedback loop is used to control the tip-sample separation so that the tunneling current between the tip and the sample remains constant. As such, the recorded z signal can be interpreted as the topography as a function of the position (x, y) of the sample.

2.3.2 Constant height mode

The main disadvantage of the constant current mode is the finite response time of the feedback loop, which limits the maximum scanning speed. This drawback also makes it harder to capture atomic scale features because the feedback responds less to high-frequency components of the tunneling current due to small surface features. An alternative is to use constant height mode, which involves turning off the feedback and recording the tunneling current while scanning in x and y. A significant drawback of constant height mode is that without feedback the tip is prone to crashing into the sample if it is not atomically flat.

In practice, samples can be scanned using a mixture of constant height and constant current modes. For this mixed mode, the system is set up for constant current mode, and as usual when the tip scans over a sharp feature, the feedback does not respond immediately and the current will not be constant. A map of the tunnel current versus position will thus show some contrast from sharp topographic

features. Thus by recording both the z-piezo voltage and the tunnel current, we can obtain mixed-mode images.

2.4 Spectroscopy

Besides being able to generate topographic images, STMs can also perform tunneling spectroscopy to measure electronic properties of a sample at the atomic scale such as the local density of states (LDOS). Tunneling spectroscopy typically involves moving to a fixed location, turning off the feedback, and then sweeping the bias voltage V while recording the tunneling current I. The feedback is then switched back on to prevent the tip from drifting into the sample.

In standard voltage-biased spectroscopy, voltage V is applied to the sample while the current I and the conductance $\mathrm{d}I/\mathrm{d}V$are acquired. The resulting $I-V$ or $\mathrm{d}I/\mathrm{d}V-V$ characteristics depend on the materials used in the junction. Next, I examine the standard cases of normal-insulator-normal (N-I-N) tunneling, normal-insulator-superconductor (N-I-S) tunneling and superconductor-insulator-superconductor (S-I-S) tunneling. In the standard approach [64] the tunnel barrier is assumed to be relatively high so that Andreev reflection effects [44] can be neglected. In Chapters 5 and 7 I present a more general discussion of $I-V$ characteristics, including effects from the Andreev processes in N-I-S and S-I-S junctions. In addition to voltage-bias spectroscopy, I also briefly discuss current-bias spectroscopy, which I used for investigating S-I-S junctions as described in Chapter 8.

As Tersoff and Hamann [60, 61] emphasized, it is important to understand that the conductance $\mathrm{d}I/\mathrm{d}V$ can produce direct information about the local density of states (LDOS) of a sample. In principle, one could measure the current at finely spaced voltages V and then numerically take a derivative of the current with respect to the voltage. However the result tends to be extremely noisy. Instead we add a sinusoidal modulation to the DC bias voltage so that $V(t) = V_0 + A\sin\omega t$, and use a lock-in amplifier to measure the resulting current I_{ac} at the frequency ω. Using a Taylor expansion of the current

$$I(V) \approx I(V_0) + \left.\frac{dI}{dV}\right|_{V=V_0} A\cos\omega t + \mathcal{O}\left(A^2\right) \tag{2.14}$$

we see that the zeroth-order term is the non-modulated current $I(V_0)$. The amplitude of the first-order term is proportional to the derivative of the current, *i.e.* the conductance $G_n = \mathrm{d}I/\mathrm{d}V$. With a suitable choice of the drive frequency and lock-in time constant, the $I(V_0)$ and $\mathrm{d}I/\mathrm{d}V$ *vs.* V_0 data can be obtained simultaneously.

Another useful technique is the current-bias mode. The $I-V$ characteristics of an S-I-S Josephson tunnel junction is often acquired by sweeping the current while measuring the voltage across the junction. This is done because the voltage will remain zero until the bias current exceeds the critical current, at which point a voltage appears across the junction. Depending on the junction parameters, the voltage may jump discontinuously from zero to a substantial value, typically on the order of the gap. In this case one also typically sees hysteretic behavior when the current sweeping direction is reversed, this hysteretic behavior is obscured by

voltage-biased technique.

Naaman *et al.* [33], for example, used the voltage-biased method to measure the $I-V$ characteristics of a superconducting tip and a Pb film junction. Unfortunately, the voltage-biased technique cannot tell the true behavior of the I(V) because of the discontinuity of the voltage jump when the critical current is exceeded. In my work, I modified the existing STM electronics to take both voltage-biased and current-biased I-V characteristics for a given junction resistance.

Figure 2.3 shows schematics for the voltage-bias mode and the current-bias mode. Figure 2.3 (a) shows a conventional setup for tunneling spectroscopy in which voltage V_b is applied to the sample and the tunneling current I is recorded as a function of V_b. Figure 2.3 (b) shows the current-bias mode which has a resistor with a large resistance R connected in series with the STM junction to fix the current I passing through the junction. A differential amplifier is used to measure the voltage V across the junction as a function of the current I. If the resistance R is much larger than the junction resistance, *i.e.* $R \gg R_J$, the current can be found from the applied voltage V_b divided by R. Otherwise, $I = V_b/(R + R_J)$ and the junction resistance needs to also be taken into account to find the current flowing through the junction.

2.4.1 N-I-N tunneling

Figure 2.4 shows a schematic diagram of electron energy levels for N-I-N tunneling. Figure 2.4 (a) shows the situation in thermal equilibrium with no applied

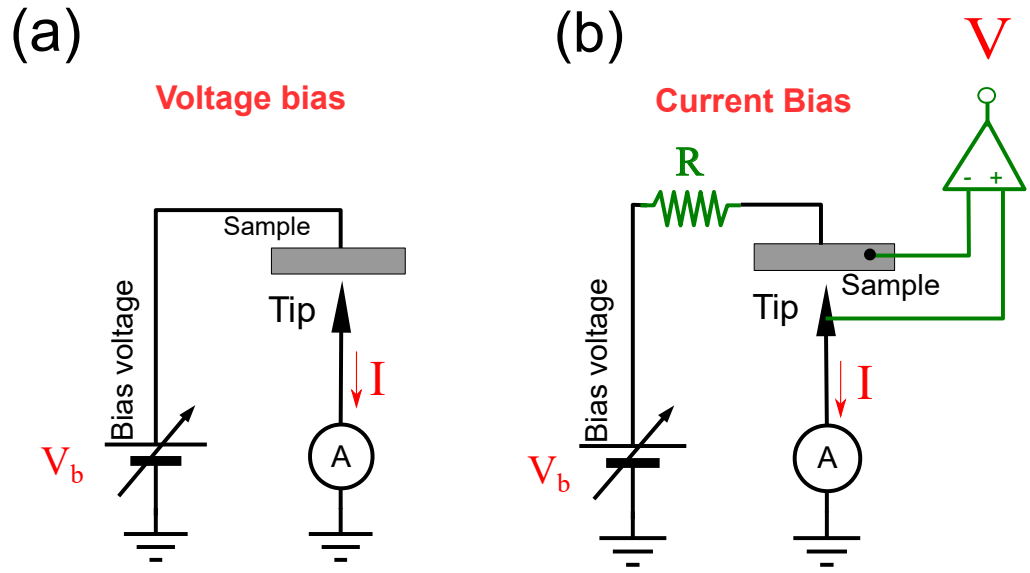

Figure 2.3: (a) Schematic diagram of spectroscopy mode using voltage bias V_b in which a voltage is applied to the sample and the current I flowing through the junction is measured with a current preamplifier. (b) In current-bias mode, a large resistor R is connected in series with the junction to set the current I through the junction and the voltage V across the junction is measured using a differential amplifier.

voltage so that both Fermi levels are aligned (the shaded light blue areas indicate filled states). Figure 2.4 (b) shows the situation when the right normal metal has a voltage +V applied while the left electrode is grounded (0 V). As shown, this effectively raises the Fermi level of the left electrode with respect to the Fermi level of the right electrode and causes a net flow of electrons from the left to the right. To calculate the net tunneling current, we need to find the difference between the rightward and leftward currents. Following Tinkham [64] we can write the current flowing from the left electrode to the right electrode as

$$I_{L\to R} = \frac{4\pi e}{\hbar}\int_{-\infty}^{\infty} |M|^2 N_1(\epsilon - eV) f(\epsilon - eV) N_2(\epsilon)(1 - f(\epsilon))d\epsilon \tag{2.15}$$

where $N_1(E)$ is the density of states on the left, $f(\epsilon) = 1/(e^{(E-\mu)/k_BT} + 1)$ is the Fermi distribution and M is the tunneling matrix element. Here $N_1(\epsilon - eV)f(\epsilon)$ represents the filled states in the left electrode and $N_2(\epsilon)(1 - f(\epsilon))$ represents the empty states in the right electrode. Similarly, the current flowing from the right electrode to the left electrode is

$$I_{R\to L} = \frac{4\pi e}{\hbar}\int_{-\infty}^{\infty} |M|^2 N_2(\epsilon) f(\epsilon) N_1(\epsilon - eV)(1 - f(\epsilon - eV))d\epsilon. \tag{2.16}$$

The total current flowing from left to right is then

$$\begin{aligned} I &= I_{L\to R} - I_{R\to L} \\ &= \frac{4\pi e}{\hbar}\int_{-\infty}^{\infty} |M|^2 N_1(\epsilon - eV)N_2(\epsilon)[f(\epsilon - eV)(1 - f(\epsilon)) - (1 - f(\epsilon - eV))f(\epsilon)]d\epsilon \\ &= \frac{4\pi e}{\hbar}\int_{-\infty}^{\infty} |M|^2 N_1(\epsilon - eV)N_2(\epsilon)[f(\epsilon - eV) - f(\epsilon)]d\epsilon \end{aligned} \tag{2.17}$$

Let's look at how Eq. (2.17) behaves at $T = 0$. Notice on the left side that for $\epsilon > eV$, we have $f(\epsilon - eV) = 0$ (see region A in Fig. 2.4 (b)) while for $\epsilon > eV$ we have $f(\epsilon) = 0$ on the right. Therefore region A contributes no current. For $0 < \epsilon < eV$ (region B in Fig. 2.4 (b)), we have $f(\epsilon - eV) = 1$ for the left electrode and $f(\epsilon) = 0$ for the right. Therefore $[f(\epsilon - eV) - f(\epsilon)] = 1$ and Eq. (2.17) gives a net current in this region. Finally for $\epsilon < 0$, we have $f(\epsilon - eV) = f(\epsilon) = 1$ in both the left and right electrode (see region C in Fig. 2.4 (b)) and therefore this region contributes no current.

Given the behavior of the Fermi function at $T = 0$, the integration range in Eq. (2.17) can be cut off at zero and eV, and Eq. (2.17) becomes

$$I = \frac{4\pi e}{\hbar}\int_{0}^{eV} |M|^2 N_1(\epsilon - eV)N_2(\epsilon)d\epsilon \tag{2.18}$$

For typical metals of interest, we can take $N_1(\epsilon - eV)$ and $N_2(\epsilon)$ as constants $N_1(0)$ and $N_2(0)$, the density of states at the Fermi level. Similarly, we will assume that

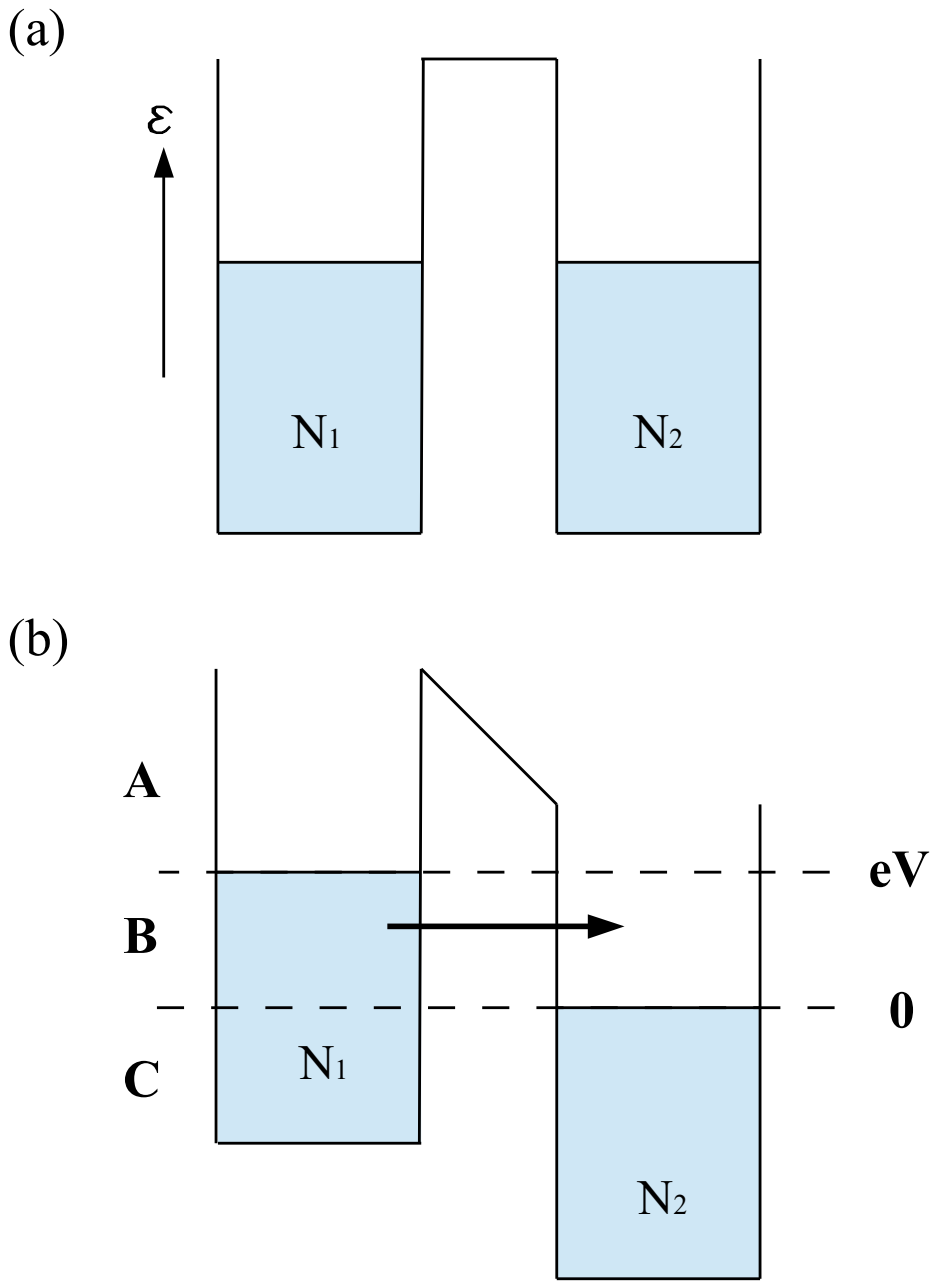

Figure 2.4: (a) Schematic of the density of states in N-I-N tunneling at $T = 0$ for ideal normal metals when no voltage is applied. (b) The right electrode is biased at voltage V above the left electrode, which effectively raises the Fermi level of the left electrode, causing a net flow of electrons from the left to the right electrode.

$|M|^2$ is independent of energy and this then gives

$$\begin{aligned} I &= \frac{4\pi e^2}{\hbar}|M|^2 N_1(0)N_2(0)V \\ &= G_{NN}V \end{aligned} \tag{2.19}$$

where the conductance of the N-I-N junction is

$$G_{NN} = \frac{4\pi e^2}{\hbar}|M^2|N_1(0)N_2(0) \tag{2.20}$$

For the same assumptions except that $T > 0$, one finds the same result [64]. Therefore we see that an N-I-N junction acts like an ideal, temperature-independent ohmic resistor.

2.4.2 N-I-S tunneling

The situation becomes more interesting if one electrode is superconducting. Tunneling experiments conducted by Giaever and Megerle [65] between a superconductor and a normal metal demonstrated that the superconducting gap could be measured electrically and this helped to further establish the validity of the BCS theory.

We can apply Eq. (2.17) to the N-I-S situation by writing [64]

$$I_{\mathrm{NS}} = \frac{4\pi e}{\hbar}\int_{-\infty}^{\infty}|M|^2 N_{n1}(\epsilon - eV)N_{s2}(\epsilon)[f(\epsilon - eV) - f(\epsilon)]d\epsilon, \tag{2.21}$$

where $N_{n1} = N_{n1}(0)$ is the density of states of the normal metal on the left and

$$N_{s2} = \begin{cases} \frac{|E|}{\sqrt{E^2-\Delta^2}} N_{n2}(0) & \text{for } |E| > \Delta \\ 0 & \text{for } |E| < \Delta \end{cases} \tag{2.22}$$

is the density of states of the superconductor on the right where $N_{n2}(0)$ is the density of states of the normal state of electrode 2. Figure 2.5 illustrates the situation for $T = 0$. Note that if the voltage V applied to the superconducting electrode is smaller than Δ/e, where Δ is the superconducting gap, there are no states for the electrons from the normal side to tunnel into the superconducting electrode. Therefore there is no tunneling current unless $eV > \Delta$. For $T = 0$, the Fermi function and superconducting density of states cut off the integration to the range $\Delta < \epsilon < eV$. For $T = 0$ and $V > \Delta/e$, Eq. (2.21) becomes

$$\begin{aligned} I_{\mathrm{NS}} &= \frac{4\pi e}{\hbar} \int_{\Delta}^{eV} |M|^2 N_{n1}(\epsilon - eV) N_{s2}(\epsilon) d\epsilon \\ &= \frac{4\pi e}{\hbar} \int_{\Delta}^{eV} |M|^2 N_{n1}(0) N_{s2}(\epsilon) d\epsilon \\ &= \frac{4\pi e}{\hbar} \int_{\Delta}^{eV} |M|^2 N_{n1}(0) N_{n2}(0) \frac{N_{s2}(\epsilon)}{N_{n2}(0)} d\epsilon \\ &= \frac{4\pi e}{\hbar} |M|^2 N_{n1}(0) N_{n2}(0) \int_{\Delta}^{eV} \frac{\epsilon}{\sqrt{\epsilon^2 - \Delta^2}} d\epsilon \\ &= \frac{G_{nn}}{e} \int_{\Delta}^{eV} \frac{\epsilon}{\sqrt{\epsilon^2 - \Delta^2}} d\epsilon \\ &= \frac{G_{nn} \sqrt{(eV)^2 - \Delta^2}}{e}. \end{aligned} \tag{2.23}$$

For $eV < \Delta$, one finds $I = 0$, while Eq. (2.23) gives the current I as function of

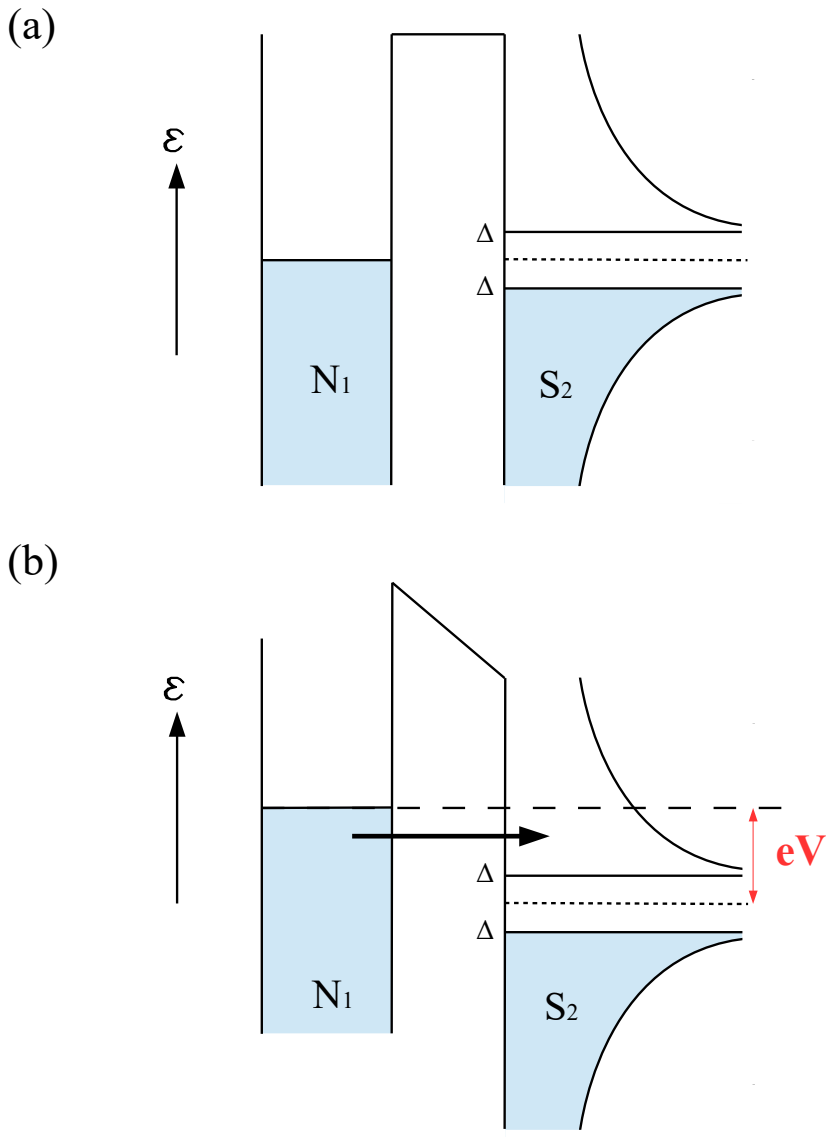

Figure 2.5: (a) Schematic drawing of energy diagram for N-I-S tunneling with no applied voltage. The left electrode (N_1) is normal while the right electrode (S_2) is superconducting. (b) The superconducting side (S_2) is voltage biased by V, causing the electrons to flow from the left to the right.

voltage V for $V > \Delta/e$. At $T = 0$, If we take the derivative of the current with respect to the voltage we can show that

$$G_{ns}(V) = \frac{dI_{ns}}{dV} = \begin{cases} \frac{G_{nn}eV}{\sqrt{eV^2-\Delta^2}} & \text{for } |eV| > \Delta \\ 0 & \text{for } |eV| < \Delta \end{cases} \tag{2.24}$$

Comparing Eq. (2.22) to Eq. (2.24) we see that the differential conductance $G_{ns}(V)$ has the same functional form as the superconducting density of state. This is an example of how $\mathrm{d}I/\mathrm{d}V$ can reveal the local density of states (LDOS), as Tersoff argued.

For $T > 0$, thermal broadening becomes important and we write

$$G_{ns} = \frac{dI_{ns}}{dV} = \frac{G_{nn}}{e}\int_{-\infty}^{\infty} \frac{\epsilon}{\sqrt{\epsilon^2 - \Delta^2}} \frac{\partial f(\epsilon - eV)}{\partial V} d\epsilon. \tag{2.25}$$

The function $\partial f/\partial V$ in Eq. (2.25) is a peak of width $k_B T$ and effectively rounds off the divergence in the density of states at the gap.

Figure 2.6 shows a plot of conductance *vs.* voltage for temperatures T= 50 mK (red), 300 mK (blue) and 1K (green) for $\Delta = 0.5$ meV. From the plot we can see there is a sudden rise of conductance around the value of superconducting gap; these are called coherence peaks. As Fig. 2.6 also shows, non-zero temperature smears out the coherence peaks.

This is a good place to briefly discuss the Dynes formula [66]. This formula has frequently been used to extract the superconducting gap from STM conductance measurements. Dynes *et al.* [66] argued that the finite lifetime of quasiparticles

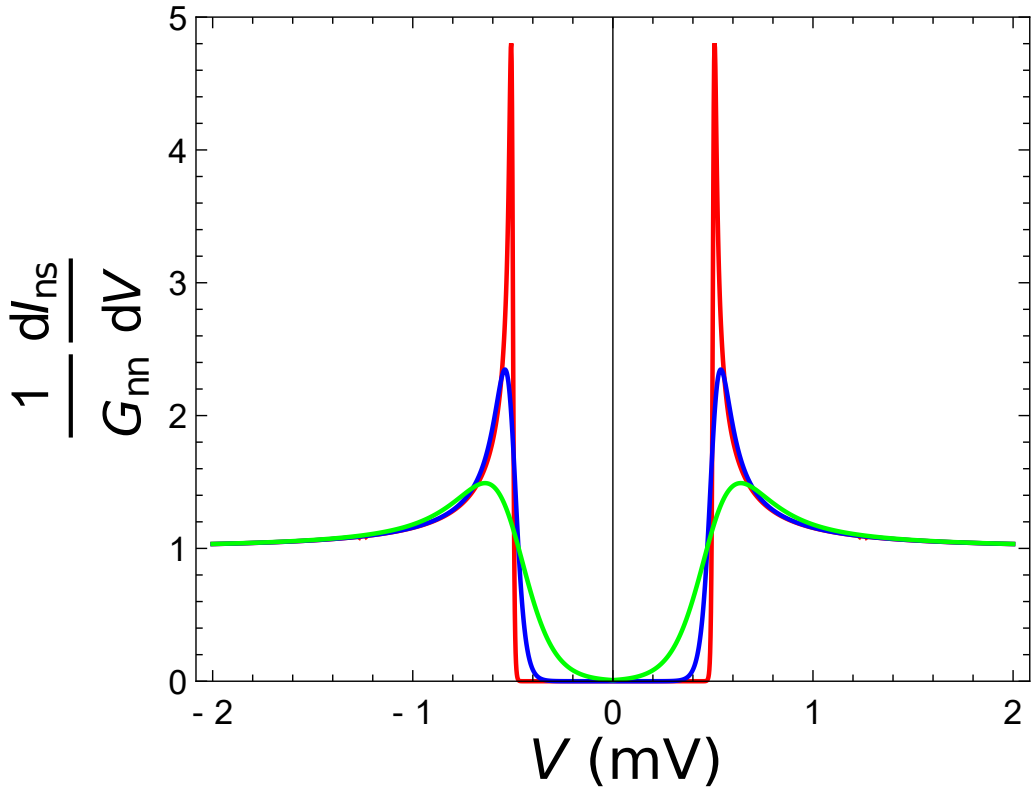

Figure 2.6: Plot of normalized conductance $\frac{1}{G_{nn}}\frac{\mathrm{d}I_{ns}}{\mathrm{d}V}$ *vs.* voltage V at different temperatures. The red curve is at 50 mK, the blue curve is at 300 mK, the green curve is at 1 K. In all three cases the superconducting gap $\Delta = 0.5$ meV. The temperature mainly broadens the coherence peaks, which occur at $V = \pm\Delta/e$.

would cause broadening of the coherence peaks. To account for the lifetime they modified the BCS density of states to :

$$\frac{N_s(\epsilon)}{N_n(0)} = \mathrm{Re}\left[\frac{\epsilon - i\Gamma}{\sqrt{(\epsilon - i\Gamma)^2 - \Delta^2}}\right] \tag{2.26}$$

where $\Gamma/\hbar$ is the quasiparticle scattering rate. The main effect of non-zero Γ is to cause broadening of the coherence peaks. The advantage of using this form is that it is simple to fit to conductance data because it is a simple analytical function. In contrast, application of Eq. (2.25) requires a careful numerical integration. Although the physical basis for Eq. (2.26) has been disputed, it captures the qualitative behavior and has found widespread application for extracting the superconducting gap value.

2.4.3 S-I-S tunneling

For S-I-S tunneling, Eq. (2.17) becomes [64]:

$$\begin{aligned} I_{\mathrm{SS}} &= \frac{4\pi e}{\hbar}\int_{-\infty}^{\infty} |M|^2 N_{s1}(\epsilon - eV) N_{s2}(\epsilon)[f(\epsilon - eV) - f(\epsilon)]d\epsilon \\ &= \frac{G_{nn}}{e}\int_{-\infty}^{\infty} \frac{N_{s1}(\epsilon - eV)}{N_{n1}(0)}\frac{N_{s2}(\epsilon)}{N_{n2}(0)}[f(\epsilon - eV) - f(\epsilon)]d\epsilon \\ &= \frac{G_{nn}}{e}\int_{-\infty}^{\infty} \frac{|\epsilon - eV|}{\sqrt{(\epsilon - eV)^2 - \Delta_1^2}}\frac{|\epsilon|}{\sqrt{\epsilon^2 - \Delta_2^2}}[f(\epsilon - eV) - f(\epsilon)]d\epsilon \end{aligned} \tag{2.27}$$

where $N_{s1}(\epsilon - eV)$ is the density of states in the left electrode, $N_{s2}(\epsilon)$ is the density of states in the right electrode, and G_{nn} is the conductance of the junction when

both electrodes are in the normal state.

Figure 2.7 shows the energy level diagram for S-I-S tunneling at $T = 0$. Notice that when $eV > \Delta_1 + \Delta_2$, quasiparticles will flow from one electrode to the other electrode, while for $eV < \Delta_1 + \Delta_2$, no current will flow. In general for $T \neq 0$ numerical integration is required to compute the $I - V$ curves. Figure 2.8 shows examples of $I - V$ characteristics obtained by numerical integration of Eq. (2.27) at temperatures of 300 mK (red), 3 K (blue) and 5 K (green). For these examples, I used $\Delta_1 = 1$ meV and $\Delta_2 = 0.5$ meV. All three curves show a sharp rise at $V = (\Delta_1 + \Delta_2)/e = 1.5$ mV. When the temperature is large enough, one also sees a sharp peak at $|\Delta_1 - \Delta_2|/e = 0.5$ mV and a region with negative differential resistance. Although the numerical integration is relatively straightforward, I did not see such peaks in my S-I-S tunneling data. Instead I saw step-like structures inside for $V < (\Delta_1 + \Delta_2)/e$. As I discuss in Chapter 7, this turned out to be due to multiple Andreev reflection (MAR) in junctions with relatively high transparency.

2.5 Cryogenic STM's

The superconductors that I investigated were TiN thin films, which had superconducting transition temperatures of $T_c \approx 4$ K, and a single niobium crystal with $T_c \simeq 9.2$ K. Clearly I needed to cool below T_c to see superconducting behavior. Furthermore, by using a much lower temperature, I could obtain less thermal broadening, and get much better resolution spectroscopic data.

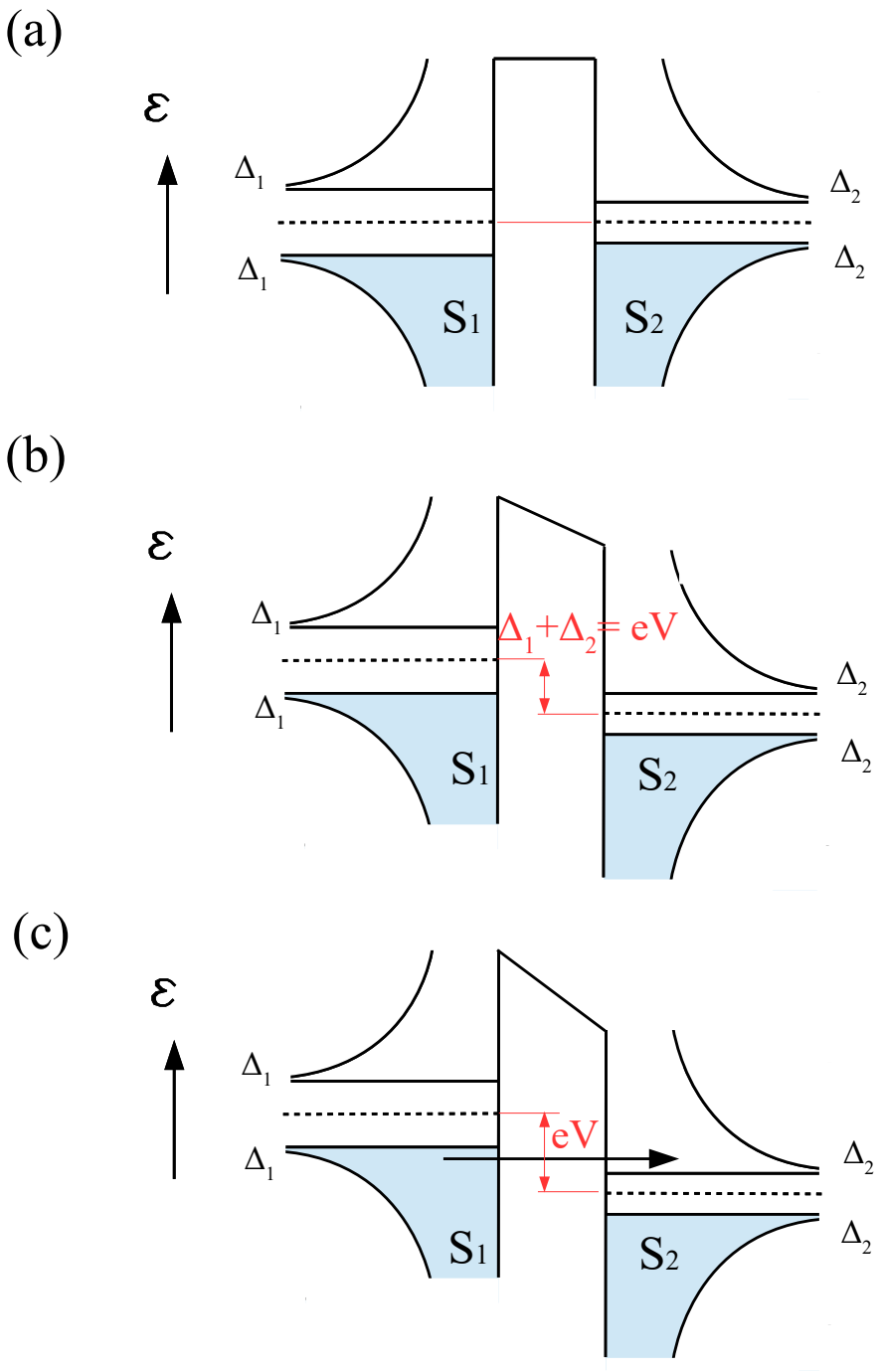

Figure 2.7: (a) Schematic drawing of electron energy levels in the left and right electrode for S-I-S tunneling at $T = 0$ for $V = 0$. (b) Energy levels for $V = (\Delta_1 + \Delta_2)/e$ and (c) $V > (\Delta_1 + \Delta_2)/e$. When the bias voltage V is greater than $(\Delta_1 + \Delta_2)/e$, a current will flow.

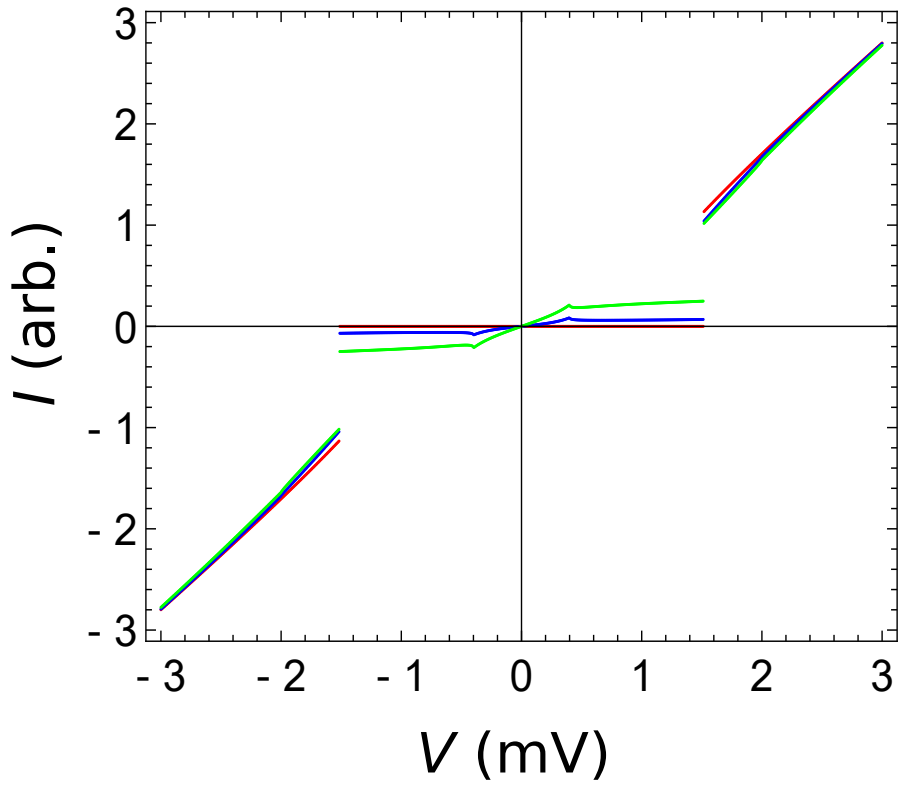

Figure 2.8: $I-V$ characteristics from numerical evaluation of Eq. (2.27) for S-I-S tunneling with $\Delta_1 = 1$ meV, and $\Delta_2 = 0.5$ meV. The red curve is for temperature $T = 300$ mK, the blue curve is for T =3 K, and the green curve is for $T = 5$ K. The current rises at $V = (\Delta_1 + \Delta_2)/e \simeq 1.5$ mV. At the higher temperatures, we see a current peak at the difference of the superconducting gaps $V = (\Delta_1 - \Delta_2)/e = 0.5$ mV.

Finally I note that a Josephson Scanning Tunneling Microscope (JSTM) must be operated at mK temperatures in order to see a measureable critical current [42, 67–70]. In a JSTM there are three important energy scales: the Josephson energy $E_J = \hbar I_0/2e$, the charging energy $E_C = e^2/2C$ and the thermal energy $k_B T$. I_0 is the critical current of the Josephson junction. In a standard STM setup, the capacitance of the tip-sample junction is on the order of fF and in my setup the critical current can be typically of order 1 nA. This leads to $E_J/k_B = 0.1$ K and $E_C/k_B = 1$ K. Therefore we need to cool our STM to $T \ll E_J/k_B$ or millikelvin temperatures using a dilution refrigerator to prevent phase diffusion from thermal excitation of the junction [34–36, 38, 71]. In addition, with $E_J << E_C$ charging effects become important and this leads to suppression of the critical current [64, 72–74] and even greater sensitivity to phase slips, as discussed in Chapter 7.

CHAPTER 3

Experimental Setup of the Millikelvin STM

In this chapter, I discuss details of the setup, construction and operation of our millikelvin scanning tunneling microscope and associated systems. In Section 3.1 I describe the working principle of a ^{3}He/^{4}He dilution refrigerator. Next in Sections 3.2, 3.3 and 3.4, I describe the design and operation of our dual-tip STM, including the wiring and filtering used from room temperature to the mK temperature stage. In Section 3.5 I discuss the accident in June 2016 which resulted in damage to the dilution refrigerator and the subsequent partial repairs which allowed compromised operation to about 0.5 K. I next describe the ultra high vacuum (UHV) sample preparation system (Section 3.6), which allowed me to prepare and transfer samples to the cold-stage while maintaining UHV conditions. Finally, I describe the operation and components of the control electronics (Section 3.7) and the preparation of Nb and vanadium STM tips (Section 3.8).

3.1 Dilution refrigerator

The working principle of a dilution refrigerator [75] is based on the behavior of liquid mixtures of ^{3}He and ^{4}He (see Figure 3.1). Liquid ^{4}He becomes superfluid [76] at 2.177 K (zero viscosity) and can flow without loss of kinetic energy. ^{3}He, which is a fermion, does not become superfluid until 2.491 mK [76]. By diluting the ^{4}He liquid with ^{3}He, the temperature of the superfluid transition is lowered. The boundary line is called the λ-line.

Above 67.5% atomic concentration of ^{3}He in ^{4}He , superfluidity does not exist. Interestingly, below 0.867 K, ^{3}He/^{4}He mixtures separate into two phases. One phase is rich in ^{3}He (the concentrated phase), and the other phase is rich in ^{4}He (the dilute phase). In the limit where the temperature of the mixture is zero, the concentrated phase becomes pure ^{3}He. However, the concentration of ^{3}He in the dilute phase does not approach zero as T goes to zero, rather it reaches a limiting concentration of 6.6% ^{3}He [75]. This phase separation and finite solubility of ^{3}He in ^{4}He is crucial to the operation of a ^{3}He-^{4}He dilution refrigerator.

Figure 3.2 shows a schematic diagram of a dilution refrigerator. For proper operation, the dilute/concentrated phase boundary should be in the mixing chamber, and the liquid level of the dilute phase should be in the still. Since ^{4}He is denser than ^{3}He, the concentrated phase floats on top of the dilute phase. The cooling power of the dilution refrigerator comes from the latent heat absorbed when ^{3}He atoms are transferred from the ^{3}He rich side to the ^{3}He poor side.

Examining Fig. 3.2, we see that the dilute phase extends from the still to the

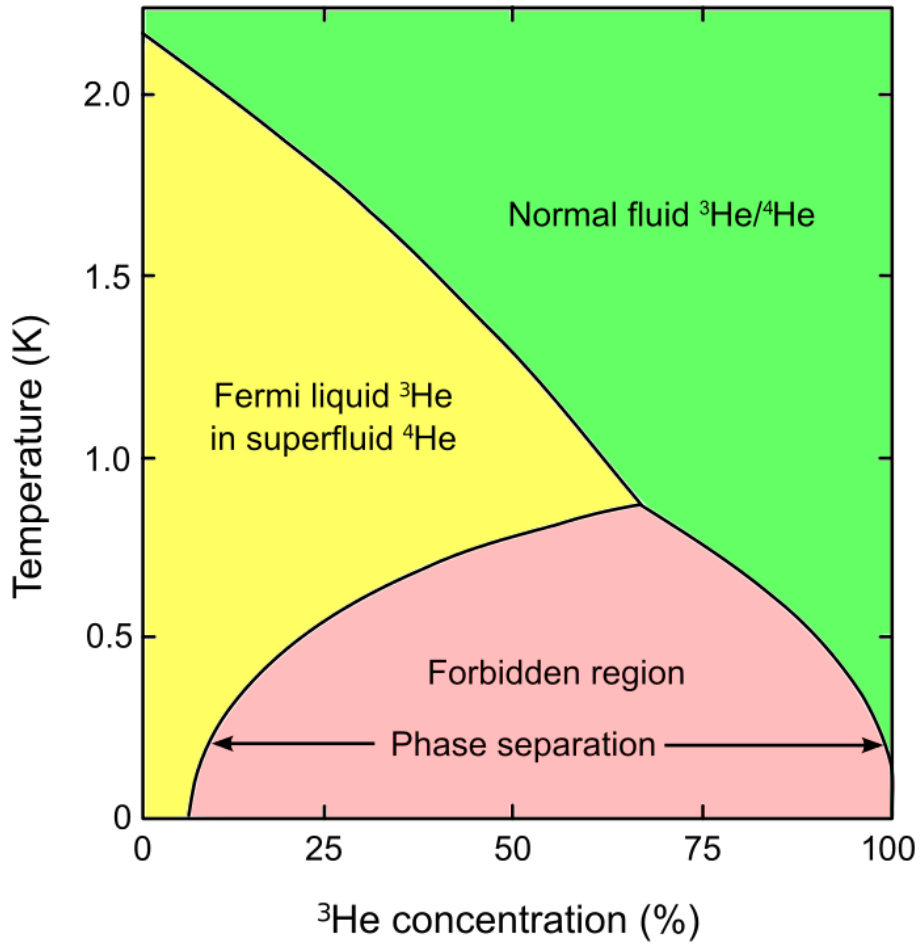

Figure 3.1: Phase diagram for ^{3}He/^{4}He mixtures from Ref. [75]. ^{4}He becomes superfluid at 2.177 K. Mixing ^{3}He with ^{4}He lowers the temperature of superfluidity boundary. At 0.87 K, liquid helium separates into two phases: a dilute phase with mostly ^{4}He and a concentrated phase with mostly ^{3}He. Note that the dilute phase has 6.6 % ^{3}He at 0 K.

mixing chamber. A pumping line is attached to the top of the still. The still operates at about 0.7 K, at which temperature the vapor pressure of ^{3}He is much larger than the vapor pressure of ^{4}He, ensuring that mostly ^{3}He evaporates. The difference in ^{3}He concentration between the still and the mixing chamber creates an osmotic pressure gradient in the ^{3}He, which acts to reduce the ^{3}He concentration in the dilute phase in the mixing chamber. In the mixing chamber ^{3}He in the concentrated phase then crosses the phase boundary to the dilute phase in order to maintain the 6.6 % ^{3}He concentration of the dilute phase. This process is effectively ^{3}He liquid evaporating into a ^{4}He vacuum and this absorbs latent heat. The latent heat is provided from the mixing chamber and results in cooling of the mixing chamber. In principle, there is no lower limit to the temperature that can be reached, but in practice heat leaks, heating of the flowing liquids and inefficiency of the heat exchangers limits the minimum temperature.

Most commercial refrigerators are now "dry" in that a separate 4K cryo-cooler is used for the initial cool-down and for cooling the returning ^{3}He gas. The additional cryogenic systems create some vibrations and noise, which are serious problems for the operation of a cryogenic STM. As a result, we use a "wet" refrigerator to cool our millikelvin STM system. This involves maintaining 4 K liquid ^{4}He around the vacuum space (see Fig. 3.2). This bath needs to be refilled with liquid helium as the liquid evaporates, but otherwise it is relatively free from vibration.

To cool the system from room temperature, I start by closing up the inner vacuum can (IVC)(see Fig. 3.2) and raising the custom made super-insulated liquid-helium cryostat [77]. I then fill this dewar with liquid nitrogen at 77 K and introduce

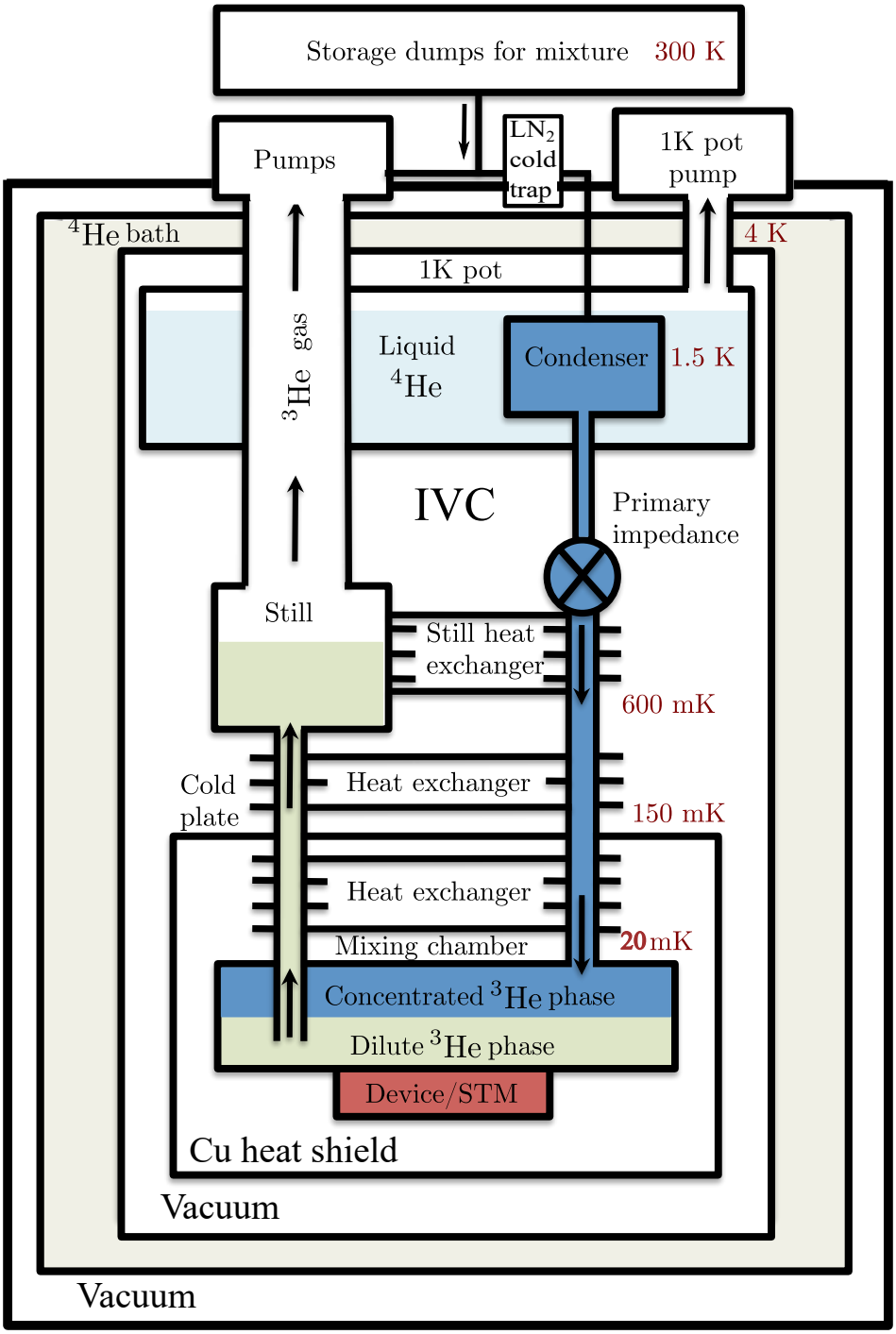

Figure 3.2: Schematic diagram of our dilution refrigerator.

a small amount of ^{3}He exchange gas into the inner vacuum can to thermally couple the dilution refrigerator unit to the 77 K bath (see Fig. 3.2). After about 1 day, the system has settled to 77 K and the liquid nitrogen is then removed. The dewar is then slowly filled with liquid helium to allow the refrigerator to cool to 4 K. Once the refrigerator is at 4 K, the exchange gas is pumped out so that the refrigerator stages are no longer thermally coupled to the bath.

With the system at 4 K and the exchange gas removed, we can begin to circulate the ^{3}He/^{4}He mixture. A small amount of mixture is released from the dump (a container that stores the mixture in gas form at room temperature) and passed through a nitrogen trap kept at 77 K. This removes impurities such as N_2 and O_2, as well as oil from the pumps. The mixture next flows through a liquid He cold trap which is inserted into the helium bath. This captures remaining impurities that were not captured from the nitrogen trap, such as H_2.

The mixture then flows into the condenser line and condenses at the 1 K pot which is actually at about 1.5 K. The 1 K pot is a small copper chamber which is connected to the ^{4}He bath through a capillary tube. Pumping on the pot sucks liquid helium from the bath and evaporation of the liquid in the pot causes cooling to about 1.5 K, which is not cold enough for the mixture to reach phase separation, but allows liquid to condense, cool and fill the heat exchangers, mixing chamber and still. To achieve phase separation, we pump on the still, which cools below 1.2 K due to evaporate of ^{3}He. The condensed mixture from the 1 K pot passes through the still heat exchanger and, as ^{3}He is preferentially pumped from the still, the still cools to the phase separation point. Additional pumping moves the phase boundary until

eventually it reaches the mixing chamber, which then cools to a base temperature of about 200 mK after several hours. With additional root pump running, it cools down to 20 mK.

3.2 Overall experimental setup of the millikelvin STM

Figure 3.3 shows the overall experimental setup of the millikelvin STM system [41]. A UHV sample preparation chamber and a UHV transfer chamber sit on top of an optical table in an rf-shielded room. The ^{3}He-^{4}He dilution refrigerator is mounted below the transfer chamber and the STM is bolted to the bottom of the mixing chamber. This design allows us to clean the sample under UHV conditions and transfer it into and out of the mK-STM without breaking vacuum, therefore preserving the quality of the sample surface. We use a horizontal magnetic transfer rod to bring samples from the preparation chamber to the transfer chamber. We then use a vertical magnetic transfer rod [41], which runs through the center axis of the dilution refrigerator to take the sample from the transfer chamber to the mK stage of the STM.

Our dilution refrigerator is a customized Oxford Instruments Kelvinox with a cooing power of 400 μW at 100 mK. The dilution refrigerator has an inner vacuum can (IVC) which is pumped to high vacuum using a scroll pump and a turbo pump prior to cooling down. The IVC and rest of the refrigerator insert sit in a custom made super-insulated liquid-helium cryostat [77]. It serves as a liquid helium bath

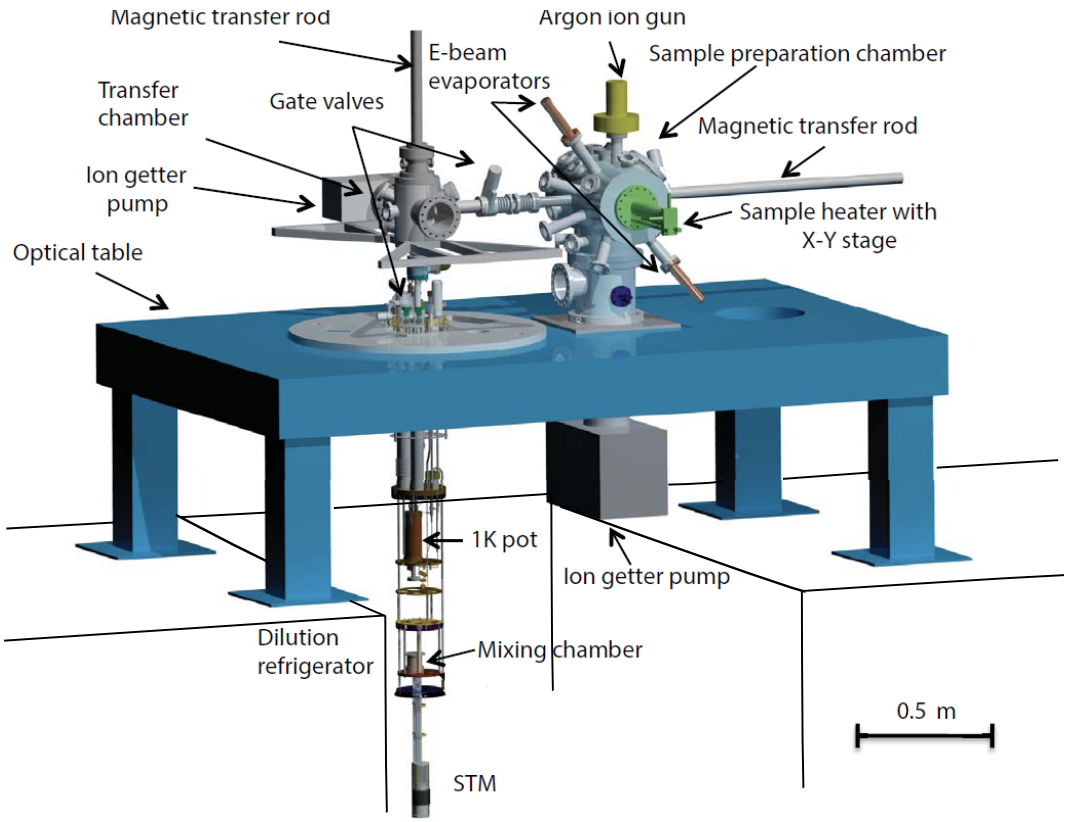

Figure 3.3: Illustration of mK-STM setup with UHV sample preparation chamber and transfer rods.

and enables our STM to thermally couple to the helium bath and cool to 4 K. The base temperature of the refrigerator was 6-7 mK, but due to the heat load from the large amount of wiring for the dual-tip STM [41], the actual operating base temperature was around 30-35 mK.

3.3 Dual-tip STM

Our STM is a highly modified co-axial Pan-style design [63] which has two independently controllable tips. The tips can be connected to operate in a SQUID configuration [42] with a superconducting sample. A detailed description of the dual-tip STM, including connection and characterization of the two electrically connected STM tips, can be found in Chapter 4.

Figure 3.4 shows the overall layout of the STM. The main body is made out of Macor. The sample is mounted on a sample stud (1) that is loaded from the top and the two STM tips (2) approach from below. The two STM tips are spaced about 1 mm apart with each tip attached to its own set of piezoelectric actuators [41]. Each tip is controlled by a piezoelectric walker (5,6) and scanner (3,4) which allow for coarse motion in z (vertical) and fine 3-D motion, respectively. The outer tip assembly is moved vertically (z) by the large outer walker, which also carries the smaller inner walker and inner tip assembly, thus moving the two tips together. The inner walker moves the inner tip vertically (z) relative to the outer walker [40, 41].

To monitor the movement of the walkers and tips, a capacitance bridge [78]

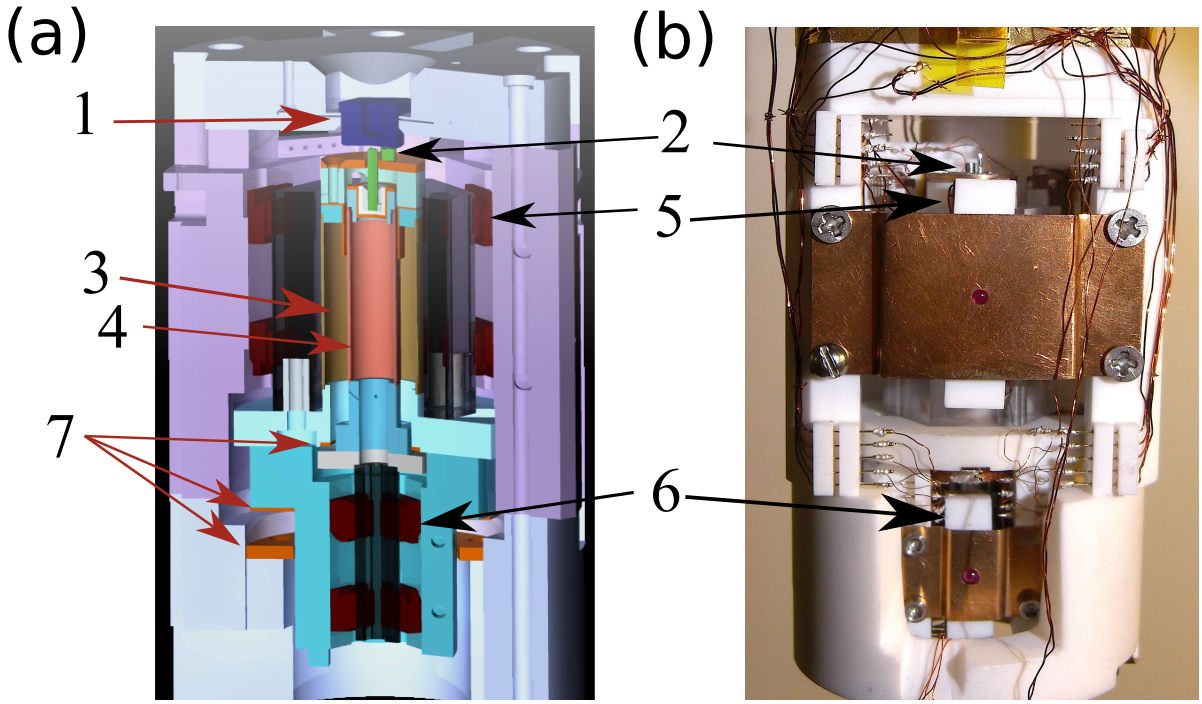

Figure 3.4: (a) Cross sectional view and (b) photograph of the dual-tip STM. Labels are (1) the sample stud, (2) two STM tips, (3) outer tip scanner, (4) inner tip scanner, (5) outer tip walker, (6) inner tip walker and (7) the capacitance sensor for the outer tip and the inner tip. Figure from [40].

was used to measure the capacitance (see Fig. 3.4) during the coarse approach of each tip to the sample. The capacitance sensor reading for the outer walker varied from 11 pF to 19 pF over the 24 mm z-range. For the inner walker, the capacitance sensor reading varied from 1.8 pF to 6 pF over the 8 mm range. At cryogenic temperatures, the maximum lateral scan range of the inner-tip piezo-tube scanner was about 2 μm while the lateral scan range of the outer-tip piezo-tube scanner was about 1 μm.

3.4 Wiring

We used two kinds of wires in our STM system to connect the room temperature electronics to the STM [41]. "Signal wires" were used for connecting to the two STM tips, for applying sample bias and for reading out the two capacitance/monitor sensors. "Drive wires" were used for supplying control/drive signals to move the two walkers (6+6 lines), to drive the x-y-z motion of the tip piezos (5+5 lines) and for the thermometry lines.

In order to transmit the very small voltages or currents carried by the signal wires, the wired need to be well-shielded against rf pickup and microphonic noise. We also need to minimize heat flow between different refrigerator stages. This was done by using semi-rigid CuNi microcoax lines from 300 K to the mixing chamber stage. Figs. 3.5-3.10 show detailed views of the signal lines at each stage. To heat sink the wires as they went from 300 K to 30 mK, the coax was clamped to Cu

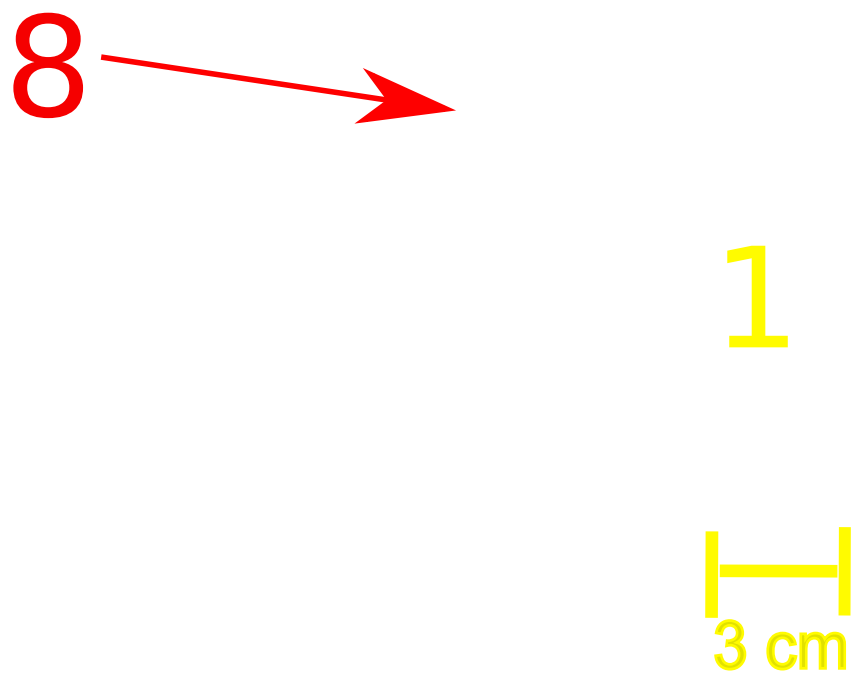

Figure 3.5: The 1 K pot (1) was custom built to 1.5 times the normal size. (8) NbTi microcoax signal wires are bolted to the Copper heat sinks.

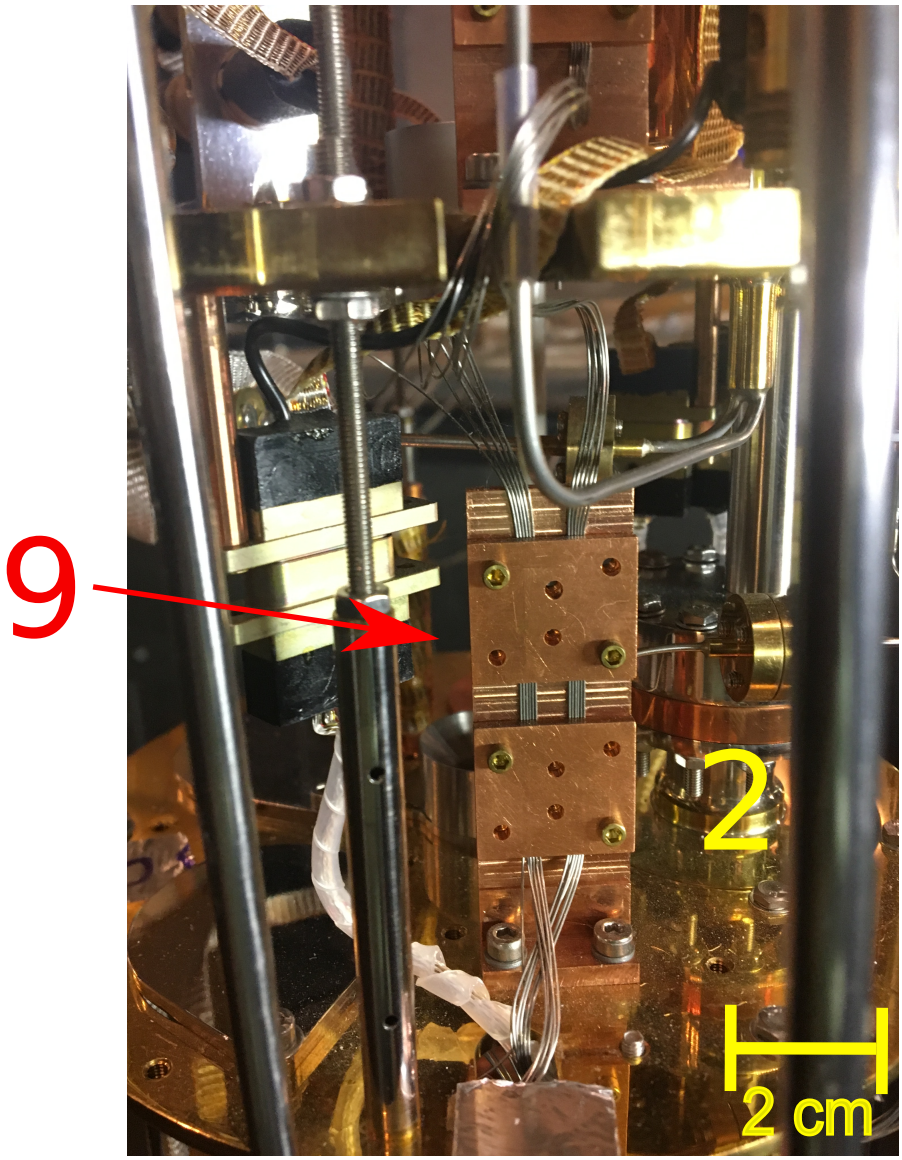

Figure 3.6: Label (2) indicates the still. NbTi microcoax signal wires are bolted to the Copper heat sinks (9).

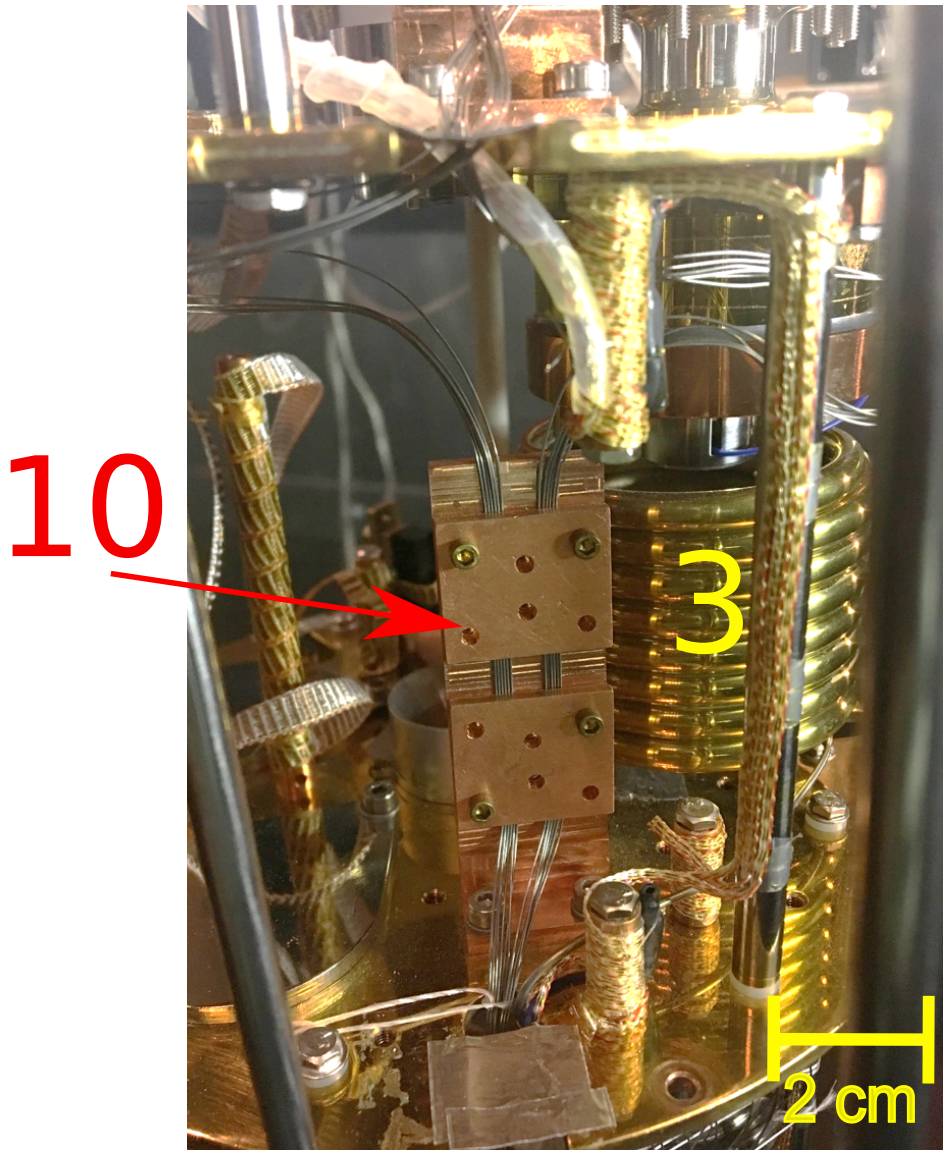

Figure 3.7: Label (3) indicates the ^{3}He/^{4}He heat exchanger. NbTi microcoax signal wires are bolted to the Copper heat sinks (10).

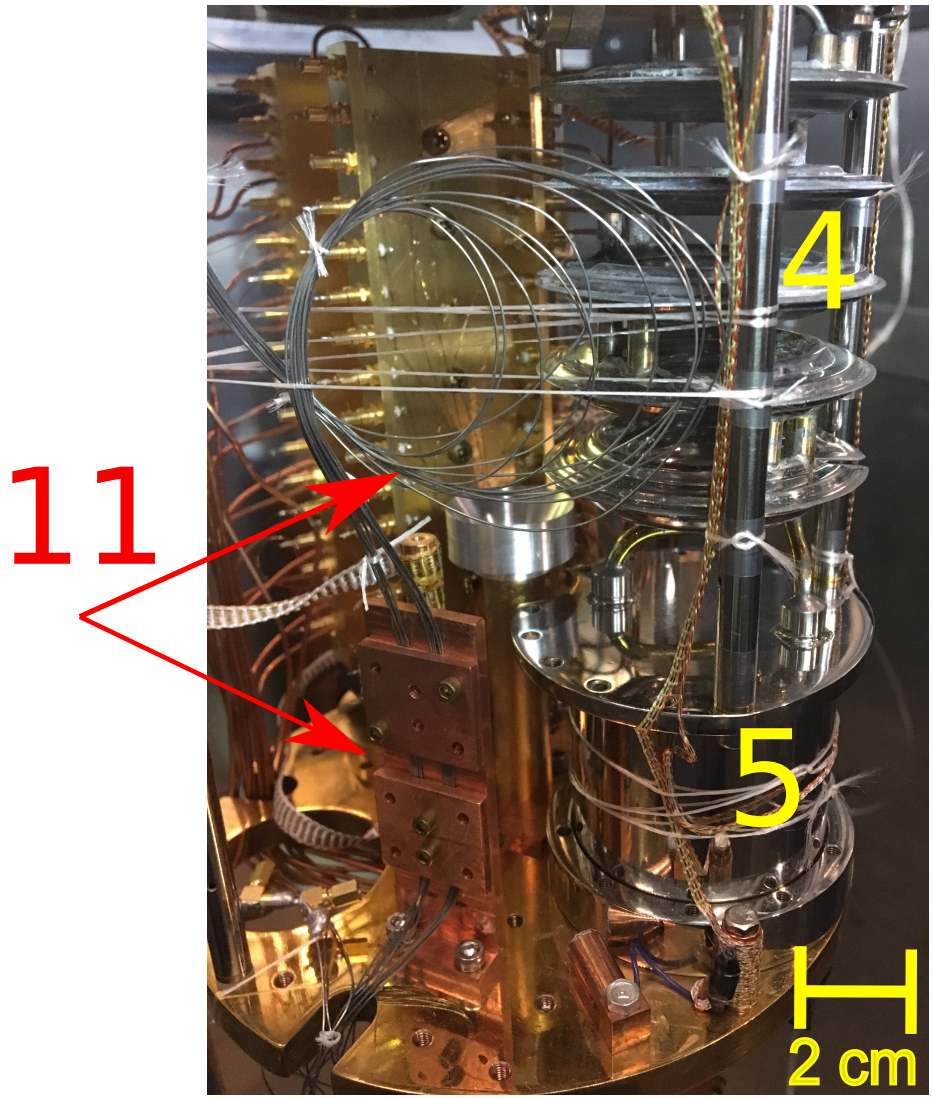

Figure 3.8: Label (4) indicates a sintered silver heat exchanger and (5) is the mixing chamber. (11) are NbTi microcoax signal wires, which are bolted to the Copper heat sinks.

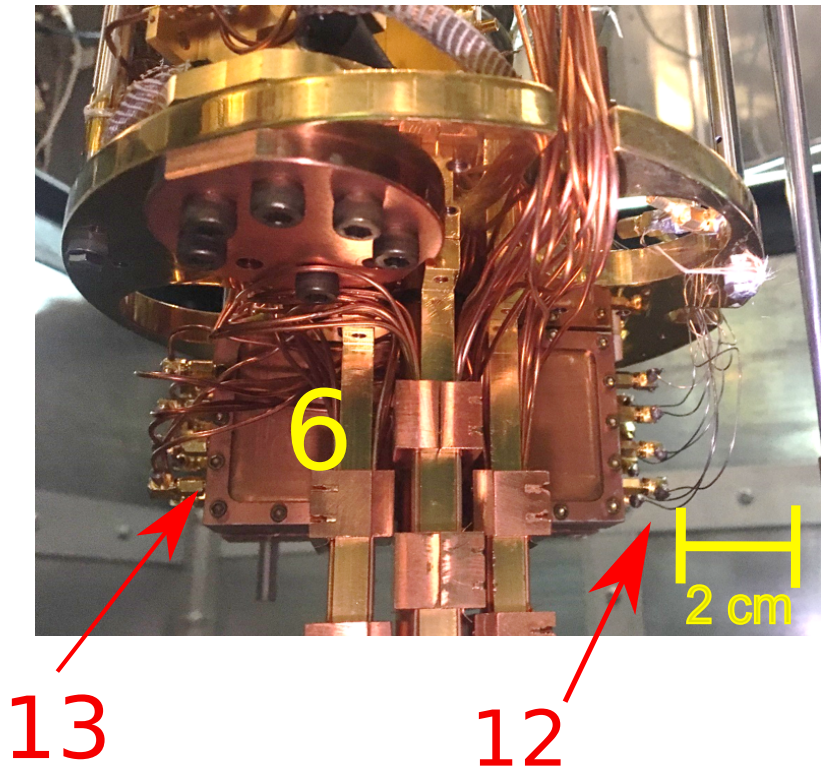

Figure 3.9: Label (6) is the bronze powder filter. The NbTi microcoax wires (12) entered the bronze powder filter with output on Cu coaxial wires (13) at the mixing chamber stage.

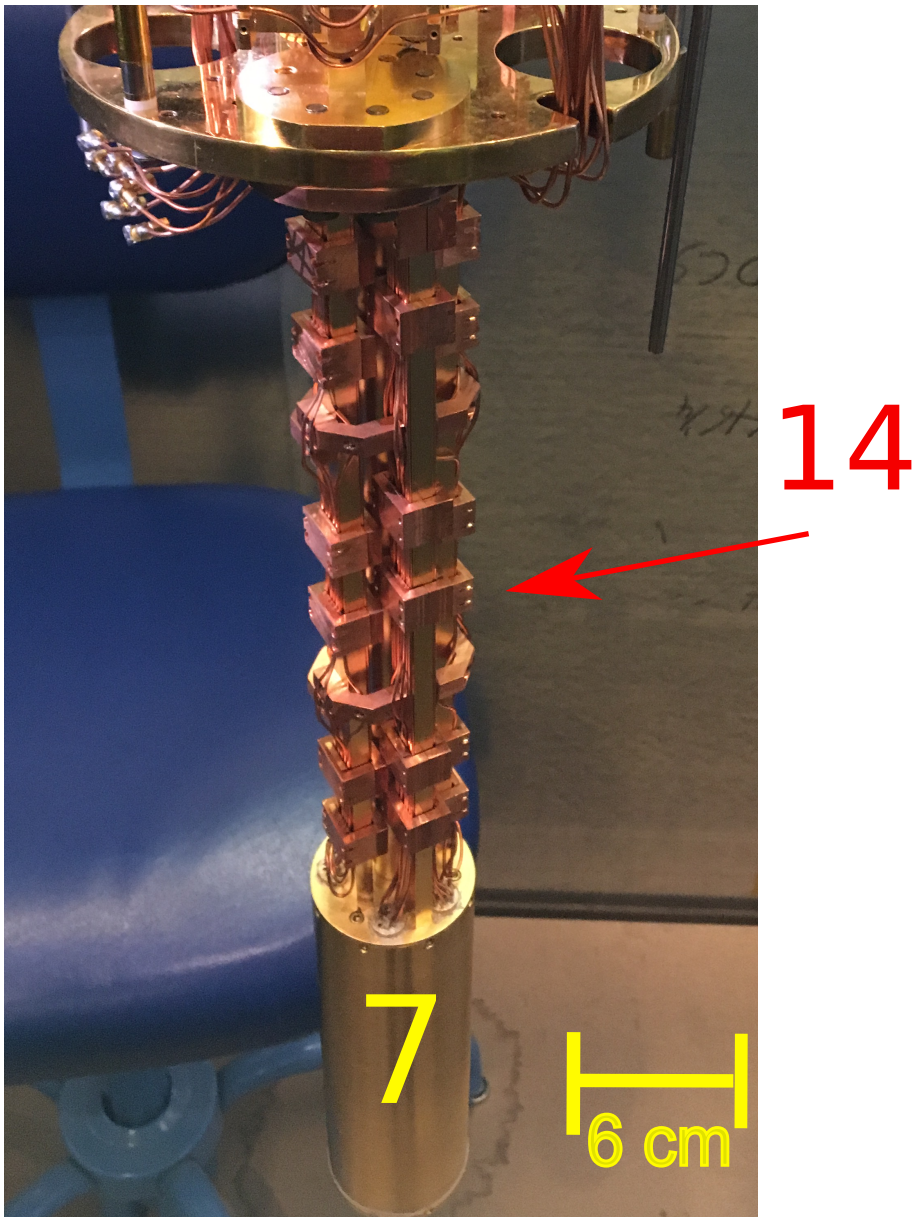

Figure 3.10: Label (7) is the can inside of which the STM is mounted. All of the Cu coaxial wires are heat sunk by clamps (14) that press the wires onto the Au-plated Cu extension.

posts at the 1K pot stage (see Fig. 3.5), the 600 mK still stage (Fig. 3.6), and 7.5 cm long posts at the 150 mK stage (Fig. 3.7). At the mixing chamber stage (Fig. 3.8), these microcoaxe lines were fed into bronze powder filters (Fig. 3.9) [79] with SSMC connectors. From the mK bronze powder filters to the STM (Fig. 3.10), the signal lines were made of semi-rigid coax with Cu shielding and an Ag-plated Cu inner conductor. The Cu coax lines helped to carry away heat from the STM tip and the sample. This was critical to cool the STM, since the main body of the STM were made from macor, which is very thermally insulating.

The drive wires were made from four Oxford Instruments wiring looms [80], each with 12 twisted pairs of 100 μm diameter wire. From 300 K to 1.4 K, two Constantan wiring looms were used as they provided a low heat load and resistances that varied only slightly with temperature. From 1.4 K to the mixing chamber, we used two CuNi-clad NbTi looms that were superconducting below 9 K. To ensure adequate thermal anchoring, the looms are wrapped around Cu heat sinks at each stage on the refrigerator. For the last section from the mixing chamber to the STM, semi-rigid Cu coax wires which are the same type used for the signal wires are used. Figure 3.11 shows detailed views of the looms and copper heat sinks at each stage. Figure 3.11 (a) shows the 1K pot. Figure 3.11 (b) shows the still and the heat exchanger at the still and the cold plate stage. Fig. 3.11 (c) shows the filters and wiring at the mixing chamber stage, while Fig. 3.11 (d) shows the filter and wiring section from the mixing chamber to the STM stage.

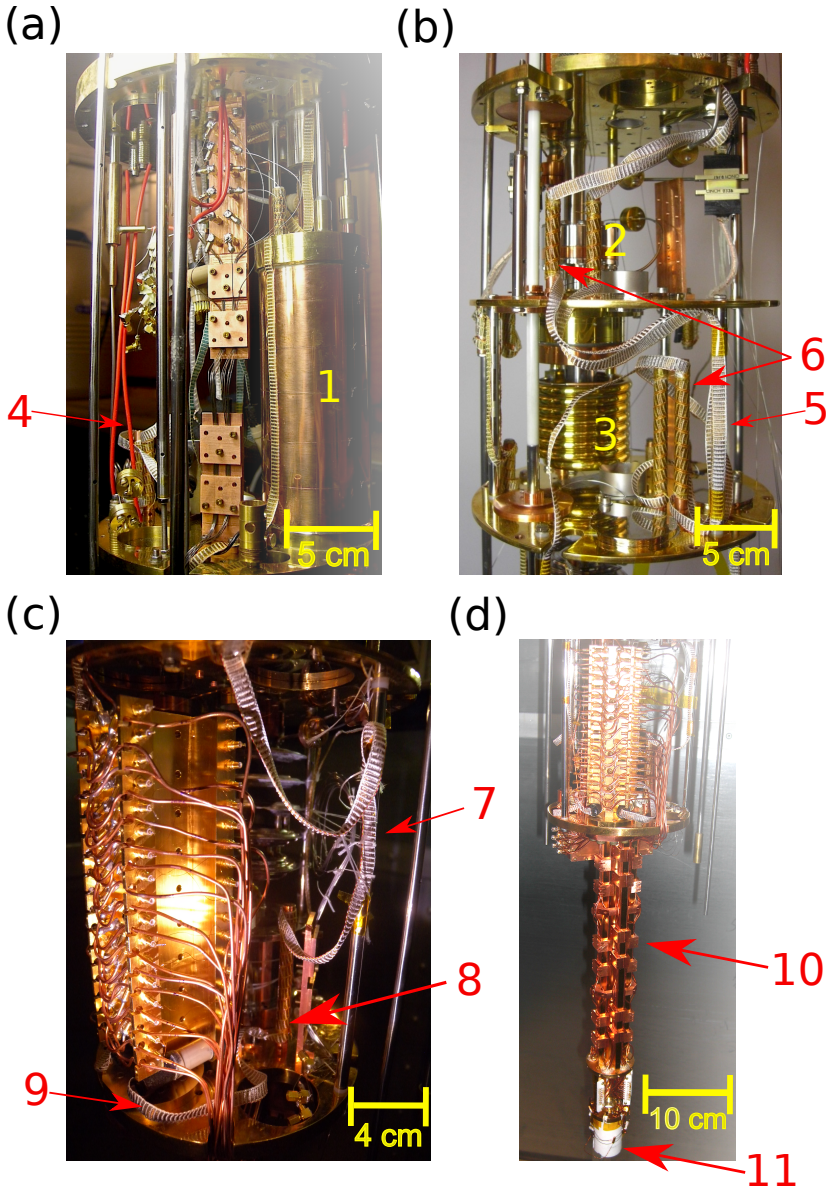

Figure 3.11: (a) Cylindrical heat sinks for the loom wires ((4),(5),(7) and (9)) are tightly bolted onto the 1K stage, (b) the still, and (c) the mixing chamber plate. (d) At the mixing chamber stage, the loom wires are soldered into a plug and connected to Cu coax lines using thin Cu wires. The signal wires and all Cu coaxial wires are heat sunk by clamps (10) that press the wires onto the Au-plated Cu extension. (11) is the STM.

3.5 Damage to the heat exchanger and partial repair

While the mixture was being removed early on June 29, 2016, a diaphragm valve between the still and the ^{3}He circulation pump broke. Air entered the system and created a complete blockage in the ^{3}He/^{4}He line. Since the 1K pot was not running at that time, the mixture slowly warmed up and eventually the remaining liquid in the refrigerator turned into gas. This caused one of the sintered silver heat exchangers to fail due to severe over-pressure and we ended up losing all the mixture. Figure 3.12 (a) shows a photograph of the broken sintered silver heat exchanger. The white objects are sintered silver plates from the inside of the heat exchanger, which increase the contact surface area with the mixture.

Due to limited funding we were not able to immediately replace the unit and instead, we applied a temporary fix to get the system back in operation. Figure 3.12 (b) shows the mixing chamber stage, detached from the rest of system. Figure 3.12 (c) shows the brass flange for the input line at the cold plate stage (2) and the bigger brass flange (3) for the still line.

To reseal the heat exchanger, I tested two solders. I first tried EutecRod 157 [81], which is a lead-free soft solder that can be used for joining capillary tubes. The second solder I tried was Wood's metal. The Wood's metal did not stick well to the surface of the heat exchanger, so I used the EuteRod 157 for the repair.

Figure 3.13 (a) shows the mixing chamber stage detached from the rest of the system and clamped onto a work table, ready for soldering. The soldering process was done at 450 °C using EutecRod 157 [81]. Once the soldering was done, a ^{4}He

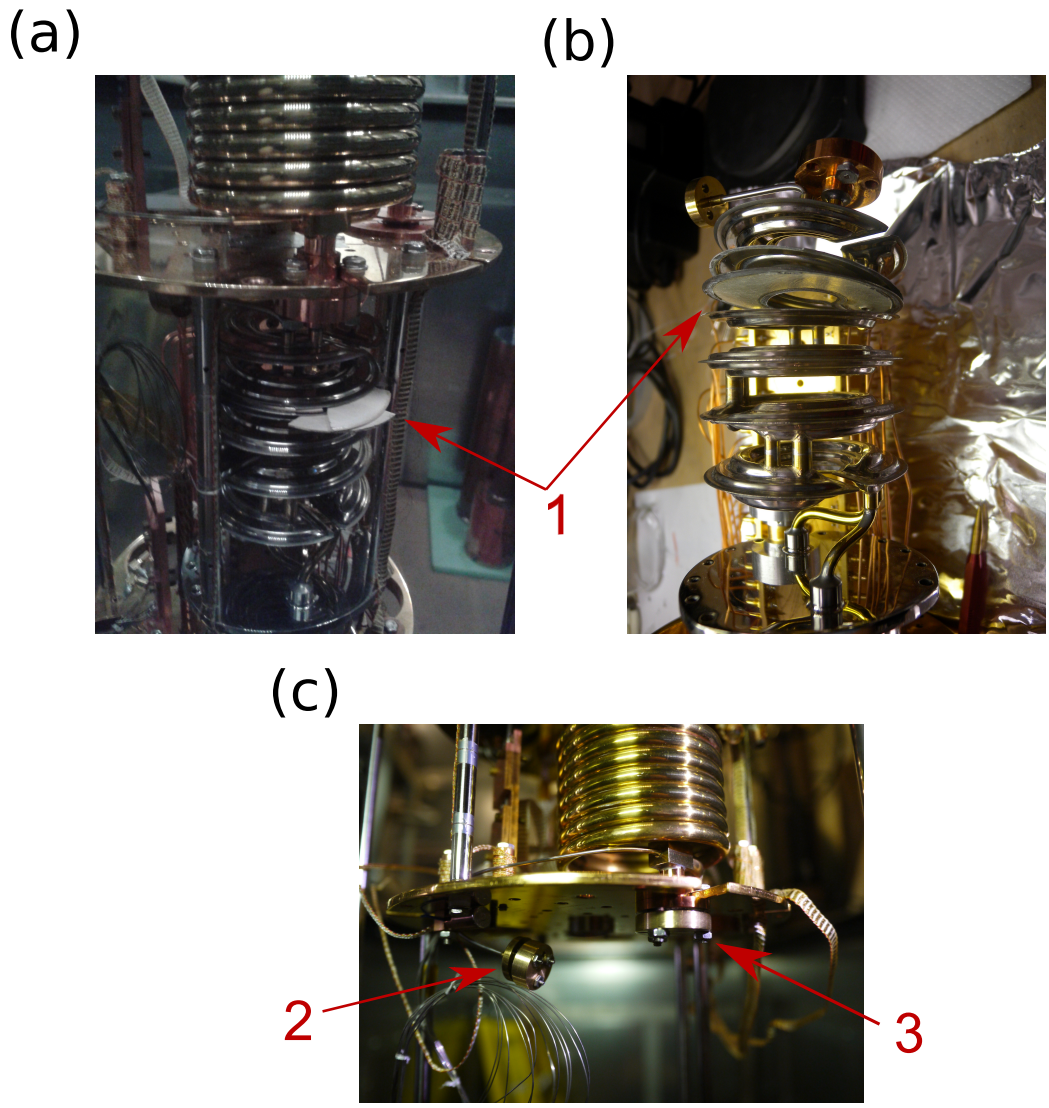

Figure 3.12: (a) and (b) show photos of the damaged second sintered silver heat exchanger. Label (1) indicates the second plate of the heat exchanger. (c) Photos of the brass flange connector (2) for the incoming line for the mixture, and the larger brass flange (3) for the return line that goes to the still.

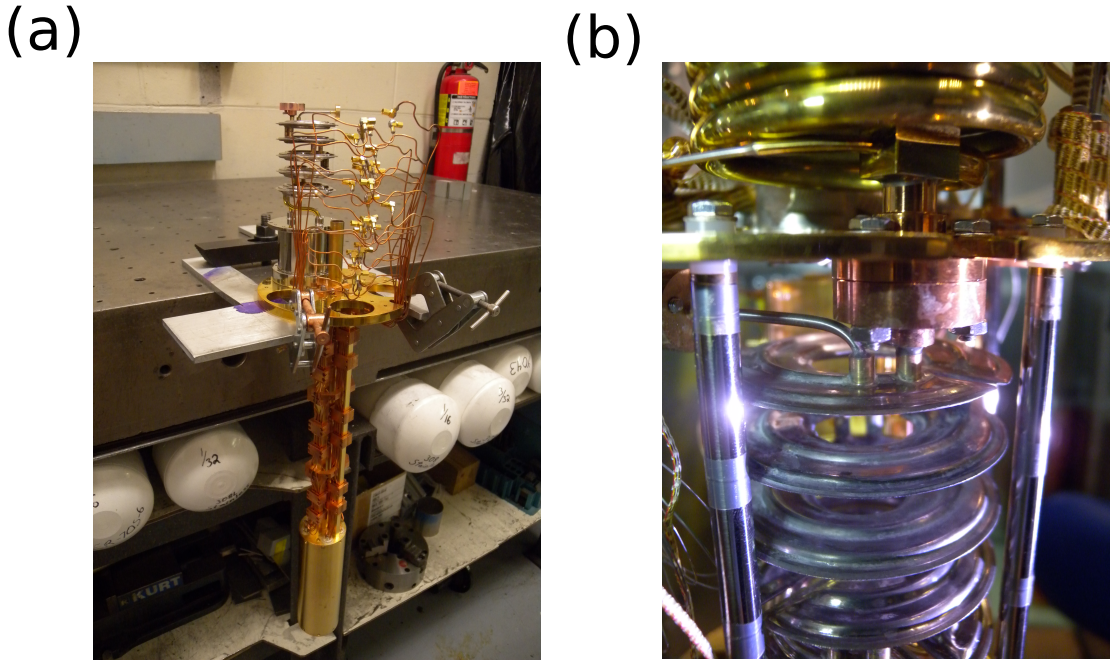

Figure 3.13: Photos of the re-sealed sintered silver heat exchanger. (a) The system is clamped onto a work table for soldering. (b) The repaired heat exchanger has been reattached to the dilution refrigerator. The color of the brass flange changed due to the soldering.

leak test was performed to verify the seal was leak tight at room temperature. After reassembling the dilution refrigerator system, we performed a leak test again with the system at 4 K. Figure 3.13 (b) shows the final result after the dilution refrigerator was reassembled.

After we replenished the mixture, the refrigerator was able to cool to a minimum temperature of only about 300 mK. However the operation was not stable and the phase boundary did not seem to be in the mixing chamber. We also found out that there was a cross leak between the input and output lines between the 1K pot and the still plate; presumably this leak was created during the accident. This was likely the main reason the system would not cool below 0.3 K. Nevertheless, the system was able to maintain a stable temperature at 500 mK and this was the temperature of the titanium nitride (TiN) data presented in Chapter 6.

3.6 Ultra high vacuum (UHV) system

Our STM system has a UHV preparation chamber and a transfer chamber that are separated by a gate valve (see Fig. 3.14). Each chamber has its own ion getter pump [82], titanium sublimation pump [83], and ion gauge [84]. To prepare the UHV environment for both chambers, we first pump it out using a turbo pump [85] backed by an oil-free scroll pump [86]. The chambers are then baked at 150 °C for 24 hours to remove water and allow outgassing.

The sample preparation chamber has a residual gas analyzer [87], two electron

beam evaporators [88], and an argon ion sputter gun [89] (see Fig. 3.15). The sample stage is attached to an XYZ manipulator [90]. Samples can be heated to 600 °C by a resistive heater or by a direct current heater.

Samples are mounted on copper, stainless steel, or molybdenum sample studs that fit into the STM. To start, we epoxy a sample to a sample stud, put it into the load lock, evacuate the load-lock, and transfer the sample into the preparation chamber. After the sample is treated (cleaned, milled, annealed, *etc.*) in the chamber, it is moved to the transfer chamber. To move samples, the sample stud sits inside a sample transfer plate and we use a magnetic transfer rod to transfer the sample plate [40]. To move a sample from the transfer chamber to the cold STM, we use a top loading system with a 3 cm diameter access shaft in the dilution refrigerator. A detailed description of the transfer mechanism can be found in Ref. [40].

3.7 Control electronics and measurement circuit

To control the two tips, each tip has its own electronics to allow it to approach and scan a sample. One of the tips is controlled by an RHK Technology STM control system [91]. It has a maximum piezo voltage of 220 V and uses analog feedback. This system uses an IVP-300 RHK trans-impedance amplifier with a conversion factor of 1 nA/V to maintain the tunnel current. The other tip is controlled by an RHK-R9 system [92]. It has a maximum piezo voltage of 220 V and uses digital

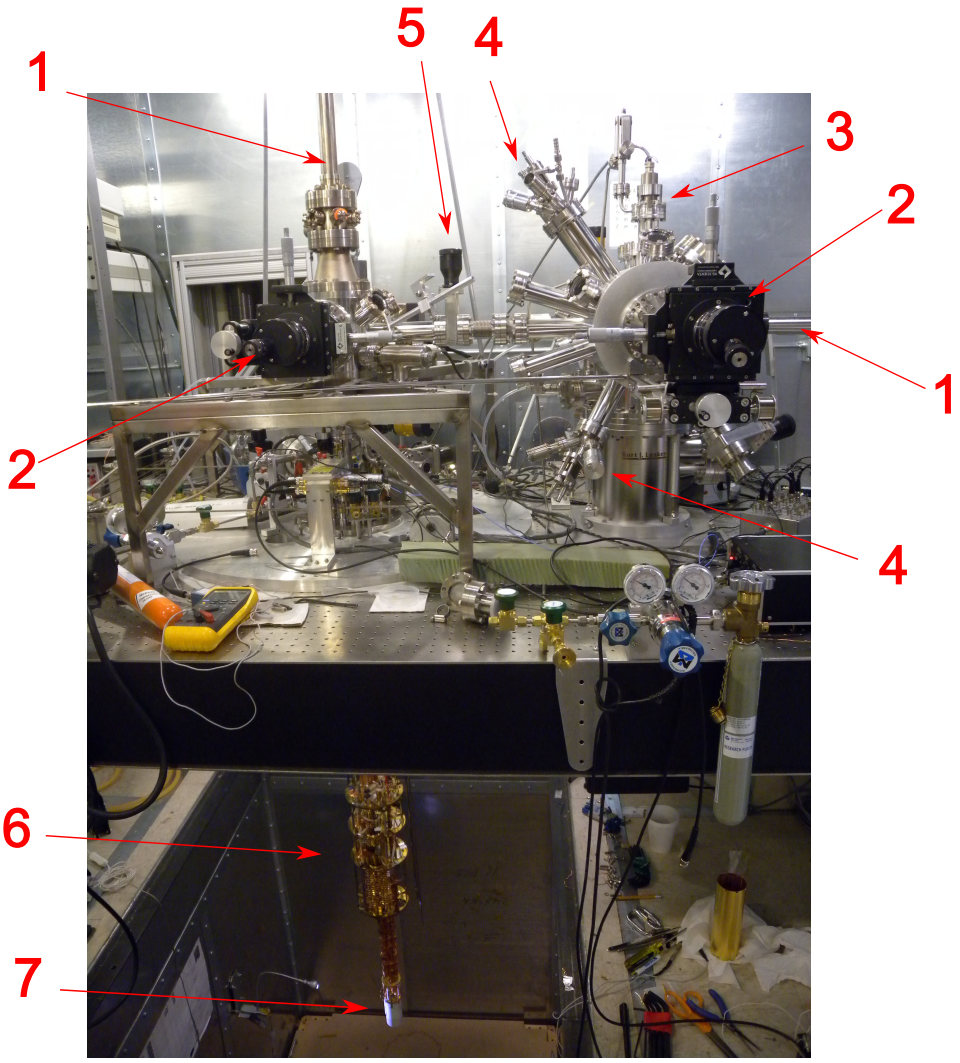

Figure 3.14: The UHV preparation chamber sits on top of an optical bench. The transfer chamber sits on top of the optical table on the left side. The dilution refrigerator is underneath the transfer chamber and the STM unit is bolted to the mixing chamber plate from below. Label (1) indicate magnetic transfer rods, (2) are the XYZ manipulators, (3) is the argon ion sputter gun, (4) are the electron beam evaporators, (5) is the gate valve, (6) is the dilution refrigerator and (7) is the STM.

feedback. The current amplifier [93] for this tip can run from 10^{-5} to 10^{-11} A/V.

In standard STM operation, the STM is run in a voltage-biased mode: a voltage bias V is applied to the sample and the tunneling current I is detected from the tip. The feedback mechanism adjusts the z-piezo to maintain a constant tunneling current as the tip scans in x-y across the sample, allowing us to image the surface topography. $I-V$ spectroscopy can be obtained by turning off the feedback and then sweeping the voltage bias V while recording the tunnel current I. A circuit diagram of the voltage-biased mode is shown in Figure 3.15 (red). In our two-tip system, the other tip can be kept away from the sample so that no current flows through that branch or it can be brought close to the sample to allow simultaneous tunneling.

To facilitate measurement of hysteretic $I-V$ characteristics we also used a relay box that let us switch from the voltage-biased mode to the current-biased mode. In current-biased mode, we sweep the current I applied to the junction and measure the voltage V across the junction. To measure $I-V$ curves in current-biased mode during a scan of a sample, we first set the junction resistance R_n while biased at a certain voltage (R_n defined as the voltage across the junction divided by the tunneling current), turn off the feedback, switch the system to the current-biased mode using the relay box, take $I-V$ curves, switch back to voltage-biased mode, and then turn the feedback loop back on, and move to the next location.

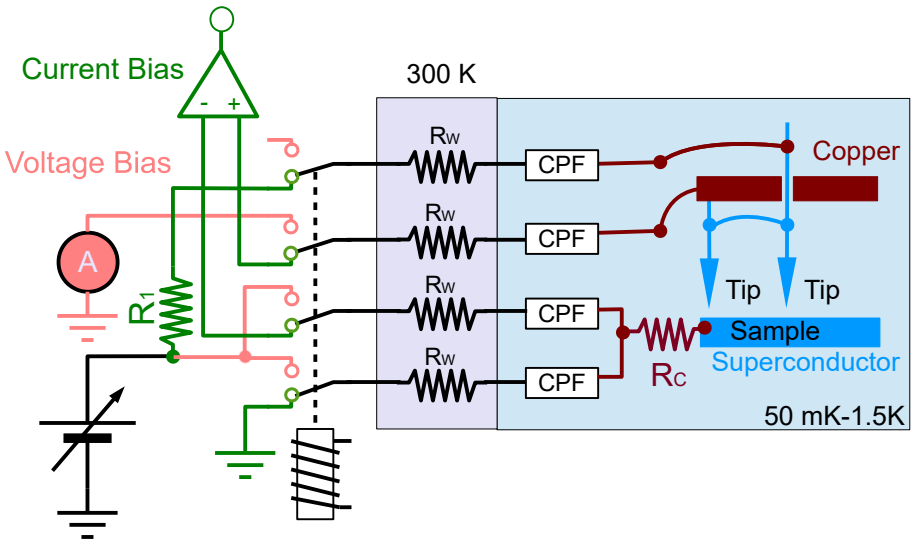

Figure 3.15: Schematic diagram of setup for interchangeable voltage-biasing mode (red) and current-biasing mode (green) using a home built relay box. We utilized the two measurement configurations in measurements of hysteretic Nb-Nb S-I-S tunneling characteristics (see Chapter 8).

3.8 STM niobium and vanadium tip preparation

Much of my research was aimed at realizing a true Josephson STM. For it to work, it is necessary to have an S-I-S junction with a non-negligible super current between a superconducting STM tip and a superconducting sample. As discussed in Chapter 8, I used a Nb crystal and a Nb superconducting tip for these tests.

The process I used for making a Nb STM tip is briefly described below. The recipe was developed by Anita Roychowdhury and additional details may be found in her thesis [40] and Ref. [94]. To make tips, I first cut 50 mm-long sections of 250 μm diameter Nb wire and place them, sticking up, in a 12 cm $\times$ 12 cm $\times$ 2 cm aluminum block. I then used a drop of Fujifilm 906-10 photoresist around each tip to glue them in place and then baked the aluminum block at 150 °C for 10 minutes. I next placed the block with its Nb tips in a plasma reactive ion etcher (RIE) [95] and etched the tips for 85 minutes. The recipe used an SF_6 gas with flow rate of 10 SCCM, a pressure of 100 mTorr, and an applied rf power of 150 W. No O_2 was used

Once the tips were etched, I chose the tip that looked sharpest and placed it into the STM. Newly made Nb tips usually lasted for about 12 hours in air at 300 K before they became too oxidized to use. This allowed enough time for us to mount the STM back onto the system, test it at room temperature, make sure it was working and then close the system and cool it to cryogenic temperatures. Once the STM reached base temperature, we usually kept it cold for a few months.

Finally, I also found out that I could use a vanadium tip as a replacement for the Nb tip. The main advantage was that it could be easily made at room

temperature and put into the tip holder right away. This process involves using pliers to rip off the end of the vanadium wire. This not only saved me time, but also meant I did not need access to the clean room equipment. This was important because there were a few months when the clean room was not running. Although vanadium tips seemed to work pretty well, as I discuss in Chapter 6 I did not observe a superconducting gap for the vanadium tips when the tip was scanning my TiN samples. This may have been due to contamination on the tip or some other issue with V. Another drawback of using the vanadium tip is that the critical temperature of vanadium is only 5.6 K. I also found that it was harder to prepare vanadium so that it had a nice sharp tip, in contrast to Pt-Ir, which are very easy to prepare so that the tip is sharp.

3.9 Conclusion

In this chapter, I described the overall layout of our millikelvin STM system including the dilution refrigerator, dual-tip STM, wiring and the UHV sample preparation system. Additional details about the construction and operation of the dual-tip STM can be found in Chapter 4.

CHAPTER 4

Simultaneously Scanning Two Connected Tips in a Dual-tip STM

4.1 Introduction

Josephson STMs that are sensitive to coherent tunneling of Cooper pairs have recently been proposed [42, 67–70]. Unlike existing STMs, in principle such systems could be used to measure variations in both the magnitude and phase of the order parameter of the superconducting state on the atomic scale.

The approach I describe here involves obtaining a phase coherent signal from an atomic size junction (J_1) by connecting it to a larger superconducting junction (J_2) using an inductive shunt L to form an asymmetric SQUID [96]. The total switching current I_s of the SQUID will be dominated by J_2 and can be determined accurately using current switching measurements [42, 97]. For $I_{01} \ll I_{02}$, the SQUID's switching current I_s achieves a maximum value of $I_{02} + I_{01}$, when the current through J_1 and J_2 are in phase. A minimum switching current of I_{02} - I_{01} results when the junctions are 180° out of phase. I_{01} and I_{02} are the critical

currents of the small and large junctions, respectively and I have assumed $I_{01} \ll I_{02} \ll \Phi_0/2L$.

By coupling J_1 to the larger junction J_2 we can lock the phase difference across J_1 with respect to J_2 and reduce its uncertainty. The relative phase difference across the two junctions is determined by the effective flux, which is the flux applied to the SQUID loop plus contributions due to the pairing symmetry of the sample at the location of the tips. By measuring the SQUID's switching current I_s versus applied flux Φ_a, one can extract the critical current I_{01} of the small junction and the effective flux for a given tip location. For example, if one junction moves from a location where it is tunneling into a positive phase in a d-wave superconductor to a location where it is tunneling into a negative phase, we would see an equivalent shift of $\Phi_0/2$ in the $I_s(\Phi_a)$ characteristic [98].

For this approach to work the tips must be independently controllable, and the connection between the tips must be superconducting and have a sufficiently low inductance. The connection must be mechanically flexible enough that the tips can be moved independently. The total loop inductance L of the SQUID should be small because the minimum uncertainty $\sigma_{\gamma 1}$ in the phase difference across the small junction is [97]

$$\sigma_{\gamma 1} \simeq \sqrt{\frac{2e^2}{\hbar}} \left(\frac{C_1}{L_{J1}} + \frac{C_1}{L} \right)^{-1/4}, \tag{4.1}$$

where $L_{J1} = \Phi_0/2\pi I_{01}$ is the Josephson inductance and C_1 the capacitance of the small junction. For $L \ll L_{J1}$ the minimum phase uncertainty will be small if $Z_s = \sqrt{L/C_1} \ll \hbar/2e^2 = R_q = 2.035$ kΩ. For a 1 nA STM junction, a 1 μA fixed

junction, a loop inductance of 1 nH, and an STM junction with total capacitance 6 fF, one finds $Z_s = 234\ \Omega$ and $\sigma_\gamma \approx 0.44$ radians, which is small enough to obtain a measurable critical current [42], provided thermal fluctuations and external noise are sufficiently small.

Sullivan *et al.* [42] completed a proof-of-principle experiment that demonstrates the phase across a small junction can be significantly stabilized by coupling to a large junction via an inductance. A small $Al/Al_2O_3/Al$ junction was first prepared (C $\sim$ 6 fF), that exhibited a highly suppressed switching current at 50 mK due to phase diffusion. An identically prepared small junction was then fabricated as part of a highly asymmetric, hysteretic SQUID with the junctions having capacitance of 100 fF and 6 fF. The switching current of the SQUID was measured, and the $I - \Phi$ curve displayed a periodic modulation of $\sim$ 1 nA on top of the $\sim$ 800 nA total switching current. This result strongly suggests that a superconducting dual-tip STM with comparable parameters will be capable of imaging the gauge invariant phase of superconductors on the atomic scale.

To construct an STM with two connected tips, we started from an existing dual-tip STM [41] that can operate at room temperature or in a dilution refrigerator with a base temperature of 30 mK. Previously, the feasibility of scanning both tips independently at mK temperatures was demonstrated using plasma-etched superconducting Nb tips [94]. In Section 4.2, I describe how I modified this system to enable operation with two tips that are electrically connected via a flexible link made from thin Nb foil. In Section 4.3, I next discuss one of the main challenges of operating two connected tips independently: only the total tunnel current through

both tips can be measured, so that a new technique for controlling both tips using one current needed to be devised. I describe a technique for keeping each tip in feedback and then demonstrate simultaneous imaging with both tips. Finally, in Section 4.4, I describe images obtained by simultaneously scanning two tips at room temperature and examine the electrical performance and mechanical characteristics of the system.

4.2 Room temperature system setup

To form a SQUID, the two tips, connecting link and sample must be superconducting. We chose to use niobium for the tips, tip holders and connecting link due to its toughness, high critical temperature, ability to make sharp tips and slow oxidation rate [94]. (Alternatively, vanadium could also be used. Vanadium wire is not as brittle as un-annealed niobium wire and it can be cut using wire cutters to produce sharp points.) By attaching the connecting link to tip holders, instead of directly to the tips, we get a stronger connection and can exchange tips without having to remake the connection. Each tip slides into a small hole in its holder and is held by friction. A disadvantage of connecting the holders is that this makes the connector longer, which increases the SQUID loop inductance L and pickup area, which would increase the phase diffusion in J_1 and make the device more sensitive to magnetic noise.

To make the link I used bow-tie shaped connectors that were cut from 25 μm

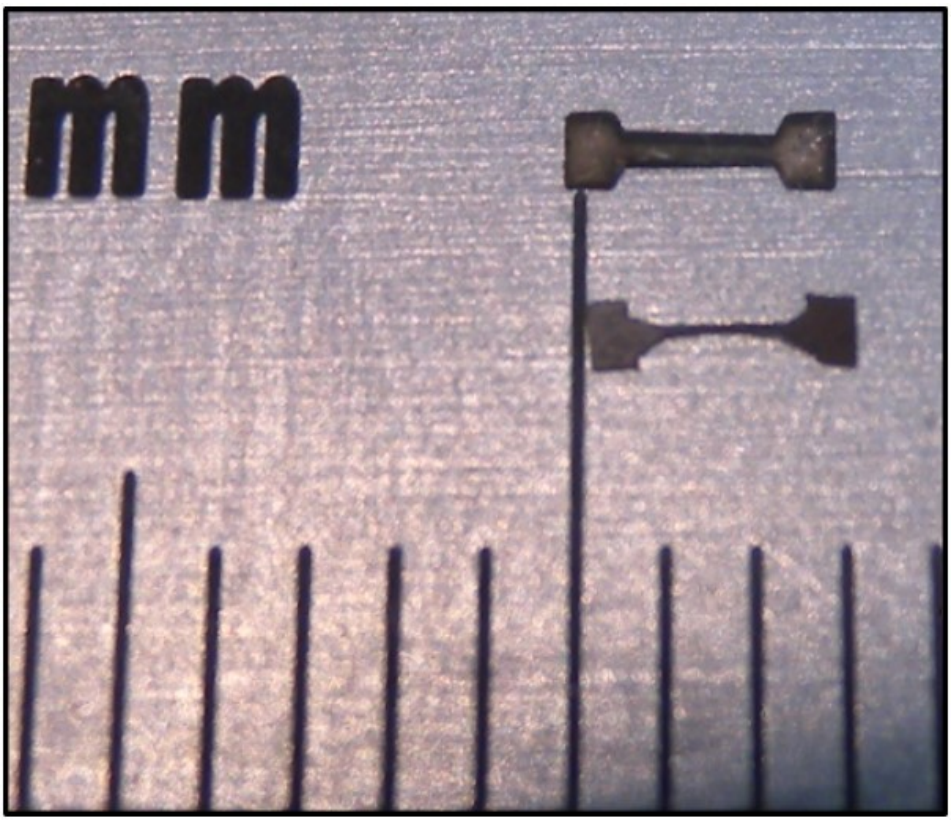

Figure 4.1: Two laser-cut Nb foil connectors shown on a ruler with 1 mm marks.

thick Nb foil (see Fig. 4.1). The cutting was done using an 800 nm wavelength laser with a 100 fs pulse length, an average power of 1 W and spindle speed of 100 rpm. The pads of the bow-tie allow a larger contact welding area to the tip holders and the neck in the bow-tie gives flexibility so that each tip does not pull too strongly on the other. The Nb connector was spot welded [99] to each tip holder (see Fig. 4.2) using a hand-held Cu spot-welding clamp.

4.3 Scanning two tips independently

With the tips electrically connected together by the Nb bowtie, the controller can only measure the sum of the tunneling current from both tips. Since an independent current signal from each tip is not available, a conventional STM constant-current feedback mode (Chapter 2) cannot be used to control the tip-sample separation of both tips simultaneously. Instead, we devised a technique that involves modulating each tip's z-piezo voltage at a different frequency and then extracting from the total current a separate feedback signal for each tip.

To understand this feedback technique, note that for a single STM tip at a distance z above a surface, the tunneling current can be written as [61] (see

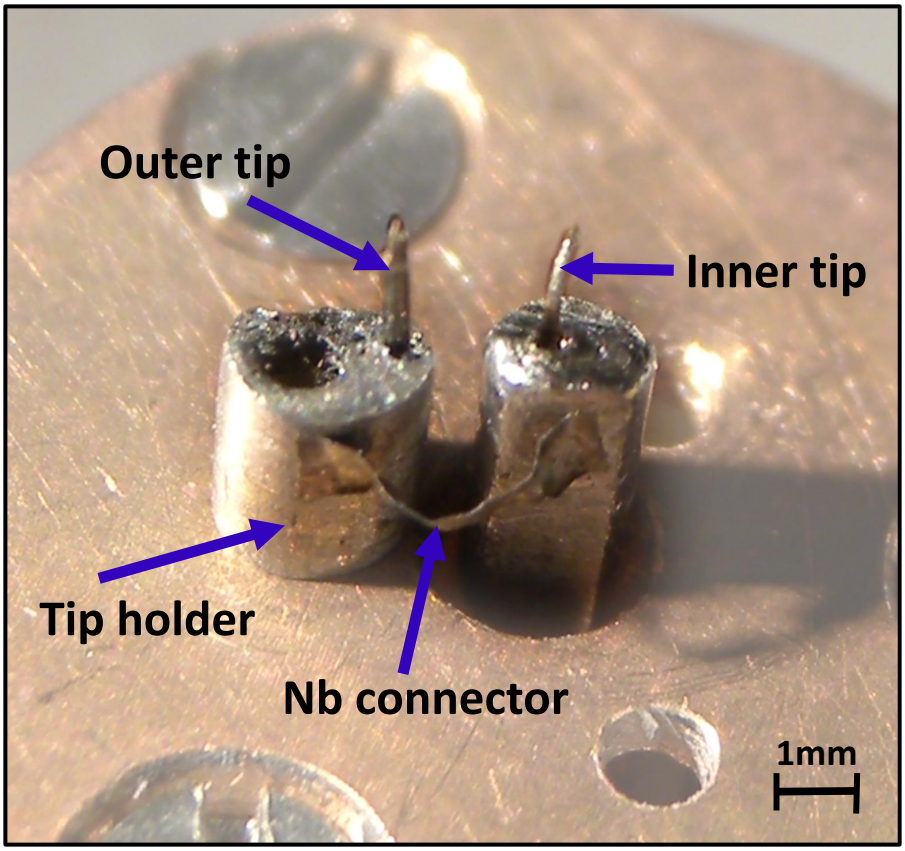

Figure 4.2: Nb tip holders connected by spot welded Nb foil.

Chapter 2)

$$I \propto \int_{-\infty}^{\infty} |M|^2 N_{\text{tip}}(\epsilon - eV) \cdot N_{\text{sample}}(\epsilon)[f(\epsilon - eV, T) - f(\epsilon, T)]d\epsilon$$
$$\propto e^{-\kappa z} \tag{4.2}$$

where T is the temperature, $1/\kappa$ is the effective tunneling length scale, ϵ is the electron energy (with respect to the Fermi level of the sample), N_{tip} is the density of states of the tip, N_{sample} is the density of states of the sample, V is the voltage applied to the sample with respect to the tip and $|M|^2$ is the tunneling matrix element, which decreases exponentially with distance from the sample.

From Eq. (4.2), the derivative of the tunneling current with respect to distance z gives

$$\frac{dI}{dz} = -\kappa I. \tag{4.3}$$

Thus the $\mathrm{d}I/\mathrm{d}z$ signal from a tip is proportional to the current I through the tip, with a constant factor of simply -κ.

Figure 4.3 shows our dual-tip electronics setup. One of the tips is controlled by an RHK Technology SPM 1000 Scanning Probe Microscope Control System [91]. It has a maximum output piezo voltage of 220 V and uses analog feedback. The other tip uses a Topometrix SPM control system [100] [obsolete] with a maximum output piezo voltage of 220 V and digital feedback.

Figure 4.4 shows an STM measurement of I versus z and Fig. 4.5 shows a measurement of $\mathrm{d}I(z)/\mathrm{d}z$ versus z, where I used a Pt-Ir tip and a Au/mica sample

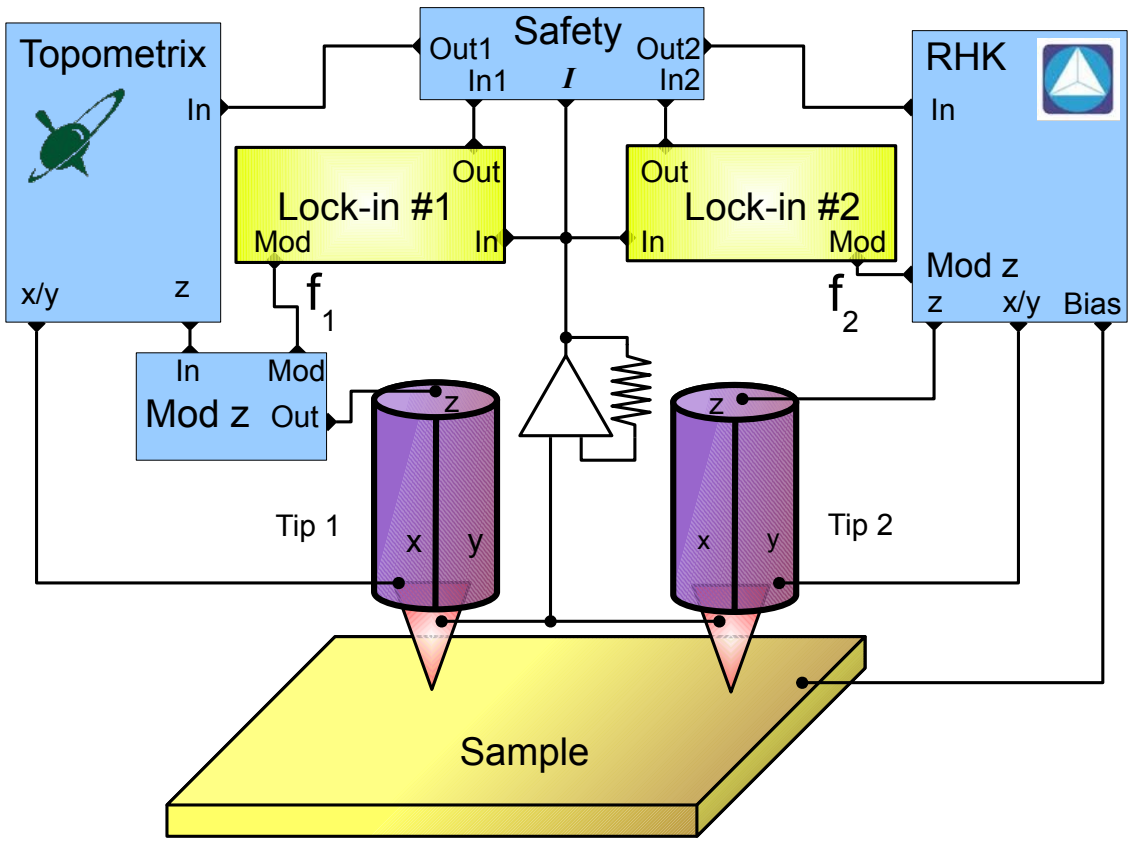

Figure 4.3: Experimental configuration for using $\mathrm{d}I/\mathrm{d}z$ signals to generate feedback for two electrically connected STM tips with two independent position controllers. The RHK electronic controller has a built-in modulation mode for the z–piezo, whereas the Topometrix system requires an external modulation box. The safety box checks the total output current and retracts both tips if the total current exceeds a set value, preventing the tips from crashing into the sample.

at room temperature. For this data, I parked the tip close enough to the sample that there was an appreciable tunneling current (nA), and turned off the feedback. I then retracted the tip a few Å from the surface while recording the tunnel current and the $\mathrm{d}I/\mathrm{d}z$ signal while the tip z position was modulated at an amplitude of 12 pm. As expected, $\mathrm{d}I/\mathrm{d}z$ and I both decreased exponentially with the tip-sample distance z. Thus the plots of I *vs.* z and $\mathrm{d}I/\mathrm{d}z$ *vs.* z are approximately straight lines on a semilog plot. Fitting Eq. (4.2) to the I(z) data, we find $1/\kappa \simeq 0.30$ nm. Since $\mathrm{d}I/\mathrm{d}z$ is proportional to I (see Fig. 4.5), we can use the $\mathrm{d}I/\mathrm{d}z$ from a z-modulated tip as a feedback error signal when operating the STM.

To distinguish the currents from each tip, we add a small modulation of a few mV at different frequencies (between 1 and 10 kHz) to the z-piezo of each tip. I then used two lock-in amplifiers to monitor the total current and detect $\mathrm{d}I/\mathrm{d}z$ at each driving frequency. In practice we found that the total current has an in-phase (resistive) component and a 90° out of phase (capacitive) component at each frequency. The amplitude of the capacitive contribution to the current is $I_c \cong 2\pi f V C d/z$, where z is the distance between the sample and the tip, C is the effective tip-sample capacitance, d is the amplitude of the tip z-modulation, and the sample is held at voltage V. For example, for $C = 10$ fF, frequency $f = 5$ kHz, bias voltage $V = 1$ V, $z = 0.5$ nm and $d = 6$ pm, the capacitive current amplitude is $I_c = 10$ pA which is not small given a typical tunneling current range of pA to nA.

Fortunately, since the two components are out of phase by 90°, we can easily measure and separate out the unwanted capacitive part; only the in-phase resistive component will obey Eq. (4.3) and be useful for generating the feedback signal. To

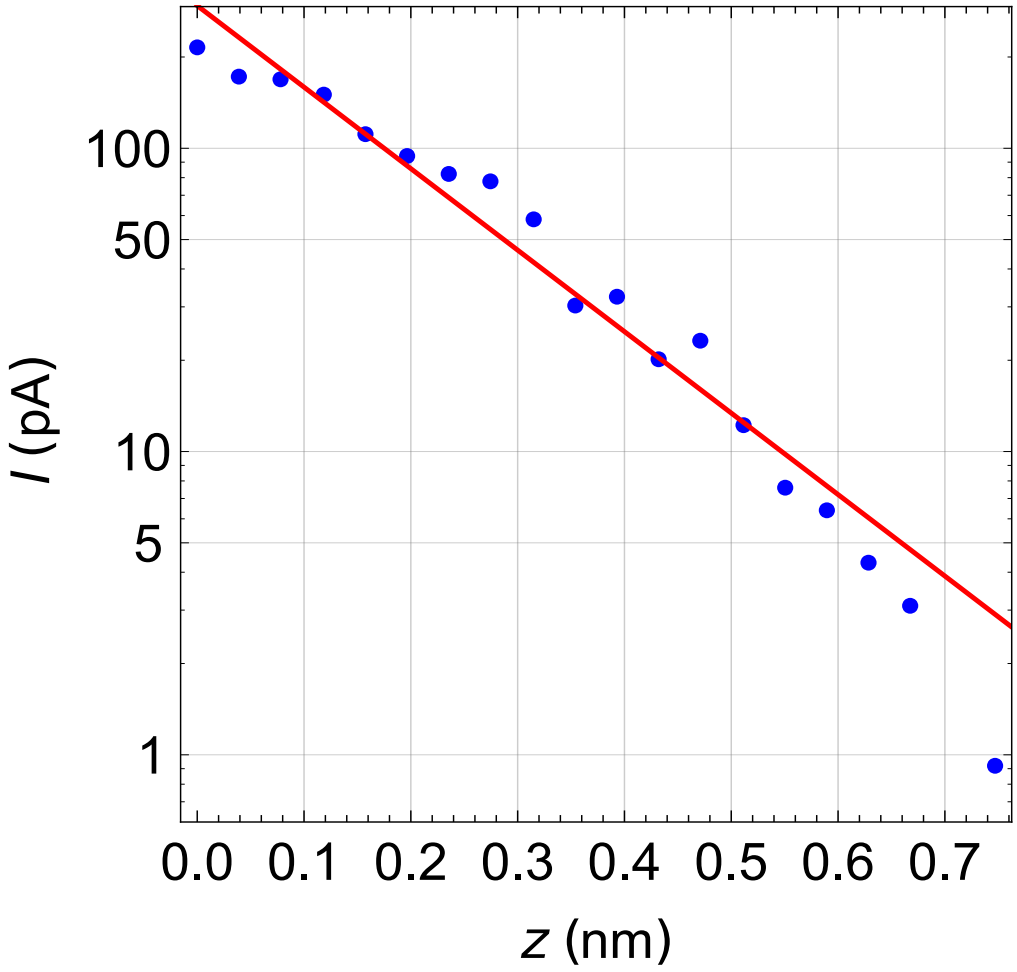

Figure 4.4: Semi-log plot of measured tunneling current I (blue points) versus distance z between a Pt-Ir tip and a Au/mica surface. The red line is a fit to an exponential decay with $1/\kappa = 0.30$ nm for z < 0.3 nm.

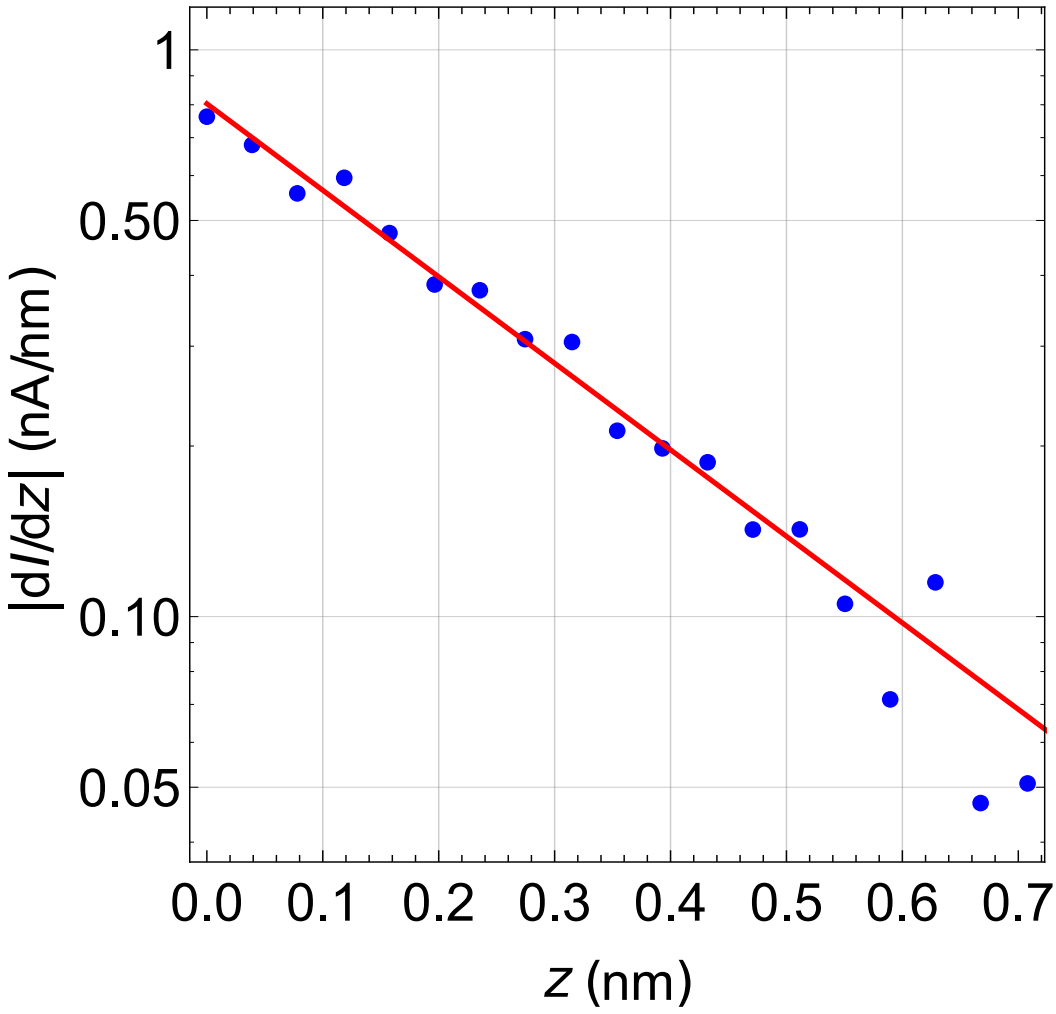

Figure 4.5: Semi-log plot of measured $|\mathrm{d}I/\mathrm{d}z|$ (blue points) versus distance z acquired simultaneously with Fig. 4.4. The red line is a fit to data for z $<$ 0.3 nm.

find the phase φ_c of the capacitive current, we measure the current while the tip is somewhat beyond the z-range where there is a detectable tunneling current. Applying an ac voltage to the scanner, we find a capacitive signal and determine the phase φ_c at which the output from the lock-in is a maximum at the applied frequency; this is the phase φ_c of the capacitive component. With the tip in tunneling range, we then extract the component at $\varphi_c \pm 90°$ using the lock-in amplifier and use this signal to generate the z-feedback signal for the tip, note this also gives a way to measure C, which is an important parameter for the STM SQUID.

There are several factors to consider when choosing the z-modulation frequency for our $\mathrm{d}I/\mathrm{d}z$ feedback technique. A high frequency is desirable because this allows a large feedback bandwidth and thus a high scan rate. If, however, the modulation frequency is much higher than the piezotube's resonant frequency, the tip will stop responding to the applied modulation voltage. Our outer scanner has a resonance at a few kHz and cuts off at 4.6 kHz, whereas for the inner scanner, the cut off is around 11 kHz. The large difference in the scanner resonance frequencies allows us to drive the two piezos with little crosstalk or interference using two well-separated frequencies.

Our use of two modulation frequencies requires some additional modifications to the standard feedback control. In standard constant current imaging mode (see Chapter 2), the feedback control system naturally prevents the tip from crashing into the sample. The tunnel current is compared to a set point and the feedback system tries to maintain this value by moving the tip toward or away from the sample. Even if the current amplifier saturates when the tip gets too close to the

sample, the error signal will be large and the feedback control will pull back the tip. However, for our $\mathrm{d}I/\mathrm{d}z$ technique we are only monitoring $\mathrm{d}I/\mathrm{d}z$. Saturating the current amplifier will cause the $\mathrm{d}I/\mathrm{d}z$ feedback signal to drop to zero, which is less than the set point, and the feedback control will push the tip forward, causing the tip to crash into the sample.

To prevent this, I incorporated a safety box into the control system (see Fig. 4.3). The inputs to the safety box (see Fig. 4.6) are the two $\mathrm{d}I/\mathrm{d}z$ signals from both lock-in amplifiers and the total tunnel current. If the total current is larger than a threshold value (typically 7 nA), the safety box outputs 10 V to the tip feedback system to force both tips to be pulled back. Otherwise the safety box just outputs the detected $\mathrm{d}I/\mathrm{d}z$ signal for each tip. A downside of this method is that both tips are pulled back, since I do not determine which tip caused the safety box to trigger. In principle, this could be determined by examining the $\mathrm{d}I/\mathrm{d}z$ signals. In practice, I set the threshold current close to the maximum output of the current amplifier and adjust the scan parameter so that the safety box is not triggered too often during a scan.

4.4 Simultaneously scanning two STM tips on test samples

To test the two-tip feedback system with both tips connected together, I used the STM to image HOPG and Au/mica samples with Pt-Ir tips at room temperature in air. In the first set of tests I brought one tip into tunnel range and scanned the

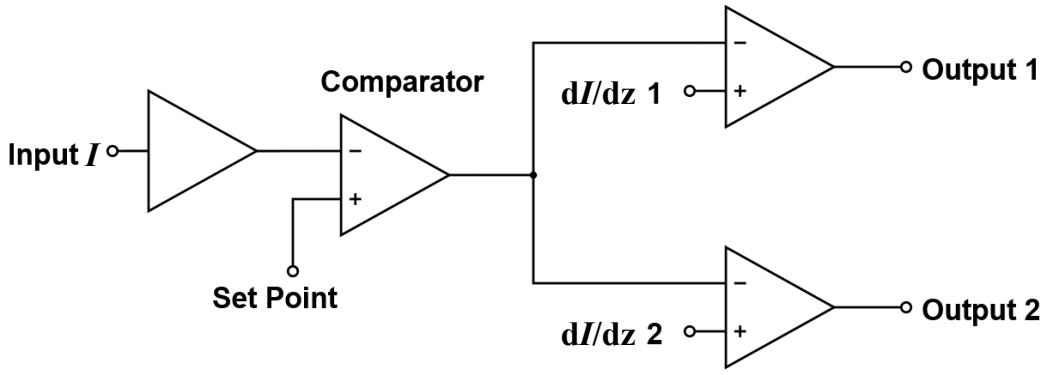

Figure 4.6: Simplified circuit for the safety box. If the combined tunneling current signal sent to Input I is higher than the set point, the output of the comparator switches from 0 V to -10 V, which makes outputs 1 and 2 switch to 10 V, causing both tips to retract. Otherwise the output of the comparator is 0 V and feedback outputs 1 and 2 are determined by the corresponding $\mathrm{d}I/\mathrm{d}z$ signal.

sample while the other tip was out of tunnel range and *vice versa*. I used the RHK controller as the feedback system and set the lock-in phase so that the capacitive contribution to the lock-in output was minimized.

Figure 4.7 shows a topographic image of the Au/mica surface that was scanned with the inner tip using its tunneling current as the feedback signal in the standard way. Single atomic layer steps are clearly seen. After the image was taken, I added a small modulation of ∼6 pm at a frequency of 9.103 kHz to the inner tip z–piezo and recorded the modulation of the current signal at that frequency using a lock-in amplifier with an averaging time constant of 0.3 ms. Figure 4.8 shows the corresponding image of the same region taken using the inner tip in $\mathrm{d}I/\mathrm{d}z$ mode. Before switching to the $\mathrm{d}I/\mathrm{d}z$ mode, I moved the tip back ∼ 20 nm out of tunnel

range. I then switched the feedback input to $\mathrm{d}I/\mathrm{d}z$, brought the tip back into tunnel range, and resumed taking images. Comparing the images, the steps in Fig. 4.7 are not as sharp as in Fig. 4.8, but overall the two images are remarkably similar, as expected.

Figure 4.9 shows an image with atomic resolution on an HOPG sample taken with the outer tip using current feedback. The corresponding image in $\mathrm{d}I/\mathrm{d}z$ mode is shown in Fig. 4.10 and it is quite similar, although some distortion is visible in Fig. 4.10 due to the feedback reacting slower during the scan. With the inner tip, we were not able to achieve atomically resolved images on HOPG. Typically, the inner tip was less stable than the outer tip because the inner scanner is located above the inner walker [41], so the overall lever arm is longer, making the inner tip more susceptible to vibration.

After demonstrating the feasibility of using the $\mathrm{d}I/\mathrm{d}z$ mode for imaging, I scanned both tips simultaneously. To do this, I used the Topometrix SPM control system for the inner tip and the RHK SPM100 for the outer tip (see Fig. 4.3). The modulation frequency was 4.517 kHz for the outer tip and 10.007 kHz for the inner tip. The threshold of the safety box was set to 6 nA and the tips were raster scanned at different rates. Figure 4.11 (a) and (b) were taken with the outer tip while Fig. 4.11 (c) and (d) were taken with the inner tip. Figure 4.11 (a) and (c) were taken with one tip scanning using $\mathrm{d}I/\mathrm{d}z$ as the feedback signal while the other tip was retracted. Figure 4.11 (b) and (d) were taken with both tips scanning at the same time and the resulting images can be compared directly to Fig. 4.11 (a) and (c). The two images taken with the outer tip are very similar. White spots in

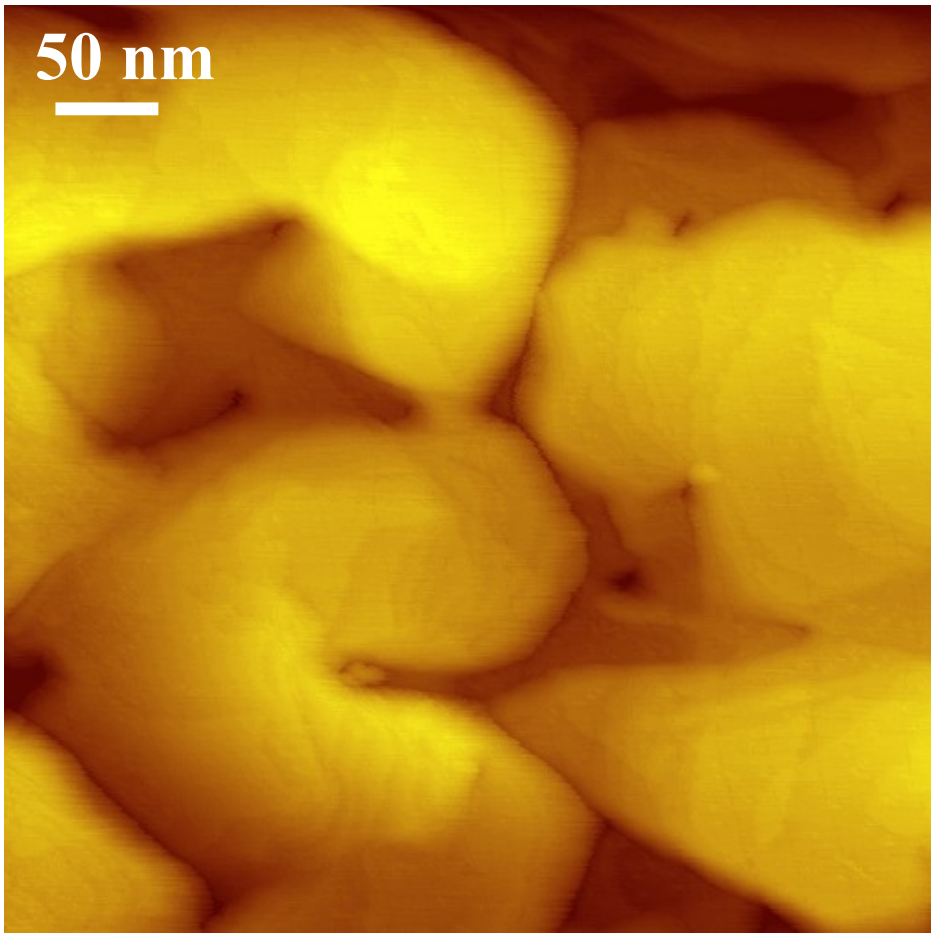

Figure 4.7: Topographic STM image of Au/mica taken with the inner Pt-Ir tip using current for generating the feedback signal for the z-piezo. The sample bias is 1 V and the tunneling current is 80 pA. The z color scale range represents the height difference of 8 nm.

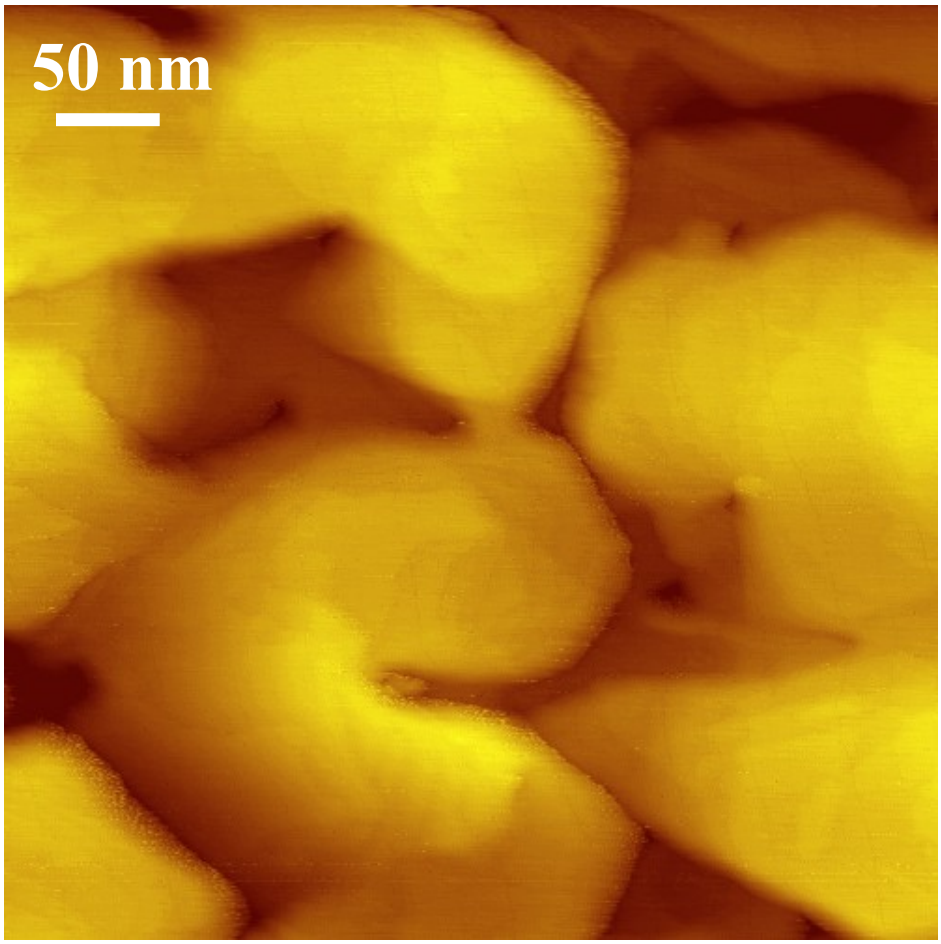

Figure 4.8: Topographic STM image of Au/mica taken with the inner Pt-Ir tip using $\mathrm{d}I/\mathrm{d}z$ for generating the feedback signal for the z-piezo. The same region as in Fig. 4.7 has been imaged.

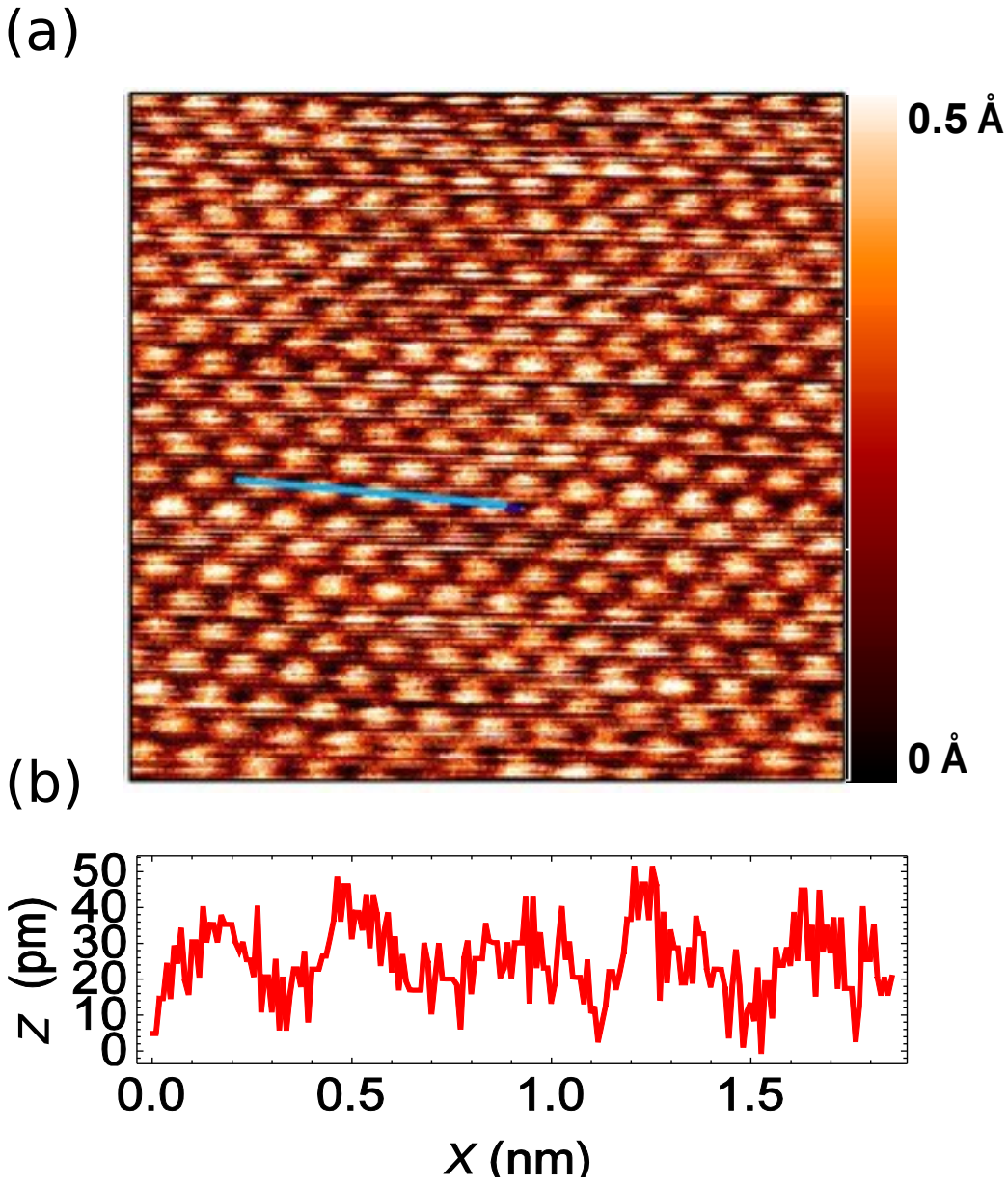

Figure 4.9: (a) Topographic STM image of HOPG showing atomic resolution taken with the outer Pt-Ir tip using current as the feedback signal. (b) Line section of the topographic signal z *vs.* x along the blue line in (a).

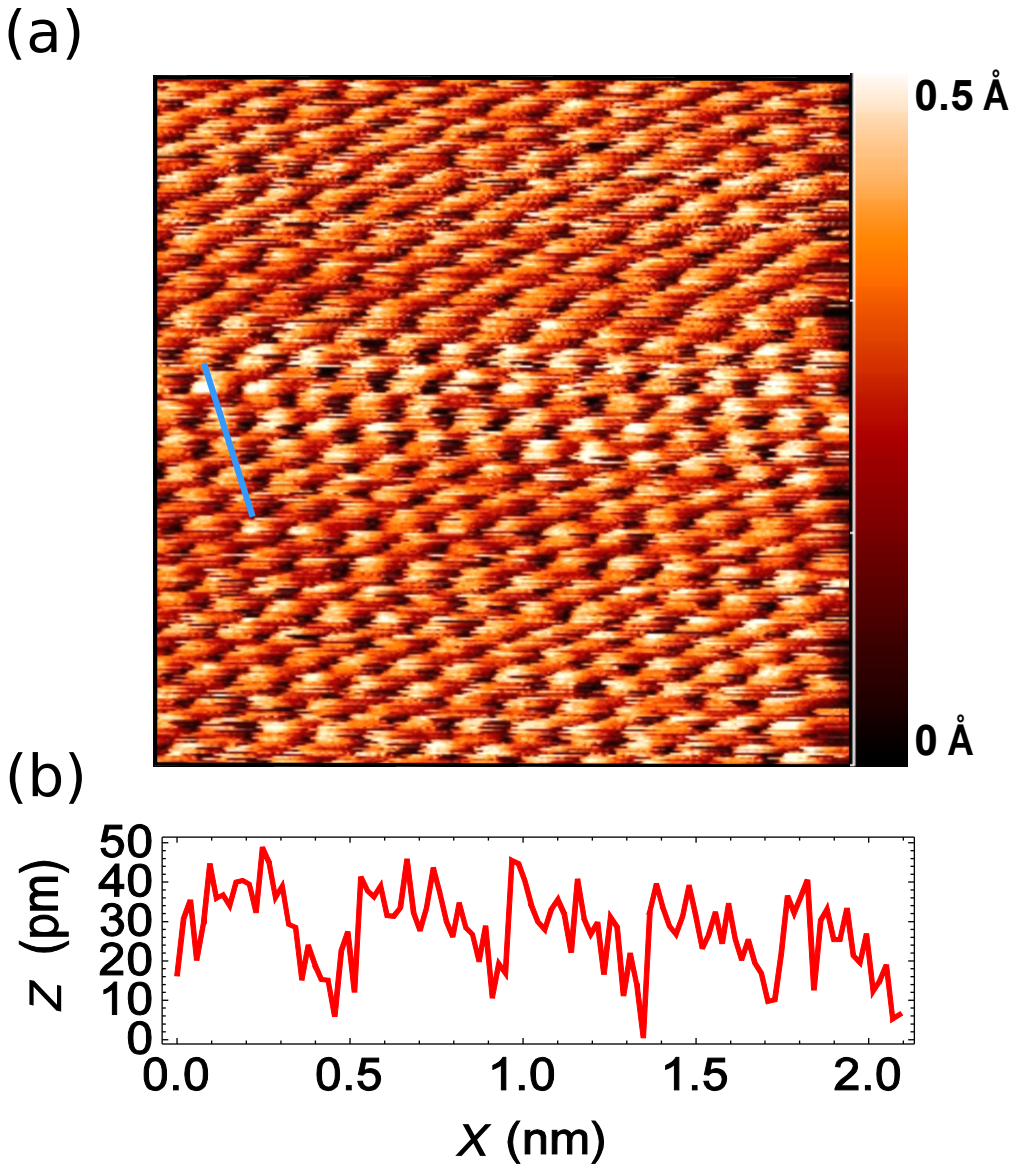

Figure 4.10: (a) Topographic STM image of HOPG showing atomic resolution taken with the outer Pt-Ir tip using $\mathrm{d}I/\mathrm{d}z$ as the feedback signal. (b) Line section of the topography z *vs.* x along the blue line in (a).

Fig. 4.11 (d) are pixels at which the outer tip scanned across a step edge and caused the safety box to trigger and retract both tips. Other than that, the tips seem not to affect each other significantly.

Although the images in Fig. 4.11 do not show obvious effects from mechanical coupling between the tips which were connected together with the Nb bow-tie, note that the inner tip assembly, due to its long lever arm, will be pulled by the outer tip if the outer tip moves a significant distance. Figure 4.12 shows an image of the HOPG sample taken with the inner tip while the outer tip was scanning at the same time with a scan range of 16 nm $\times$ 16 nm. The appearance of the steps was not affected significantly while the outer tip was scanning over this small range. For comparison, Fig. 4.13 shows an image of the same region taken using the inner tip, but this time while the outer tip was moved around a 2 μm$\times$ 2 μm region. Initially the outer tip was at the bottom right corner of the total scan area. After scanning a few lines with the inner tip, we moved the outer tip to the bottom left corner of its scan area and waited for a few lines while the inner tip kept scanning. We repeated the same procedure, moving the outer tip to the other corners before returning the outer tip back to the starting corner and repeating the entire cycle.

Comparison of Fig. 4.12 and Fig. 4.13 shows that while Fig. 4.13 was being acquired the inner tip moved significantly each time the position of the outer tip changed. The white arrows and labels 1 to 4 indicate the image sections for which the outer tip was at the extreme corner of its scan range (see inset). Analysis of the images shows that the inner tip moved by about 40 nm in Fig. 4.13 when the outer tip changed from position 1 to position 2 (indicated by a green line at 45° with

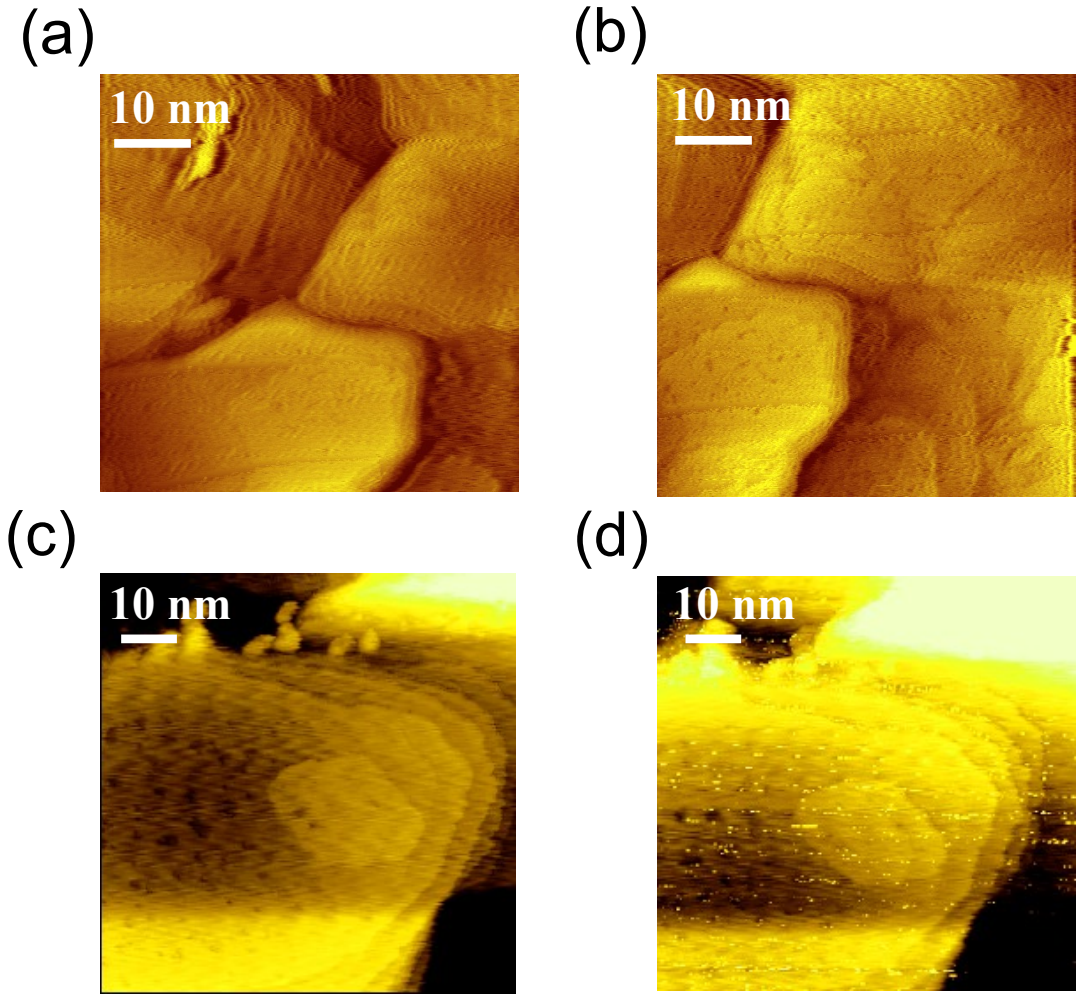

Figure 4.11: Topographic STM images of Au on mica. The top row images (a) and (b) were taken using the outer tip with a z-modulation frequency of 4.517 kHz. Bottom row images (c) and (d) were taken using the inner tip and a z-modulation frequency of 10.007 kHz. (a) and (c) used $\mathrm{d}I/\mathrm{d}z$ as feedback input while the other tip was out of tunneling range. Images (b) and (d) were taken simultaneously, *i.e.* with both tips scanning at the same time. White spots in (d) are pixels where the safety box retracted both tips when the outer tip scanned over a large step edge.

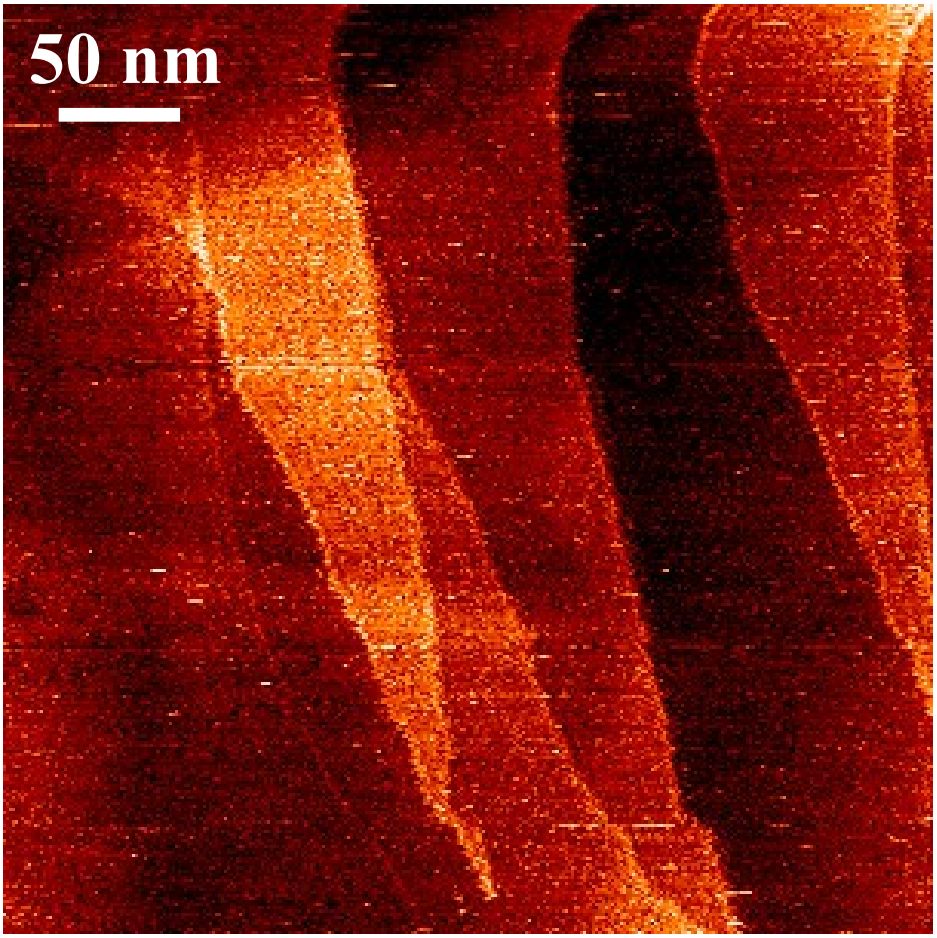

Figure 4.12: Topographic images taken with the inner STM tip on the surface of HOPG while at the same time, the outer tip was scanning a 16 nm $\times$ 16 nm area.

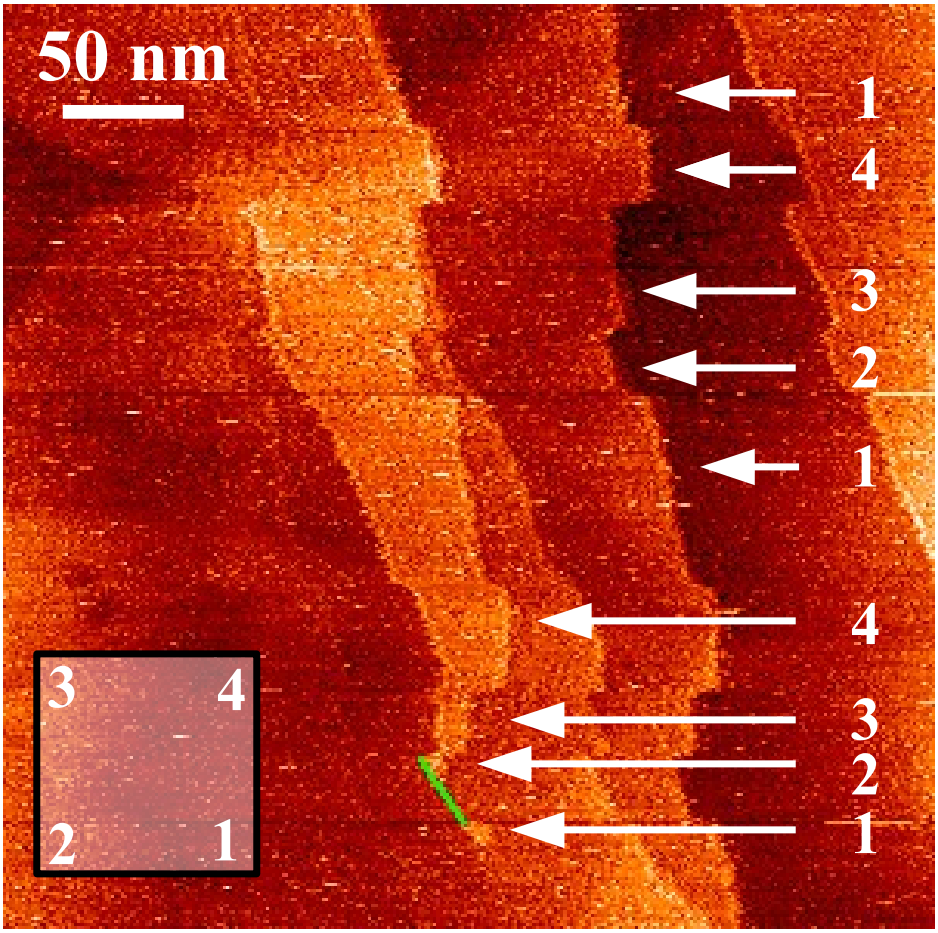

Figure 4.13: Topographic images taken with the inner STM tip on the surface of HOPG while, at the same time, the outer tip was moved around its maximum 2 μm $\times$ 2 μm scan area. Step edges are shifted due to the outer tip pulling the inner tip as the outer tip is moved to a new location. Labels 1, 2, 3, 4 indicate the corner at which the outer tip was located when the inner tip was scanning the corresponding lines. The green line shows the inner tip displacement vector change when the outer tip moved from corner 1 to corner 2.

respect to the horizontal axis). This corresponds to a reduction by about a factor of 50 in the relative motion of the inner tip due to the outer tip, indicating a very flexible connection. We note that motion of the inner tip has a much smaller effect on the outer tip due to the greater rigidity of the outer tip walker. This behavior suggests it would be best to use the outer tip as a large fixed junction (reference junction) and use the inner tip as the small junction for scanning across the sample to image changes in superconducting phase.

4.5 Conclusions

In this chapter I described how I electrically connected two tips together in a dual-tip STM using a bowtie shaped Nb foil connector. I also described images of HOPG and Au/mica samples obtained with the system at room temperature. Both tips showed good images, with the outer tip obtaining atomically resolved images on HOPG. Using $\mathrm{d}I/\mathrm{d}z$ feedback, I obtained topographic images, successfully scanned both tips at the same time and measured the mechanical coupling between the tips. These results are a significant step towards using our dual-tip STM to measure the gauge-invariant phase on a superconducting sample.

CHAPTER 5

Superconductivity and BTK Theory

In Section 5.1 I start by describing the basic principles of superconductivity and the Bardeen-Cooper-Schrieffer (BCS) theory. I introduce a few important concepts which will be used throughout the thesis, namely the superconducting gap Δ, critical temperature T_c, and density of states $D(E)$. In Section 5.2 I then discuss the theory of Andreev reflection and subgap structure observed in the $I-V$ characteristics of N-I-S junctions. When an electron-like quasiparticle is incident on an S-N interface from the normal side, a hole-like quasiparticle is reflected at the interface due to the Andreev reflection, thus creating a Cooper pair on the superconducting side. In the discussion for the BTK theory, I show that the theory describes an S-N junction for arbitrary transparency. This is different from the behavior of a standard N-I-S junction in the low transparency limit (tunneling limit) that I described in the Chapter 2.

5.1 Introduction to superconductivity

The Bardeen, Cooper, Schrieffer (BCS) theory [101, 102] provides a microscopic quantum description of superconducting phenomena. A key feature of the theory is that two electrons with opposite momenta can bind together to form a Cooper pair [103]. The attractive force is due to the first electron polarizing the medium (lattice) by attracting positive ions. The ions in turn attract the second electron. The effective attractive interaction between the electrons can overcome the Coulomb repulsion between electrons, which is reduced by screening.

At sufficiently low temperature, the formation of Cooper pairs creates an instability in the Fermi sea of electrons, and the Cooper pairs condense into a single ground state. The BCS ground state wavefunction of the electrons can be written as [101, 102]

$$|\Psi_{BCS}\rangle = \prod_{k=k_1,k_2....k_n} (u_k + \nu_k c^\dagger_{k,\uparrow} c^\dagger_{-k,\downarrow}) |\Phi_0\rangle \tag{5.1}$$

where $c^\dagger_{k,\uparrow} c^\dagger_{-k,\downarrow}$ is the pair creation operator with zero total momentum, $|\nu_k|^2$ is the probability of the pair being occupied, $|u_k|^2 = 1 - |v_k|^2$ is the probability that the pair is unoccupied and $|\Phi_0\rangle$ is the vacuum sate with no particles present.

The BCS Hamiltonian of a superconducting system can be written as [101, 102]:

$$\hat{H} = \sum_{k,\sigma} (\epsilon_k - \mu) c^\dagger_{k,\sigma} c_{k,\sigma} + \sum_{k,l} V_{kl} c^\dagger_{k,\uparrow} c^\dagger_{-k,\downarrow} c_{-l,\downarrow} c_{l,\uparrow} \tag{5.2}$$

The first term is the kinetic energy of all the free electrons with respect to the chemical potential μ of the system. The second term is the attractive interaction

between electrons with interaction coupling strength V_{kl}.

Given Eq. (5.1) and Eq. (5.2) the goal is to find the parameters u_k and ν_k for the ground state such that the energy $E{=}\langle\Psi_{BCS}|\,\hat{H}\,|\Psi_{BCS}\rangle$ is minimized. The easiest way to do this is to use a variational method [101, 102]. However the technique is somewhat clumsy when dealing with excited states that occur for $T > 0$. Instead, I will use mean-field theory [104, 105] to handle both the ground state and excited states. I note that this approach only works well in standard BCS theory in the weak-coupling limit [106, 107].

The ground state of a BCS superconductor is a many-body state composed of a phase-coherent superposition of pairs of electrons occupying states $(k\uparrow, -k\downarrow)$. Due to the coherence, operators $c_{-k\downarrow}c_{k\uparrow}$ can have non zero expectation values and we can write $c_{-k\downarrow}c_{k\uparrow} = \langle c_{-k\downarrow}c_{k\uparrow}\rangle + (c_{-k\downarrow}c_{k\uparrow} - \langle c_{-k\downarrow}c_{k\uparrow}\rangle)$, where the second term can be small. Substituting this expression into the interaction term in the Hamiltonian Eq. (5.2), one finds:

$$\begin{aligned}\hat{H} = \sum_{k,\sigma}(\epsilon_k - \mu)c^\dagger_{k,\sigma}c_{k,\sigma} + \sum_{k,l}V_{kl}(\langle c^\dagger_{k\uparrow}c^\dagger_{-k\downarrow}\rangle\,\langle c_{-l\downarrow}c_{l\uparrow}\rangle + \langle c^\dagger_{k\uparrow}c^\dagger_{-k\downarrow}\rangle(c_{-l\downarrow}c_{l\uparrow} \\ - \langle c_{-l\downarrow}c_{l\uparrow}\rangle) + (c^\dagger_{k\uparrow}c^\dagger_{-k\downarrow} - \langle c^\dagger_{k\uparrow}c^\dagger_{-k\downarrow}\rangle)\,\langle c_{-l\downarrow}c_{l\uparrow}\rangle) \\ = \sum_{k,\sigma}(\epsilon_k - \mu)c^\dagger_{k,\sigma}c_{k,\sigma} + \sum_{k,l}V_{kl}(\langle c^\dagger_{k\uparrow}c^\dagger_{-k\downarrow}\rangle c_{-l\downarrow}c_{l\uparrow} + c^\dagger_{k\uparrow}c^\dagger_{-k\downarrow}\,\langle c_{-l\downarrow}c_{l\uparrow}\rangle \\ - \langle c^\dagger_{k\uparrow}c^\dagger_{-k\downarrow}\rangle\,\langle c_{-l\downarrow}c_{l\uparrow}\rangle)\end{aligned} \tag{5.3}$$

Defining the order parameter $\Delta_k = -\sum_l V_{kl}\langle c_{-l\downarrow}c_{l\uparrow}\rangle$, the Hamiltonian then becomes

$$\hat{H} = \sum_{k,\sigma}(\epsilon_k - \mu)c^\dagger_{k,\sigma}c_{k,\sigma} - \sum_k(\Delta^\dagger_k c_{-k\downarrow}c_{k\uparrow} + \Delta_k c^\dagger_{k\uparrow}c^\dagger_{-k\downarrow} - \Delta_k\langle c^\dagger_{k\uparrow}c^\dagger_{-k\downarrow}\rangle) \tag{5.4}$$

The last sum in Eq. (5.4) is just a constant term, which we will retain because of the condensation energy of the superconducting state.

To diagonize the Hamiltonian, we introduce the quasiparticle operators $\gamma_{k0}, \gamma^\dagger_{k1}$ via the Bogoliubov-Valatin transformation [105]

$$\begin{aligned} c_{k\uparrow} &= u^*_k\gamma_{k0} + \nu_k\gamma^\dagger_{k1} \\ c^\dagger_{-k\downarrow} &= -\nu^*_k\gamma_{k0} + u_k\gamma^\dagger_{k1} \end{aligned} \tag{5.5}$$

I now rewrite Eq. (5.4) in the matrix form

$$\hat{H} = \sum_k\left[\begin{pmatrix} c^\dagger_{k\uparrow} & c_{-k\downarrow}\end{pmatrix}\begin{pmatrix}\xi_k & -\Delta_k \\ -\Delta^\dagger_k & -\xi_k\end{pmatrix}\begin{pmatrix}c_{k\uparrow} \\ c^\dagger_{-k\downarrow}\end{pmatrix} + \xi_k + \Delta_k b^\dagger_k\right] \tag{5.6}$$

where $\xi_k = \epsilon_k - \mu$ and $b_k = \langle c_{-k\downarrow}c_{k\uparrow}\rangle$. Using Eq. (5.5), we can now write

$$\begin{aligned}\hat{H} = \sum_k\Bigg[&\begin{pmatrix}\gamma^\dagger_{k0} & \gamma_{k1}\end{pmatrix}\begin{pmatrix}u_k & -\nu_k \\ \nu^*_k & u^*_k\end{pmatrix}\begin{pmatrix}\xi_k & -\Delta_k \\ -\Delta^+_k & -\xi_k\end{pmatrix}\begin{pmatrix}u^*_k & \nu_k \\ -\nu^*_k & u_k\end{pmatrix}\begin{pmatrix}\gamma_{k0} \\ \gamma^\dagger_{k1}\end{pmatrix} \\ &+\xi_k + \Delta_k b^\dagger_k\Bigg]\end{aligned} \tag{5.7}$$

To diagonize the Hamiltonian Eq. (5.7) in the γ basis, we expand the middle

three matrices and choose the u_k and ν_k so that the coefficients of the off-diagonal terms $\gamma_{k0}^\dagger\gamma_{k1}^\dagger$ and $\gamma_{k1}\gamma_{k0}$ vanish. Multiplying out the three middle matrices from Eq. (5.7) gives:

$$\begin{pmatrix} (|u_k|^2 - |\nu_k|^2)\xi_k + \Delta_k u_k \nu_k^* + \Delta_k^* u_k^* \nu_k & 2u_k\nu_k\xi_k - u_k^2\Delta_k + \nu_k^2\Delta_k^* \\ 2u_k^*\nu_k^*\xi_k - u_k^{*2}\Delta_k^* + \nu_k^{*2}\Delta_k & -((|u_k|^2 - |\nu_k|^2)\xi_k + \Delta_k u_k\nu_k^* + \Delta_k^* u_k^*\nu_k) \end{pmatrix} \tag{5.8}$$

The coefficients of the unwanted (off-diagonal) terms will vanish if

$$2\xi_k u_k \nu_k + \Delta_k^* \nu_k^2 - \Delta_k u_k^2 = 0 \tag{5.9}$$

Multiplying Eq. (5.9) by Δ_k^*/u_k^2 gives:

$$2\frac{\xi_k u_k \nu_k \Delta_k^*}{u_k^2} + \frac{\Delta_k^* \nu_k^2 \Delta_k^*}{u_k^2} - \Delta_k \Delta_k^* = 0 \tag{5.10}$$

Rearranging gives:

$$(\frac{\Delta_k^*\nu_k}{u_k})^2 + 2\xi_k(\frac{\Delta_k^*\nu_k}{u_k}) - |\Delta_k|^2 = 0 \tag{5.11}$$

and solving the resulting quadratic equation gives:

$$\frac{\Delta_k^*\nu_k}{u_k} = \sqrt{\xi_k^2 + |\Delta_k|^2} - \xi_k = E_k - \xi_k \tag{5.12}$$

where

$$E_k = \sqrt{\xi_k^2 + |\Delta_k|^2} \tag{5.13}$$

and E_k is the quasiparticle energy. From Eq. (5.13) the minimum energy to excite a single quasiparticle is the energy gap $|\Delta_k|$. The quantity Δ_k is also the order parameter [64, 108, 109] for the superconducting state and vanishes for $T > T_c$.

Given the normalization requirement $|u_k|^2 + |v_k|^2 = 1$ and Eq. (5.12), we can write:

$$|\nu_k|^2 = 1 - |u_k|^2 = \frac{1}{2}(1 - \frac{\xi_k}{E_k}) \tag{5.14}$$

The remaining diagonal terms in Hamiltonian Eq. (5.7) can be evaluated and the Hamiltonian becomes

$$\hat{H} = \sum_k E_k(\gamma_{k0}^\dagger \gamma_{k0} + \gamma_{k1}^\dagger \gamma_{k1}) + \sum_k (\xi_k + \Delta_k b_k^\dagger - E_k) \tag{5.15}$$

The last term is the energy difference between the superconducting state and normal state at $T = 0$, and is called the condensation energy. Equation (5.15) gives the excitation energy from the ground state in terms of the number operators $\gamma_k^\dagger \gamma_k$. Therefore the γ_k describe the excitations of the systems. They are called 'Bogoliubov qausiparticles' or 'Bogoliubovons'.

To see what the γ_{k0} and γ_{k1} mean physically, I invert the transformation

Eq. (5.5), and get

$$\begin{aligned}\gamma_{k0}^{\dagger} &= u_k^* c_{k\uparrow}^{\dagger} - \nu_k^* c_{-k\downarrow} \\ \gamma_{k1}^{\dagger} &= u_k^* c_{-k\downarrow}^{\dagger} + \nu_k^* c_{k\uparrow}\end{aligned} \tag{5.16}$$

$\gamma_{k0}^{\dagger}$ effectively creates Bogoliubovon of momentum k and spin $\uparrow$, since $c_{-k\downarrow}$ subtracts a particle with $(-k\downarrow)$ from the system, which is the same as adding a particle $(k\uparrow)$. Similarly, $\gamma_{k1}^{\dagger}$ creates a Bogoliubovon with wave vector $-k$ and spin $\downarrow$.

Inserting Eq. (5.5) into the equation for the order parameter $\Delta_k = -\sum_l V_{kl}\langle c_{l\downarrow} c_{l\uparrow}\rangle$, one finds:

$$\Delta_k = -\sum_l V_{kl} u_l^* \nu_l (1 - \langle \gamma_{l0}^{\dagger}\gamma_{l0}\rangle - \langle \gamma_{l1}^{\dagger}\gamma_{l1}\rangle). \tag{5.17}$$

At $T = 0$, no quasiparticles are excited and Eq. (5.17) becomes

$$\Delta_k = -\sum_l V_{kl} u_l^* \nu_l = -\frac{1}{2}\sum_l V_{kl}\frac{|\Delta_l|}{E_l} \tag{5.18}$$

where the BCS interaction is,

$$V_{kl} = \begin{cases} -V & \text{if } |\xi_k| < \hbar\omega \\ 0 & \text{otherwise.} \end{cases} \tag{5.19}$$

Here ω is the Debye cutoff frequency of the ions in the lattice. This means that the electron-phonon interaction happens within a thin shell near the Fermi surface. In the BCS model of the elctron-phonon interaction [101, 102], the gap is constant and does not vary with the direction of $\overline{k}$, *i.e.* it is isotropic or s-wave symmetric. This model can be extended to describe unconventional superconductivity where

the order parameter (energy gap Δ) has other symmetries. For example, p-wave superconductors [110] or d-wave superconductors [111].

Inserting V_{kl} from Eq. (5.19) into Eq. (5.18) one obtains a self-consistency equation

$$\Delta = \begin{cases} \frac{V}{2}\sum_{\overline{k}} \frac{\Delta}{E_k} & \text{if } |\xi_{\overline{k}}| < \hbar\omega \\ 0 & \text{otherwise.} \end{cases} \tag{5.20}$$

Note in Eq. (5.20) that the sum is over a thin shell around the Fermi energy with $|\xi_k| = |\epsilon_k - \mu| < \hbar\omega$. The sum over $\overline{k}$ can be replaced by an integration over energy ξ from $-\hbar\omega$ to $\hbar\omega$. Canceling the gap Δ from both sides, Eq. (5.20) becomes

$$1 = V\int_0^{\hbar\omega} \frac{1}{\sqrt{\xi^2+\Delta^2}} D(\xi)d\xi \tag{5.21}$$

The factor of 2 in Eq. (5.20) disappears due to the symmetry of the integration over ξ. To proceed, I substitute $\xi = x\Delta$ and note that the normal metal density of states $D(\xi)$ can be taken as constant D_0 over the small integration range provided $\hbar\omega \ll E_F$. Equation (5.21) becomes

$$\begin{aligned} 1 &= VD_0\int_0^{\hbar\omega/\Delta} \frac{\Delta dx}{\Delta\sqrt{1+x^2}} = VD_0\int_0^{\hbar\omega/\Delta} \frac{dx}{\sqrt{1+x^2}} \\ &= VD_0\int_0^{\tanh^{-1}(\hbar\omega/\Delta)} \frac{\sec^2\theta d\theta}{\sec\theta} = VD_0\int_0^{\tanh^{-1}(\hbar\omega/\Delta)} \sec\theta d\theta \\ &= VD_0\ln|\sec\theta+\tan\theta||_0^{\tanh^{-1}(\hbar\omega/\Delta)} = VD_0\ln|\sqrt{1+x^2}+x||_0^{\hbar\omega/\Delta} \\ &= VD_0\sinh^{-1}x|_0^{\hbar\omega/\Delta} = VD_0\sinh^{-1}(\frac{\hbar\omega}{\Delta}) \end{aligned} \tag{5.22}$$

The gap equation then becomes

$$\Delta = \frac{\hbar\omega}{\sinh(1/VD_0)} \approx 2\hbar\omega e^{-1/D_0 V} \tag{5.23}$$

The last approximation is valid in the limit $VD_0 \ll 1$.

For finite temperatures, the presence of quasiparticles needs to be taken into account. The probability of having a quasiparticle excitation with energy E_k is given by the Fermi function

$$f(E_k) = \frac{1}{e^{E_k/k_BT} + 1} \tag{5.24}$$

Equation (5.17) then becomes [64, 101, 102]:

$$\Delta_k = -\sum_l V_{kl} u_l^* \nu_l [1 - 2(f(E_l))] = -\sum_l V_{kl} \frac{\Delta}{2E_l} \tanh\left(\frac{E_l}{2k_BT}\right) \tag{5.25}$$

Again using Eq. (5.19) and assuming that Δ is independent of the $\overline{k}$ direction, I obtain an implicit equation for the gap as a function of temperature:

$$\frac{1}{V} = \frac{1}{2}\sum_k \frac{\tanh(E_k/2k_BT)}{E_k} \tag{5.26}$$

Similar to the $T = 0$ case, I get

$$\frac{1}{V} = \int_0^{\hbar\omega} \frac{\tanh\left(\sqrt{\xi^2 + \Delta^2}/2k_BT\right)}{\sqrt{\xi^2 + \Delta^2}} D(\xi) d\xi \tag{5.27}$$

Using equation Eq. (5.27), one can find the superconducting gap as a function

of temperature T and the critical temperature where the gap disappears and the material becomes a normal metal. Substituting $\Delta = 0$ at $T = T_c$, we get:

$$1 = VD_0 \int_0^{\hbar\omega} \frac{\tanh(\xi/2k_BT_c)}{\xi} d\xi. \tag{5.28}$$

With $\xi/2k_BT_c = x$, Eq. (5.28) becomes

$$1 = VD_0 \int_0^{\hbar\omega/2k_BT} \frac{\tanh(x)dx}{x} = VD_0(\ln x \tanh x|_0^{\hbar\omega/2k_BT} - \int_0^{\hbar\omega/2k_BT} \ln x \sec^2 x dx) \tag{5.29}$$

Assuming $\hbar\omega \gg 2k_BT$, one finds:

$$\frac{1}{VD} = (\ln(\hbar\omega/2k_BT) - \ln 0.44) \tag{5.30}$$

and thus

$$k_BT_c = 1.136\hbar\omega e^{-1/VD_0} \tag{5.31}$$

If we compare Eq. (5.23) and Eq. (5.31), we obtain a relationship between the superconducting gap $\Delta(0)$ at zero temperature $T = 0$ and the critical temperature T_c,

$$\frac{\Delta(0)}{k_BT_c} = \frac{2}{1.13} = 1.764 \tag{5.32}$$

Thus there is a direct relationship between the critical temperature T_c and the superconducting gap $\Delta(0)$ at $T = 0$ in conventional BCS theory.

Finally to calculate the superconducting gap as a function of temperature [64], we have to use numerical integration, as there is no direct way of simplifying Eq. (5.27). In Fig. 5.1, I plot the superconducting gap Δ versus the temperature T from the BCS theory. The temperature T is normalized to the critical temperature T_c and the superconducting gap Δ is normalized to the superconducting gap $\Delta(0)$ at zero temperature. From the plot, we can see that the superconducting gap does not vary much until $T \geq 0.4T_c$ of the critical temperature of the material. Other than T_c and $\Delta(0)$, this behavior does not depend on the material, provided the material has s-wave pairing and a weak electron-phonon coupling constant.

5.1.1 Density of states

Here I derive the density of the excited states in a superconducting material.

In a normal metal, states above the Fermi energy can be occupied by exciting an electron, while an empty electron state below the Fermi level can be treated as a hole excitation. The density N(E) of excited states in a superconductor obeys:

$$N(E)dE = N(\xi)d\xi \tag{5.33}$$

For a metal made which contains a non-interacting Fermi gas, $d\xi/dE = 1$, and $N_n(E) = N_n(\xi)$.

In the superconducting case, there are no excited states with $|E| < \Delta$, but we

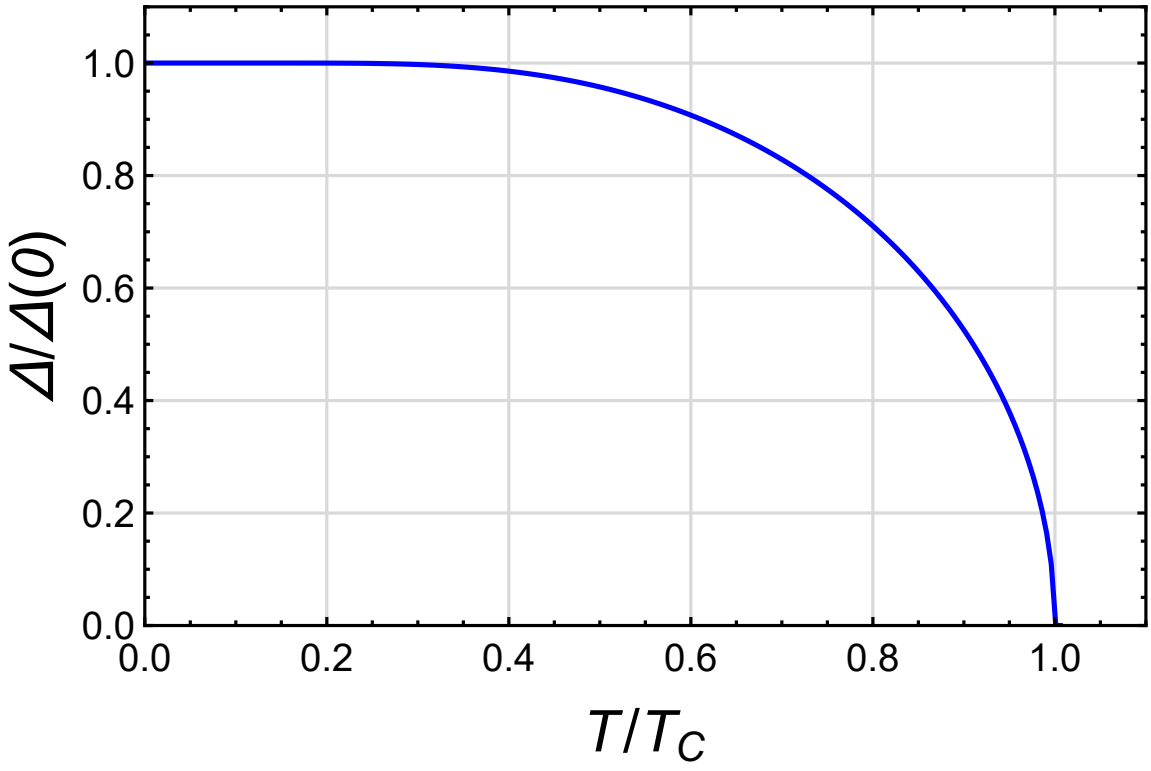

Figure 5.1: Normalized BCS superconducting gap Δ/Δ_0 as a function of normalized temperature T/T_c.

still have

$$N_s(E)dE = N_n(\xi)d\xi \tag{5.34}$$

since we are only interested in energies that are within a few meV from the Fermi energy (the typical energy scale of Δ), we can take $N_n(\xi) = N_n(0)$ as constant. From Eq. (5.34) and Eq. (5.13), we then find

$$\frac{N_s(E)}{N_n(0)} = \frac{d\xi}{dE} = \begin{cases} \frac{E}{\sqrt{E^2-\Delta^2}} & (|E| > \Delta) \\ 0 & (|E| < \Delta) \end{cases} \tag{5.35}$$

Figure 5.2 shows a plot of $N_s(E)/N_n(0)$ as a function of E. Note in particular that the density of states diverges as E approaches Δ from above, while for $|E| < \Delta$, there is zero density of states.

5.2 Andreev reflection

In Chapter 2, I discussed the current-voltage characteristics of tunnel junctions made with a normal metal electrode and a superconducting electrode. For S-I-N tunneling the main takeaway was that since there are no states in the superconductor with energy $|E| < \Delta$, there was no tunneling current for $|eV| < \Delta$ at $T = 0$. However experimentally when the tunnel barrier is low enough, step-like increments of the current occurs for $|E| < \Delta$. This phenomenon is explained by Andreev reflection [44]. Andreev first considered the situation where there is no tunnel barrier. For a

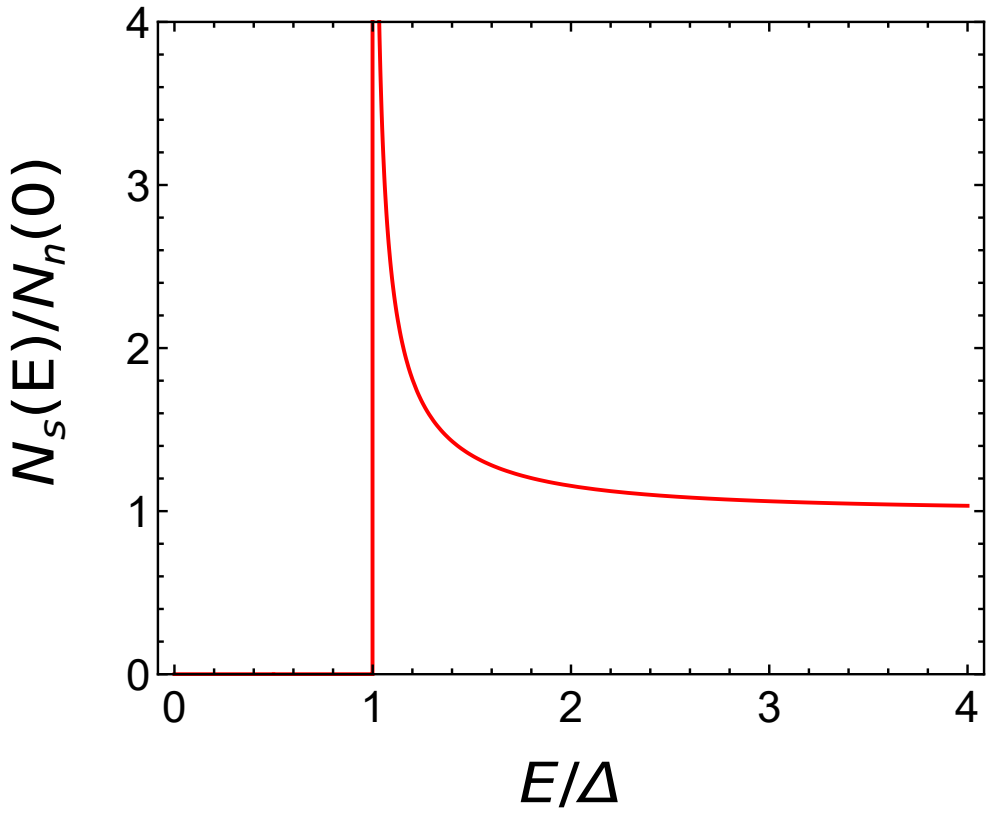

Figure 5.2: Normalized plot of density of states of a superconductor as a function of energy.

quasiparticle with momentum $\hbar k_F$ and a plane wave as a trial function, he solved the superconducting Bogoliubov-de-Gennes equation [64, 104, 105, 112]. After ignoring higher order terms in the Hamiltonian, he found a wavefunction with one component representing an electron traveling to the right in the normal metal and another component representing a hole traveling to the left in the normal metal. When the electrons are incident on the S-N interface from the normal metal at energies $E < \Delta$, they cannot enter the superconductor because there are no available quasiparticle states with $E < \Delta$. Instead, Andreev's solution reveals that a hole is reflected back and a Cooper pair with charge $2e$ is added to the superconductor. This process is called Andreev reflection.

Blonder, Tinkham, and Klapwijk (BTK) [45] generalized Andreev's picture to obtain the $I-V$ curve of S-N interfaces with different transparency [44]. To do this they introduced a δ-function potential barrier of strength Z at the S-N interface and solved the Bogoliubov equations [45] to find the probability of tunneling as a function of Z. When the barrier is high, $Z \gg 1$, one recovers the tunnel limit results described in Chapter 2. This is the high-Z limit where Andreev effects are suppressed. In contrast, when $Z \ll 1$, the barrier height is low, the interface is very transparent, most of the electrons are Andreev reflected, and Andreev effects dominate the conductance.

5.2.1 BTK theory

To find the $I-V$ characteristics of a normal–superconductor junction, the key idea of the BTK theory is to use the Bogoliubov Hamiltonian Eq. (5.6) to find the wavefunctions of electrons and quasiparticles in the normal electrode and superconducting electrode. To deal with the interface, they included a δ-function potential. Matching the wavefunctions at the interface yields the transmission and reflection coefficients.

For the superconductor, one can start from Eq. (5.6) and write the one-dimensional Bogoliubov equation [45, 64]:

$$\begin{pmatrix} -\frac{\hbar^2}{2m}\frac{\partial^2}{\partial x^2} - \mu + H_0\delta(x) & \Delta(x) \\ \Delta^*(x) & \frac{\hbar^2}{2m}\frac{\partial^2}{\partial x^2} + \mu - H_0\delta(x) \end{pmatrix} \begin{pmatrix} u(x) \\ \nu(x) \end{pmatrix} = E \begin{pmatrix} u(x) \\ \nu(x) \end{pmatrix} \tag{5.36}$$

On the normal side there is no superconducting gap and Eq. (5.36) reduces to

$$\begin{pmatrix} -\frac{\hbar^2}{2m}\frac{\partial^2}{\partial x^2} - \mu & 0 \\ 0 & \frac{\hbar^2}{2m}\frac{\partial^2}{\partial x^2} + \mu \end{pmatrix} \begin{pmatrix} u(x) \\ \nu(x) \end{pmatrix} = E \begin{pmatrix} u(x) \\ \nu(x) \end{pmatrix} \tag{5.37}$$

Solving this equation for the eigenvalues E, we obtain $E = +\sqrt{(\frac{\hbar^2 k^2}{2m} - \mu)^2}$ where $\mu = \frac{\hbar^2 k_F^2}{2m}$. One solution corresponds to an electron with wavevector $\overline{k_e}$ such that $\overline{k_e} > k_F$ and energy $E = \frac{\hbar^2 k_e^2}{2m} - \mu$, the other solution corresponds to a hole with wavevector $\overline{k_h}$ such that $|\overline{k_h}| < k_F$ and energy $E = -\frac{\hbar^2 k_h^2}{2m} + \mu$. The solutions for the

wave function can then be written as

$$\Psi_e(x) = \begin{pmatrix} 1 \\ \\ 0 \end{pmatrix} e^{\pm ik_e x}, \qquad \text{where} \quad k_e = \sqrt{\frac{2m}{\hbar^2}(E+\mu)} \tag{5.38a}$$

$$\Psi_h(x) = \begin{pmatrix} 0 \\ \\ 1 \end{pmatrix} e^{\pm ik_h x}, \qquad \text{where} \quad k_h = \sqrt{\frac{2m}{\hbar^2}(\mu-E)} \tag{5.38b}$$

On the superconducting side, we obtain $E = +\sqrt{(\frac{\hbar^2 q^2}{2m} - \mu)^2 + \Delta^2}$ where $\mu = \frac{\hbar^2 k_F^2}{2m}$. Again there are two solution for the energy, $\sqrt{E^2 - \Delta^2} = \frac{\hbar^2 q_e^2}{2m} - \mu$ for the electron case with $q_e > k_F$, and $\sqrt{E^2 - \Delta^2} = -\frac{\hbar^2 q_h^2}{2m} + \mu$ for the hole case with $q_h < k_F$. The wavefunction on the superconducting side can be written as

$$\Psi_e(x) = \begin{pmatrix} u_0 \\ \\ \nu_0 \end{pmatrix} e^{\pm iq_e x}, \qquad \text{where} \quad q_e = \sqrt{\frac{2m}{\hbar^2}(\sqrt{E^2-\Delta^2}+\mu)} \tag{5.39a}$$

$$\Psi_h(x) = \begin{pmatrix} \nu_0 \\ \\ u_0 \end{pmatrix} e^{\pm iq_h x}, \qquad \text{where} \quad q_h = \sqrt{\frac{2m}{\hbar^2}(\mu-\sqrt{E^2-\Delta^2})} \tag{5.39b}$$

If we plug in the energy E and wavefunction defined in Eq. (5.39) into Eq. (5.36), we get $u_0 = \sqrt{\frac{1}{2}(1 + \frac{\sqrt{E^2-\Delta^2}}{E})}$ and $\nu_0 = \sqrt{\frac{1}{2}(1 - \frac{\sqrt{E^2-\Delta^2}}{E})}$. The form for u_0 and ν_0 are the same as in Eq. (5.14).

Given Eq. (5.38) for the wavefunction in the normal (left) electrode and Eq. (5.39) for the wavefunction for the superconductor (right) side, we now assume that the wavefunction for the left side has incident and reflected waves. The incident electron wave function, incoming from the normal left electrode towards

the interface S-N, is

$$\Psi_{\text{in}}(x) = \frac{1}{\sqrt{v_e}} \begin{pmatrix} 1 \\ 0 \end{pmatrix} e^{ik_e x} \tag{5.40}$$

This wave is reflected back into the normal left region and consists of a left-moving electron and a a left-moving hole. Note that the momentum k of a left moving hole will be negative [113] and thus

$$\Psi_{\text{reflect}}(x) = \frac{r_{ee}}{\sqrt{v_e}} \begin{pmatrix} 1 \\ 0 \end{pmatrix} e^{-ik_e x} + \frac{r_{he}}{\sqrt{v_h}} \begin{pmatrix} 0 \\ 1 \end{pmatrix} e^{+ik_h x}. \tag{5.41}$$

Here r_{ee} represents the amplitude of the reflection coefficient of the electron, r_{he} represents the amplitude of the Andreev reflection coefficient of the holes from incident electrons and $v_e \simeq v_h \simeq v_F$ is the Fermi velocity on the left side.

On the right side (superconductor), the transmitted wave contains right-moving electron-like particles and right-moving hole-like particles

$$\Psi_{\text{trans}}(x) = \frac{t_{ee}}{\sqrt{w_e}} \begin{pmatrix} u_0 \\ \nu_0 \end{pmatrix} e^{+iq_e x} + \frac{t_{he}}{\sqrt{w_h}} \begin{pmatrix} \nu_0 \\ u_0 \end{pmatrix} e^{-iq_h x} \tag{5.42}$$

where t_{ee} is the amplitude of the transmission coefficient of the electron and t_{he} is the amplitude of the transmission coefficient of the holes. I note that the wavefunctions are normalized by the different velocities w and v, on the respective sides of the barrier, due to conservation of probability. To determine the velocity of the electrons

and holes in the normal electrode and superconductor electrode, we can use the relation $v = \frac{1}{\hbar}\left|\frac{dE}{dk}\right|$ to obtain:

$$\begin{aligned} v_e &= \frac{\hbar k_e}{m} \simeq v_F & v_h &= \frac{\hbar k_h}{m} \simeq v_F \\ w_e &= \frac{\sqrt{E^2-\Delta^2}}{E}\frac{\hbar q_e}{m} & w_h &= \frac{\sqrt{E^2-\Delta^2}}{E}\frac{\hbar q_h}{m} \end{aligned} \tag{5.43}$$

Finally, we need to match the two wavefunctions at the S-N interface. From Eq. (5.36), we have

$$(-\frac{\hbar^2}{2m}\frac{\partial^2}{\partial x^2} - \mu)u(x) + H_0\delta(x)u(x) + \Delta(x)\nu(x) = Eu(x) \tag{5.44}$$

Integrating the equation over an infinitesimal section spanning the boundary at $x = 0$, we obtain

$$-\frac{\hbar^2}{2m}\left.\frac{\partial u}{\partial x}\right|_{0^-}^{0^+} + H_0u(0) = 0 \tag{5.45a}$$

$$\frac{\partial u(0^+)}{\partial x} - \frac{\partial u(0^-)}{\partial x} = \frac{2mH_0}{\hbar^2}u(0) \tag{5.45b}$$

This is also true for the $\nu(x)$ case. Thus we obtain four equations that need to be

satisfied at the boundary:

$$u(0^+) = u(0^-) \tag{5.46a}$$

$$\nu(0^+) = \nu(0^-) \tag{5.46b}$$

$$\frac{\partial u(0^+)}{\partial x} - \frac{\partial u(0^-)}{\partial x} = \frac{2mH_0}{\hbar^2}u(0) \tag{5.46c}$$

$$\frac{\partial \nu(0^+)}{\partial x} - \frac{\partial \nu(0^-)}{\partial x} = \frac{2mH_0}{\hbar^2}\nu(0) \tag{5.46d}$$

We now plug Eq. (5.40), Eq. (5.41) and Eq. (5.42), into Eq. (5.46) and arrive at four equations for the parameters $t_{ee}, t_{he}, r_{ee}, r_{he}$:

$$\frac{1}{\sqrt{v_e}} + \frac{r_{ee}}{\sqrt{v_e}} = \frac{t_{ee}}{\sqrt{w_e}}u_0 + \frac{t_{he}}{\sqrt{w_h}}\nu_0 \tag{5.47a}$$

$$\frac{r_{he}}{\sqrt{v_h}} = \frac{t_{ee}}{\sqrt{w_e}}\nu_0 + \frac{t_{he}}{\sqrt{w_h}}u_0 \tag{5.47b}$$

$$iq_e\frac{t_{ee}}{\sqrt{w_e}}u_0 - iq_h\frac{t_{he}}{\sqrt{w_h}}\nu_0 - ik_e\frac{1}{\sqrt{v_e}} + ik_e\frac{r_{ee}}{\sqrt{v_e}} = \frac{2mH_0}{\hbar^2}(\frac{1}{\sqrt{v_e}} + \frac{r_{ee}}{\sqrt{v_e}}) \tag{5.47c}$$

$$iq_e\frac{t_{ee}}{\sqrt{w_e}}\nu_0 - iq_h\frac{t_{he}}{\sqrt{w_h}}u_0 - ik_h\frac{r_{he}}{\sqrt{v_e}} = \frac{2mH_0}{\hbar^2}\frac{r_{he}}{\sqrt{v_e}} \tag{5.47d}$$

Blonder *et al.* [45] solved these four equations Eq. (5.47) by using a semi-classical approximation. This approximation is based on the fact that E and Δ are relatively small compared to the Fermi energy μ. To proceed, in Eq. (5.38) and Eq. (5.39), we retain just the lowest order in k, with $k_e = k_h = q_e = q_h = k_f = \sqrt{\frac{2m\mu}{\hbar^2}}$

so that Eq. (5.43) then becomes

$$v_e = v_h = \frac{\hbar k_f}{m} \tag{5.48a}$$

$$w_e = w_h = \frac{\sqrt{E^2 - \Delta^2}}{E}\frac{\hbar k_f}{m} \tag{5.48b}$$

Plugging Eq. (5.48) into Eq. (5.47) and solving the four equations for the four parameters, we obtain:

$$r_{he} = \frac{u_0\nu_0}{u_0^2 + Z^2(u_0^2 - \nu_0^2)} \tag{5.49a}$$

$$r_{ee} = \frac{(Z^2 + iZ)(\nu_0^2 - u_0^2)}{u_0^2 + Z^2(u_0^2 - \nu_0^2)} \tag{5.49b}$$

$$t_{ee} = \frac{(1 - iZ)u_0\sqrt{u_0^2 - \nu_0^2}}{u_0^2 + Z^2(u_0^2 - \nu_0^2)} \tag{5.49c}$$

$$t_{he} = \frac{iZ\nu_0\sqrt{u_0^2 - \nu_0^2}}{u_0^2 + Z^2(u_0^2 - \nu_0^2)} \tag{5.49d}$$

where the barrier height parameter is $Z = H_0 m/\hbar^2 k_f = H_0/\hbar v_f$.

The transmission and reflection coefficients can be obtained from Eq. (5.49). Here we preserve the convention in Ref. [45]. $A = |r_{he}|^2$ gives the probability of Andreev reflection. $B = |r_{ee}|^2$ gives the ordinary reflection probability of electrons, $C = |t_{ee}|^2$ is the transmission amplitude of electrons without branch crossing while $D = |t_{he}|^2$ is the transmission of the holes with branch crossing. Table 5.1 gives A, B, C, D for both $E > \Delta$ and $E < \Delta$, where $u_0 = \sqrt{\frac{1}{2}(1 + \frac{\sqrt{E^2-\Delta^2}}{E})}$, $\nu_0 = \sqrt{\frac{1}{2}(1 - \frac{\sqrt{E^2-\Delta^2}}{E})}$, for the $E > \Delta$ case. For $E < \Delta$, we have to use the defi-

Table 5.1: Transmission and reflection coefficients in the BTK theory. A is the probability of Andreev reflection. B is the probability of ordinary reflection of electrons. C is the probability of transmission of the electrons. D is the probability of transmission of the holes.

	A	B	C	D
$E > \Delta$	$\frac{u_0^2\nu_0^2}{[u_0^2+Z^2(u_0^2-\nu_0^2)]^2}$	$\frac{(u_0^2-\nu_0^2)Z^2(1+Z^2)}{[u_0^2+Z^2(u_0^2-\nu_0^2)]^2}$	$\frac{u_0^2(u_0^2-\nu_0^2)(1+Z^2)}{[u_0^2+Z^2(u_0^2-\nu_0^2)]^2}$	$\frac{\nu_0^2(u_0^2-\nu_0^2)}{[u_0^2+Z^2(u_0^2-\nu_0^2)]^2}$
$E < \Delta$	$\frac{\Delta^2}{E^2+(\Delta^2-E^2)(1+2Z^2)^2}$	$1-A$	0	0

nition $u_0 = \sqrt{\frac{1}{2}(1+i\frac{\sqrt{\Delta^2-E^2}}{E})}$, $\nu_0 = \sqrt{\frac{1}{2}(1-i\frac{\sqrt{\Delta^2-E^2}}{E})}$ and plug into Eq. (5.49). I note that in this case $C = D = 0$.

In Fig. 5.3, I plot the coefficients A (blue) and B (red) as a function of energy for different values of Z. As we can see in Fig. 5.3(a), $Z = 0$ is the ideal transparent limit. In this case $A = 1$ inside the gap, meaning all incident electrons in the N-region are Andreev reflected as holes. For energies above the gap, we see that an electron has a finite probability to be transmitted as an electron. On the other hand, for $E < \Delta$ and $Z \gg 1$ (see Fig. 5.3(d)), the electrons are almost completely reflected as electrons, and there is barely any Andreev reflection. This is also the reason why in the tunnel limit, no current flows across the junction for $V < \Delta/e$. Note also that for $E < \Delta$: $A = 1 - B$, *i.e.* the probability of transmission plus reflection must be equal to 1. So an increased probability of electron reflection will lead to a decrease of Andreev reflection.

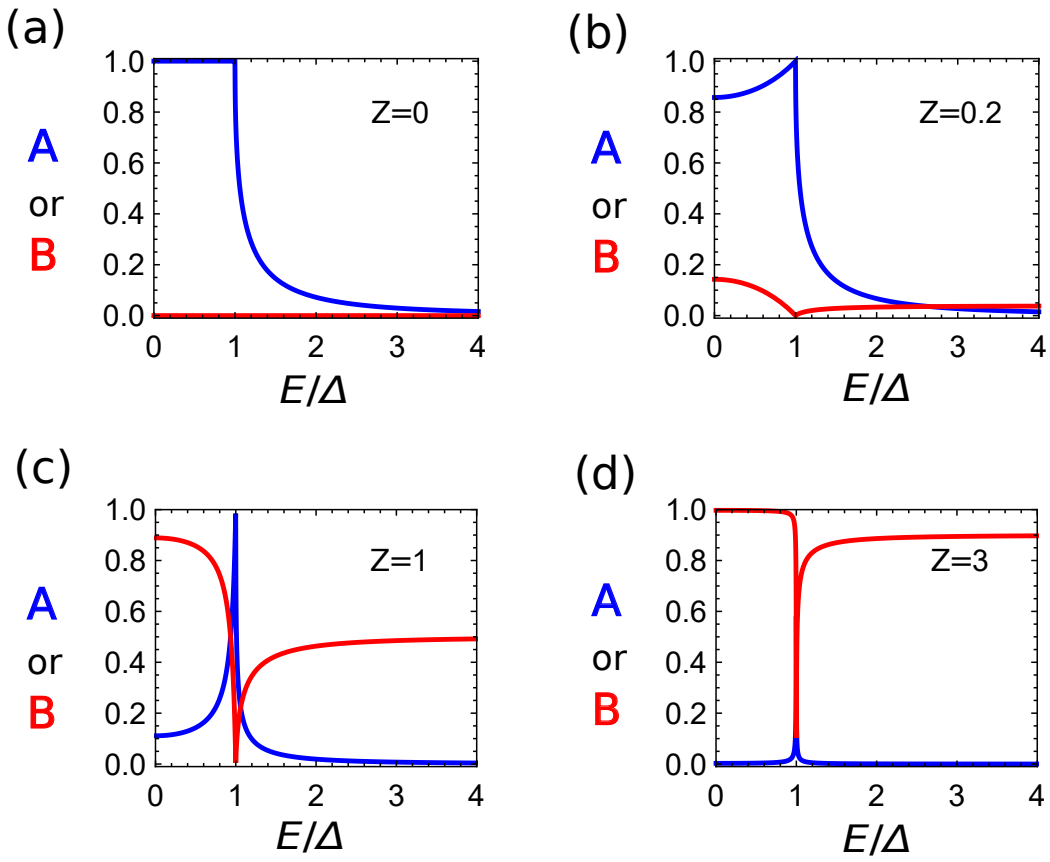

Figure 5.3: (a)-(d) plot of Andreev reflection probability A (blue) and normal electron reflection amplitude B (red) as a function of normalized energy E/Δ at different values of the barrier height Z. For $Z = 0$ and $E < \Delta$, all electrons are Andreev reflected at the interface. For $E > \Delta$ electrons are partially reflected. For $Z \gg 1$, the electrons are completely reflected for $E < \Delta$ and partially transmitted for $E > \Delta$.

5.2.2 Calculation of I-V Characteristics for S-I-N junction from the BTK model

In this section I discuss the BTK model for how the current-voltage characteriscis behave as a function of the barrier height Z. The derivation is somewhat complicated and a very nice and detailed derivation can be found in lecture notes from Kopnin [114].

Essentially there are four processes that contribute to current flowing across an S-I-N interface. The first process is due to electrons that are incident on the S/N interface from the normal side. Such electrons have a probability to be Andreev reflected as holes and normally reflected as electrons, while the rest will be transmitted as quasiparticles into the superconducting side. The second process is due to holes incident on the S/N interface from the normal side. The third process involves electron-like quasiparticles starting out on the superconducting side and transferring electrons or holes to the normal side. The last process involves hole-like quasiparticles incident on the S/N interface from the superconductor. We need to sum up the current from these processes to get the total current. One finds a fairly simple expression by considering the resulting net current on the normal side [45]:

$$I = 2N(0)ev_f\sigma \int_{-\infty}^{\infty} [f_0(E - eV) - f_0(E)](1 + A(E) - B(E))dE. \tag{5.50}$$

Here $N(0)$ is the density of states of single spins at the Fermi energy μ, σ is the effective cross sectional area of the junction, and v_f is the Fermi velocity of the

electrons in the normal metal. The normal junction resistance $R_n = 1/2N(0)e^2v_f\sigma$. Another way of looking at this expression is that incoming electrons with unity probability are Andreev reflected as holes with probability $A(E)$, which increases the electron flow. The probability $B(E)$ describes normally reflected electrons which decrease the net flow of electrons through the interface. Taking the derivative of I with respect to the voltage V, we get the conductance:

$$G_{ns}(V) = \frac{dI}{dV} = \frac{1}{eR_n}\int_{-\infty}^{\infty} \frac{\partial f_0(E-eV)}{\partial V}(1 + A(E) - B(E))dE \tag{5.51}$$

Scanning tunneling microscopy (STM) enables us to measure the conductance G versus V, which can be compared directly to Eq. (5.51). The resulting $\mathrm{d}I/\mathrm{d}V$curves depend strongly on the transparency parameter Z, provided Z is not too large compared to unity.

Figure 5.4 shows an example of plots of the conductance versus energy for $Z = 0$ (red), 0.5 (blue), 1.5 (green), and 5 (purple) at 75 mK. As we can see, when the junction is very transparent ($Z = 0$) and $eV < \Delta$, the conductance is doubled in value compared to the conductance at $eV \gg \Delta$. Conversely, in the tunnel limit $Z \gg 1$, there is zero conductance for $eV < \Delta$, recovering the traditional S-I-N tunnel junction behavior discussed in Fig. 2.6.

For comparison, Fig. 5.5 shows an example of plots of the conductance versus energy for $Z = 0$ (orange), 0.5 (cyan), 1.5 (yellow), and $Z = 5$ (magenta) at $T = 500$ mK. As we can see, thermal broadening rounds off conductance peaks, and the effect shows up more in the tunnel limit ($Z \gg 0$) than in the low Z limit.

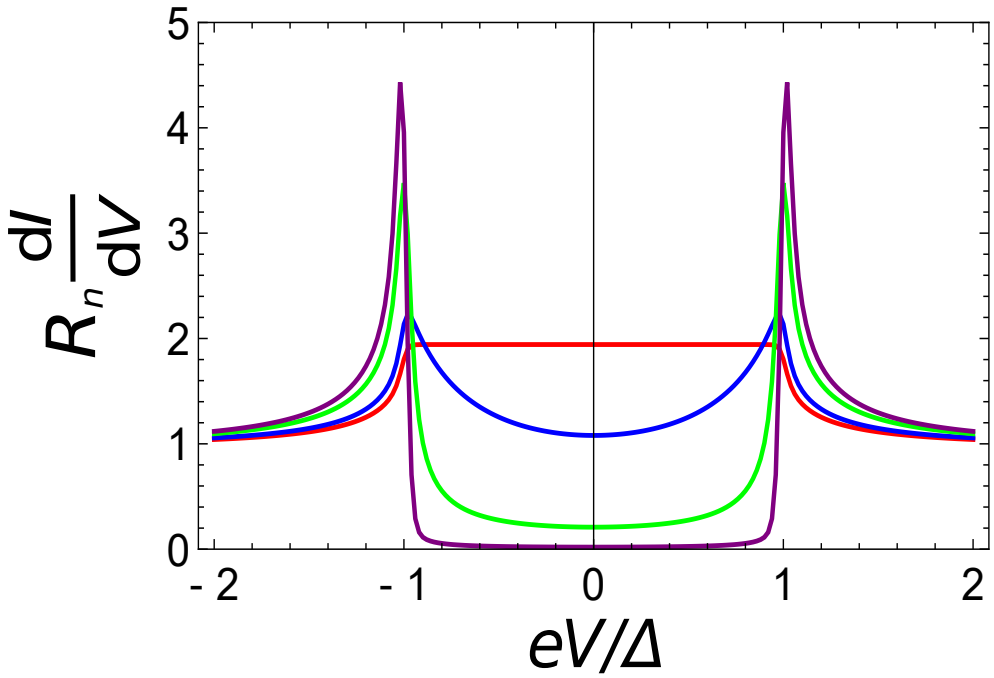

Figure 5.4: Normalized BTK S-I-N conductance $R_n \mathrm{d}I/\mathrm{d}V$ as a function of normalized voltage eV/Δ at a temperature of T=75 mK for superconducting gap Δ =0.5 meV. Red curve is for $Z = 0$, blue for $Z = 0.5$, green for $Z = 1.5$ and purple for $Z = 5$. Notice that in the very transparent limit ($Z \approx 0$), the conductance becomes twice that of the normal state. In the tunnel limit $Z \gg 0$, the curve recovers the classic tunneling limit.

When the junction is very transparent ($Z = 0$) the conductance at edge $eV \sim \Delta$ is rounded but this is less obvious than rounding of the coherence peak in the high Z limit.

Figure 5.6 shows all the curves from Fig. 5.4 and Fig. 5.5. From the plot we see that the coherence peaks in the limit $Z \to \infty$ is effected strongly due to the thermal broadening. In contrast, for the low-barrier case $Z \approx 0$, the curves appear to be only slightly rounded around $eV \sim \Delta$.

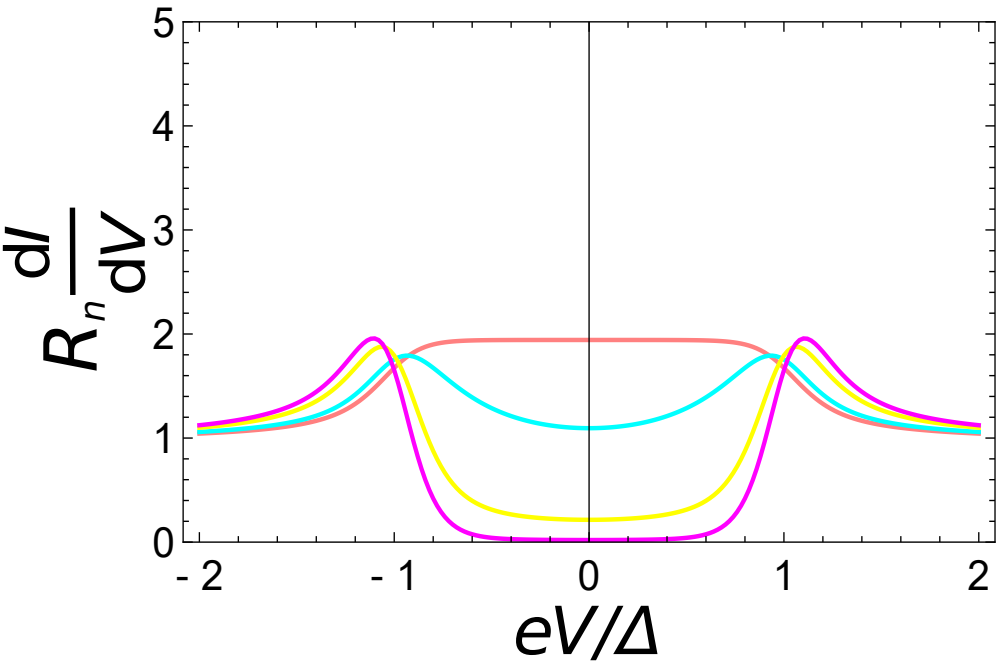

Figure 5.5: Normalized BTK S-I-N conductance $R_n \mathrm{d}I/\mathrm{d}V$ as a function of normalized voltage eV/Δ at a temperature of T=500 mK for superconducting gap Δ =0.5 meV. Orange curve is for $Z = 0$, cyan is for $Z = 0.5$, yellow is for $Z = 1.5$ and magenta is for $Z = 5$. Comparing Fig. 5.4 to Fig. 5.5, we see that thermal broadening affects the curves more for $Z \gg 0$ than for $(Z \ll 1)$.

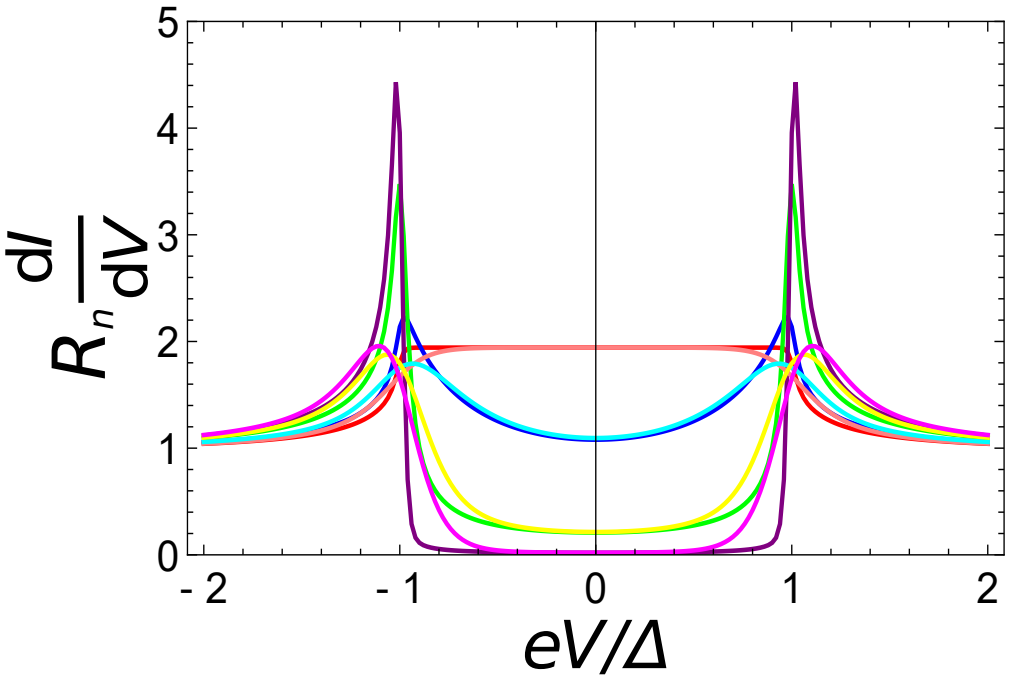

Figure 5.6: Overlapping of all curves shown in Fig. 5.4 and Fig. 5.5 to get a better comparison of the thermal broadening effect for different barrier height Z.

CHAPTER 6

Scanning Andreev Tunneling Microscopy of Titanium Nitride Thin Films

6.1 Introduction

Thin-film superconducting titanium nitride (TiN) has attracted recent interest because it can have very low loss and this makes it attractive for building microwave resonators and possibly other devices for applications in quantum computation [46–50]. TiN can also have a high kinetic inductance and this also makes it potentially interesting for constructing superconducting microwave kinetic inductance detectors for x-ray spectroscopy and sub-millimeter-wave astronomy telescopes [51–55]. In practice, good superconducting films of TiN are not so easy to grow reproducibly. In particular the loss, the superconducting critical temperature T_c, the micro-structure, grain size and stress all depend on the growth conditions. Although kinetic inductance measurements suggest a well-defined gap [53], atomic scale scanning tunneling microscopy (STM) [20] of typical films show very rough surfaces and small grains. Furthermore measurements of thin TiN films have re-

vealed a superconductor-insulator transition and inhomogeneous superconducting gap [115–117].

In this chapter, I describe my results on scanning tunneling microscopy [41] of superconducting 50 nm and 25 nm thick TiN films taken at 500 mK. In Section 6.2, I discuss some basic properties of the films. In Section 6.3, I show fine scale maps of the 50 nm film which show significant spatial variations in the superconducting gap that are correlated with the topography. In addition I observed a distinct zero-bias conductance peak at some locations. Such peaks are characteristic of Andreev S/N tunneling [44] through a high transparency barrier, as opposed to conventional superconductor-normal quasiparticle tunneling [66, 118] through a low transparency barrier. Using an analysis based on the Blonder-Tinkham-Klapwijk (BTK) model of Andreev tunneling [45] (see Chapter 5), I extract maps of the superconducting gap Δ, temperature T and barrier height Z and examine some interesting features in the maps. In Section 6.4, I then show the topography and maps of Δ, Z and T on a larger scale. I find that both the 50 nm thick and 25 nm thick films show significant variations in Δ. Much of the variation in Δ in the thicker film (50 nm) appears to be due to variations in the local temperature, while in the thinner film (25 nm) the Δ variations are correlated with variations in the barrier height. Finally, in Section 6.5, I discuss some possible explanations of the T variations and the correlations between Δ, Z and T.

6.2 TiN film growth and basic characteristics

Our TiN films were deposited by Kevin Osborn's group [119] on a high resistivity (100) silicon wafer ($\rho > 20000\ \mu\Omega \cdot \mathrm{cm}$, float-zone). The substrate was pretreated in an O_2 plasma for 30 s before being put into the sputtering system. After evacuating the sputter chamber, the substrate was heated to 350°C. During DC magnetron sputtering 400 W of rf power was applied to a 7.6 cm diameter Ti target while maintaining a pressure of 3.5 mTorr with Ar and N_2 gas flowing at 15 SCCM and 10 SCCM, respectively.

The T_c of the 50 nm thick film was found to be 4.7 K using an inductive measurement while the 25 nm TiN film had T_c=3.6 K. From T_c, the BCS coherence length was estimated to be $\xi = 18$ nm for the 50 nm thick film and $\xi = 15$ nm for the 25 nm thick film. (Measurements were done by Serena Merteen from Leonardo Civale's group at Los Alamos National Laboratory.) Resonators made from the 50 nm film showed an internal quality factor of $Q_i = 2{\times}10^5$, whether or not an O_2 pretreatment was used, while the 25 nm thick film had $Q_i = 1.5{\times}10^4$ with an O_2 pretreatment, compared to $Q_i = 2{\times}10^5$ without O_2 pretreatmeant. (Quality factor measurements were done from Kevin Osborn's group at Laboratory for Physical Sciences.) For the 50 nm film $k_F l = \hbar(3\pi^2 n)^{2/3}/e^2\rho n^{1/3} \approx 24$, while $k_F l \approx 16$ for the 25 nm film, where n is the carrier density obtained from Hall measurements and ρ is the resistivity. Based on these values neither films violates the Ioffe-Regel limit [120] and both films are weakly disordered.

Prior to imaging with the STM, each film was mounted on an STM sample

stud [41], and then sonicated in isopropanol for five minutes to remove dust particles. The sample was then transferred to the custom UHV setup [41] and the surface was cleaned by sputtering using 750 eV Ar ions while gently heating the sample at $T \sim 300$ °C for 60 minutes. We note that heating the TiN samples above 400 °C caused T_c to decrease substantially. The sample was then transferred without breaking vacuum to the cold-stage of a mK-STM [41] for imaging with a vanadium tip or a Nb tip. The vanadium tip was used to image the 50 nm thick TiN film while the Nb tip was used to image the 25 nm thick TiN film.

Since niobium has a critical temperature T_c of 9.2 K and vanadium has a critical temperature T_c of 5.03 K, one may ask why we see an S-I-N junction. The possible reason is that since the TiN film is very granular and the surface is not flat, the tip easily picks up debris from the surface which makes it an effectively normal tip. Another possible reason is that for spectroscopy measurements, I needed to set the sample bias as low as 5 meV. This leads to a junction resistance of over 50 MΩ and places the tip close to the sample. Normally in an STM, the sample bias is around 1 V when STM performs surface imaging, and the junction resistance is around 1 GΩ. Due to how close the tip is to the sample when performing spectroscopy measurements, the tip can easily pick up debris and become normal. I note that I did find some data sets that showed S-I-S behavior, however the tip changed after acquiring just part of the spectroscopic map (see Appendix B).

6.3 STM measurements and Andreev effects

Figure 6.1 (a) shows an STM topographic map of a 42 nm × 42 nm region on the 50 nm thick TiN film. This image was acquired at 0.5 K using a vanadium tip and there are 256 × 256 pixels. I used a voltage bias $V = 4$ mV and a tunneling current $I = 100$ pA. In this false color topographic image, blue and purple are higher grains while red and yellow are lower. The surface is very granular.

As the topography was being measured for Fig. 6.1 (a), I-V curves were also acquired at 128 × 128 pixels by sweeping the bias voltage V from 4 mV to -4 mV while recording the tunnel current I. Conductance $\mathrm{d}I/\mathrm{d}V$ versus V curves were also obtained simultaneously by adding a small ac modulation voltage (140 μV) to the voltage bias and using a lock-in amplifier to extract the ac signal from the tunnel current.

Figure 6.1 (b)-(f) show $\mathrm{d}I/\mathrm{d}V$ *vs.* V curves at five selected locations in Fig. 6.1 (a) taken at 0.5 K using a vanadium tip. The range of behavior is striking. Qualitatively Figs. 6.1 (b) and (c) show a clearly recognizable superconducitng gap, as expected for superconducting-normal tunneling through a convenional low-trasnparency barrier [64], although there appears to be much more leakage current at low voltages than expected. On the other hand, Fig. 6.1 (d) seems to show a gap and coherence peaks, but the conductance at zero volts is almost the same as at high voltage, which is not what is expected for a conventional S/N tunnel barrier. Finally, Figs. 6.1 (e) and (f) show a distinct peak in the conductance at zero bias, reaching about two or three times the conductance at high voltage, respectively. This is what is expected

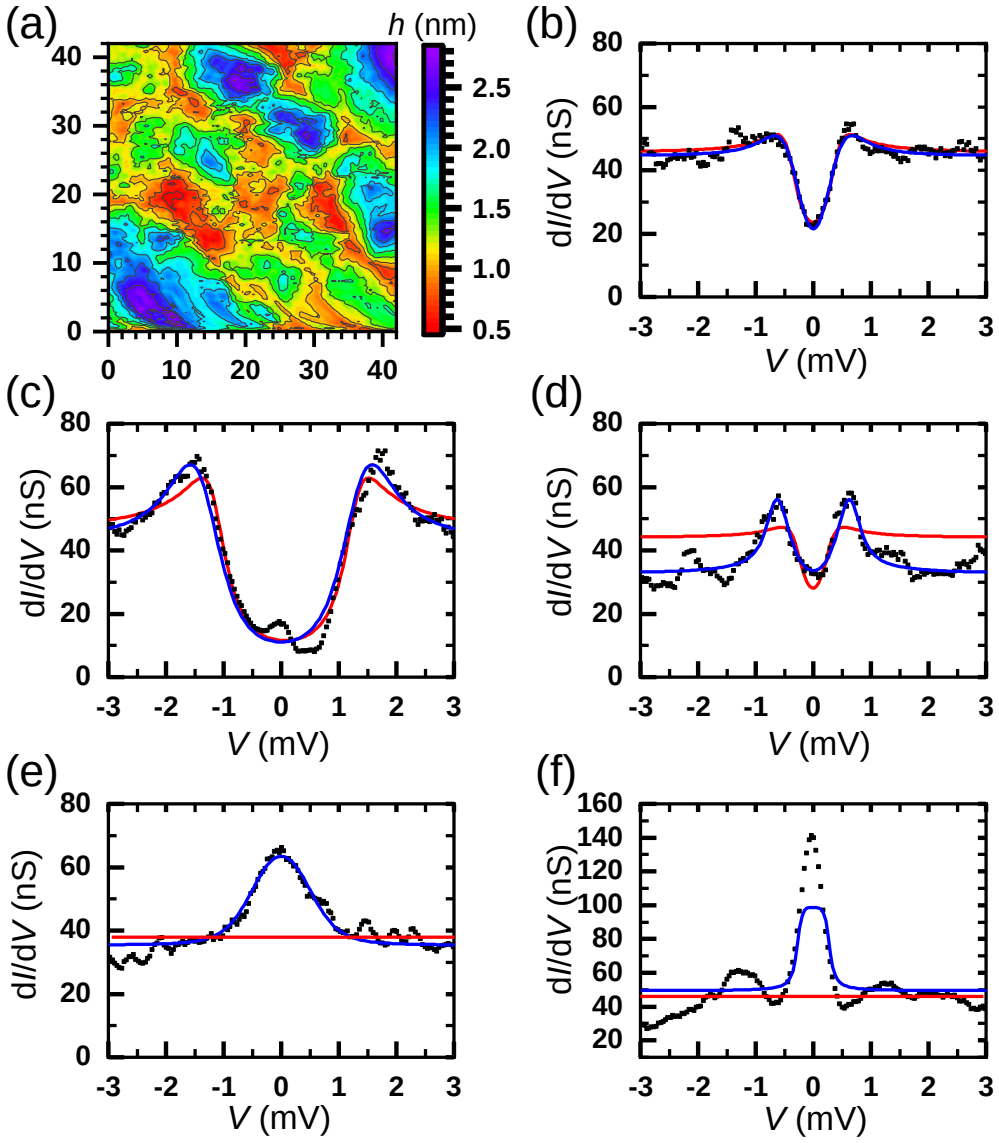

Figure 6.1: (a) Fine scale (42 nm × 42 nm) topographic map of 50 nm thick TiN film at a temperature of 0.5 K using a vanadium tip. (b) Measured conductance dI/dV versus voltage V (black points) at (x,y)=(36.42 nm, 9.19 nm) as well as fit to BTK model (blue) for Z = 3.15 and $\Delta = 0.35$ meV and Dynes model (red) for $\Delta = 0.395$ and Γ = 0.235 meV. (c) Measured dI/dV *vs.* V (black points) at (x,y)=(26.91 nm, 13.78 nm) as well as fit to BTK model (blue) for Z = 1.44 and $\Delta = 1.39$ meV and Dynes model (red) for $\Delta = 1.274$ and $\Gamma = 0.34$ meV. (d)-(f) dI/dV *vs.* V at (2.63 nm, 5.25 nm), (8.20 nm, 36.09 nm) and (34.78 nm, 13.45 nm), respectively. Blue curves are fit to BTK model for Z =0.56, 0.00294 and 0.00217, respectively, and Δ =0.66, 0.44, 0.25, respectively.

from S/N tunneling through a highly transparent barrier when Andreev reflection [44, 45] is taken into account. Reexamining the curve in Fig. 6.1 (d), it appears consistent with Andreev tunneling through a barrier that is of intermediate barrier height.

To analyze the conductance *vs.* V data, I fit it to the conductance from the BTK [45] model of Andreev reflection at a superconductor/normal interface. The key model parameter is the barrier height parameter Z of the interface. For Z much less than 1, the interface is very transparent, i.e. $D = 1/(1+Z^2) \approx 1$ while for Z much greater than 1, the barrier has a low transparency, i.e. $D = 1/(1+Z^2) \approx 1$ and one recovers the conventional S/N tunneling limit [118]. As discussed in Chapter 5, the BTK model conductance can be expressed as [45]:

$$G(V) = A_0 \times \int_{-\infty}^{\infty} \frac{\partial f_0(E-eV)}{\partial V}(1 + A(E) - B(E))\mathrm{d}E. \tag{6.1}$$

Here $f_0(E)$ is the Fermi function, which is dependent on the temperature T, $A(E)$ is the amplitude of the Andreev reflection at the S/N interface, $B(E)$ is the amplitude for the reflection of normal electrons of energy E and $A_0 = (1+Z^2)/(eR_N)$. $A(E)$ and $B(E)$ depend on the barrier height Z of the barrier and the superconducting gap Δ [45]:

$$A(E) = \begin{cases} \frac{\Delta^2}{[E^2+(\Delta^2-E^2)(1+2Z^2)^2]}, & \text{for } E < \Delta \\ \frac{\Delta^2}{[E+\sqrt{E^2-\Delta^2}(1+2Z^2)]^2}, & \text{for } E > \Delta \end{cases} \tag{6.2}$$

$$B(E) = \begin{cases} 1 - \frac{\Delta^2}{[E^2+(\Delta^2-E^2)(1+2Z^2)^2]}, & \text{for } E < \Delta \\ \frac{4Z^2(1+Z^2)(E^2-\Delta^2)}{[E+\sqrt{E^2-\Delta^2}(1+2Z^2)]^2}, & \text{for } E > \Delta. \end{cases} \tag{6.3}$$

I evaluated Eqs.(6.1) to (6.3) numerically and varied Δ, T and Z to obtain the best fit to the measured $\mathrm{d}I/\mathrm{d}V vs.$ V curve at each location. As the blue curves in Figs. 6.1 (b)-(f) show, we find good qualitative agreement except for the curve in Fig. 6.1 (f).

For comparison, the red curves in Figs. 6.1 (b)-(f) show fits to the conductance in a junction with a conventional tunnel junction characteristic, *i.e.* through a low transparency barrier, with a Dynes gap function [66]. In this case we can write:

$$G(V = \frac{1}{eR_n}\int_{-\infty}^{\infty} \frac{\partial f_0(E-eV)}{\partial V} \frac{E - i\Gamma}{\sqrt{(E-i\Gamma)^2 - \Delta^2}} \mathrm{d}E \tag{6.4}$$

here Γ is the broadening parameter, $f_0(E)$ is the Fermi function and Δ is the gap. Comparing the measurements (blue) to the Dynes fits (red) in Figs. 6.1 (b)-(f), we see reasonable fits for Figs. 6.1 (b) and (c), but quantitatively and qualitatively poor fits in Figs. 6.1 (d)-(f) where the best fits yield $\Delta \simeq 0$.

Table 6.1 summarizes the fit parameters (Δ, Z, T) obtained from the BTK fits shown in Fig. 6.1 (blue). The curves have significantly different gaps, temperatures, and Z values. For example, for Fig. 6.1 (b) I found $Z = 3.15$, which is somewhat large compared to 1, indicating the junction is not far from being in the conventional S/N tunneling limit [64]. For comparison, fitting to the curve in Fig. 6.1 (d) yield $Z = 0.56$, which indicates a fairly transparent barrier. BTK fits to Figs. 6.1 (e)

and (f) yielded $Z \cong 0.003$ and $Z \cong 0.002$, respectively, which indicates a highly transparent barrier. I note in particular the BTK fit in Figs. 6.1 (e) is reasonable and the behavior is just what one expects for Andreev tunneling in a highly transparent S/N junction.

I note that this application of the BTK model only assumed a single channel with well-defined Z, Δ and T. Better fits could be obtained by allowing for two or more channels with different Z. Also, the BTK fit in Fig. 6.1 (e) is not good around the zero bias voltage and it might suggest that mid-gap states are present [26].

Although only a few sample curves are shown in Fig. 6.1, the range of behavior is just what one expects from S/N Andreev tunneling through barriers that range from highly transparent (Fig. 6.1 (e) and (f)) to low transparency (Fig. 6.1 (b) and (c)). Although the fits to the BTK model are not perfect, they much more faithfully represent the data than the fit to a Dynes model, Eq. (6.4). Thus I conclude that Andreev effects are important in interpreting the STM data from our TiN samples and that using a Dynes model here would potentially result in a mistaken interpretation.

To better understand the sample, I took additional images of the region (see Fig. 6.2). Figure 6.2 (a) shows the same topographic STM image as in Fig. 6.1 (a), with a different color scale. Figure 6.2 (b) shows a topographic image of the same region, scanned just before taking the spectroscopy. It shows the grains more clearly and there is no apparent drift (white boxes in (a) and (b) represent the same area). Figure 6.2 (c) shows a topographic image of a larger region on the same 50 nm film. There seems to be some features on the grains that line up in different directions on

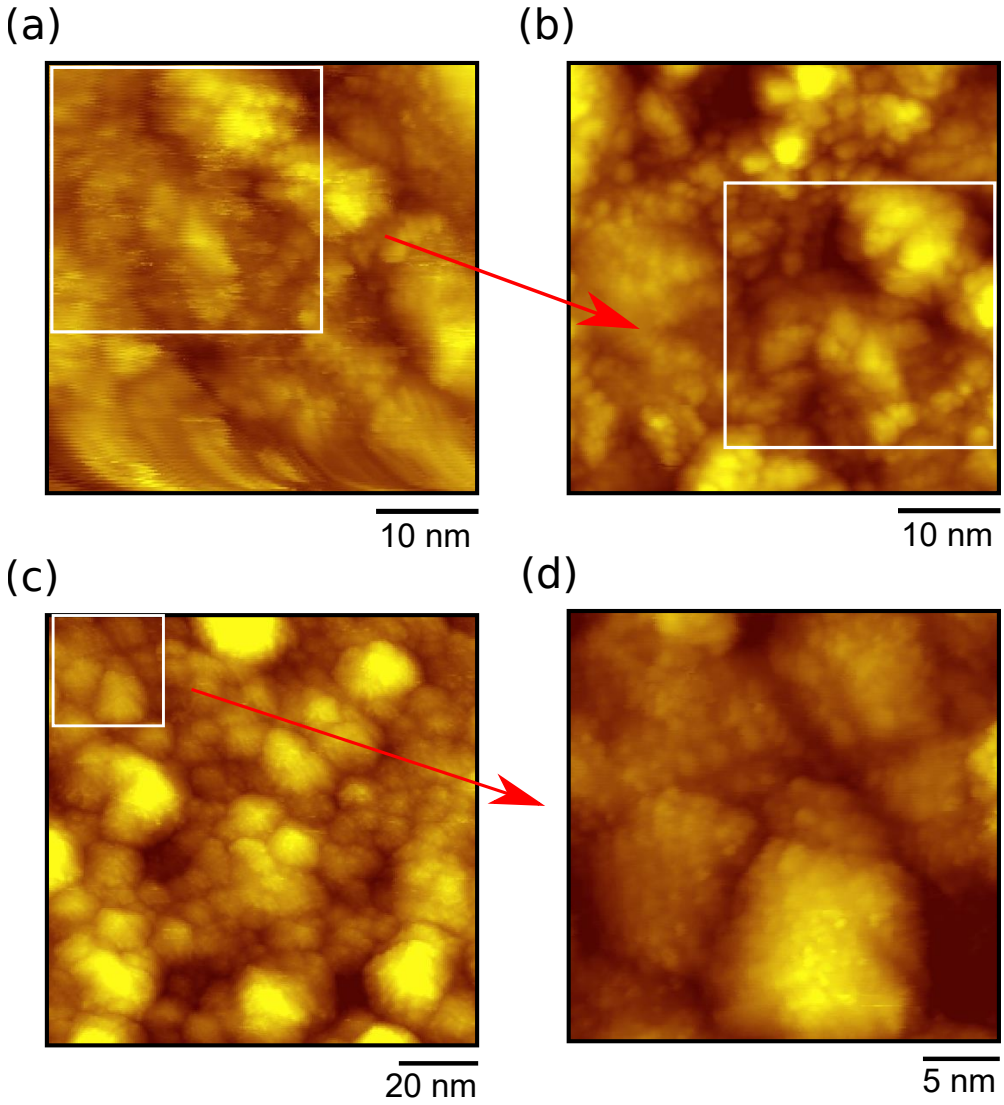

Figure 6.2: (a) Topographic image showing the same data as Fig. 6.1 (a) but with a different color palette. (b) This image was taken before the spectroscopy data and has better resolution and less drift. (c) Another nice topographic image of the sample and (d) high resolution image showing fine texture on top of individual grains.

Table 6.1: Extracted parameters (Δ, T, Z) from fitting the conductance curves in Figs. 6.1 (b)-(f) to the BTK model Eq. (6.1).

No.	Δ (meV)	T (K)	Z
(b)	0.35	1.95	3.15
(c)	1.39	2.43	1.44
(d)	0.66	0.94	0.56
(e)	0.44	2.60	0.003
(f)	0.25	0.42	0.002

different grains, with no clear step structure. Figure 6.2 (d) shows a fine scale image with many small grains decorated with particles that have different alignment on each grain. The surface is clearly poly-crystalline, with a grain size of order 10 nm in this small region.

Figure 6.3 (a) again shows the topography of the 50 nm TiN film, while Figs. 6.3(b)-(d) show the corresponding maps of Δ, T and Z obtained from fitting the conductance curves at each point to the BTK model. Again, all the data was taken at 0.5 K. First, note that there are distinct, spatially correlated variations in all four maps, but they are most obvious in the topography and gap, *i.e.* Figs. 6.3 (a) and (b). If we compare the topography in Fig. 6.3 (a) to the Δ map in Fig. 6.3 (b) one sees a distinct correspondence between the colors. Thus for example, topographically high points (blue in Fig. 6.3 (a)) correspond to small values of Δ (blue in Fig. 6.3 (b)). Similar but less pronounced variations in T are evident in Fig. 6.3

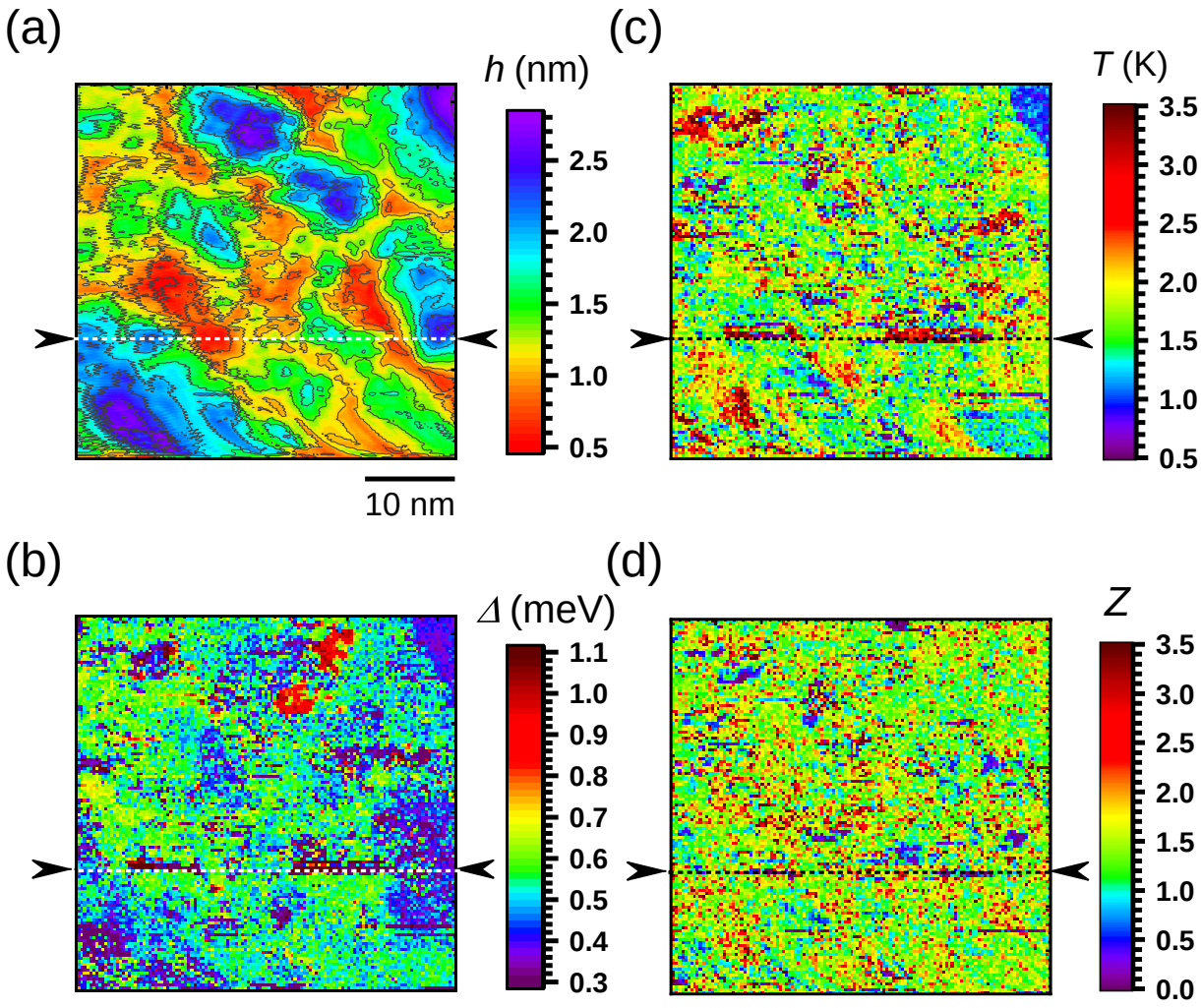

Figure 6.3: (a) Topographic and (b) false color map of superconducting gap Δ for 50 nm thick TiN film. (c) Maps of temperature T and (d) barrier height Z, all from fitting the conductance curves to the BTK model. The dark blue regions indicate locations with a zero bias conductance peak and small Z. All of these data was taken at 0.5 K using a vanadium tip.

(c), with higher points tending to give higher temperature. Such topography correlated variations are also present in Z, but they are much less obvious due to larger point-to-point random variations.

To verify that the large spatially correlated variations in the gap are directly visible in the raw data, Fig. 6.4 shows a false color plot of $\mathrm{d}I/\mathrm{d}V$ *vs.* V along a line cut (indicated by arrows in Fig. 6.3 (b)). Distinct regions are clearly visible where the superconducting gap differs by a factor of 2. The transition appears to be abrupt on the nm scale, perhaps suggesting grain-to-grain variations from one disconnected grain to another. One also sees a section with a prominent zero-bias conductance peak (red), consistent with Andreev effects in an S/N junction with a high transparency. The fact that TiN shows large local variations in Δ is perhaps not surprising given the granular nature of the films. Also, variations in barrier height Z are not surprising because they are likely due to surface contamination or local damage created while preparing the film. What is surprising is to see correlations between the topography and T or Z. To understand what is going on, I acquired additional data, including on the 25 nm TiN film, as discussed in the next section.

6.4 Δ, Z, T, h correlations in the 50 nm and 25 nm films

Figure 6.5 shows larger scale topographic images of the 50 nm and 25 nm TiN films. Both of the films were very granular. From analysis of the images, the maximum grain size of the 50 nm thick film was 20 nm while for 25 nm thick film

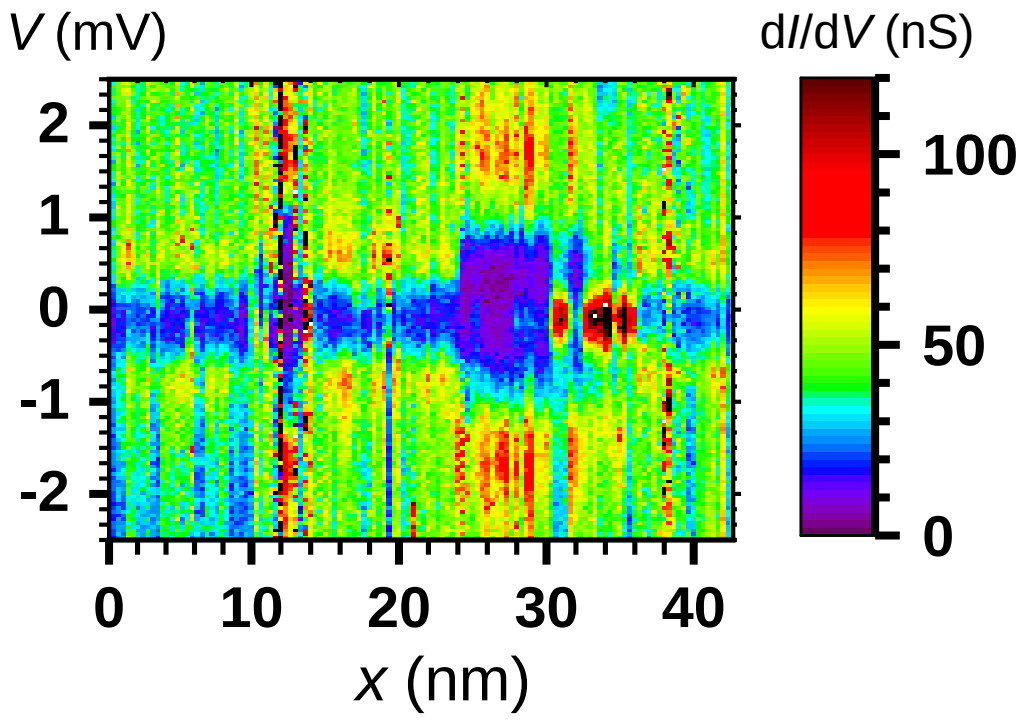

Figure 6.4: False color plot of conductance $\mathrm{d}I/\mathrm{d}V$ versus position x and voltage V along the line cut indicated by black arrows in Fig. 6.3 (a).

Table 6.2: General properties of the 50 nm and 25 nm thick TiN film.

Film thickness	T_c (K)	ξ (K)	Q_i	roughness (nm)	grain sizes (nm)
50 nm	4.7	18	2×10^5	4	20
25 nm	3.6	15	1.5×10^4	2	10

the average grain size was about 10 nm. The surface roughness is 4 nm for the 50 nm thick film and 2 nm for the 25 nm thick film. Overall we see that the thicker (50 nm) film had a rougher surface and a larger grain size. Table 6.2 summarizes a few properties of the two films.

Figure 6.6 (a) shows a 350 $\times$ 160 nm^2 topographic image of the 50 nm film acquired at 500 mK taken with a vanadium tip. For this image, we used a voltage bias V = 4 mV and a tunneling current I = 100 pA. The resulting topographic map had 256 $\times$ 113 points, and I acquired spectra at each location. Figure 6.6 (b) shows the corresponding map of the superconducting gap Δ obtained by fitting the conductance dI/dV *vs.* V data at each location to the BTK model, Eq. (6.1). Gray points in the map indicate curves where we did not obtain a good fit (see Appendix A). Figure 6.6 (c) shows a line section through the topographic image (gray) and the gap map (blue). Examining the plot, we see that the superconducting gap is strongly anti-correlated with surface height (note the reversed scale for Δ). To verify that this is not an artifact from fitting to the BTK model, I also show in red the gap extracted from a fit to the Dynes model, Eq. (6.4). Although Eq. (6.4) does not fit the conductance data as well as Eq. (6.1), the resulting line section

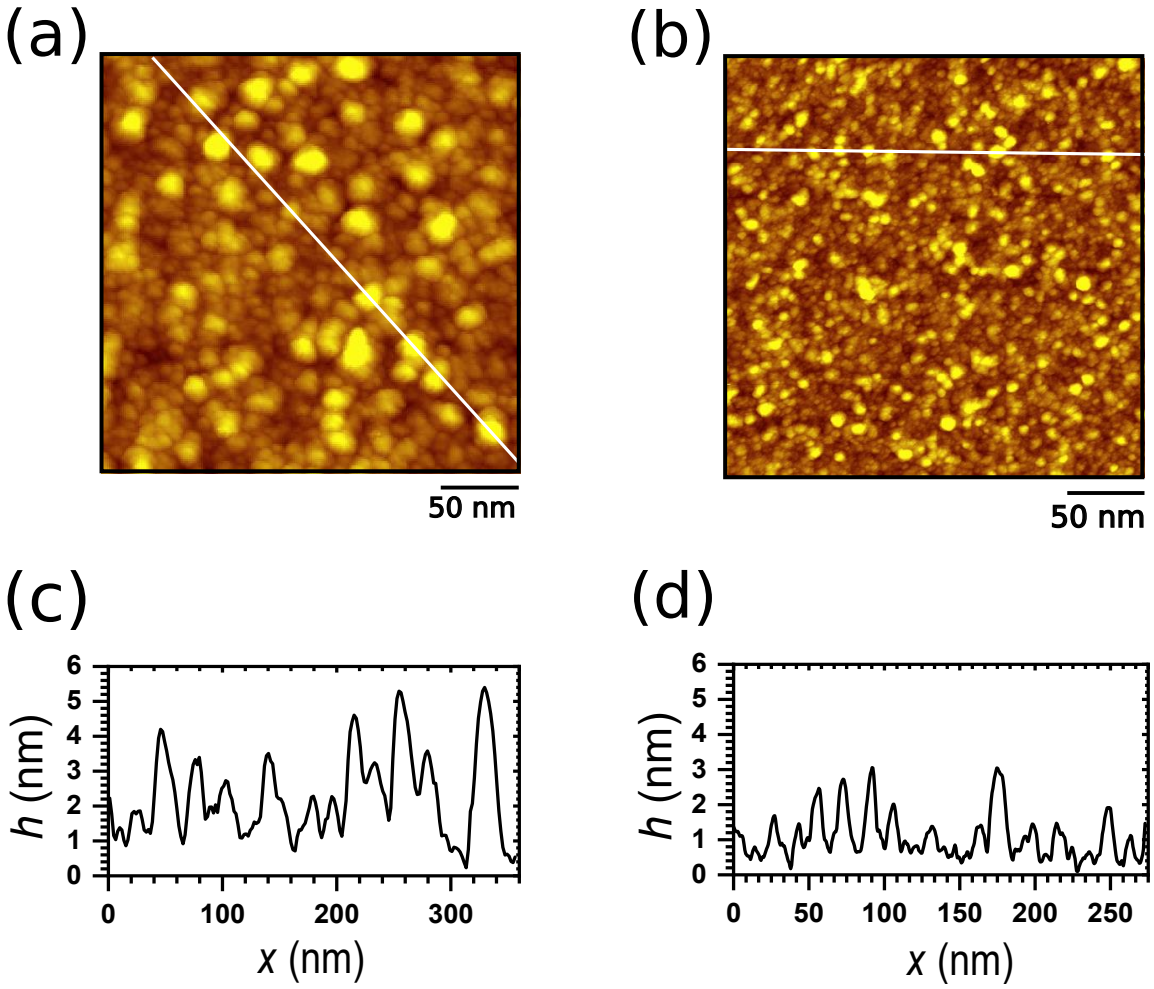

Figure 6.5: (a) Topographic image of 50 nm thick TiN film and (b) the 25 nm TiN film. (c) Line section along white line in (a), and (d) along white line in (b), showing surface height versus distance x along line.

plot nevertheless shows the same qualitative anti-correlation between Δ and the topography.

Figure 6.7 (b) and (c) show the corresponding map of the temperature T and the barrier height Z from fitting the conductance data to the BTK model. Comparing the topography Fig. 6.7 (a) to the gap, temperature and barrier height maps, we again see some remarkable correlations: the higher the grain, the smaller the superconducting gap and the higher the temperature. The barrier height map appears featureless.

Similar behavior shows up in the 25 nm thick TiN film. Figure 6.8 (a) shows a 280 nm$\times$ 112 nm topographic image of the 25 nm thick film taken at $T = 0.5$ K with a Nb tip. The grains in the image are somewhat distorted by a tip artifact; the actual grain size is somewhat smaller (Fig. 6.5 (b)). Spectroscopy data was taken at 256 $\times$ 101 = 25856 locations; I *vs.* V and dI/dV *vs.* V were recorded simultaneously. Figure 6.8 (b) shows the corresponding map of Δ, extracted by fitting conductance curves at each point to the BTK model. Examining the topographic image (Fig. 6.8 (a)) and the gap (Fig. 6.8 (b)), we again see a distinct anti-correlation, with higher regions having smaller superconducting gap. To see more clearly the correlation between the topography and the gap, Fig. 6.8 (c) shows a line cut through the surface topography (gray) and the BTK gap map Δ (blue). For comparison we also show Δ extracted from fitting to the Dynes gap model (red). Again note the reverse scale for Δ. As with the 50 nm thick film, the 25 nm film shows a remarkable anti-correlation between surface height and gap.

Figure 6.9 (b)-(c) show the corresponding maps of T and Z, extracted by

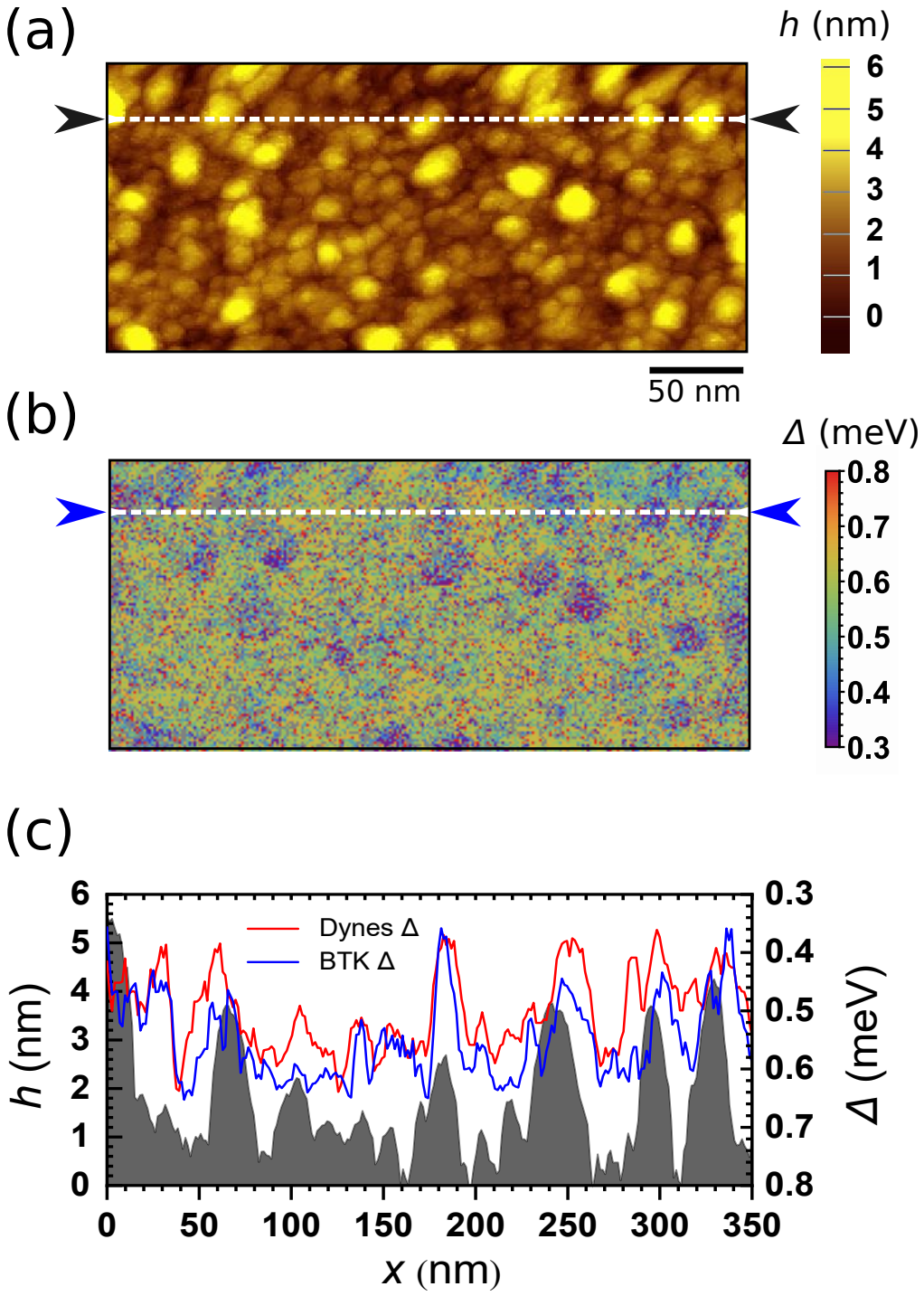

Figure 6.6: (a) Topography of 50 nm thick TiN film taken at 100 pA and 4 mV bias showing rough surface. (b) Corresponding maps of the gap Δ. (c) Line section through (a) and (b) showing anti-correlation between the gap and topography (gray). Note reversed scale for Δ, i.e. large gaps correspond to small h. Red curve shows Δ *vs.* x from fits to the Dynes model. All data taken at $T = 0.5$ K using a vanadium tip.

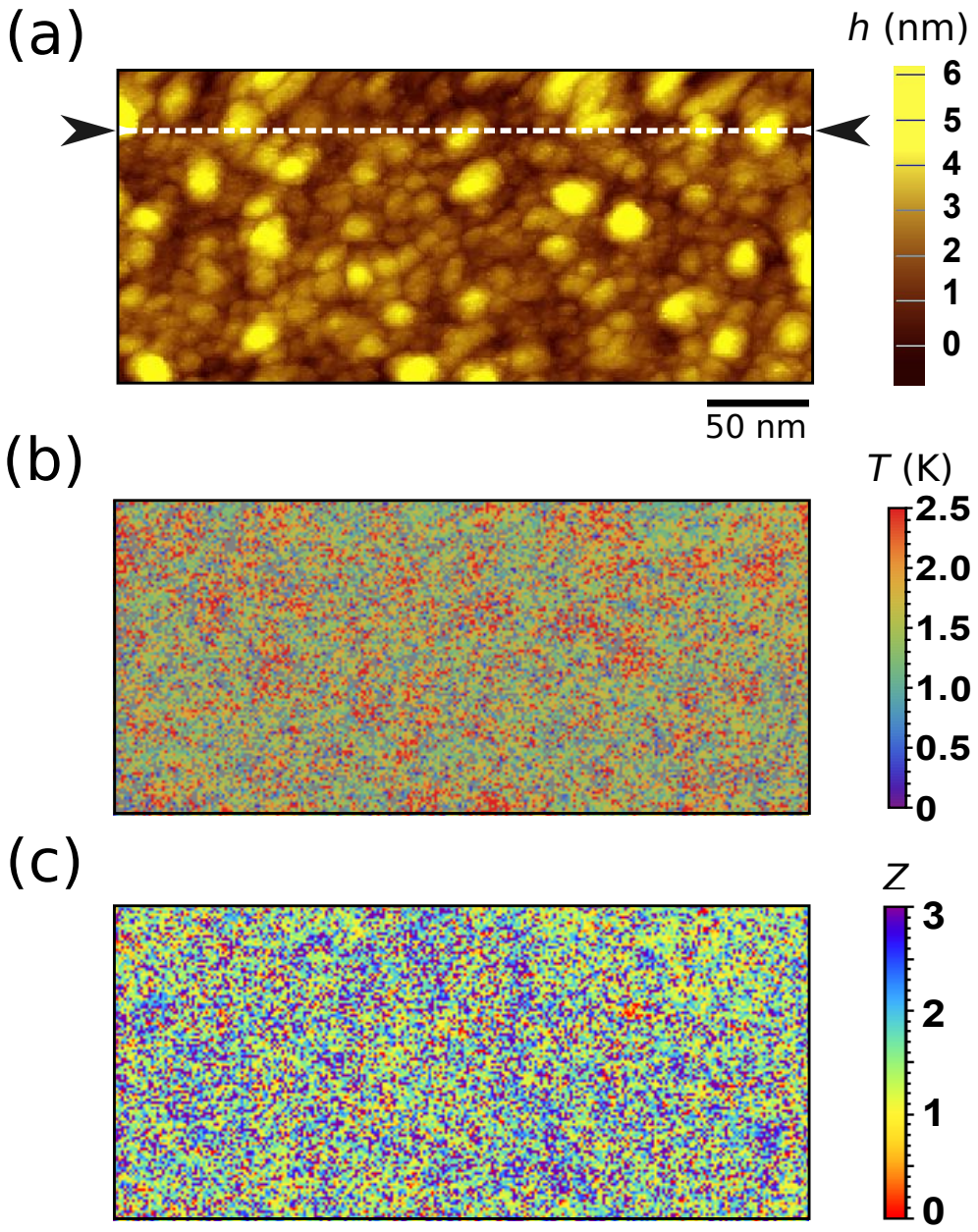

Figure 6.7: (a) Topography of 50 nm thick TiN film taken at 100 pA and 4 mV bias showing rough surface. Corresponding maps of the (b) temperature T and (c) barrier height parameter Z from fits to the BTK model. All data taken at $T = 0.5$ K using a vanadium tip.

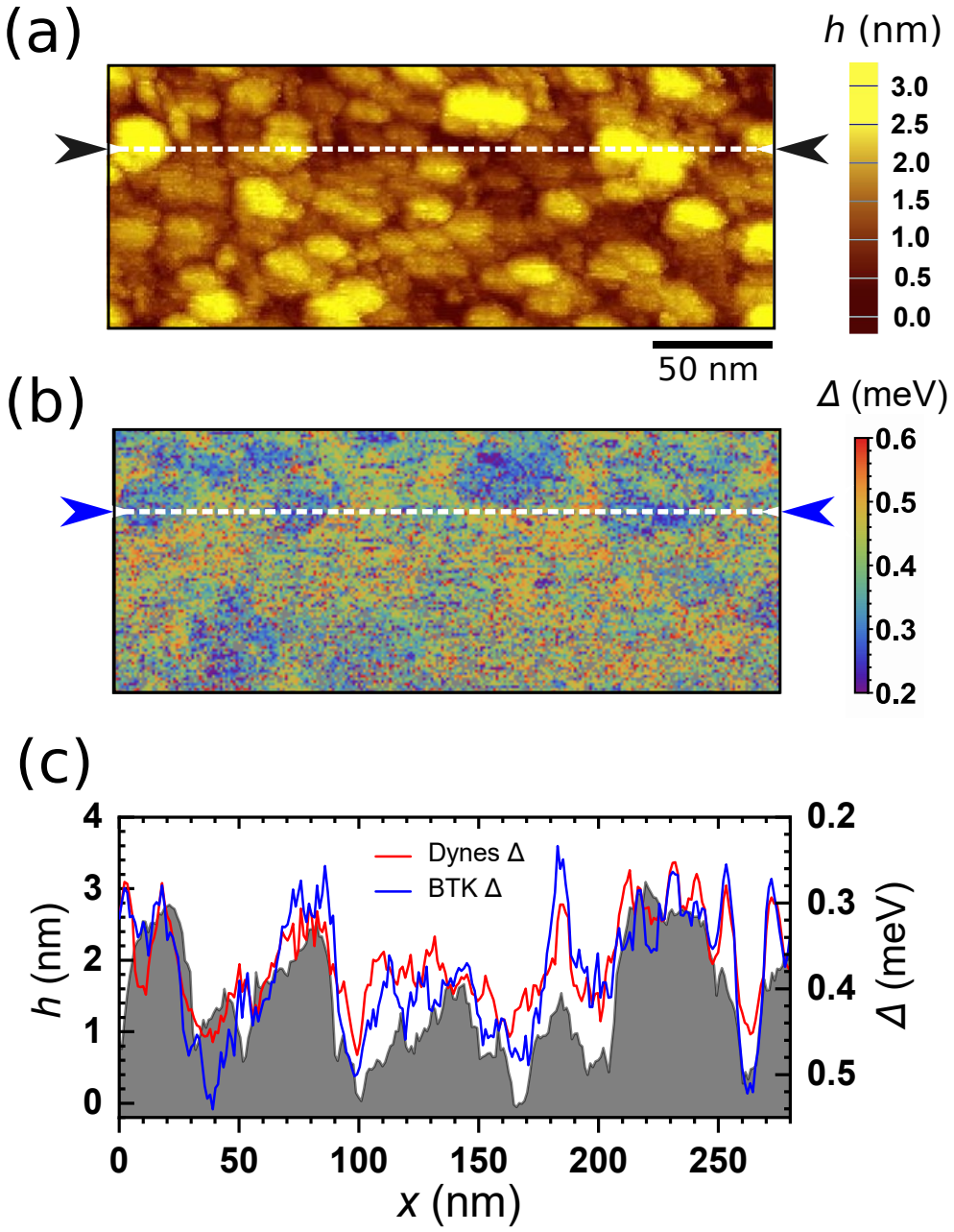

Figure 6.8: (a) Topography of 25 nm thick TiN film taken at I=100 pA and V=3 mV. There is some distortion from the rough surface imaging the tip shape, instead of the tip imaging the surface. (b) Corresponding map of gap Δ. (c) Line sections through (a) and (b) showing anti-correlation between the gap Δ (blue) and the topography h (gray). Note reversed scale for Δ, *i.e.* large gaps correspond to small h. Red curve shows Δ *vs.* x from fits to the Dynes model. All data taken at $T = 0.5$ K using a Nb tip.

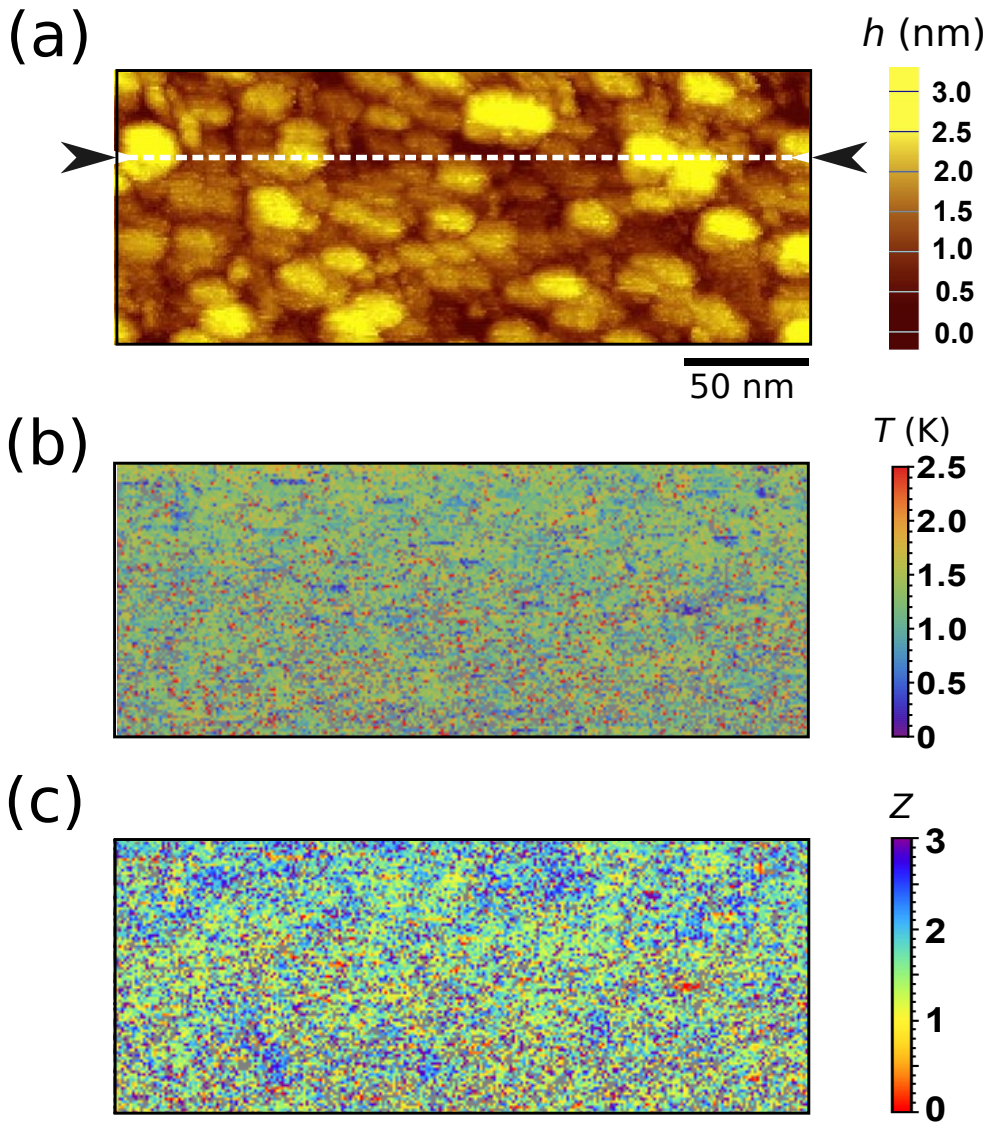

Figure 6.9: (a) Topography of 25 nm thick TiN film taken at I=100 pA and V=3 mV. There is some distortion from the rough surface imaging the tip shape, instead of the tip imaging the surface. Corresponding maps of (b) temperature T and (c) barrier parameter Z extracted from fits to the BTK model. All data taken at $T = 0.5$ K using a Nb tip.

fitting conductance curves at each point to the BTK model. Unlike what I found in the 50 nm film, the temperature map for the 25 nm film (see Fig. 6.9 (b)) shows little obvious correlation with the topography. On the other hand, the Z map (see Fig. 6.9 (c)) reveals that high Z regions tend to have lower superconducting gap (see Fig. 6.8 (b)), which was not obvious in the 50 nm thick film in Fig. 6.7 (c).

To better understand the range over which the gap is varying, the blue curve in Fig. 6.10 (a) shows the histogram of gap values obtained from Fig. 6.6 (b) on the 50 nm thick film. The red curve shows the results from the Dynes fits. In general, the gap distribution from the BTK fits is more symmetric than that of the Dynes fit, which as we noted above does not do a good job of capturing the observed behavior. In addition, the Dynes fit gives counts at Δ=0 meV, because of its inability to fit data with a zero bias conductance peak, while no such points occur in the histogram of Δ from the BTK fits. Fig. 6.10 (b) shows the corresponding histograms for the 25 nm film for the data set shown in Fig. 6.8 (b). Note that the histogram for the 50 nm film has a peak at about 0.6 meV, while the histogram for the 25 nm has a peak at about 0.4 meV. This is only qualitatively consistent with the T_c measurements, which gave $T_c = 4.7$ K for the 50 nm thick film and $T_c = 3.6$ K for the 25 nm thick film; for a BCS superconductor, these transition temperature would imply a gap of about 0.72 meV for the 25 nm film and about 0.55 meV for the 50 nm thick film.

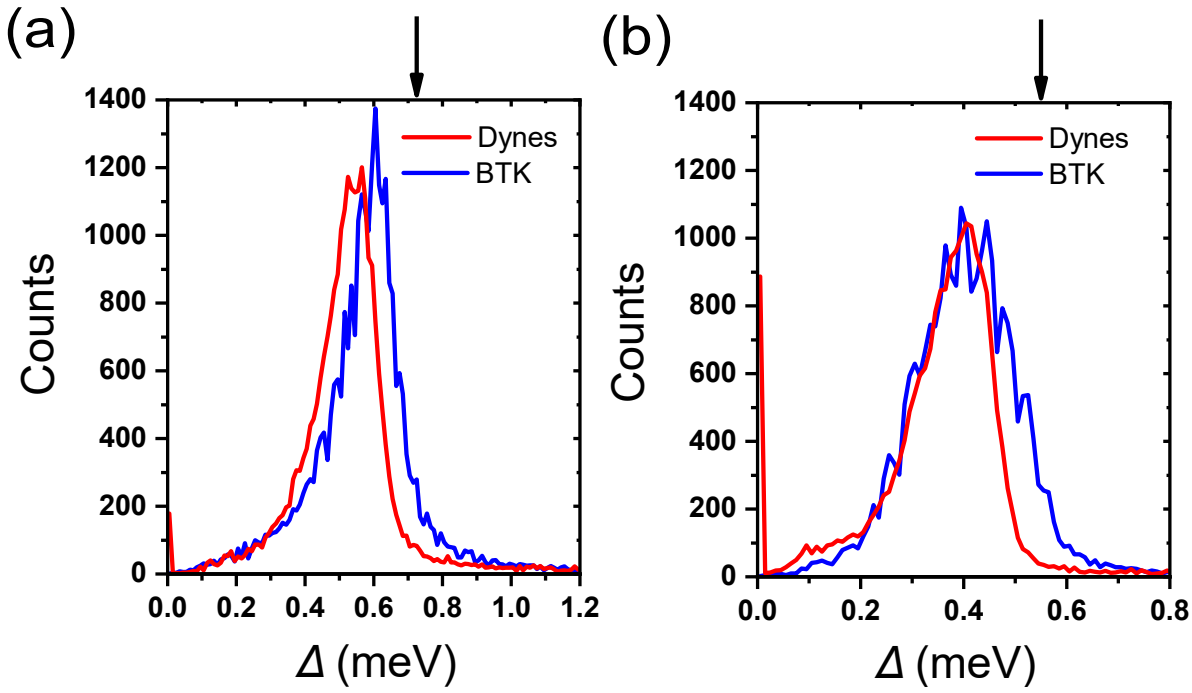

Figure 6.10: The blue curves show histograms of the superconducting gap from (a) the gap map in Fig. 6.6 (b) for the 50 nm thick film and (b) the gap map in Fig. 6.8 (b) for the 25 nm thick film. Red curves show histograms of the superconducting gap using the Dynes fit. Black arrows indicate Δ from measured T_c of the film.

6.5 Physical mechanism causing correlations between Δ, T, Z and h

To check whether my local measurements of the gap were consistent with weak-coupling BCS theory, I measured the temperature dependence of the gap at a fixed location. Figure 6.11 shows selected, averaged conductance curves as a function of temperature from the 25 nm TiN film. These were obtained by increasing T, and using a vanadium tip at a fixed location. Above 2.65 K, there was no hint of the superconducting gap and we see a featureless background curve from the normal state. Below 2.5 K, we see a clear gap and coherence peaks that both increase as T decreases.

To understand what might be producing the correlations between h *vs.* Δ, I did some further analysis of the maps shown in Fig. 6.6 and Fig. 6.8. Figure 6.12 shows the correlation between Δ and h from the smaller scale 50 nm TiN film (42 $\times$ 42 nm^2), the large scale 50 nm TiN film (350 $\times$ 160 nm^2) and the large scale 25 nm TiN film (280 $\times$ 112 nm^2). Here the binned height is plotted (red, left axis) *vs.* the binned superconducting gap. For reference, I also show the number of counts within each superconducting gap bin size of 0.01 meV (black, right axis). In each case, we clearly see that the height h of the surface and Δ are anti-correlated.

For comparison, Fig. 6.13 shows the 3D relation between Δ, Z and T for the small scale 50 nm, large scale 50 nm and 25 nm film. For the 50 nm thick TiN film, the superconducting gap is strongly anti-correlated with T (see red projected

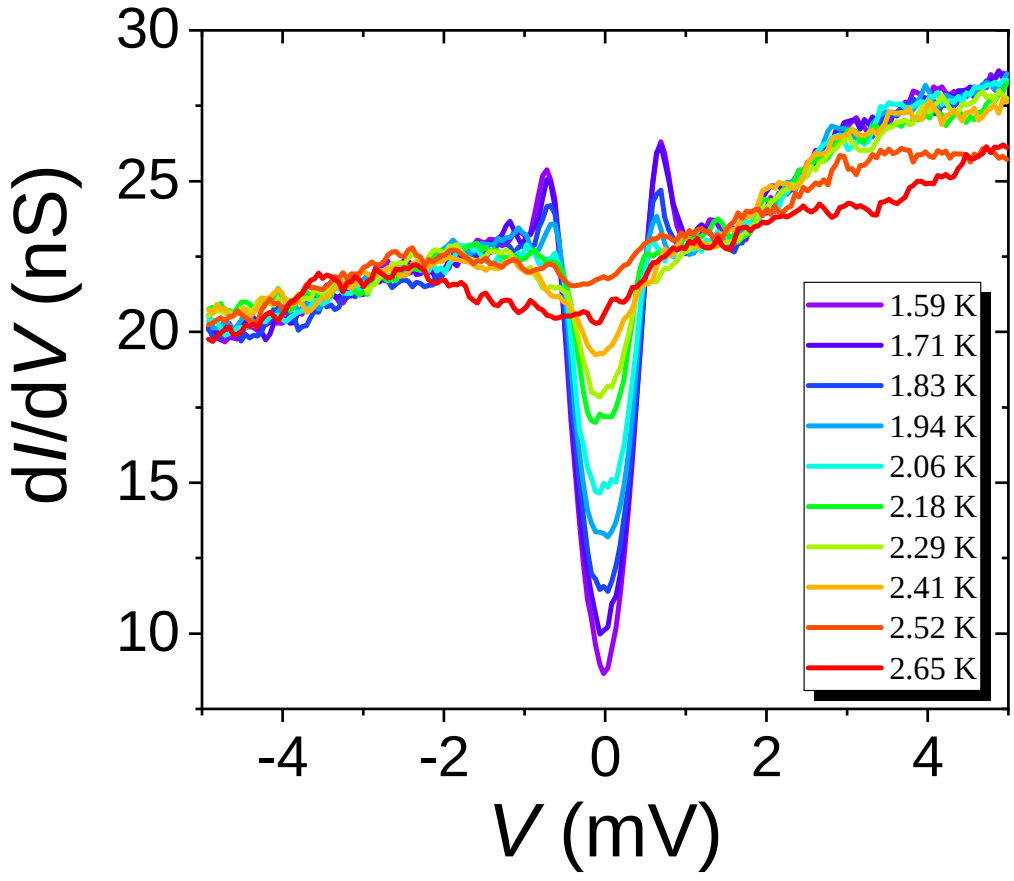

Figure 6.11: Temperature dependence of the conductance dI/dVcurves *vs*. V at a fixed location on the 25 nm TiN film. For $T > 2.5$ K, no superconducting gap was observed.

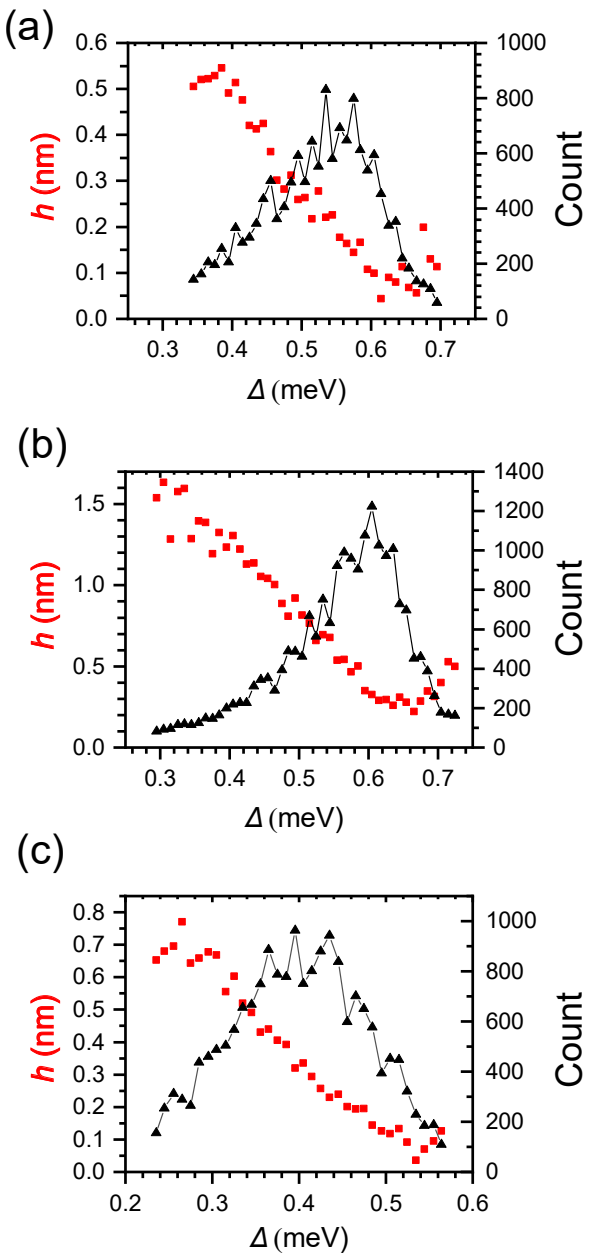

Figure 6.12: (a) Black points show the histogram of the superconducting gap Δ with a bin size of 0.01 meV and red points show the corresponding average height h versus the gap of points corresponding to this height for the 42 × 42 nm^2 image of the 50 nm TiN film. (b) Corresponding plots for the 350 × 116 nm^2 image of the 50 nm film and for the (c) 280 × 112 nm^2 image of the 25 nm film.

curve in Fig. 6.13 (a)); the higher the temperature T, the lower the gap Δ. This behavior suggests that the gap is being reduced at some locations due to heating. In contrast, for the 25 nm film, Δ appears to be well correlated with Z, and less well correlated with T, which varies over a small range. This behavior suggests that there are thermally disconnected regions in the thick film, but not in the thin film. Given that TiN films can have large stress [121], this suggests that the thicker films are cracking and producing grains which may be poorly connected to the rest of the film.

We know that surface roughness is higher in the 50 nm film, indicating that the grains stick out further from the surface. During tunneling spectroscopy measurements, heat is generated due to the tunneling current (Joule heating) and it will have a harder time dissipating from disconnected higher grains. Therefore those regions should show a higher temperature. This argument works for the 50 nm film as a possible explanation for why there is a smaller gap on higher grains. However, for the 25 nm film the temperature map does not show a similar correlation with h. Instead we see a clear correlation between Z and h. Therefore the lower superconducting gap in parts of the 25 nm film does not appear to be due to an increase in temperature, but something such as surface damage or contamination that causes an increase in the barrier height Z while suppressing Δ.

Figure 6.14 illustrates a possible mechanism which would generate correlations in Δ, T, Z and h. During Ar ion cleaning isolated grains will charge up, leaving disconnected regions that stick up and are less clean. This leads to a higher barrier height in regions with a smaller superconducting gap and these are also regions that

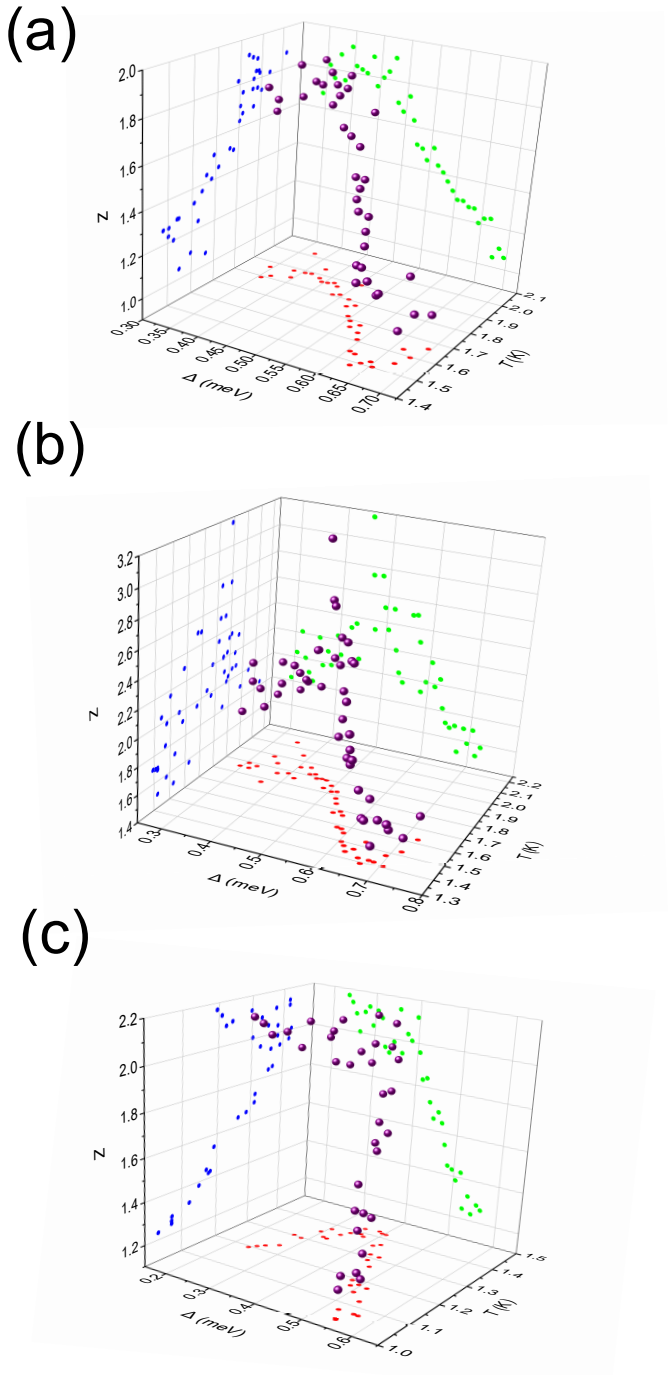

Figure 6.13: Three-dimensional scatter plots show correlation between the superconducting gap Δ, temperature T and barrier height Z for the (a) 42 × 42 nm^2 image of the 50 nm film, (b) 350 × 116 nm^2 image of the 50 nm film and (c) 280 × 112 nm^2 image of the 25 nm film.

tend to stick up. Since isolated grains may also be thermally disconnected, they will also correspond to higher T.

6.6 Conclusions

In conclusion, I used an STM to image 50 nm and 25 nm thick TiN films at 500 mK. The films show rough granular surfaces, and a large variations in the superconducting gap that are anti-correlated with the topography. My BTK analysis of conductance provided a better fit to the data than fitting to the Dynes model. It also allowed me to extract temperature and transparency maps, and accounted for distinct Andreev features in the spectroscopy that occur for highly transparent tunnel barriers. I found a puzzling correlation between topography, Δ, T and Z, with reduced gap and higher barriers and higher temperature on higher surfaces. This may be due in part to increased heating from poor thermal conduction in disconnected grains, which also leads to higher barriers on top of the grains because the grains are not cleaned well during ion milling because they charge up.

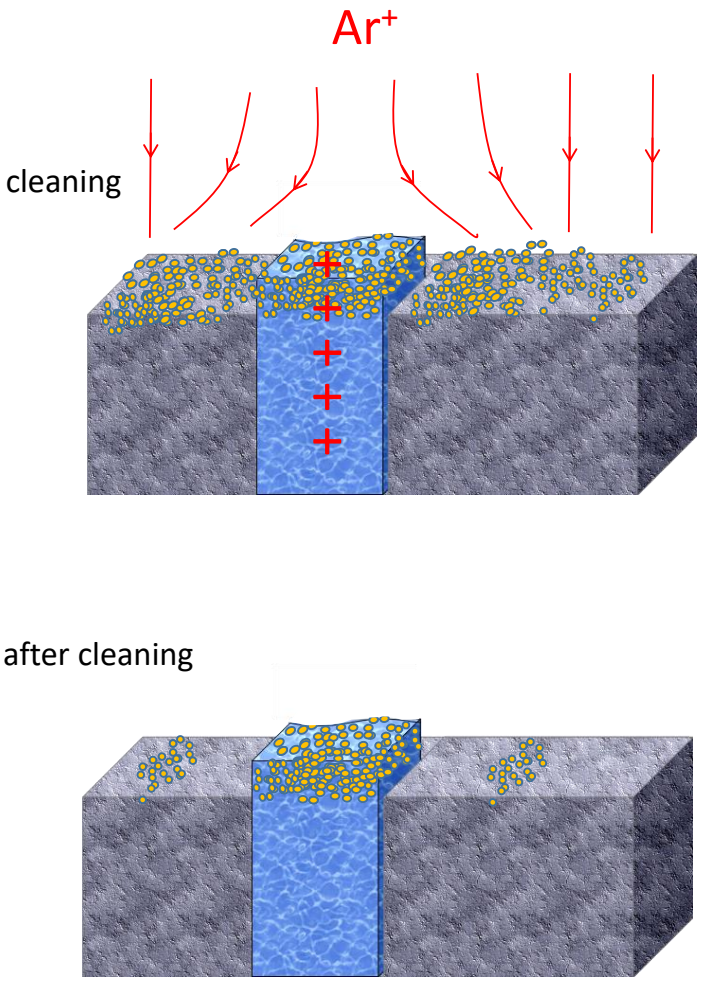

Figure 6.14: Illustration showing isolated grains will charge up during the Ar ion cleaning, leaving disconnected regions that stick up and are less clean, which gives a higher barrier height Z and reduced gap, and will heat up more because they are disconnected.

CHAPTER 7

Theory of the I-V characteristics in S-I-S Junctions with Multiple Andreev Reflection

7.1 Introduction

In Chapter 5 and Chapter 6, I described the physics of S-I-N junctions, including the phenomenon of Andreev reflection. In this chapter, I examine S-I-S junctions. When two superconductors with gap Δ are connected by a weak link, the current rises when the voltage $V = 2\Delta/e$. In addition, Andreev effects give current steps at subgap voltages $V = \Delta/en$, where n is a positive integer. The theory used to explain this phenomenon involves Multiple Andreev Reflections (MAR) and the Josephson effect [30, 31]. In the Josephson effect two superconductors are coupled by a weak link and current can flow through the junction without any voltage applied. This current is called supercurrent and the junction is called a Josephson junction.

In Section 7.2 and Section 7.3, I discuss the approach developed by Averin and Bardas [122] to describe MAR behavior in symmetrical S-I-S junctions with trans-

parency $D = 1$ and $D \neq 1$. This theory describes the current-voltage charasteristics of a single S-I-S superconducting channel with arbitrary transmission [122–125]. While there have been many theoretical descriptions of MAR, many are not easy to follow. Moreover, most of the calculations, including Averin and Bardas's, assumed the two superconductors had the same superconducting gap. In my STM, the S-I-S junction formed by the tip and the sample were usually asymmetrical, i.e. the tip and sample had different gaps. I then need a theory that can describe asymmetrical junctions.

In Section 7.4 I generalize the scattering approach developed by Averin *et al.* [122] to the asymmetrical case, and demonstrate that this yields results that are in agreement with Wu *et al.* [126], who used a Green's function approach to describe MAR in asymmetrical Josephson junctions. I make some general comments about asymmetrical junctions and describe results for the supercurrent and subgap current from this model.

In Section 7.5, I discuss the dc and ac Josephson effects. In Section 7.6, I examine expressions for the critical current derived previously and my derivation of MAR effects in asymmetrical junctions. Finally, in Section 7.7, I conclude with a summary of my main results from the analysis.

7.2 MAR in symmetrical junction with transparency $D = 1$

7.2.1 Averin-Bardas model

In 1995, Averin and Bardas (AB) presented an accesible description of Andreev and ac Josephson effects in an S-I-S junction with a single quantum channel [122]. They considered a model of a junction as a short constriction between two superconductors and obtained a quantitative description of the current-voltage characteristics and how it depends on the temperature and barrier transparency. The single quantum channel can be thought of as a normal channel (Δ=0) and, depending on the transparency, the junction can be used to describe S-N-S or S-I-S tunneling.

Figure 7.1 shows an illustration of the AB model of an S-I-S junction. The left lead is a superconductor with gap Δ_1 and the right lead is an superconductor with gap Δ_2. The center is the weak link, which acts as a scattering region for quasiparticles. If there is no scattering, the link is completely transparent, and the channel has transparency $D = 1$. On the other hand, if the scattering is not zero the quantum channel will not be completely transparent, and the transparency parameter D will be between 0 and 1. Here the transparency D is different from the barrier height Z defined in Chapter 6. However they are related as $D = 1/(1 + Z^2)$. Andreev reflections [44, 45] happen at each S/N interface and quasiparticles also scatter within the link region. This leads to the possibility of multiple Andreev reflections and multiple scattering, which greatly complicates the analysis. Averin

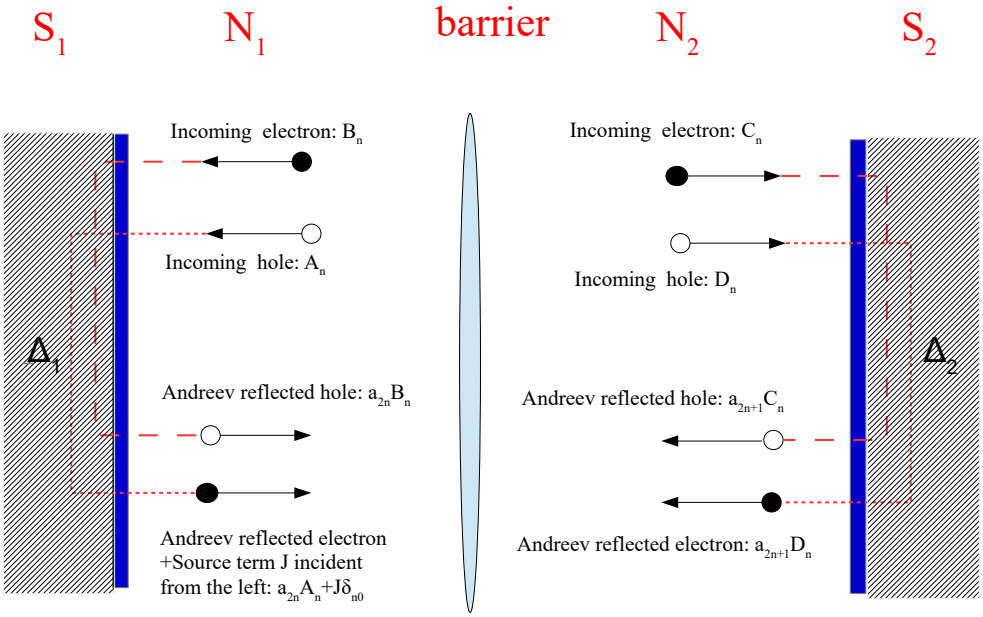

Figure 7.1: Illustrate of Andreev reflections off of two S/N interfaces

and Bardas proceeded by defining a scattering matrix and determining separate relations for Andreev reflections at each S/N boundary.

As I discussed in Chapter 5, Andreev reflection at an NS interface can be characterized by a reflection amplitude a that depends on quasiparticle energy ε [122]:

$$a(\varepsilon) = \frac{1}{\Delta} \times \begin{cases} \varepsilon - sgn(\varepsilon)(\varepsilon^2 - \Delta^2)^{1/2}, & \text{for} \quad |\varepsilon| > \Delta \\ \varepsilon - i(\Delta^2 - \varepsilon^2)^{1/2}, & \text{for} \quad |\varepsilon| < \Delta \end{cases} \tag{7.1}$$

AB then defined a scattering matrix to account for the weak link [122]:

$$S_{el} = \begin{pmatrix} r & t \\ t & -r^* t/t^* \end{pmatrix}. \tag{7.2}$$

where r is the probability of the quasiparticle being reflected in the normal region, and t is the probability of the quasiparticle being transmitted in the normal region. Here the transparency is $D{=}|t|^2 = 1/(1+Z^2)$. They then wrote the wavefunctions in region 1 in the channel (see Fig. 7.1) generated by a quasiparticle incident from the left superconductor as [122]:

$$\psi_{el} = \sum_n [(a_{2n}A_n + J\delta_{n0})e^{ikx} + B_n e^{-ikx}]e^{-i(\varepsilon+2neV)t/\hbar} \tag{7.3a}$$

$$\psi_h = \sum_n [A_n e^{ikx} + a_{2n}B_n e^{-ikx}]e^{-i(\varepsilon+2neV)t/\hbar} \tag{7.3b}$$

Here k and ε are the wave-vector and energy of the incident quasiparticle, and $a_m = a(\varepsilon + meV)$. The second term in Eq. (7.3a) corresponds to a quasiparticle incident from the superconductor, which produces an electron in the normal region with effective source amplitude $J(\varepsilon) = [1{-}|a(\varepsilon)|^2]^{1/2}$. For this case the wave function in region 2 of the channel (see Fig. 7.1) can be written as,

$$\psi_{el} = \sum_n [C_n e^{ikx} + a_{2n+1}D_n e^{-ikx}]e^{-i(\varepsilon+(2n+1)eV)t/\hbar} \tag{7.4a}$$

$$\psi_h = \sum_n [a_{2n+1}C_n e^{ikx} + D_n e^{-ikx}]e^{-i(\varepsilon+(2n+1)eV)t/\hbar} \tag{7.4b}$$

where the sum over n represents contributions from multiple reflections and is taken over all integers from -∞ to ∞.

From the basic properties of waves, we can relate the incoming electrons to the outgoing electrons in regions 1 and 2 using a scattering matrix. Similarly there will be a scattering matrix connecting the holes in the two regions. AB wrote this as:

$$\begin{pmatrix} B_n \\ C_n \end{pmatrix} = S_{el} \begin{pmatrix} a_{2n} A_n + J\delta_{n0} \\ a_{2n+1} D_n \end{pmatrix}, \quad \begin{pmatrix} A_n \\ D_{n-1} \end{pmatrix} = S_h \begin{pmatrix} a_{2n} B_n \\ a_{2n-1} C_{n-1} \end{pmatrix} \tag{7.5}$$

where

$$S_h = S_{el}^*, \quad S_{el} = \begin{pmatrix} r & t \\ t & -\frac{r^* t}{t^*} \end{pmatrix}. \tag{7.6}$$

At this point in this paper [122], AB present a recursion relation for finding the A_n, B_n, C_n and D_n. The authors omit detailed steps and only consider the case where the left and right superconductors have the same gap. This is clearly not true in our case, and it is important to understand how to find the recursion relation before trying to generalize it to our situation where the superconducting gaps are different on the left and right.

If we stare at the Eq. (7.5), we see that B_n is a function of A_n and D_n. Moving the equation around, we get D_n as a function of A_n and B_n. Since C_n is a function of A_n and D_n, we can now use $D_n(A_n, B_n)$ to get $C_n(A_n, B_n)$. From Eq. (7.5) I find:

$$B_n = ra_{2n}A_n + rJ\delta_{n0} + ta_{2n+1}D_n \tag{7.7a}$$

$$C_n = ta_{2n}A_n + tJ\delta_{n0} - \frac{r^*t}{t^*}a_{2n+1}D_n \tag{7.7b}$$

To proceed, I rearrange Eq. (7.7a) and plug it into Eq. (7.7b) to get C_n and D_n as a function of A_n and B_n:

$$D_n = \frac{1}{ta_{2n+1}}B_n - \frac{ra_{2n}}{ta_{2n+1}}A_n - \frac{rJ\delta_{n0}}{ta_{2n+1}} \tag{7.8}$$

$$C_n = (\frac{|r|^2}{t^*}a_{2n} + ta_{2n})A_n - \frac{r^*}{t^*}B_n + (\frac{|r|^2}{t^*} + t)J\delta_{n0} \tag{7.9}$$

Similarly for the hole equation, I find:

$$A_n = r^*a_{2n}B_n + t^*a_{2n-1}C_{n-1} \tag{7.10a}$$

$$D_{n-1} = t^*a_{2n}B_n - \frac{rt^*}{t}a_{2n-1}C_{n-1} \tag{7.10b}$$

From Eq. (7.10a), we can write:

$$A_{n+1} = r^*a_{2n+2}B_{n+1} + t^*a_{2n+1}C_n \tag{7.11}$$

I now substitute C_n from Eq. (7.9) into Eq. (7.11) to get:

$$\begin{aligned} A_{n+1} &= r^* a_{2n+2} B_{n+1} + t^* a_{2n+1}[(\frac{|r|^2}{t^*} a_{2n} + t a_{2n}) A_n - \frac{r^*}{t^*} B_n + (\frac{|r|^2}{t^*} + t) J\delta_{n0}] \\ &= r^* a_{2n+2} B_{n+1} + R a_{2n} a_{2n+1} A_n + D a_{2n} a_{2n+1} A_n - r^* a_{2n+1} B_n \\ &\qquad + R a_{2n+1} J\delta_{n0} + D a_{2n+1} \end{aligned} \tag{7.12}$$

and thus:

$$A_{n+1} - a_{2n+1} a_{2n} A_n = \sqrt{R}(a_{2n+2} B_{n+1} - a_{2n+1} B_n) + J a_1 \delta_{n0} \tag{7.13}$$

where R=$|r|^2$. Equation (7.13) is exactly the same as the second recursion relation Eq. (5) from the AB paper [122].

To derive the recursion relation for B_n, I proceed as follows. From Eq. (7.10b), I can rewrite :

$$D_n = t^* a_{2n+2} B_{n+1} - \frac{r t^*}{t} a_{2n+1} C_n \tag{7.14}$$

Plugging in D_n and C_n from Eq. (7.8) and Eq. (7.9) then gives

$$\begin{aligned}
&\tfrac{1}{ta_{2n+1}}B_n - \tfrac{ra_{2n}}{ta_{2n+1}}A_n - \tfrac{rJ\delta_{n0}}{ta_{2n+1}} \\
&\qquad = t^* a_{2n+2}B_{n+1} - \tfrac{rt^*}{t}a_{2n+1}[(\tfrac{|r|^2}{t^*}a_{2n} + ta_{2n})A_n - \tfrac{r^*}{t^*}B_n + (\tfrac{|r|^2}{t^*} + t)J\delta_{n0}] \\
&a_{2n+1}^2 ra_{2n}A_n - ra_{2n}A_n \\
&\qquad = Da_{2n+1}a_{2n+2}B_{n+1} + [a_{2n+1}^2 R - 1]B_n + rJ\delta_{n0} - a_{2n+1}^2 rJ\delta_{n0} \\
&ra_{2n}A_n = D\tfrac{a_{2n+1}a_{2n+2}}{a_{2n+1}^2-1}B_{n+1} + \tfrac{a_{2n+1}^2 R-1}{a_{2n+1}^2-1}B_n - rJ\delta_{n0}
\end{aligned} \tag{7.15}$$

Eq. (7.15) is important because it shows that A_n is related to B_{n+1} and B_n. Plugging Eq. (7.15) into Eq. (7.13) gives us a recursion relation for B_{n+1}, B_n, B_{n-1} which eventually gives me the first recursion relation Eq. (5) from the AB paper [122].

To proceed, I rewrite the index from Eq. (7.13) so that

$$A_n - a_{2n-1}a_{2n-2}A_{n-1} = R^{1/2}(B_n a_{2n} - B_{n-1}a_{2n-1}) + Ja_1\delta_{n-1,0} \tag{7.16}$$

Plugging A_n from Eq. (7.15) into Eq. (7.16), I get:

$$\begin{aligned}
&\frac{D}{ra_{2n}}\frac{a_{2n+1}a_{2n+2}}{a_{2n+1}^2-1}B_{n+1} + \frac{1}{ra_{2n}}\frac{a_{2n+1}^2R-1}{a_{2n+1}^2-1}B_n - \frac{J}{a_{2n}}\delta_{n0} \\
&-\frac{Da_{2n-1}^2a_{2n}}{r(a_{2n-1}^2-1)}B_n - \frac{a_{2n-1}}{r}(\frac{a_{2n-1}^2R-1}{a_{2n-1}^2-1})B_{n-1} + Ja_{2n-1}\delta_{n-1,0} \\
&= \sqrt{R}(a_{2n}B_n - a_{2n-1}B_{n-1}) + Ja_1\delta_{n-1,0}
\end{aligned} \tag{7.17}$$

After rearranging terms, I arrive at the first recursion relation Eq. (5) in the AB

paper [122]:

$$\frac{Da_{2n+1}a_{2n+2}}{1-a_{2n+1}^2}B_{n+1} - (\frac{a_{2n+1}^2R-1}{a_{2n+1}^2-1} - \frac{Da_{2n-1}^2a_{2n}^2}{a_{2n-1}^2-1}$$
$$-Ra_{2n}^2)B_n + (\frac{a_{2n-1}a_{2n}(a_{2n-1}^2R-1)}{a_{2n-1}^2-1} - Ra_{2n}a_{2n-1})B_{n-1}$$
$$= -rJ\delta_{n,0} - rJa_2a_1\delta_{n-1,0} + rJa_2a_1\delta_{n-1,0} \tag{7.18}$$

This recursion relation is important because it gives us the wavefunction amplitudes A_n and B_n for different transparency D. From the wavefunction, we can determine an expression for the current flowing through the S-I-S junction, as I discuss in the next section. After that, I discuss how to generalize to the case of different gaps for the left and right superconductors.

7.2.2 Finding the expression for the current when the gaps are the same

In this section, I work out Eq. (6) from Averin-Bardas. This gives the current through an S-I-S junction when the superconductors have the same gap and there is Multiple Andreev Reflection (MAR). This will help us understand the physics and how to generalize to the case where the left and right superconductors have different gaps. To simplify the discussion, I examine the situation for D=1. This is the case of no scattering of the electrons or holes, i.e. a completely transparent weak link with $Z = 0$.

For an electron-like quasiparticle with energy ε that is incident from the left

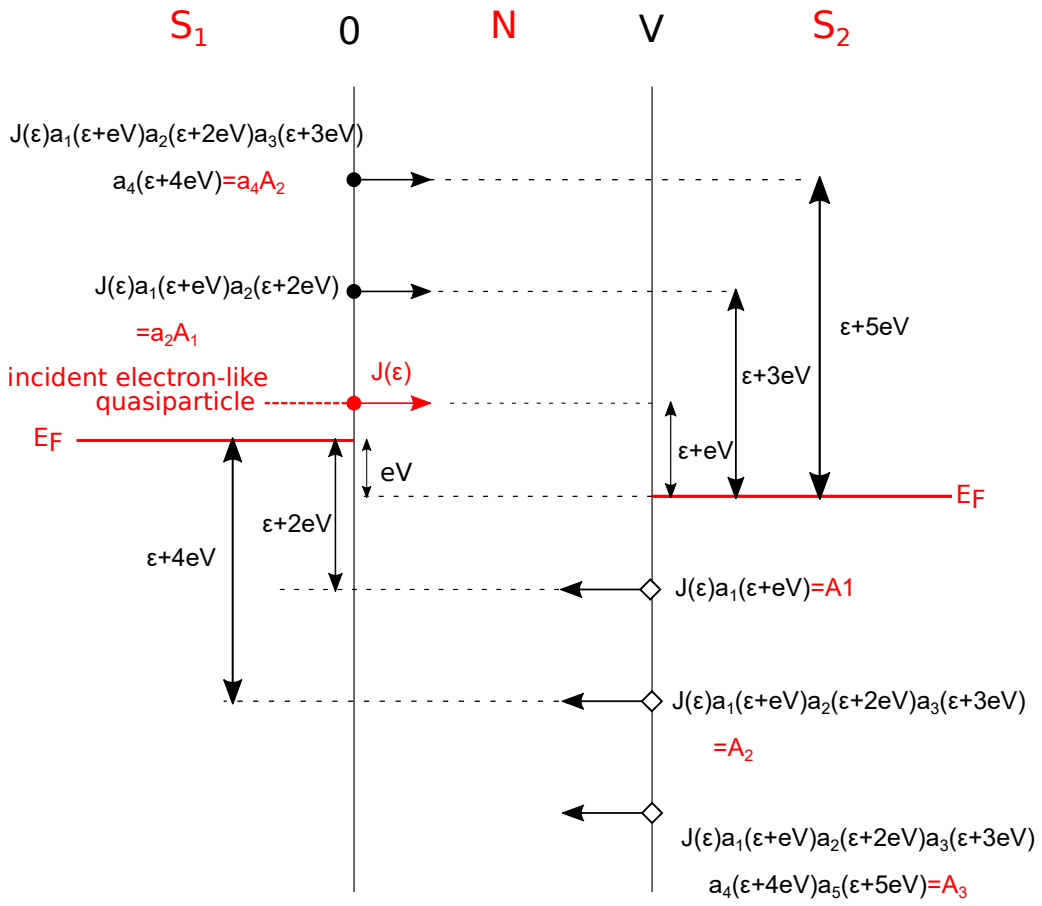

Figure 7.2: Configuration of the multiple Andreev reflection at transparency $D = 1$. An electron-like quasiparticle (filled circle) is incident from the left with energy ε and is Andreev reflected with amplitude A as a hole (open diamond) from the right S/N interface. Note that a hole below the Fermi level has positive energy.

superconducting electrode onto the S/N interface, the probability amplitude of an electron being created in the normal region is [122]: $J = \sqrt{1 - |a(\varepsilon)|^2}$. I now assume voltage V is applied to the right electrode and the left electrode is at 0 V (Fig. 7.2). Again for simplicity, I consider $D = 1$, so there is no scattering, and nothing is reflected back while traveling in the normal region, so that all particles reach the right electrode. Since the right electrode is at voltage V ($V > 0$), the quasiparticle arrives at the right electrode with $E{=}\varepsilon + eV$. The particle will then be Andreev reflected back [44, 122] as a hole with amplitude $a_1(\varepsilon + eV)$. This Andreev reflected hole will travel back to the left, and since it is a hole, it will pick up additional energy eV and reach the left electrode with energy $\varepsilon + 2eV$. It will then be Andreev reflected as an electron with amplitude $a_2(\varepsilon{+}2eV)$, etc. (see Fig. 7.2). Keep in mind that, if the energy $E = |\varepsilon + neV|$ after reflection is smaller than the superconducting gap Δ of the electrode at the interface, then the electron will be Andreev reflected as a hole.

Since $D = 1$, we have $R = 0$ in the scattering matrix Eq. (7.6), and the scattering matrices become

$$S_h = S_{el}^* \quad \text{and} \quad S_{el} = \begin{pmatrix} 0 & 1 \\ 1 & 0 \end{pmatrix}. \tag{7.19}$$

Plugging this into Eq. (7.5), I get four relations:

$$B_n = a_{2n+1} D_n \tag{7.20a}$$

$$C_n = a_{2n} A_n + J\delta_{n0} \tag{7.20b}$$

$$A_n = a_{2n-1} C_{n-1} \tag{7.20c}$$

$$D_{n-1} = a_{2n} B_n \tag{7.20d}$$

In this case, with $D = 1$, $A_0 = 0$, there is no scattering so $B_n = 0$ and thus $D_n = 0$.

From Eq. (7.20), I can now construct A_n and C_n recursively. For example: $C_0 = J, A_1 = a_1 C_0 = a_1 J, C_1 = a_2 A_1, A_2 = a_3 C_1 = a_3 a_2 a_1 J$, etc. We can also see that the A_n are only non-zero for positive n and for $D = 1$, I find

$$A_{-3} = A_{-2} = A_{-1} = A_0 = 0 \tag{7.21a}$$

$$A_1(\varepsilon, V) = J(\varepsilon) a_1(\varepsilon + eV) \tag{7.21b}$$

$$A_2(\varepsilon, V) = J(\varepsilon) a_1(\varepsilon + eV) a_2(\varepsilon + 2eV) a_3(\varepsilon + 3eV) \tag{7.21c}$$

$$A_3(\varepsilon, V) = J(\varepsilon) a_1(\varepsilon + eV) a_2(\varepsilon + 2eV) a_3(\varepsilon + 3eV) a_4(\varepsilon + 4eV) a_5(\varepsilon + 5eV) \tag{7.21d}$$

$$\vdots \tag{7.21e}$$

Thus, the $A_n(\varepsilon, V)$ are functions of the incident quasiparticle amplitude J at energy ε and the quasiparticle picks up energy eV each time it transits the normal region.

From Eq. (7.18), Eq. (7.20) and Eq. (7.3) the wavefunction can now be written as:

$$\psi_{el} = \sum_n [(a_{2n}A_n + J\delta_{n0})e^{ikx}]e^{-i(\varepsilon+2neV)t/\hbar} \tag{7.22a}$$

$$\psi_h = \sum_n [A_n e^{ikx}]e^{-i(\varepsilon+2neV)t/\hbar} \tag{7.22b}$$

where the n's are positive integers. Notice that the electron wavefunction has components traveling to the right, represented as e^{ikx}, while the hole wavefunction has components traveling to the left, represented as e^{ikx}; note that the hole travels in the opposite direction of the k vector [113].

From the wavefunction, we can calculate the electron and the hole probability current density using the well-known quantum expression:

$$j = \frac{\hbar}{2mi}(\psi^* \boldsymbol{\nabla}\psi - \psi \boldsymbol{\nabla}\psi^*) \tag{7.23}$$

For the electron probability current density, I find:

$$\psi_{el} = e^{ikx}(Je^{-i\varepsilon t/\hbar} + a_2 A_1 e^{-i(\varepsilon+2eV)t/\hbar} + a_4 A_2 e^{-i(\varepsilon+4eV)t/\hbar} + a_6 A_3 e^{-i(\varepsilon+6eV)t/\hbar} + ...) \tag{7.24a}$$

$$\psi^*_{el} = e^{-ikx}(Je^{i\varepsilon t/\hbar} + a^*_2 A^*_1 e^{i(\varepsilon+2eV)t/\hbar} + a^*_4 A^*_2 e^{i(\varepsilon+4eV)t/\hbar} + a^*_6 A^*_3 e^{i(\varepsilon+6eV)t/\hbar} + ...) \tag{7.24b}$$

and thus:

$$\begin{aligned} j_{el} = \frac{\hbar}{2mi} * 2ik\Big(& [|J|^2 + |a_2|^2|A_1|^2 + |a_4|^2|A_2|^2 + |a_6|^2|A_3|^2 + ...] \\ & + [Ja_2^*A_1^* + a_2A_1a_4^*A_2^* + a_4A_2a_6^*A_3^* + ...]e^{i2eVt/\hbar} \\ & + [Ja_4^*A_2^* + a_2A_1a_6^*A_3^* + a_4A_2a_8^*A_4^* + ...]e^{i4eVt/\hbar} + [...]e^{i6eVt/\hbar} + ... \\ & + [J^*a_2A_1 + a_2^*A_1^*a_4A_2 + a_4^*A_2^*a_6A_3 + ...]e^{-i2eVt/\hbar} \\ & + [J^*a_4A_2 + a_2^*A_1^*a_6A_3 + a_4^*A_2^*a_8A_4 + ...]e^{-i4eVt/\hbar} + [...]e^{-i6eVt/\hbar} + ...\Big) \end{aligned} \tag{7.25}$$

For the probability current density from the holes that are generated by electron-like quasiparticles incident from the left, I find:

$$\psi_h = e^{ikx}(A_1e^{-i(\varepsilon+2eV)t/\hbar} + A_2e^{-i(\varepsilon+4eV)t/\hbar} + A_3e^{-i(\varepsilon+6eV)t/\hbar} + ...) \tag{7.26a}$$

$$\psi_h^* = e^{-ikx}(A_1^*e^{i(\varepsilon+2eV)t/\hbar} + A_2^*e^{i(\varepsilon+4eV)t/\hbar} + A_3^*e^{i(\varepsilon+6eV)t/\hbar} + ...) \tag{7.26b}$$

$$\begin{aligned} j_h = \frac{\hbar}{2mi} * 2ik\Big(& [|A_1|^2 + |A_2|^2 + |A_3|^2 + ...] \\ & + [A_1^*A_2 + A_2^*A_3 + ..]e^{-i2eVt/\hbar} + [A_1^*A_3 + A_2^*A_4 + ..]e^{-i4eVt/\hbar} + [..]e^{-i6eVt/\hbar} + ... \\ & + [A_2^*A_1 + A_3^*A_2 + ..]e^{i2eVt/\hbar} + [A_3^*A_1 + A_4^*A_2 + ..]e^{i4eVt/\hbar} + [...]e^{i6eVt/\hbar} + ...\Big) \end{aligned} \tag{7.27}$$

The total probability current density is then $j = j_{el} + j_h$, where the direction of the charge flow has been taking care of from the definition of the wavefunction

Eq. (7.22). I find

$$
\begin{aligned}
j(\varepsilon,t) = \frac{\hbar k}{m}\Big(& [|J|^2 + |A_1|^2(1+|a_2|^2) + |A_2|^2(1+|a_4|^2) + |A_3|^2(1+|a_6|^2) + ...] \\
& + [Ja_2^*A_1^* + A_1A_2^*(1+a_2a_4^*) + A_2A_3^*(1+a_4a_6^*) + ...]e^{i2eVt/\hbar} \\
& + [Ja_4^*A_2^* + A_1A_3^*(1+a_2a_6^*) + A_2A_4^*(1+a_4a_8^*) + ...]e^{i4eVt/\hbar} + [...]e^{i6eVt/\hbar} + ... \\
& + [J^*a_2A_1 + A_2A_1^*(1+a_4a_2^*) + A_3A_2^*(1+a_6a_4^*) + ...]e^{-i2eVt/\hbar} \\
& + [J^*a_4A_2 + A_3A_1^*(1+a_6a_2^*) + A_4A_2^*(1+a_8a_4^*) + ...]e^{-i4eVt/\hbar} + [...]e^{-i6eVt/\hbar} \\
& + ...\Big)
\end{aligned}
\tag{7.28}
$$

Equation (7.28) gives the probability current density due to an electron-like quasiparticle with energy ε incident from the left superconducting electrode. The probability current density can be written as a sum of Fourier components:

$$
j(\varepsilon,t) = \frac{\hbar k}{m}\sum_{K=0,\pm1,\pm2,..} j_K(\varepsilon,V)e^{i2KeVt/\hbar} \tag{7.29}
$$

where K are integers. Summing up the probability current density from all energies, weighted by the Fermi distribution, I obtain the total probability current density coming from the left electrode.

Since this is a 1-channel problem, the total electrical or charge current is directly proportional to the probability current density, and I can write:

$$
I_L(t) = \frac{e}{2\pi\hbar}\frac{m}{\hbar k}\int_{-\infty}^{\infty} d\varepsilon j(\varepsilon,t)f(\varepsilon) \tag{7.30}
$$

where $f(\varepsilon)$ is the Fermi distribution for the incident quasiparticle at energy ε. For the left electrode, this gives

$$\begin{aligned} I_L(\varepsilon,t) = \frac{e}{2\pi\hbar}\int d\varepsilon\Big(&[|J|^2 + |A_1|^2(1+|a_2|^2) + |A_2|^2(1+|a_4|^2) + |A_3|^2(1+|a_6|^2) \\ &+ ...] + [Ja_2^*A_1^* + A_1A_2^*(1+a_2a_4^*) + A_2A_3^*(1+a_4a_6^*) + ...]e^{i2eVt/\hbar} \\ &+ [Ja_4^*A_2^* + A_1A_3^*(1+a_2a_6^*) + A_2A_4^*(1+a_4a_8^*) + ...]e^{i4eVt/\hbar} + [...]e^{i6eVt/\hbar} + ... \\ &+ [J^*a_2A_1 + A_2A_1^*(1+a_4a_2^*) + A_3A_2^*(1+a_6a_4^*) + ...]e^{-i2eVt/\hbar} \\ &+ [J^*a_4A_2 + A_3A_1^*(1+a_6a_2^*) + A_4A_2^*(1+a_8a_4^*) + ...]e^{-i4eVt/\hbar} + [...]e^{-i6eVt/\hbar} \\ &+ ...\Big) \times \frac{1}{e^{\varepsilon/k_BT}+1} = \sum_{K=-\infty}^{\infty} I_L^{(K)}(\varepsilon)e^{i2KeVt/\hbar} \end{aligned} \tag{7.31}$$

where the last expression is written as a sum over Fourier components.

This completes half of the story. For the net current, we also have to consider the current due to electron-like quasiparticles incident from the right electrode. This is similar to the case discussed above of quasiparticles incident from the left electrode, however an electron-like quasiparticle traveling from right to left picks up energy $-eV$ rather than eV as it traverses the normal region.

To proceed, note again that for $D = 1$, I will have $B_n = 0$ and $D_n = 0$, i.e. no scattered wave. Since the right electrode has applied voltage V, it effectively shifts the Fermi level down. To simplify the equations, I consider an electron-like quasiparticle incident from the right with energy $\varepsilon + eV$ and source term $J(\varepsilon + eV)$. Examining Fig. 7.3, one can see that when an electron travels from right to left, it loses energy eV, and thus then Andreev reflection amplitude at the left S/N

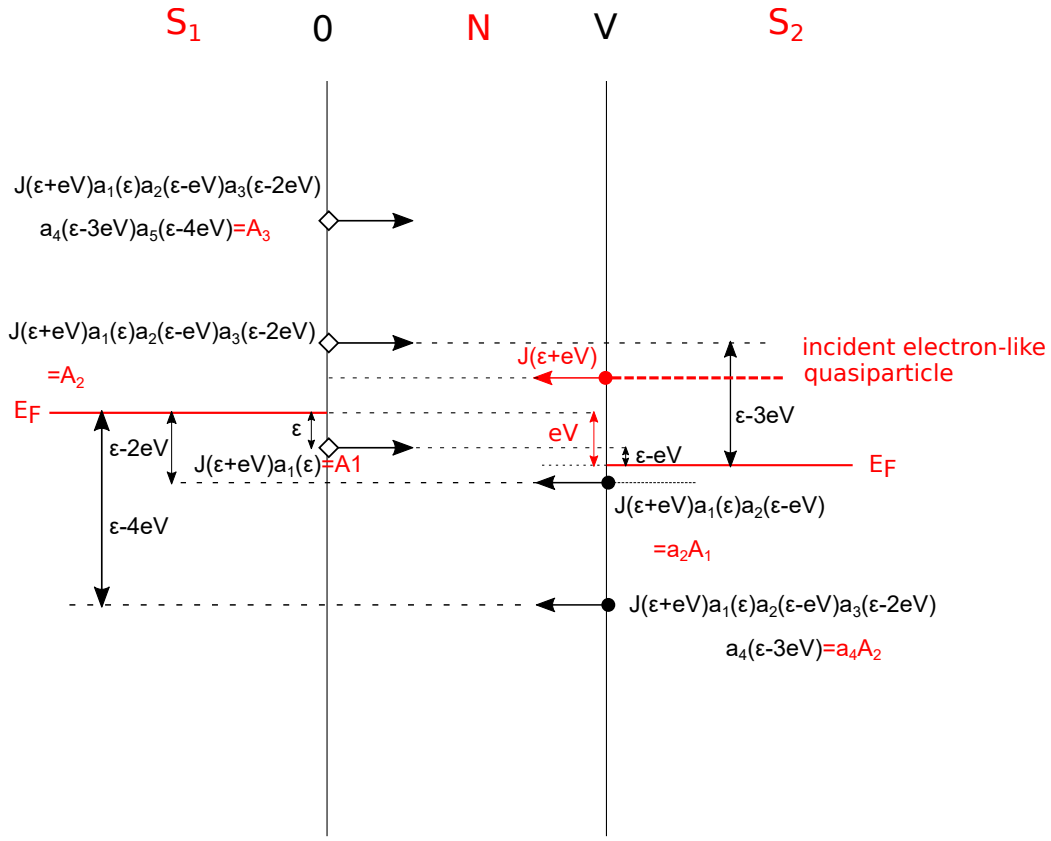

Figure 7.3: Illustration of multiple Andreev reflection of an electron-like quasiparticle that is incident at ε from the right electrode. Since the right electrode has voltage V, it effectively brings down the Fermi level of the right side.

interface will be $a_1(\varepsilon + eV - eV) = a_1(\varepsilon)$. Thus the energy of the electron that will be Andreev reflected as an hole is ε. The hole will travel to the right, and it loses energy eV, which gives a reflection amplitude of $a_2(\varepsilon - eV)$ at the right electrode. This process continues and each time the particle's energy decreases by eV when traveling across the normal region. Thus I obtain:

$$A_{-3} = A_{-2} = A_{-1} = A_0 = 0 \tag{7.32a}$$

$$A_1(\varepsilon + eV, -V) = J(\varepsilon + eV)a_1(\varepsilon) \tag{7.32b}$$

$$A_2(\varepsilon + eV, -V) = J(\varepsilon + eV)a_1(\varepsilon)a_2(\varepsilon - eV)a_3(\varepsilon - 2eV) \tag{7.32c}$$

$$A_3(\varepsilon + eV, -V) = J(\varepsilon + eV)a_1(\varepsilon)a_2(\varepsilon - eV)a_3(\varepsilon - 2eV)a_4(\varepsilon - 3eV)a_5(\varepsilon - 4eV) \tag{7.32d}$$

$$\vdots \tag{7.32e}$$

The wave function due to an electron-like quasiparticle incident from the right side is thus, for $D = 1$:

$$\psi_{el} = \sum_n [(a_{2n}A_n + J\delta_{n0})e^{-ikx}]e^{-i(\varepsilon - 2neV)t/\hbar} \tag{7.33a}$$

$$\psi_h = \sum_n [A_n e^{-ikx}]e^{-i(\varepsilon - 2neV)t/\hbar} \tag{7.33b}$$

The corresponding current due to electron-like quasiparticles incident from the right

is then:

$$I_R(\varepsilon,t) = -\frac{e}{2\pi\hbar}\int_{-\infty}^{\infty} d\varepsilon\Big(\big[|J|^2 + |A_1|^2(1+|a_2|^2) + |A_2|^2(1+|a_4|^2) + |A_3|^2(1+|a_6|^2$$
$$+ ...] + [Ja_2^*A_1^* + A_1A_2^*(1+a_2a_4^*) + A_2A_3^*(1+a_4a_6^*) + ...]e^{-i2eVt/\hbar}$$
$$+ [Ja_4^*A_2^* + A_1A_3^*(1+a_2a_6^*) + A_2A_4^*(1+a_4a_8^*) + ...]e^{-i4eVt/\hbar} + [..]e^{-i6eVt/\hbar} + ...$$
$$+ [J^*a_2A_1 + A_2A_1^*(1+a_4a_2^*) + A_3A_2^*(1+a_6a_4^*) + ...]e^{i2eVt/\hbar}$$
$$+ [J^*a_4A_2 + A_3A_1^*(1+a_6a_2^*) + A_4A_2^*(1+a_8a_4^*) + ...]e^{i4eVt/\hbar} + [...]e^{i6eVt/\hbar} + ...\Big)$$
$$\times \frac{1}{e^{(\varepsilon-\mu_R)/k_BT}+1} = \sum_{K=-\infty}^{\infty} I_R^{(K)}(\varepsilon)e^{i2KeVt/\hbar} \tag{7.34}$$

where the last expression is written as a sum over Fourier components. Also note in Eq. (7.34) that the chemical potential μ_R of the right electrode is -eV.

I can now find the total current by combining the current from the left and the right side. For simplicity, let's look at the DC case. Taking the zeroth Fourier component $K = 0$ in Eq. (7.31) and Eq. (7.34), I find:

$$I_{DC} = \int_{-\infty}^{\infty} d\varepsilon(I_L^0(\varepsilon) + I_R^0(\varepsilon))$$
$$= \frac{e}{2\pi\hbar}\Bigg[\int_{-\infty}^{\infty} d\varepsilon[|J(\varepsilon)|^2 + |A_1(\varepsilon,V)|^2(1+|a_2(\varepsilon+2eV)|^2) + |A_2(\varepsilon,V)|^2(1$$
$$+ |a_4(\varepsilon+4eV)|^2) + |A_3(\varepsilon,V)|^2(1+|a_6(\varepsilon,V)|^2) + ...]\frac{1}{e^{\varepsilon/k_BT}+1}$$
$$- \int_{-\infty}^{\infty} d\varepsilon[|J(\varepsilon+eV)|^2 + |A_1(\varepsilon+eV,-V)|^2(1+|a_2(\varepsilon+eV-2eV)|^2)$$
$$+ |A_2(\varepsilon+eV,-V)|^2(1+|a_4(\varepsilon+eV-4eV)|^2) + |A_3(\varepsilon+eV,-V)|^2(1+$$
$$|a_6(\varepsilon+eV-6eV)|^2) + ...]\frac{1}{e^{(\varepsilon+eV)/k_BT}+1}\Bigg] \tag{7.35}$$

Substituting for the A_n from Eq. (7.21) and Eq. (7.32), I can write

$$
\begin{aligned}
I_{DC} = \frac{e}{2\pi\hbar}\Bigg[& \int_{-\infty}^{\infty} d\varepsilon [|J(\varepsilon)|^2 + |J(\varepsilon)|^2|a_1(\varepsilon+eV)|^2 + |J(\varepsilon)|^2|a_1(\varepsilon+eV)|^2 \\
& |a_2(\varepsilon+2eV)|^2 + |J(\varepsilon)|^2|a_1(\varepsilon+eV)|^2|a_2(\varepsilon+2eV)|^2|a_3(\varepsilon+3eV)|^2 ...] \frac{1}{e^{\varepsilon/k_BT}+1} \\
& - \int_{-\infty}^{\infty} d\varepsilon [|J(\varepsilon+eV)|^2 + |J(\varepsilon+eV)|^2|a_1(\varepsilon)|^2 + |J(\varepsilon+eV)|^2|a_1(\varepsilon)|^2|a_2(\varepsilon-eV)|^2 \\
& + |J(\varepsilon+eV)|^2|a_1(\varepsilon)|^2|a_2(\varepsilon-eV)|^2|a_3(\varepsilon-2eV)|^2 ...] \frac{1}{e^{(\varepsilon+eV)/k_BT}+1} \Bigg]
\end{aligned}
\tag{7.36}
$$

Let's look at the $|J(\varepsilon)|^2$ terms first. I find:

$$
\begin{aligned}
& \int_{-\infty}^{\infty} d\varepsilon \left(|J(\varepsilon)|^2 \frac{1}{e^{\varepsilon/k_BT}+1} - |J(\varepsilon+eV)|^2 \frac{1}{e^{(\varepsilon+eV)/k_BT}+1} \right) \\
& = \int_{-\infty}^{\infty} d\varepsilon \left((1-|a(\varepsilon)|^2) \frac{1}{e^{\varepsilon/k_BT}+1} - (1-|a(\varepsilon+eV)|^2) \frac{1}{e^{(\varepsilon+eV)/k_BT}+1} \right) \\
& = \int_{-\infty}^{\infty} d\varepsilon \Bigg[\left(\frac{1}{e^{\varepsilon/k_BT}+1} - \frac{1}{e^{(\varepsilon+eV)/k_BT}+1} \right) - \left(|a(\varepsilon)|^2 \frac{1}{e^{\varepsilon/k_BT}+1} \right. \\
& \left. - |a(\varepsilon+eV)|^2 \frac{1}{e^{(\varepsilon+eV)/k_BT}+1} \right) \Bigg] = eV
\end{aligned}
\tag{7.37}
$$

This eV is the first term in Eq. (6) in Averin and Bardas [122].

For the rest of the terms, I change variables for the incoming current from the right. Defining $\varepsilon' = \varepsilon + eV$, I can now write Eq. (7.36) as

$$
\begin{aligned}
I_{DC} = \frac{e^2V}{2\pi\hbar} + \frac{e}{2\pi\hbar}\Bigg[& \int_{-\infty}^{\infty} d\varepsilon [|J(\varepsilon)|^2|a_1(\varepsilon+eV)|^2 + |J(\varepsilon)|^2|a_1(\varepsilon+eV)|^2|a_2(\varepsilon+2eV)|^2 \\
& + |J(\varepsilon)|^2|a_1(\varepsilon+eV)|^2|a_2(\varepsilon+2eV)||a_3(\varepsilon+3eV)|^2 ...] \frac{1}{e^{\varepsilon/k_BT}+1} \\
& - \int_{-\infty+eV}^{\infty+eV} d\varepsilon' [|J(\varepsilon')|^2|a_1(\varepsilon'-eV)|^2 + |J(\varepsilon')|^2|a_1(\varepsilon'-eV)|^2|a_2(\varepsilon'-2eV)|^2
\end{aligned}
$$

$$+ |J(\varepsilon')|^2 |a_1(\varepsilon' - eV)|^2 |a_2(\varepsilon' - 2eV)|^2 |a_3(\varepsilon' - 3eV)|^2 ...] \frac{1}{e^{\varepsilon'/k_BT} + 1} \Bigg] \tag{7.38}$$

We see there is some kind of the symmetry for the case of equal gaps. From the definition of $J(\varepsilon) = \sqrt{(1 - |a(\varepsilon)|^2)}$, this is an even function: $J(\varepsilon)$=$J(-\varepsilon)$. In terms of $a(\varepsilon)$, by inspecting the definition from Eq. (7.1), we get the following relation:

$$\begin{cases} a(-E) &= -a(E) = -a^*(E), \quad \text{for} \quad |E| > \Delta \\ a(-E) &= -a^*(E), \quad\quad\quad\quad\quad\quad \text{for} \quad |E| < \Delta \end{cases} \tag{7.39}$$

I use E to represent the total energy of the particle to avoid confusion in the notation. ε is the original energy that the incident particle carries. V is the voltage that the incident quasiparticle sees. Thus:

$$\begin{aligned} a_n(-\varepsilon, -V) = a(-\varepsilon - neV) &= a(-E) \\ &= -a^*(E) = -a^*(\varepsilon + neV) = -a_n^*(\varepsilon, V) \end{aligned} \tag{7.40}$$

Using Eq. (7.40), I can show that there is a relation between $A_1(\varepsilon, V) = J(\varepsilon)a_1(\varepsilon + eV)$ and $A_1(-\varepsilon, -V) = J(-\varepsilon)a_1(-\varepsilon - eV)$, where I find:

$$A_1(-\varepsilon, -V) = -A_1^*(\varepsilon, V) \tag{7.41}$$

This relation holds for $A_1, A_2, A_3...$, as each A_n has an odd number of factors of $a(\varepsilon)$,

therefore it always picks up a minus sign. Thus the general relation for $A(\varepsilon, V)$ is:

$$A_n(-\varepsilon, -V) = -A_n^*(\varepsilon, V) \tag{7.42}$$

as stated by AB [122].

Using Eq. (7.41) and Eq. (7.42), the negative ε' terms in Eq. (7.38) can combine with the positive ε terms, and I find:

$$\begin{aligned}
I_{DC} = \frac{e}{2\pi\hbar}\Bigg[& eV + \int_{-\infty}^{\infty} d\varepsilon [|J(\varepsilon)|^2 |a_1(\varepsilon + eV)|^2 + |J(\varepsilon)|^2 |a_1(\varepsilon + eV)|^2 |a_2(\varepsilon + 2eV)|^2 \\
& + |J(\varepsilon)|^2 |a_1(\varepsilon + eV)|^2 |a_2(\varepsilon + 2eV)|^2 |a_3(\varepsilon + 3eV)|^2 ...] \frac{1}{e^{\varepsilon/k_BT} + 1} \\
& - \int_{-\infty - eV}^{\infty - eV} d\varepsilon [|J(-\varepsilon)|^2 |a_1(-\varepsilon - eV)|^2 + |J(-\varepsilon)|^2 |a_1(-\varepsilon - eV)|^2 \\
& |a_2(-\varepsilon - 2eV)|^2 + |J(-\varepsilon)|^2 |a_1(-\varepsilon - eV)|^2 |a_2(-\varepsilon - 2eV)|^2 |a_3(-\varepsilon - 3eV)|^2 \\
& ...] \frac{1}{e^{-\varepsilon/k_BT} + 1} \Bigg] \\
= \frac{e}{2\pi\hbar}\Bigg[& eV + \int_{-\infty}^{\infty} d\varepsilon [|J(\varepsilon)|^2 |a_1(\varepsilon + eV)|^2 + |J(\varepsilon)|^2 |a_1(\varepsilon + eV)|^2 |a_2(\varepsilon + 2eV)|^2 \\
& + |J(\varepsilon)|^2 |a_1(\varepsilon + eV)|^2 |a_2(\varepsilon + 2eV)|^2 |a_3(\varepsilon + 3eV)|^2 \\
& ...] (\frac{1}{e^{\varepsilon/k_BT} + 1} - \frac{1}{e^{-\varepsilon/k_BT} + 1}) \\
& - \int_{-\infty - eV}^{-\infty} d\varepsilon [|J(-\varepsilon)|^2 |a_1(-\varepsilon - eV)|^2 + |J(-\varepsilon)|^2 |a_1(-\varepsilon - eV)|^2 |a_2(-\varepsilon - 2eV)|^2 \\
& + |J(-\varepsilon)|^2 |a_1(-\varepsilon - eV)|^2 |a_2(-\varepsilon - 2eV)|^2 |a_3(-\varepsilon - 3eV)|^2 ...] \frac{1}{e^{-\varepsilon/k_BT} + 1} \\
& + \int_{\infty - eV}^{\infty} d\varepsilon [|J(-\varepsilon)|^2 |a_1(-\varepsilon - eV)|^2 + |J(-\varepsilon)|^2 |a_1(-\varepsilon - eV)|^2 |a_2(-\varepsilon - 2eV)|^2 \\
& + |J(-\varepsilon)|^2 |a_1(-\varepsilon - eV)|^2 |a_2(-\varepsilon - 2eV)|^2 |a_3(-\varepsilon - 3eV)|^2 ...] \frac{1}{e^{-\varepsilon/k_BT} + 1} \Bigg] \\
= \frac{e}{2\pi\hbar}\Bigg[& eV - \int_{-\infty}^{\infty} d\varepsilon \tanh\left(\frac{\varepsilon}{2k_BT}\right) \Big(|J(\varepsilon)|^2 |a_1(\varepsilon + eV)|^2 + |J(\varepsilon)|^2 |a_1(\varepsilon + eV)|^2
\end{aligned}$$

$$
\begin{aligned}
&|a_2(\varepsilon+2eV)|^2 + |J(\varepsilon)|^2|a_1(\varepsilon+eV)|^2|a_2(\varepsilon+2eV)|^2|a_3(\varepsilon+3eV)|^2...\Big) \\
&- \int_{\infty}^{\infty+eV} d\varepsilon\Big(|J(\varepsilon)|^2|a_1(\varepsilon-eV)|^2 + |J(\varepsilon)|^2|a_1(\varepsilon-eV)|^2|a_2(\varepsilon-2eV)|^2 \\
&+ |J(\varepsilon)|^2|a_1(\varepsilon-eV)|^2|a_2(\varepsilon-2eV)|^2|a_3(\varepsilon-3eV)|^2...\Big)\frac{1}{e^{\varepsilon/k_BT}+1} \\
&+ \int_{-\infty}^{-\infty+eV} d\varepsilon\Big(|J(\varepsilon)|^2|a_1(\varepsilon-eV)|^2 + |J(\varepsilon)|^2|a_1(\varepsilon-eV)|^2|a_2(\varepsilon-2eV)|^2 \\
&+ |J(\varepsilon)|^2|a_1(\varepsilon-eV)|^2|a_2(\varepsilon-2eV)|^2|a_3(\varepsilon-3eV)|^2...\Big)\frac{1}{e^{\varepsilon/k_BT}+1}\Bigg] \\
&= \frac{e}{2\pi\hbar}\Bigg[eV - \int_{-\infty}^{\infty} d\varepsilon \tanh\left(\frac{\varepsilon}{2k_BT}\right)\Big(|J(\varepsilon)|^2|a_1(\varepsilon+eV)|^2 + |J(\varepsilon)|^2|a_1(\varepsilon+eV)|^2 \\
&|a_2(\varepsilon+2eV)|^2 + |J(\varepsilon)|^2|a_1(\varepsilon+eV)|^2|a_2(\varepsilon+2eV)|^2|a_3(\varepsilon+3eV)|^2...\Big)\Bigg]
\end{aligned}
\tag{7.43}
$$

The second integral vanishes because the Fermi function vanishes as $\varepsilon \to \infty$. The last integral also vanishes because $a(\varepsilon)$ goes to zero as $\varepsilon \to -\infty$, as can be seen from Eq. (7.1). Later on, when I consider the case where D is not equal to 1, the last term will need to be reexamined.

A similar analysis can be done with the other Fourier components in Eq. (7.31) and Eq. (7.34). In particular, I find that for the first Fourier component $K = 1$:

$$
\begin{aligned}
I_{AC} &= I_L^1(t) + I_R^1(t) \\
&= e^{i2eVt/\hbar}\frac{e}{2\pi\hbar}\int_{-\infty}^{\infty} d\varepsilon[J(\varepsilon)a_2^*(\varepsilon,V)A_1^*(\varepsilon,V) + A_1(\varepsilon,V)A_2^*(\varepsilon,V)(1+a_2(\varepsilon,V) \\
&\quad a_4^*(\varepsilon,V)) + A_2(\varepsilon,V)A_3^*(\varepsilon,V)(1+a_4(\varepsilon,V)a_6^*(\varepsilon,V)) + ...]\frac{1}{e^{\varepsilon/k_BT}+1} \\
&- e^{i2eVt/\hbar}\frac{e}{2\pi\hbar}\int_{-\infty+eV}^{\infty+eV} d\varepsilon[J^*(\varepsilon)a_2(\varepsilon,-V)A_1(\varepsilon,-V) + A_1^*(\varepsilon,-V)A_2(\varepsilon,-V)(1 \\
&\quad + a_2^*(\varepsilon,-V)a_4(\varepsilon,-V)) + A_2^*(\varepsilon,-V)A_3(\varepsilon,-V)(1+a_4^*(\varepsilon,-V)a_6(\varepsilon,-V))
\end{aligned}
$$

$$+ ...]\frac{1}{e^{\varepsilon/k_BT}+1} \tag{7.44}$$

This can be rearranged to give

$$\begin{aligned}
I_{AC} = e^{i2eVt/\hbar}\frac{e}{2\pi\hbar}\int_{-\infty}^{\infty} d\varepsilon[&J(\varepsilon)a_2^*(\varepsilon,V)A_1^*(\varepsilon,V) + A_1(\varepsilon,V)A_2^*(\varepsilon,V)(1+a_2(\varepsilon,V)\\
&a_4^*(\varepsilon,V)) + A_2(\varepsilon,V)A_3^*(\varepsilon,V)(1+a_4(\varepsilon,V)a_6^*(\varepsilon,V)) + ...]\frac{1}{e^{\varepsilon/k_BT}+1}\\
- e^{i2eVt/\hbar}\frac{e}{2\pi\hbar}\int_{-\infty-eV}^{\infty-eV} d\varepsilon[&J^*(-\varepsilon)a_2(-\varepsilon,-V)A_1(-\varepsilon,-V) + A_1^*(-\varepsilon,-V)\\
&A_2(-\varepsilon,-V)(1+a_2^*(-\varepsilon,-V)a_4(-\varepsilon,-V)) + A_2^*(-\varepsilon,-V)A_3(-\varepsilon,-V)\\
&(1+a_4^*(-\varepsilon,-V)a_6(-\varepsilon,-V)) + ...]\frac{1}{e^{-\varepsilon/k_BT}+1}\\
= -e^{i2eVt/\hbar}\frac{e}{2\pi\hbar}\int_{-\infty}^{\infty} d\varepsilon\tanh&\left(\frac{\varepsilon}{2k_BT}\right)[J(\varepsilon)a_2^*(\varepsilon,V)A_1^*(\varepsilon,V)\\
&+ A_1(\varepsilon,V)A_2^*(\varepsilon,V)(1+a_2(\varepsilon,V)a_4^*(\varepsilon,V)) + A_2(\varepsilon,V)A_3^*(\varepsilon,V)\\
&(1+a_4(\varepsilon,V)a_6^*(\varepsilon,V)) + ...]\\
- e^{i2eVt/\hbar}\frac{e}{2\pi\hbar}\int_{\infty}^{\infty+eV} d\varepsilon[&J^*(\varepsilon)a_2(\varepsilon,-V)A_1(\varepsilon,-V) + A_1^*(\varepsilon,-V)A_2(\varepsilon,-V)\\
&(1+a_2^*(\varepsilon,-V)a_4(\varepsilon,-V)) + A_2^*(\varepsilon,-V)A_3(\varepsilon,-V)(1+a_4^*(\varepsilon,-V)a_6(\varepsilon,-V))\\
&+ ...]\frac{1}{e^{\varepsilon/k_BT}+1}\\
+ e^{i2eVt/\hbar}\frac{e}{2\pi\hbar}\int_{-\infty}^{-\infty+eV} d\varepsilon[&J^*(\varepsilon)a_2(\varepsilon,-V)A_1(\varepsilon,-V) + A_1^*(\varepsilon,-V)A_2(\varepsilon,-V)\\
&(1+a_2^*(\varepsilon,-V)a_4(\varepsilon,-V)) + A_2^*(\varepsilon,-V)A_3(\varepsilon,-V)(1+a_4^*(\varepsilon,-V)a_6(\varepsilon,-V))\\
&+ ...]\frac{1}{e^{\varepsilon/k_BT}+1}
\end{aligned} \tag{7.45}$$

Finally I find:

$$I_{AC} = -e^{i2eVt/\hbar}\frac{e}{2\pi\hbar}\int_{-\infty}^{\infty} d\varepsilon \tanh\left(\frac{\varepsilon}{2k_BT}\right)[J(\varepsilon)a_2^*(\varepsilon,V)A_1^*(\varepsilon,V) + A_1(\varepsilon,V)A_2^*(\varepsilon,V)$$
$$(1 + a_2(\varepsilon,V)a_4^*(\varepsilon,V)) + A_2(\varepsilon,V)A_3^*(\varepsilon,V)(1 + a_4(\varepsilon,V)a_6^*(\varepsilon,V)) + ...] \tag{7.46}$$

If we do the analysis for all the Fourier components, I find:

$$I(t) = \sum_k I_k e^{i2keVt/\hbar} \tag{7.47}$$

where

$$I_k = 2 \times \frac{e}{2\pi\hbar}[eV\delta_{k0} - \int_{-\infty}^{\infty} d\varepsilon \tanh\left(\frac{\varepsilon}{2k_BT}\right)\big(J(\varepsilon)(a_{2k}^*A_k^* + a_{-2k}A_{-k})$$
$$+ \sum_{n=-\infty}^{\infty}(1 + a_{2n}a_{2(n+k)}^*)(A_nA_{n+k}^*)\big)] \tag{7.48}$$

I note that this expression has A_k=0 for $k < 0$ and it holds only for the very special case where there is no scattering, *i.e.* $D = 1$.

Examining Eq. (7.48), we see that the current component I_k has a leading factor of 2. This accounts for a hole-like quasiparticle incident from the left and a hole-like quasiparticle incident from the right, where the sum of both terms contributes exactly the same as an electron-like quasiparticle incident from the right and an electron-like quasiparticle incident from the left. However this situation only applies when the left and right superconductors have the same gap Δ. In a later

section, we will see that when the electrons have different gaps, one needs to consider four different scenarios (electron-like quasiparticle incident from the left, electron-like quasiparticle incident from the right, hole-like quasiparticle incident from the left, hole-like quasiparticle incident from the right) in order to obtain the correct current expression.

7.3 MAR in symmetrical junction with $D \neq 1$

To find the current where the barrier transparency $D \neq 1$, we need to account for quasiparticles being reflected at the barrier in the weak link (see Fig. 7.1). For $D \neq 1$, when a quasiparticle is incident from the left the wave function is

$$\psi_{el} = \sum_n [(a_{2n}A_n + J\delta_{n0})e^{ikx} + B_n e^{-ikx}]e^{-i(\varepsilon+2neV)t/\hbar} \tag{7.49a}$$

$$\psi_h = \sum_n [A_n e^{ikx} + a_{2n}B_n e^{-ikx}]e^{-i(\varepsilon+2neV)t/\hbar} \tag{7.49b}$$

From this wavefunction, we can get the total probability current $j = j_{el} + j_h$ using Eq. (7.23). As we see above the wavefunction of the electron and the hole have taken care of the current flow.

For the electron wave function:

$$\psi_{el} = e^{ikx}(a_{-4}A_{-2}e^{-i(\varepsilon-4eV)t/\hbar} + a_{-2}A_{-1}e^{-i(\varepsilon-2eV)t/\hbar} + (J + a_0A_0)e^{-i\varepsilon t/\hbar}$$
$$+ a_2A_1e^{-i(\varepsilon+2eV)t/\hbar} + a_4A_2e^{-i(\varepsilon+4eV)t/\hbar} + a_6A_3e^{-i(\varepsilon+6eV)t/\hbar} + ...)$$

$$+ e^{-ikx}(B_{-2}e^{-i(\varepsilon-4eV)t/\hbar} + B_{-1}e^{-i(\varepsilon-2eV)t/\hbar} + B_0e^{-i\varepsilon t/\hbar} + B_1e^{-i(\varepsilon+2eV)t/\hbar}$$

$$+ B_2e^{-i(\varepsilon+4eV)t/\hbar} + ...) \tag{7.50}$$

and thus

$$\psi^*_{el} = e^{-ikx}(a^*_{-4}A^*_{-2}e^{i(\varepsilon-4eV)t/\hbar} + a^*_{-2}A^*_{-1}e^{i(\varepsilon-2eV)t/\hbar} + (J + a^*_0A^*_0)e^{i\varepsilon t/\hbar}$$

$$+ a^*_2A^*_1e^{i(\varepsilon+2eV)t/\hbar} + a^*_4A^*_2e^{i(\varepsilon+4eV)t/\hbar} + a^*_6A^*_3e^{i(\varepsilon+6eV)t/\hbar} + ...)$$

$$+ e^{ikx}(B^*_{-2}e^{i(\varepsilon-4eV)t/\hbar} + B^*_{-1}e^{i(\varepsilon-2eV)t/\hbar} + B^*_0e^{i\varepsilon t/\hbar}$$

$$+ B^*_1e^{i(\varepsilon+2eV)t/\hbar} + B^*_2e^{i(\varepsilon+4eV)t/\hbar} + ...). \tag{7.51}$$

I then find the probability current density:

$$j_{el} = \frac{\hbar}{2mi} * 2ik\Bigg\{\Bigg([... + |a_{-4}|^2|A_{-2}|^2 + |a_{-2}|^2|A_{-1}|^2 + |J|^2 + J(a_0A_0 + a^*_0A^*_0)$$

$$+ |a_0|^2|A_0|^2 + |a_2|^2 + |A_1|^2 + |a_4|^2|A_2|^2 + |a_6|^2|A_3|^2 + ...] - [... + |B_{-2}|^2 + |B_{-1}|^2$$

$$+ |B_0|^2 + |B_1|^2 + |B_2|^2 + ...]\Bigg) + \Bigg([...a_{-4}A_{-2}a^*_{-2}A^*_{-1} + a_{-2}A_{-1}(J + a^*_0A^*_0)$$

$$+ (J + a_0A_0)a^*_2A^*_1 + a_2A_1a^*_4A^*_2 + a_4A_2a^*_6A^*_3 + ...] - [... + B_{-2}B^*_{-1} + B_{-1}B^*_0$$

$$+ B_0B^*_1 + B_1B^*_2 + ...]\Bigg)e^{i2eVt/\hbar} + [...]e^{i4eVt/\hbar} + [...]e^{i6eVt/\hbar} + ...$$

$$+ \Bigg([... + a_{-2}A_{-1}a^*_{-4}A^*_{-2} + a^*_{-2}A^*_{-1}(J + a_0A_0) + (J + a^*_0A^*_0)a_2A_1 + a^*_2A^*_1a_4A_2$$

$$+ a^*_4A^*_2a_6A_3 + ...] - [... + B_{-1}B^*_{-2} + B_0B^*_{-1} + B_1B^*_0 + B_2B^*_1 + ...]\Bigg)e^{-i2eVt/\hbar}$$

$$+ [...]e^{-i4eVt/\hbar} + [...]e^{-i6eVt/\hbar} + ...\Bigg\} \tag{7.52}$$

For the hole wave function:

$$\psi_h = e^{ikx}(A_{-2}e^{-i(\varepsilon-4eV)t/\hbar} + A_{-1}e^{-i(\varepsilon-2eV)t/\hbar} + A_0e^{-i\varepsilon t/\hbar} + A_1e^{-i(\varepsilon+2eV)t/\hbar} + A_2e^{-i(\varepsilon+4eV)t/\hbar} + ...) + e^{-ikx}(a_{-4}B_{-2}e^{-i(\varepsilon-4eV)t/\hbar} + a_{-2}B_{-1}e^{-i(\varepsilon-2eV)t/\hbar} + a_0B_0e^{-i\varepsilon t/\hbar} + a_2B_1e^{-i(\varepsilon+2eV)t/\hbar} + a_4B_2e^{-i(\varepsilon+4eV)t/\hbar} + ...) \tag{7.53}$$

and thus

$$\psi_h^* = e^{-ikx}(A_{-2}^*e^{i(\varepsilon-4eV)t/\hbar} + A_{-1}^*e^{i(\varepsilon-2eV)t/\hbar} + A_0^*e^{i\varepsilon t/\hbar} + A_1^*e^{i(\varepsilon+2eV)t/\hbar} + A_2^*e^{i(\varepsilon+4eV)t/\hbar} + ...) + e^{ikx}(a_{-4}^*B_{-2}^*e^{i(\varepsilon-4eV)t/\hbar} + a_{-2}^*B_{-1}^*e^{i(\varepsilon-2eV)t/\hbar} + a_0^*B_0^*e^{i\varepsilon t/\hbar} + a_2^*B_1^*e^{i(\varepsilon+2eV)t/\hbar} + a_4^*B_2^*e^{i(\varepsilon+4eV)t/\hbar} + ...) \tag{7.54}$$

I then find the probability current density:

$$\begin{aligned} j_h = \frac{\hbar}{2mi} * 2ik\Big\{\Big(&- [... + |A_{-2}|^2 + |A_{-1}|^2 + |A_0|^2 + |A_1|^2 + |A_2|^2 + ...] \\ &+ [|a_{-4}|^2|B_{-2}|^2 + |a_{-2}|^2|B_{-1}|^2 + |a_0|^2|B_0|^2 + |a_2|^2|B_1|^2 + |a_4|^2|B_2|^2 + ...]\Big) \\ &+ \Big(- [A_1A_2^* + A_0A_1^* + A_{-1}A_0^* + A_{-2}A_{-1}^*...] + [a_2B_1a_4^*B_2^* + a_0B_0a_2^*B_1^* \\ &+ a_{-2}B_{-1}a_0^*B_0^* + a_{-4}B_{-2}a_{-2}^*B_{-1}^*]\Big)e^{i2eVt/\hbar} + [...]e^{i4eVt/\hbar} + [...]e^{i6eVt/\hbar} + ... \\ &+ \Big(- [A_1^*A_2 + A_0^*A_1 + A_{-1}^*A_0 + A_{-2}^*A_{-1}...] + [a_2^*B_1^*a_4B_2 + a_0^*B_0^*a_2B_1 \\ &+ a_{-2}^*B_{-1}^*a_0B_0 + a_{-4}^*B_{-2}^*a_{-2}B_{-1}]\Big)e^{-i2eVt/\hbar} + [...]e^{-i4eVt/\hbar} + [...]e^{-i6eVt/\hbar} + ...\Big\} \end{aligned} \tag{7.55}$$

From Eq. (7.52) and Eq. (7.55), I can now get a version of Averin and Bardas's Eq. (6) in [122] that is valid for all D:

$$I(t) = \sum_k I_k e^{i2keVt/\hbar} \tag{7.56}$$

where

$$\begin{aligned} I_k = 2 \times \frac{e}{2\pi\hbar}\Bigg\{ & eV\delta_{k0} - \int_{-\infty}^{\infty} d\varepsilon \tanh\left(\frac{\varepsilon}{2k_BT}\right)\Big[J(\varepsilon)(a_{2k}^* A_k^* + a_{-2k}A_{-k}) \\ & + \sum_{n=-\infty}^{\infty}(1 + a_{2n}a_{2(n+k)}^*)(A_n A_{n+k}^* - B_n B_{n+k}^*)\Big] + \int_{-\infty}^{-\infty+eV} d\varepsilon\Big[J(\varepsilon)(a_{2k}^* A_k^* \\ & + a_{-2k}A_{-k}) + \sum_{n=-\infty}^{\infty}(1 + a_{2n}a_{2(n+k)}^*)(A_n A_{n+k}^* - B_n B_{n+k}^*)\Big]\frac{1}{e^{\varepsilon/k_BT}+1}\Bigg\} \\ = \frac{e}{\pi\hbar}\Bigg\{ & eVD\delta_{k0} - \int_{-\infty}^{\infty} d\varepsilon \tanh\left(\frac{\varepsilon}{2k_BT}\right)\Big[J(\varepsilon)(a_{2k}^* A_k^* + a_{-2k}A_{-k}) \\ & + \sum_{n=-\infty}^{\infty}(1 + a_{2n}a_{2(n+k)}^*)(A_n A_{n+k}^* - B_n B_{n+k}^*)\Big]\Bigg\} \end{aligned} \tag{7.57}$$

I note that the $eVD\ \delta_{k0}$ term in the final expression is not equal to eV in this case because the last term does not disappear when $D \neq 1$. One finds that the $B_0 B_0^*$ terms in the sum yield eVR, which then combine with the first term $eV - eVR = eVD$. Note that in Eq. (7.57) the A and B terms are in general non-zero for all k, which are the integers $0, \pm1, \pm2, \pm3, ...$

To calculate the $I - V$ characteristics from Eq. (7.57), one needs to use the definition of $a(\varepsilon)$ from Eq. (7.1) to plug into the recursion relation Eq. (7.18) and Eq. (7.13) to get A_n, B_n. Once I have the A_n and B_n terms, I plug them into Eq. (7.57) and numerically integrate the equation to get the current at coltage V

(see Appendix C).

Figure 7.4 shows the calculated dc $I-V$ characteristics of an S-I-S junction that I obtained from Eq. (7.57) for k=0. The different curves are for different transparency D. For example, for $D = 0.01$ and $T = 0$, the barrier has low transparency, and the junction I(V) curve goes to the conventional S-I-S tunneling limit [64]. There is a clear rise in the current at the sum of the superconducting gaps, but no obvious subgap behavior on this scale. In contrast, the other curves with $D \geq 0.1$ are for more transparent junctions, and these show current steps at $eV = 2\Delta/n$, where $n = 1, 2, 3...$is an integer.

7.4 MAR in Asymmetrical junctions

In the previous section I showed how to obtain Averin and Bardas's expression for the I(V) characteristics of an S-I-S junction when both electrodes have the same gap. Here I generalize their approach to the case where the electrodes have different superconducting gaps. The key thing to note is that the Andreev reflection amplitude will now depend on which interface is reflecting the particle. To simplify the discussion, let's again start by looking at the case $D = 1$. Consider an electron-like quasiparticle incident from the left with energy ε and a voltage V applied to the right electrode. Now when a transmitted electron goes from the left to the right interface, its energy becomes $\varepsilon + eV$ and the Andreev reflection amplitude will be $A_1(\varepsilon, V) = J^L(\varepsilon)a_1^R(\varepsilon + eV)$. An Andreev reflected hole will then travel from

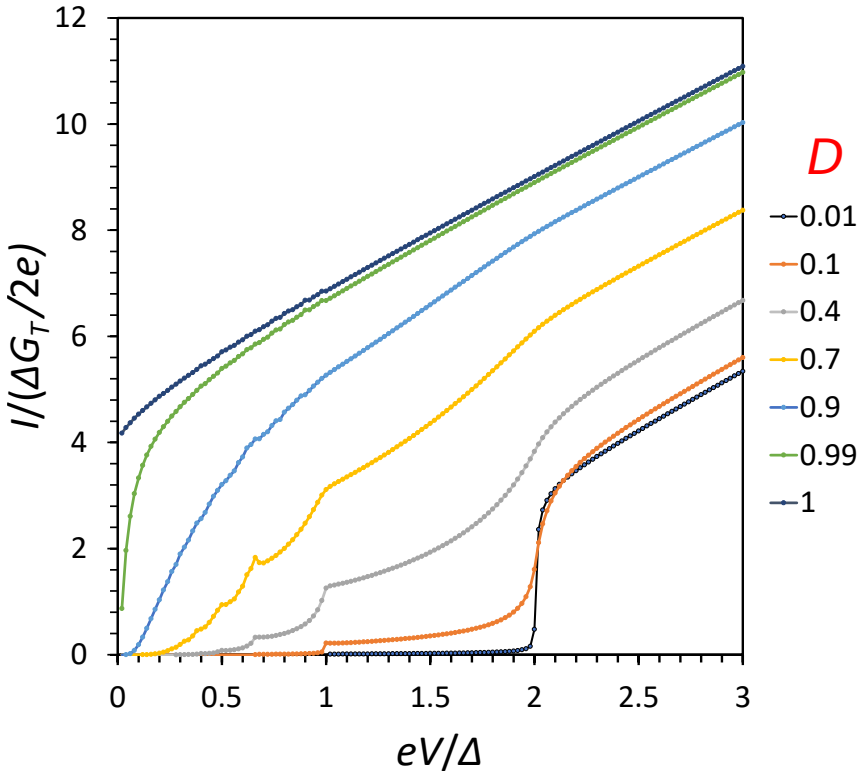

Figure 7.4: Calculated $I-V$ characteristics of a symmetrical S-I-S junction with MAR. The superconducting gap is the same for the two superconductors and the different curves correspond to D values of 1, 0.99, 0.9, 0.7, 0.4, 0.1 and 0.01 from top to bottom. G_T is the normal state conductance of the channel $G_T = e^2 D/\pi\hbar$.

right to left and pick up extra energy eV. This hole will be Andreev reflected at the left interface, producing a rightward traveling electron with amplitude $a_2^L(\varepsilon)A_1$ $=J^L(\varepsilon)a_1^R(\varepsilon+eV)a_2^L(\varepsilon+2eV)$. When the electron again travels to the right, it picks up another energy increment of eV and at the right interface yields an Andreev reflected hole with amplitude $J^L(\varepsilon)a_1^R(\varepsilon+eV)a_2^L(\varepsilon+2eV)a_3^R(\varepsilon+3eV)$. This is the same process shown in Fig. 7.2, it is just that we need to keep in mind that the left and right sides produce different reflection amplitudes because they may have different gaps.

As we can see from this description, all the odd indices for a_n come from the right electrode, and all the even indices for a_n are from the left electrode. To get A_1, A_2, A_3..., we have to calculate the amplitude using corresponding a_{even}^L and a_{odd}^R. To help keep things straight, we emphasize that here we first consider quasiparticles incident from the left electrode at energy ε, and now we relabel the A_1, A_2,.. as $A_{1L}(\varepsilon,V), A_{2L}(\varepsilon,V), A_{3L}(\varepsilon,V)$... We will go on to consider quasiparticles incident from the right.

Previously for the case of electrodes with the same superconducting gap, I obtained Eq. (7.39) and Eq. (7.42). These relations are important because they allowed me to simplify the calculation of the current. For the case of different gaps, I need to re-examine these relations to see if they still hold.

To see what happens to Eq. (7.42), let's examine the situation when an electron-like quasiparticle is coming from the right electrode with energy $-\varepsilon$ and the left electrode is at the potential of 0 V while the right electrode is at the potential of V. When it goes from the right to the left interface, its energy decreases by

eV with respect to the Fermi energy on the left side. An Andreev reflected hole with amplitude $A_1(-\varepsilon,-V) = J^R(-\varepsilon)a_1^L(-\varepsilon - eV)$ will then travel from the left to the right and its energy decreases by eV on reaching the right side. An Andreev reflected electron then propagates from the right to the left with amplitude $a_2^R(-\varepsilon - 2eV)A_1$ $=J^R(-\varepsilon)a_1^L(-\varepsilon - eV)a_2^R(-\varepsilon - 2eV)$. At the left interface the electron energy will again decrease by eV, and an Andreev reflected hole will be generated with amplitude $A_2 = J^R(-\varepsilon)a_1^L(-\varepsilon - eV)a_2^R(-\varepsilon - 2eV)a_3^L(-\varepsilon - 3eV)....etc.$

Clearly $A_1(\varepsilon, V) = J^L(\varepsilon)a_1^R(\varepsilon + eV)$ and $A_1(-\varepsilon,-V) = J^R(-\varepsilon)a_1^L(-\varepsilon - eV)$ if the gaps are not equal, i.e.

$$A_1(\varepsilon, V) \neq -A_1^*(-\varepsilon,-V) \tag{7.58}$$

because $a_1^R(\varepsilon + eV)$ is different than $a_1^L(-\varepsilon - eV)$ because of the different gaps.

Therefore, to calculate the total current, we have to first calculate the current I_L from quasiparticles incident from the left by summing over all possible energies and weighting them by the Fermi distribution. I then need to find the current I_R due to quasiparticles incident from the right superconductor by summing over all possible energies and weighting with the Fermi distribution. I can then find $I = I_L - I_R$, which is the net current that flows through the junction.

Let's again start by finding the dc part. Starting from Eq. (7.43) and keeping track of the left and right, I can write,

$$I_{DC} = I_L + I_R$$

$$
\begin{aligned}
&= \frac{e}{2\pi\hbar}\Bigg[\int_{-\infty}^{\infty} d\varepsilon[\left|J^L(\varepsilon)\right|^2 + \left|J^L(\varepsilon)\right|^2\left|a_1^R(\varepsilon+eV)\right|^2 + \left|J^L(\varepsilon)\right|^2\left|a_1^R(\varepsilon+eV)\right|^2 \\
&\qquad \left|a_2^L(\varepsilon+2eV)\right|^2 + \left|J^L(\varepsilon)\right|^2\left|a_1^R(\varepsilon+eV)\right|^2\left|a_2^L(\varepsilon+2eV)\right|^2 \\
&\qquad \left|a_3^R(\varepsilon+3eV)\right|^2 ...]\frac{1}{e^{\varepsilon/k_BT}+1} \\
&- \int_{-\infty}^{\infty} d\varepsilon[\left|J^R(\varepsilon+eV)\right|^2 + \left|J^R(\varepsilon+eV)\right|^2\left|a_1^L(\varepsilon)\right|^2 + \left|J^R(\varepsilon+eV)\right|^2\left|a_1^L(\varepsilon)\right|^2 \\
&\qquad \left|a_2^R(\varepsilon-eV)\right|^2 + \left|J^R(\varepsilon+eV)\right|^2\left|a_1^L(\varepsilon)\right|^2\left|a_2^R(\varepsilon-eV)\right|^2 \\
&\qquad \left|a_3^L(\varepsilon-2eV)\right|^2 ...]\frac{1}{e^{(\varepsilon+eV)/k_BT}+1}\Bigg] \\
&= \frac{e}{2\pi\hbar}\Bigg[\int_{-\infty}^{\infty} d\varepsilon[\left|J^L(\varepsilon)\right|^2 + \left|J^L(\varepsilon)\right|^2\left|a_1^R(\varepsilon+eV)\right|^2 + \left|J^L(\varepsilon)\right|^2\left|a_1^R(\varepsilon+eV)\right|^2 \\
&\qquad \left|a_2^L(\varepsilon+2eV)\right|^2 + \left|J^L(\varepsilon)\right|^2\left|a_1^R(\varepsilon+eV)\right|^2\left|a_2^L(\varepsilon+2eV)\right|^2 \\
&\qquad \left|a_3^R(\varepsilon+3eV)\right|^2 ...]\frac{1}{e^{\varepsilon/k_BT}+1} \\
&- \int_{-\infty+eV}^{\infty+eV} d\varepsilon[\left|J^R(\varepsilon)\right|^2 + \left|J^R(\varepsilon)\right|^2\left|a_1^L(\varepsilon-eV)\right|^2 + \left|J^R(\varepsilon)\right|^2\left|a_1^L(\varepsilon-eV)\right|^2 \\
&\qquad \left|a_2^R(\varepsilon-2eV)\right|^2 + \left|J^R(\varepsilon)\right|^2\left|a_1^L(\varepsilon-eV)\right|^2\left|a_2^R(\varepsilon-2eV)\right|^2 \\
&\qquad \left|a_3^L(\varepsilon-3eV)\right|^2 ...]\frac{1}{e^{\varepsilon/k_BT}+1}\Bigg] \qquad (7.59)
\end{aligned}
$$

To proceed I now arrange things to make the integration limits look much nicer. This will result in an expression with the same "format" as Averin found in a paper on multi-channel MAR for the case of identical gaps [127]. Working with the limits of integration, I can write:

$$
\begin{aligned}
I_{DC} = \frac{e}{2\pi\hbar}\Bigg[&\int_{-\infty-eV}^{\infty} d\varepsilon[\left|J^L(\varepsilon)\right|^2 + \left|J^L(\varepsilon)\right|^2\left|a_1^R(\varepsilon+eV)\right|^2 + \left|J^L(\varepsilon)\right|^2\left|a_1^R(\varepsilon+eV)\right|^2 \\
&\left|a_2^L(\varepsilon+2eV)\right|^2 + \left|J^L(\varepsilon)\right|^2\left|a_1^R(\varepsilon+eV)\right|^2\left|a_2^L(\varepsilon+2eV)\right|^2
\end{aligned}
$$

$$
\begin{aligned}
&\left|a_3^R(\varepsilon+3eV)\right|^2 ...]\frac{1}{e^{\varepsilon/k_BT}+1} \\
&-\int_{-\infty-eV}^{\infty} d\varepsilon[\left|J^R(\varepsilon+eV)\right|^2+\left|J^R(\varepsilon+eV)\right|^2\left|a_1^L(\varepsilon)\right|^2+\left|J^R(\varepsilon+eV)\right|^2\left|a_1^L(\varepsilon)\right|^2 \\
&\qquad \left|a_2^R(\varepsilon-eV)\right|^2+\left|J^R(\varepsilon+eV)\right|^2\left|a_1^L(\varepsilon)\right|^2\left|a_2^R(\varepsilon-eV)\right|^2 \\
&\qquad \left|a_3^L(\varepsilon-2eV)\right|^2 ...]\frac{1}{e^{(\varepsilon+eV)/k_BT}+1}\Bigg] \\
&=\frac{e}{2\pi\hbar}\Bigg[\int_{-\infty-eV}^{\infty} d\varepsilon[\left|J^L(\varepsilon)\right|^2+\left|J^L(\varepsilon)\right|^2\left|a_1^R(\varepsilon+eV)\right|^2+\left|J^L(\varepsilon)\right|^2\left|a_1^R(\varepsilon+eV)\right|^2 \\
&\qquad \left|a_2^L(\varepsilon+2eV)\right|^2+\left|J^L(\varepsilon)\right|^2\left|a_1^R(\varepsilon+eV)\right|^2\left|a_2^L(\varepsilon+2eV)\right|^2 \\
&\qquad \left|a_3^R(\varepsilon+3eV)\right|^2 ...]\frac{1}{e^{\varepsilon/k_BT}+1} \\
&-\int_{-\infty}^{\infty+eV} d\varepsilon[\left|J^R(\varepsilon)\right|^2+\left|J^R(\varepsilon)\right|^2\left|a_1^L(\varepsilon-eV)\right|^2+\left|J^R(\varepsilon)\right|^2\left|a_1^L(\varepsilon-eV)\right|^2 \\
&\qquad \left|a_2^R(\varepsilon-2eV)\right|^2+\left|J^R(\varepsilon)\right|^2\left|a_1^L(\varepsilon-eV)\right|^2\left|a_2^R(\varepsilon-2eV)\right|^2 \\
&\qquad \left|a_3^L(\varepsilon-3eV)\right|^2 ...]\frac{1}{e^{\varepsilon/k_BT}+1}\Bigg] \\
&=\frac{e}{2\pi\hbar}\Bigg\{\int_{-\infty-eV}^{\infty} d\varepsilon\Bigg[\left|J^L(\varepsilon)\right|^2+\left|J^L(\varepsilon)\right|^2\left|a_1^R(\varepsilon+eV)\right|^2+\left|J^L(\varepsilon)\right|^2\left|a_1^R(\varepsilon+eV)\right|^2 \\
&\qquad \left|a_2^L(\varepsilon+2eV)\right|^2+\left|J^L(\varepsilon)\right|^2\left|a_1^R(\varepsilon+eV)\right|^2\left|a_2^L(\varepsilon+2eV)\right|^2 \\
&\qquad \left|a_3^R(\varepsilon+3eV)\right|^2 ...\Bigg]\frac{1}{e^{\varepsilon/k_BT}+1} \\
&-\int_{-\infty-eV}^{\infty} d\varepsilon\Bigg[\left|J^R(-\varepsilon)\right|^2+\left|J^R(-\varepsilon)\right|^2\left|a_1^L(-\varepsilon-eV)\right|^2+\left|J^R(-\varepsilon)\right|^2 \\
&\qquad \left|a_1^L(-\varepsilon-eV)\right|^2\left|a_2^R(-\varepsilon-2eV)\right|^2+\left|J^R(-\varepsilon)\right|^2\left|a_1^L(-\varepsilon-eV)\right|^2 \\
&\qquad \left|a_2^R(-\varepsilon-2eV)\right|^2\left|a_3^L(-\varepsilon-3eV)\right|^2 ...\Bigg]\frac{1}{e^{-\varepsilon/k_BT}+1}\Bigg\}
\end{aligned}
\tag{7.60}
$$

Note that when the gap of the left and right electrodes are the same, the term in square brackets in each integral is the same and the two integrals can be combined such that the two Fermi functions produce an overall leading factor of $\frac{1}{e^{\varepsilon/k_BT}+1}-$

$\frac{1}{e^{-\varepsilon/k_BT}+1} = -\tanh\left(\frac{\varepsilon}{2k_BT}\right)$. This yields an equation for the current that has the same overall form as Eq. (4) in Averin's multi channel paper [127].

Unfortunately, when the electrodes have different gaps, a quasiparticle will have different reflection amplitudes at the left and right S/N interfaces. In this case I realized that it was necessary to explicitly consider the hole-like quasiparticle current incident from the left and right, as well as the electron-like quasiparticle incident from the left and right, a total of four separate processes.

Let's now consider the situation when a hole-like quasiparticle is incident from left superconducting electrode onto the right S/N interface and voltage V is applied to the right electrode. Figure 7.5 illustrates this situation for a hole-like quasiparticle incident above the Fermi energy with energy ε. In contrast to the case of an electron, the Fermi level for the holes on the right electrode is shifted upwards; *i.e.* the hole loses kinetic energy as it moves from left to right across the normal region. Considering the $D = 1$ case, A_n can then be written as:

$$A_{-3} = A_{-2} = A_{-1} = A_0 = 0 \tag{7.61}$$

$$A_{1h}(\varepsilon, -V) = J^L(\varepsilon)a_1^R(\varepsilon - eV) \tag{7.62}$$

$$A_{2h}(\varepsilon, -V) = J^L(\varepsilon)a_1^R(\varepsilon - eV)a_2^L(\varepsilon - 2eV)a_3^R(\varepsilon - 3eV) \tag{7.63}$$

$$A_{3h}(\varepsilon, -V) = J^L(\varepsilon)a_1^R(\varepsilon - eV)a_2^L(\varepsilon - 2eV)a_3^R(\varepsilon - 3eV)a_4^L(\varepsilon - 4eV)a_5^R(\varepsilon - 5eV) \tag{7.64}$$

The wavefunction produced when a hole-like quasiparticle is incident from the left can then be written as

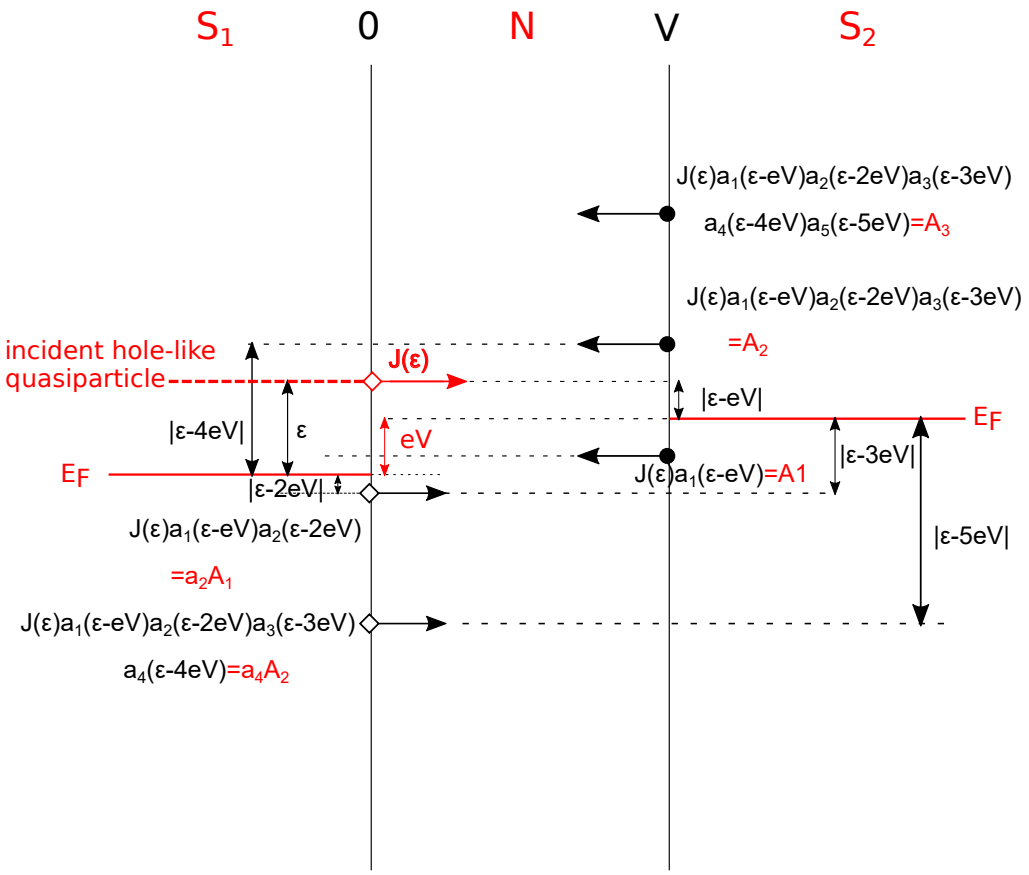

Figure 7.5: Illustration of multiple Andreev reflection for transparency $D = 1$ for a hole-like quasiparticle incident from the left with energy ε and voltage V applied to the right electrode while the left electrode is grounded. The hole experiences repulsive force from the right electrode and decreases its kinetic energy. This effectively shifts the Fermi energy of the holes on the right electrode up by eV.

$$\psi_h = \sum_n [(a_{2n}A_n + J\delta_{n0})e^{-ikx}]e^{-i(\varepsilon-2neV)t/\hbar} \tag{7.65}$$

$$\psi_{el} = \sum_n [A_n e^{-ikx}]e^{-i(\varepsilon-2neV)t/\hbar} \tag{7.66}$$

The electrical current that is then produced by an incoming hole from the left, can then be written as:

$$\begin{aligned} I_{Lh}(\varepsilon,t) = -\frac{e}{2\pi\hbar}\int d\varepsilon \Big(& [|J|^2 + |A_1|^2(1+|a_2|^2) + |A_2|^2(1+|a_4|^2) + |A_3|^2(1+|a_6|^2) \\ & + ...] + [Ja_2^*A_1^* + A_1A_2^*(1+a_2a_4^*) + A_2A_3^*(1+a_4a_6^*) + ...]e^{-i2eVt/\hbar} \\ & + [Ja_4^*A_2^* + A_1A_3^*(1+a_2a_6^*) + A_2A_4^*(1+a_4a_8^*) + ...]e^{-i4eVt/\hbar} + [..]e^{-i6eVt/\hbar} \\ & + ... + [J^*a_2A_1 + A_2A_1^*(1+a_4a_2^*) + A_3A_2^*(1+a_6a_4^*) + ...]e^{i2eVt/\hbar} \\ & + [J^*a_4A_2 + A_3A_1^*(1+a_6a_2^*) + A_4A_2^*(1+a_8a_4^*) + ...]e^{i4eVt/\hbar} + [...]e^{i6eVt/\hbar} \\ & + ... \Big) \times \frac{1}{e^{\varepsilon/k_BT}+1} \end{aligned} \tag{7.67}$$

I also need to consider the situation when there is a hole-like quasiparticle incident from the right with energy $\varepsilon - eV$ and voltage V is applied to the right. As shown in Fig. 7.6, this time the hole increases its kinetic energy each time it travels from the right to the left. I can then write for this process:

$$A_{-3} = A_{-2} = A_{-1} = A_0 = 0 \tag{7.68}$$

$$A_{1h}(\varepsilon - eV, V) = J^R(\varepsilon - eV)a_1^L(\varepsilon) \tag{7.69}$$

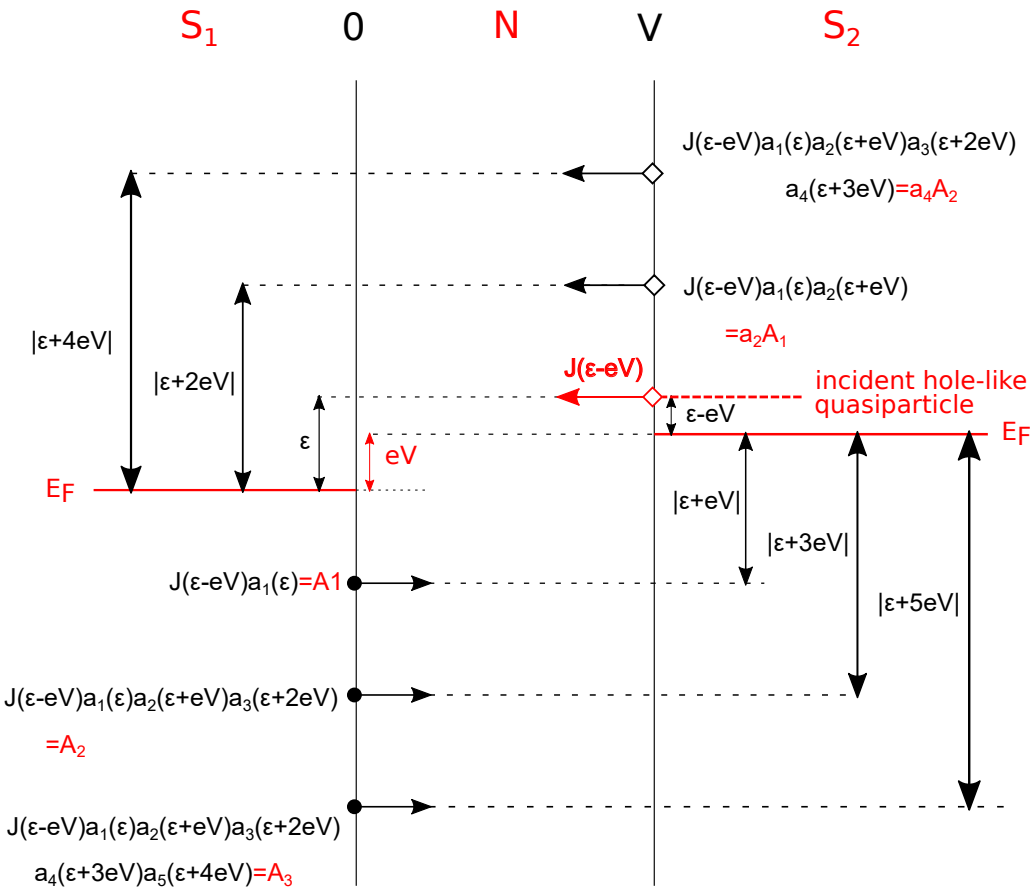

Figure 7.6: Illustration of multiple Andreev reflection for a hole-like quasiparticle incident with energy $\varepsilon - eV$ from the right electrode, which has voltage V applied. The hole increases its kinetic energy when it moves from right to left.

$$A_{2h}(\varepsilon - eV, V) = J^R(\varepsilon - eV)a_1^L(\varepsilon)a_2^R(\varepsilon + eV)a_3^L(\varepsilon + 2eV) \tag{7.70}$$

$$A_{3h}(\varepsilon - eV, V) = J^R(\varepsilon - eV)a_1^L(\varepsilon)a_2^R(\varepsilon + eV)a_3^L(\varepsilon + 2eV)a_4^R(\varepsilon + 3eV)a_5^L(\varepsilon + 4eV) \tag{7.71}$$

The resulting wavefunction for the case of a hole incident from the right electrode, then can be written as:

$$\psi_h = \sum_n [(a_{2n}A_n + J\delta_{n0})e^{ikx}]e^{-i(\varepsilon+2neV)t/\hbar} \tag{7.72}$$

$$\psi_{el} = \sum_n [A_n e^{ikx}]e^{-i(\varepsilon+2neV)t/\hbar} \tag{7.73}$$

The electrical current produced by the hole incident from the right side is then:

$$\begin{aligned} I_{Rh}(\varepsilon, t) = \frac{e}{2\pi\hbar}\int d\varepsilon \Big(& [|J|^2 + |A_1|^2(1 + |a_2|^2) + |A_2|^2(1 + |a_4|^2) + |A_3|^2(1 + |a_6|^2) \\ & + ...] + [Ja_2^*A_1^* + A_1A_2^*(1 + a_2a_4^*) + A_2A_3^*(1 + a_4a_6^*) + ...]e^{i2eVt/\hbar} \\ & + [Ja_4^*A_2^* + A_1A_3^*(1 + a_2a_6^*) + A_2A_4^*(1 + a_4a_8^*) + ...]e^{i4eVt/\hbar} + [...]e^{i6eVt/\hbar} + ... \\ & + [J^*a_2A_1 + A_2A_1^*(1 + a_4a_2^*) + A_3A_2^*(1 + a_6a_4^*) + ...]e^{-i2eVt/\hbar} \\ & + [J^*a_4A_2 + A_3A_1^*(1 + a_6a_2^*) + A_4A_2^*(1 + a_8a_4^*) + ...]e^{-i4eVt/\hbar} \\ & + [...]e^{-i6eVt/\hbar} + ... \Big) \times \frac{1}{e^{(\varepsilon-\mu_R)/k_BT} + 1} \end{aligned} \tag{7.74}$$

where the chemical potential μ_R of the right electrode is $-eV$.

The total dc current due to hole-like quasiparticles incoming from the left and right can now be expressed as:

$$I_{DCh} = \frac{e}{2\pi\hbar}\Big[- \int_{-\infty}^{\infty} d\varepsilon [\big|J^L(\varepsilon)\big|^2 + \big|J^L(\varepsilon)\big|^2\big|a_1^R(\varepsilon - eV)\big|^2 + \big|J^L(\varepsilon)\big|^2\big|a_1^R(\varepsilon - eV)\big|^2$$

$$
\begin{aligned}
&\left|a_2^L(\varepsilon-2eV)\right|^2+\left|J^L(\varepsilon)\right|^2\left|a_1^R(\varepsilon-eV)\right|^2\left|a_2^L(\varepsilon-2eV)\right|^2\\
&\left|a_3^R(\varepsilon-3eV)\right|^2...]\frac{1}{e^{\varepsilon/k_BT}+1}\\
&+\int_{-\infty}^{\infty}d\varepsilon[\left|J^R(\varepsilon-eV)\right|^2+\left|J^R(\varepsilon-eV)\right|^2\left|a_1^L(\varepsilon)\right|^2+\left|J^R(\varepsilon-eV)\right|^2\left|a_1^L(\varepsilon)\right|^2\\
&\left|a_2^R(\varepsilon+eV)\right|^2+\left|J^R(\varepsilon-eV)\right|^2\left|a_1^L(\varepsilon)\right|^2\left|a_2^R(\varepsilon+eV)\right|^2\\
&\left|a_3^L(\varepsilon+2eV)\right|^2...]\frac{1}{e^{(\varepsilon-eV)/k_BT}+1}\Bigg]\\
&=\frac{e}{2\pi\hbar}\Bigg[-\int_{-\infty}^{\infty}d\varepsilon[\left|J^L(\varepsilon)\right|^2+\left|J^L(\varepsilon)\right|^2\left|a_1^R(\varepsilon-eV)\right|^2+\left|J^L(\varepsilon)\right|^2\left|a_1^R(\varepsilon-eV)\right|^2\\
&\left|a_2^L(\varepsilon-2eV)\right|^2+\left|J^L(\varepsilon)\right|^2\left|a_1^R(\varepsilon-eV)\right|^2\left|a_2^L(\varepsilon-2eV)\right|^2\\
&\left|a_3^R(\varepsilon-3eV)\right|^2...]\frac{1}{e^{\varepsilon/k_BT}+1}\\
&+\int_{-\infty-eV}^{\infty-eV}d\varepsilon[\left|J^R(\varepsilon)\right|^2+\left|J^R(\varepsilon)\right|^2\left|a_1^L(\varepsilon+eV)\right|^2+\left|J^R(\varepsilon)\right|^2\left|a_1^L(\varepsilon+eV)\right|^2\\
&\left|a_2^R(\varepsilon+2eV)\right|^2+\left|J^R(\varepsilon)\right|^2\left|a_1^L(\varepsilon+eV)\right|^2\left|a_2^R(\varepsilon+2eV)\right|^2\\
&\left|a_3^L(\varepsilon+3eV)\right|^2...]\frac{1}{e^{\varepsilon/k_BT}+1}\Bigg]
\end{aligned}
\tag{7.75}
$$

To summarize where we are in the calculation, I now have Eq. (7.59) for the current due to electron-like quasiparticles incident from the left and right. I also have the current due to hole-like quasiparticles incident from the left and right superconductors Eq. (7.75). Adding the electron-like quasiparticle current and the hole-like quasiparticle current, I get the total dc current.

$$
\begin{aligned}
I_{DC}&=I_{DCe}+I_{DCh}\\
&=\frac{e}{2\pi\hbar}\Bigg[\int_{-\infty}^{\infty}d\varepsilon[\left|J^L(\varepsilon)\right|^2+\left|J^L(\varepsilon)\right|^2\left|a_1^R(\varepsilon+eV)\right|^2+\left|J^L(\varepsilon)\right|^2\left|a_1^R(\varepsilon+eV)\right|^2
\end{aligned}
$$

$$\left|a_2^L(\varepsilon+2eV)\right|^2+\left|J^L(\varepsilon)\right|^2\left|a_1^R(\varepsilon+eV)\right|^2\left|a_2^L(\varepsilon+2eV)\right|^2$$

$$\left|a_3^R(\varepsilon+3eV)\right|^2...]\frac{1}{e^{\varepsilon/k_BT}+1}$$

$$-\int_{-\infty+eV}^{\infty+eV}d\varepsilon[\left|J^R(\varepsilon)\right|^2+\left|J^R(\varepsilon)\right|^2\left|a_1^L(\varepsilon-eV)\right|^2+\left|J^R(\varepsilon)\right|^2\left|a_1^L(\varepsilon-eV)\right|^2$$

$$\left|a_2^R(\varepsilon-2eV)\right|^2+\left|J^R(\varepsilon)\right|^2\left|a_1^L(\varepsilon-eV)\right|^2\left|a_2^R(\varepsilon-2eV)\right|^2$$

$$\left|a_3^L(\varepsilon-3eV)\right|^2...]\frac{1}{e^{\varepsilon/k_BT}+1}$$

$$-\int_{-\infty}^{\infty}d\varepsilon[\left|J^L(\varepsilon)\right|^2+\left|J^L(\varepsilon)\right|^2\left|a_1^R(\varepsilon-eV)\right|^2+\left|J^L(\varepsilon)\right|^2\left|a_1^R(\varepsilon-eV)\right|^2$$

$$\left|a_2^L(\varepsilon-2eV)\right|^2+\left|J^L(\varepsilon)\right|^2\left|a_1^R(\varepsilon-eV)\right|^2\left|a_2^L(\varepsilon-2eV)\right|^2$$

$$\left|a_3^R(\varepsilon-3eV)\right|^2...]\frac{1}{e^{\varepsilon/k_BT}+1}$$

$$+\int_{-\infty-eV}^{\infty-eV}d\varepsilon[\left|J^R(\varepsilon)\right|^2+\left|J^R(\varepsilon)\right|^2\left|a_1^L(\varepsilon+eV)\right|^2+\left|J^R(\varepsilon)\right|^2\left|a_1^L(\varepsilon+eV)\right|^2$$

$$\left|a_2^R(\varepsilon+2eV)\right|^2+\left|J^R(\varepsilon)\right|^2\left|a_1^L(\varepsilon+eV)\right|^2\left|a_2^R(\varepsilon+2eV)\right|^2$$

$$\left|a_3^L(\varepsilon+3eV)\right|^2...]\frac{1}{e^{\varepsilon/k_BT}+1}\Bigg] \tag{7.76}$$

Regrouping terms and changing variables, I find:

$$I_{DC}=\frac{e}{2\pi\hbar}\Bigg[\int_{-\infty}^{\infty}d\varepsilon[\left|J^L(\varepsilon)\right|^2+\left|J^L(\varepsilon)\right|^2\left|a_1^R(\varepsilon+eV)\right|^2+\left|J^L(\varepsilon)\right|^2\left|a_1^R(\varepsilon+eV)\right|^2$$

$$\left|a_2^L(\varepsilon+2eV)\right|^2+\left|J^L(\varepsilon)\right|^2\left|a_1^R(\varepsilon+eV)\right|^2\left|a_2^L(\varepsilon+2eV)\right|^2$$

$$\left|a_3^R(\varepsilon+3eV)\right|^2...]\frac{1}{e^{\varepsilon/k_BT}+1}$$

$$-\int_{-\infty}^{\infty}d\varepsilon[\left|J^L(-\varepsilon)\right|^2+\left|J^L(-\varepsilon)\right|^2\left|a_1^R(-\varepsilon-eV)\right|^2+\left|J^L(-\varepsilon)\right|^2\left|a_1^R(-\varepsilon-eV)\right|^2$$

$$\left|a_2^L(-\varepsilon-2eV)\right|^2+\left|J^L(-\varepsilon)\right|^2\left|a_1^R(-\varepsilon-eV)\right|^2\left|a_2^L(-\varepsilon-2eV)\right|^2$$

$$\left|a_3^R(-\varepsilon-3eV)\right|^2...]\frac{1}{e^{-\varepsilon/k_BT}+1}$$

$$
\begin{aligned}
&- \int_{-\infty+eV}^{\infty+eV} d\varepsilon [\left|J^R(\varepsilon)\right|^2 + \left|J^R(\varepsilon)\right|^2 \left|a_1^L(\varepsilon - eV)\right|^2 + \left|J^R(\varepsilon)\right|^2 \left|a_1^L(\varepsilon - eV)\right|^2 \\
&\qquad \left|a_2^R(\varepsilon - 2eV)\right|^2 + \left|J^R(\varepsilon)\right|^2 \left|a_1^L(\varepsilon - eV)\right|^2 \left|a_2^R(\varepsilon - 2eV)\right|^2 \\
&\qquad \left|a_3^L(\varepsilon - 3eV)\right|^2 ...] \frac{1}{e^{\varepsilon/k_BT} + 1} \\
&+ \int_{-\infty+eV}^{\infty+eV} d\varepsilon [\left|J^R(-\varepsilon)\right|^2 + \left|J^R(-\varepsilon)\right|^2 \left|a_1^L(-\varepsilon + eV)\right|^2 + \left|J^R(-\varepsilon)\right|^2 \\
&\qquad \left|a_1^L(-\varepsilon + eV)\right|^2 \left|a_2^R(-\varepsilon + 2eV)\right|^2 + \left|J^R(-\varepsilon)\right|^2 \left|a_1^L(-\varepsilon + eV)\right|^2 \\
&\qquad \left|a_2^R(-\varepsilon + 2eV)\right|^2 \left|a_3^L(-\varepsilon + 3eV)\right|^2 ...] \frac{1}{e^{-\varepsilon/k_BT} + 1} \Bigg] \qquad (7.77)
\end{aligned}
$$

Additional simplification gives:

$$
\begin{aligned}
I_{DC} = \frac{e}{2\pi\hbar} \Bigg[&\int_{-\infty}^{\infty} d\varepsilon [\left|J^L(\varepsilon)\right|^2 + \left|J^L(\varepsilon)\right|^2 \left|a_1^R(\varepsilon + eV)\right|^2 + \left|J^L(\varepsilon)\right|^2 \left|a_1^R(\varepsilon + eV)\right|^2 \\
&\qquad \left|a_2^L(\varepsilon + 2eV)\right|^2 + \left|J^L(\varepsilon)\right|^2 \left|a_1^R(\varepsilon + eV)\right|^2 \left|a_2^L(\varepsilon + 2eV)\right|^2 \\
&\qquad \left|a_3^R(\varepsilon + 3eV)\right|^2 ...] (\frac{1}{e^{\varepsilon/k_BT} + 1} - \frac{1}{e^{-\varepsilon/k_BT} + 1}) \\
&- \int_{-\infty+eV}^{\infty+eV} d\varepsilon [\left|J^R(\varepsilon)\right|^2 + \left|J^R(\varepsilon)\right|^2 \left|a_1^L(\varepsilon - eV)\right|^2 + \left|J^R(\varepsilon)\right|^2 \left|a_1^L(\varepsilon - eV)\right|^2 \\
&\qquad \left|a_2^R(\varepsilon - 2eV)\right|^2 + \left|J^R(\varepsilon)\right|^2 \left|a_1^L(\varepsilon - eV)\right|^2 \left|a_2^R(\varepsilon - 2eV)\right|^2 \\
&\qquad \left|a_3^L(\varepsilon - 3eV)\right|^2 ...] (\frac{1}{e^{\varepsilon/k_BT} + 1} - \frac{1}{e^{-\varepsilon/k_BT} + 1}) \\
= \frac{e}{2\pi\hbar} \Bigg[&\int_{-\infty}^{\infty} d\varepsilon [\left|J^L(\varepsilon)\right|^2 + \left|J^L(\varepsilon)\right|^2 \left|a_1^R(\varepsilon + eV)\right|^2 + \left|J^L(\varepsilon)\right|^2 \left|a_1^R(\varepsilon + eV)\right|^2 \\
&\qquad \left|a_2^L(\varepsilon + 2eV)\right|^2 + \left|J^L(\varepsilon)\right|^2 \left|a_1^R(\varepsilon + eV)\right|^2 \left|a_2^L(\varepsilon + 2eV)\right|^2 \\
&\qquad \left|a_3^R(\varepsilon + 3eV)\right|^2 ...] (\frac{1}{e^{\varepsilon/k_BT} + 1} - \frac{1}{e^{-\varepsilon/k_BT} + 1}) \\
&- \int_{-\infty}^{\infty} d\varepsilon [\left|J^R(\varepsilon)\right|^2 + \left|J^R(\varepsilon)\right|^2 \left|a_1^L(\varepsilon - eV)\right|^2 + \left|J^R(\varepsilon)\right|^2 \left|a_1^L(\varepsilon - eV)\right|^2 \\
&\qquad \left|a_2^R(\varepsilon - 2eV)\right|^2 + \left|J^R(\varepsilon)\right|^2 \left|a_1^L(\varepsilon - eV)\right|^2 \left|a_2^R(\varepsilon - 2eV)\right|^2
\end{aligned}
$$

$$\left|a_3^L(\varepsilon-3eV)\right|^2...](\frac{1}{e^{\varepsilon/k_BT}+1}-\frac{1}{e^{-\varepsilon/k_BT}+1})$$
$$-\int_{\infty}^{\infty+eV}d\varepsilon\left|J^R(\varepsilon)\right|^2(\frac{1}{e^{\varepsilon/k_BT}+1}-\frac{1}{e^{-\varepsilon/k_BT}+1})$$
$$+\int_{-\infty}^{-\infty+eV}d\varepsilon\left|J^R(\varepsilon)\right|^2(\frac{1}{e^{\varepsilon/k_BT}+1}-\frac{1}{e^{-\varepsilon/k_BT}+1})\Bigg] \tag{7.78}$$

Since $J^R(\varepsilon)=\sqrt{1-\left|a_0^R(\varepsilon)\right|^2}$ and $|a_R|\to 0$ as $\varepsilon\to\infty$, the second to last integral reduces to $-\lim_{L\to\infty}\int_L^{L+eV}d\varepsilon(-\frac{1}{e^{-\varepsilon/k_BT}+1})=eV$. Similarly the last integral also reduces to eV. Therefore the dc current for the case of $D=1$ and different gaps case can be written as:

$$I_{DC}=\frac{e}{2\pi\hbar}\Bigg[2eV-\int_{-\infty}^{\infty}d\varepsilon\tanh\left(\frac{\varepsilon}{2k_BT}\right)[\left|J^L(\varepsilon)\right|^2+\left|J^L(\varepsilon)\right|^2\left|a_1^R(\varepsilon+eV)\right|^2$$
$$+\left|J^L(\varepsilon)\right|^2\left|a_1^R(\varepsilon+eV)\right|^2\left|a_2^L(\varepsilon+2eV)\right|^2+\left|J^L(\varepsilon)\right|^2\left|a_1^R(\varepsilon+eV)\right|^2$$
$$+\left|a_2^L(\varepsilon+2eV)\right|^2\left|a_3^R(\varepsilon+3eV)\right|^2...]$$
$$+\int_{-\infty}^{\infty}d\varepsilon\tanh\left(\frac{\varepsilon}{2k_BT}\right)[\left|J^R(\varepsilon)\right|^2+\left|J^R(\varepsilon)\right|^2\left|a_1^L(\varepsilon-eV)\right|^2+\left|J^R(\varepsilon)\right|^2$$
$$\left|a_1^L(\varepsilon-eV)\right|^2\left|a_2^R(\varepsilon-2eV)\right|^2+\left|J^R(\varepsilon)\right|^2\left|a_1^L(\varepsilon-eV)\right|^2\left|a_2^R(\varepsilon-2eV)\right|^2$$
$$\left|a_3^L(\varepsilon-3eV)\right|^2...]\Bigg] \tag{7.79}$$

To check this expression, if $\Delta_1=\Delta_2$ then Eq. (7.79) becomes

$$I_{DC}=\frac{e}{2\pi\hbar}\Bigg[2eV-\int_{-\infty}^{\infty}d\varepsilon\tanh\left(\frac{\varepsilon}{2k_BT}\right)[|J(\varepsilon)|^2+|J(\varepsilon)|^2|a_1(\varepsilon+eV)|^2+|J(\varepsilon)|^2$$
$$|a_1(\varepsilon+eV)|^2|a_2(\varepsilon+2eV)|^2+|J(\varepsilon)|^2|a_1(\varepsilon+eV)|^2$$
$$|a_2(\varepsilon+2eV)|^2|a_3(\varepsilon+3eV)|^2...]$$

$$
\begin{aligned}
&+\int_{-\infty}^{\infty} d\varepsilon \tanh\left(\frac{\varepsilon}{2k_BT}\right)[|J(\varepsilon)|^2+|J(\varepsilon)|^2|a_1(\varepsilon-eV)|^2+|J(\varepsilon)|^2 \\
&\quad |a_1(\varepsilon-eV)|^2|a_2(\varepsilon-2eV)|^2+|J(\varepsilon)|^2|a_1(\varepsilon-eV)|^2|a_2(\varepsilon-2eV)|^2 \\
&\quad |a_3(\varepsilon-3eV)|^2...]\Bigg] \\
&=\frac{e}{2\pi\hbar}\Bigg[2eV-\int_{-\infty}^{\infty} d\varepsilon \tanh\left(\frac{\varepsilon}{2k_BT}\right)[|J(\varepsilon)|^2|a_1(\varepsilon+eV)|^2+|J(\varepsilon)|^2 \\
&\quad |a_1(\varepsilon+eV)|^2|a_2(\varepsilon+2eV)|^2+|J(\varepsilon)|^2|a_1(\varepsilon+eV)|^2 \\
&\quad |a_2(\varepsilon+2eV)|^2|a_3(\varepsilon+3eV)|^2...] \\
&\quad +\int_{-\infty}^{\infty} d\varepsilon \tanh\left(-\frac{\varepsilon}{2k_BT}\right)[|J(-\varepsilon)|^2|a_1(-\varepsilon-eV)|^2+|J(-\varepsilon)|^2 \\
&\quad |a_1(-\varepsilon-eV)|^2|a_2(-\varepsilon-2eV)|^2+|J(-\varepsilon)|^2|a_1(-\varepsilon-eV)|^2 \\
&\quad |a_2(-\varepsilon-2eV)|^2|a_3(-\varepsilon-3eV)|^2...]\Bigg] \\
&=\frac{e}{2\pi\hbar}\Bigg[2eV-2\int_{-\infty}^{\infty} d\varepsilon \tanh\left(\frac{\varepsilon}{2k_BT}\right)[|J(\varepsilon)|^2|a_1(\varepsilon+eV)|^2+|J(\varepsilon)|^2 \\
&\quad |a_1(\varepsilon+eV)|^2|a_2(\varepsilon+2eV)|^2+|J(\varepsilon)|^2|a_1(\varepsilon+eV)|^2 \\
&\quad +|a_2(\varepsilon+2eV)|^2|a_3(\varepsilon+3eV)|^2...]\Bigg] \\
&=\frac{e}{\pi\hbar}\Bigg[eV-\int_{-\infty}^{\infty} d\varepsilon \tanh\left(\frac{\varepsilon}{2k_BT}\right)[|J(\varepsilon)|^2|a_1(\varepsilon+eV)|^2+|J(\varepsilon)|^2 \\
&\quad |a_1(\varepsilon+eV)|^2|a_2(\varepsilon+2eV)|^2+|J(\varepsilon)|^2|a_1(\varepsilon+eV)|^2 \\
&\quad +|a_2(\varepsilon+2eV)|^2|a_3(\varepsilon+3eV)|^2...]\Bigg]
\end{aligned}
\tag{7.80}
$$

which is the same as Eq. (7.43) for the case $D = 1$ except Eq. (7.80) is twice as large because we included both hole-like quasiparticles incident from the left and right and electron-like quasiparticle incident from the left and right.

I can now generalize to the case of two different gaps and transparency D not

restricted to one. Consider for example the $k = 1$ Fourier component which gives the $e^{i2eVt/\hbar}$ terms. To make the source of each contribution clearer, I use subscripts R and L to label contributions that are from the right (R) and left (L) interfaces or electrodes. Thus I find from:

$$\begin{aligned}
I_{AC} = e^{i2eVt/\hbar}\frac{e}{2\pi\hbar}\int_{-\infty}^{\infty} d\varepsilon[&J_L(\varepsilon)a^*_{2L}(\varepsilon,V)A^*_{1L}(\varepsilon,V) + A_{1L}(\varepsilon,V)A^*_{2L}(\varepsilon,V)\\
&(1+a_{2L}(\varepsilon,V)a^*_{4L}(\varepsilon,V)) + A_{2L}(\varepsilon,V)A^*_{3L}(\varepsilon,V)\\
&(1+a_{4L}(\varepsilon,V)a^*_{6L}(\varepsilon,V)) + ...]\frac{1}{e^{\varepsilon/k_BT}+1}\\
- e^{i2eVt/\hbar}\frac{e}{2\pi\hbar}\int_{-\infty}^{\infty} d\varepsilon[&J^*_R(\varepsilon)a_{2R}(\varepsilon,-V)A_{1R}(\varepsilon,-V) + A^*_{1R}(\varepsilon,-V)A_{2R}(\varepsilon,-V)\\
&(1+a^*_{2R}(\varepsilon,-V)a_{4R}(\varepsilon,-V)) + A^*_{2R}(\varepsilon,-V)A_{3R}(\varepsilon,-V)\\
&(1+a^*_{4R}(\varepsilon,-V)a_{6R}(\varepsilon,-V) + ...]\frac{1}{e^{\varepsilon/k_BT}+1}\\
- e^{i2eVt/\hbar}\frac{e}{2\pi\hbar}\int_{-\infty}^{\infty} d\varepsilon[[&J^*_L(\varepsilon)a_{2L}(\varepsilon,-V)A_{1L}(\varepsilon,-V) + A_{2L}(\varepsilon,-V)A^*_{1L}(\varepsilon,-V)\\
&(1+a_{4L}(\varepsilon,-V)a^*_{2L}(\varepsilon,-V)) + A_{3L}(\varepsilon,-V)A^*_{2L}(\varepsilon,-V)\\
&(1+a_{6L}(\varepsilon,-V)a^*_{4L}(\varepsilon,-V)) + ...]\frac{1}{e^{\varepsilon/k_BT}+1}\\
+ e^{i2eVt/\hbar}\frac{e}{2\pi\hbar}\int_{-\infty}^{\infty} d\varepsilon[&J_R(\varepsilon)a^*_{2R}(\varepsilon,V)A^*_{1R}(\varepsilon,V) + A_{1R}(\varepsilon,V)A^*_{2R}(\varepsilon,V)\\
&(1+a_{2R}(\varepsilon,V)a^*_{4R}(\varepsilon,V)) + A_{2R}(\varepsilon,V)A^*_{3R}(\varepsilon,V)\\
&(1+a_{4R}(\varepsilon,V)a^*_{6R}(\varepsilon,V)) + ...]\frac{1}{e^{\varepsilon/k_BT}+1}
\end{aligned} \tag{7.81}$$

The first term in Eq. (7.81) comes from electron-like quasiparticles that are incident from the left electrode. The second term is due to electron-like quasiparticles that are incident from the right electrode. The third term is due to hole-like quasipar-

ticles that are incident from the left electrode and the last term is due to hole-like quasiparticles that are incident from the right electrode.

Examining the first term and the third term, we will show that they can be combined. Similarly, we will see that the second and the fourth terms can be combined. To see this, I change the integration variable from ε to -ε in the third and the fourth terms, and after some rearranging so that the two L terms are first and the R terms second:

$$\begin{aligned}
I_{AC} = e^{i2eVt/\hbar}\frac{e}{2\pi\hbar}\Bigg[& \int_{-\infty}^{\infty} d\varepsilon [J_L(\varepsilon)a^*_{2L}(\varepsilon,V)A^*_{1L}(\varepsilon,V) + A_{1L}(\varepsilon,V)A^*_{2L}(\varepsilon,V) \\
& (1+a_{2L}(\varepsilon,V)a^*_{4L}(\varepsilon,V)) + A_{2L}(\varepsilon,V)A^*_{3L}(\varepsilon,V) \\
& (1+a_{4L}(\varepsilon,V)a^*_{6L}(\varepsilon,V)) + ...]\frac{1}{e^{\varepsilon/k_BT}+1} \\
- & \int_{-\infty}^{\infty} d\varepsilon [[J^*_L(-\varepsilon)a_{2L}(-\varepsilon,-V)A_{1L}(-\varepsilon,-V) + A_{2L}(-\varepsilon,-V)A^*_{1L}(-\varepsilon,-V) \\
& (1+a_{4L}(-\varepsilon,-V)a^*_{2L}(-\varepsilon,-V)) + A_{3L}(-\varepsilon,-V)A^*_{2L}(-\varepsilon,-V) \\
& (1+a_{6L}(-\varepsilon,-V)a^*_{4L}(-\varepsilon,-V)) + ...]\frac{1}{e^{-\varepsilon/k_BT}+1} \\
- & \int_{-\infty}^{\infty} d\varepsilon [J^*_R(\varepsilon)a_{2R}(\varepsilon,-V)A_{1R}(\varepsilon,-V) + A^*_{1R}(\varepsilon,-V)A_{2R}(\varepsilon,-V) \\
& (1+a^*_{2R}(\varepsilon,-V)a_{4R}(\varepsilon,-V)) + A^*_{2R}(\varepsilon,-V)A_{3R}(\varepsilon,-V) \\
& (1+a^*_{4R}(\varepsilon,-V)a_{6R}(\varepsilon,-V)) + ...]\frac{1}{e^{\varepsilon/k_BT}+1} \\
+ & \int_{-\infty}^{\infty} d\varepsilon [J_R(-\varepsilon)a^*_{2R}(-\varepsilon,V)A^*_{1R}(-\varepsilon,V) + A_{1R}(-\varepsilon,V)A^*_{2R}(-\varepsilon,V) \\
& (1+a_{2R}(-\varepsilon,V)a^*_{4R}(-\varepsilon,V)) + A_{2R}(-\varepsilon,V)A^*_{3R}(-\varepsilon,V) \\
& (1+a_{4R}(-\varepsilon,V)a^*_{6R}(-\varepsilon,V)) + ...]\frac{1}{e^{-\varepsilon/k_BT}+1}\Bigg]
\end{aligned} \tag{7.82}$$

I can now use Eq. (7.39) and Eq. (7.42) to simplify Eq. (7.82) and arrive at

$$\begin{aligned} I_{AC} = e^{i2eVt/\hbar}\frac{e}{2\pi\hbar}\Bigg[& -\int_{-\infty}^{\infty} d\varepsilon [J_L(\varepsilon)a^*_{2L}(\varepsilon,V)A^*_{1L}(\varepsilon,V) + A_{1L}(\varepsilon,V)A^*_{2L}(\varepsilon,V) \\ & (1+a_{2L}(\varepsilon,V)a^*_{4L}(\varepsilon,V)) + A_{2L}(\varepsilon,V)A^*_{3L}(\varepsilon,V) \\ & (1+a_{4L}(\varepsilon,V)a^*_{6L}(\varepsilon,V)) + ...]\tanh\left(\frac{\varepsilon}{2k_BT}\right) \\ & + \int_{-\infty}^{\infty} d\varepsilon [J^*_R(\varepsilon)a_{2R}(\varepsilon,-V)A_{1R}(\varepsilon,-V) + A^*_{1R}(\varepsilon,-V)A_{2R}(\varepsilon,-V) \\ & (1+a^*_{2R}(\varepsilon,-V)a_{4R}(\varepsilon,-V)) + A^*_{2R}(\varepsilon,-V)A_{3R}(\varepsilon,-V) \\ & (1+a^*_{4R}(\varepsilon,-V)a_{6R}(\varepsilon,-V)) + ...]\tanh\left(\frac{\varepsilon}{2k_BT}\right)\Bigg] \end{aligned} \tag{7.83}$$

Finally take all the Fourier components and combine them with the dc term, we get the final current expression for the case of different gaps:

$$I(t) = \sum_k I_k e^{i2keVt/\hbar} \tag{7.84}$$

where the k-th Fourier component is:

$$\begin{aligned} I_k = \frac{e}{2\pi\hbar}\Bigg[& 2eVD\delta_{k0} - \int_{-\infty}^{\infty} d\varepsilon \tanh\left(\frac{\varepsilon}{2k_BT}\right)\Big(J^L(\varepsilon)(a^{*(L)}_{2k}A^{*(L)}_k + a^{(L)}_{-2k}A^{(L)}_{-k}) \\ & + \sum_n (1+a^{(L)}_{2n}a^{*(L)}_{2(n+k)})(A^{(L)}_n A^{*(L)}_{n+k} - B^{(L)}_n B^{*(L)}_{n+k})\Big) \\ & + \int_{-\infty}^{\infty} d\varepsilon \tanh\left(\frac{\varepsilon}{2k_BT}\right)\Big(J^R(\varepsilon)(a^{(R)}_{2k}A^{(R)}_k + a^{*(R)}_{-2k}A^{*(R)}_{-k}) \\ & + \sum_n (1+a^{*(R)}_{2n}a^{(R)}_{2(n+k)})(A^{*(R)}_n A^{(R)}_{n+k} - B^{*(R)}_n B^{(R)}_{n+k})\Bigg]. \end{aligned} \tag{7.85}$$

In this expression $a^{(L)}_{m->odd} = a^{Right}(\varepsilon + meV)$ and $a^{(L)}_{m->even} = a^{Left}(\varepsilon + meV)$.

Note that for a quasiparticle incident from the left, the Andreev reflection amplitude depends on the interface it hits. If it is an odd number subscript, then the Andreev reflection amplitude is for the right superconducting gap (Δ_R). On the contrary, for an even number, the Andreev reflection amplitude is for the left superconducting gap (Δ_L). Similarly for a quasiparticle incident from the right, $a^{(R)}_{m->odd} = a^{Left}(\varepsilon - meV)$ and $a^{(R)}_{m->even} = a^{Right}(\varepsilon - meV)$; the odd indices are for the left superconducting gap (Δ_L) while the even indices use the right superconducting gap (Δ_R). Thus:

$$a^{Left}(\varepsilon) = \frac{1}{\Delta_L} \times \begin{cases} \varepsilon - sgn(\varepsilon)(\varepsilon^2 - \Delta_L^2)^{1/2}, & |\varepsilon| > \Delta_L \\ \varepsilon - i(\Delta_L^2 - \varepsilon^2)^{1/2}, & |\varepsilon| < \Delta_L \end{cases} \tag{7.86}$$

while

$$a^{Right}(\varepsilon) = \frac{1}{\Delta_R} \times \begin{cases} \varepsilon - sgn(\varepsilon)(\varepsilon^2 - \Delta_R^2)^{1/2}, & |\varepsilon| > \Delta_R \\ \varepsilon - i(\Delta_R^2 - \varepsilon^2)^{1/2}, & |\varepsilon| < \Delta_R. \end{cases} \tag{7.87}$$

To calculate the $I - V$ characteristics from Eq. (7.57) for the asymmetrical junction with the MAR effect, one needs to use the definition of $a(\varepsilon)$ from Eq. (7.86) and Eq. (7.87) to plug into the recursion relation Eq. (7.18) and Eq. (7.13) to get $A_n^{(R)}$, $A_n^{(L)}$, $B_n^{(R)}$ and $B_n^{(L)}$. However keep in mind that the two electrodes have different superconducting gap, thus we need to be careful of which Andreev reflection amplitude to use. For example, the recursion relation for an incoming electron incident from the left can be expressed as:

$$A^{(L)}_{n+1} - a^R_{2n+1} a^L_{2n} A^{(L)}_n = \sqrt{R}(a^L_{2n+2} B^{(L)}_{n+1} - a^R_{2n+1} B^{(L)}_n) + J a^R_1 \delta_{n0} \tag{7.88}$$

and

$$D\frac{a^R_{2n+1}a^L_{2n+2}}{1-(a^L_{2n+1})^2}B^{(L)}_{n+1} - \left[D\left(\frac{(a^R_{2n+1})^2}{1-(a^R_{2n+1})^2}+\frac{(a^L_{2n})^2}{1-(a^R_{2n-1})^2}\right)+1-(a^L_{2n})^2\right]B^{(L)}_n$$
$$+D\frac{a^L_{2n}a^R_{2n-1}}{1-a^R_{2n-1}}B^{(L)}_{n-1} = -\sqrt{R}J\delta_{n,0} \quad (7.89)$$

we then obtain $A^{(L)}_n$ and $B^{(L)}_n$ terms. Similarly, I can also get $A^{(R)}_n$ and $B^{(R)}_n$. I plug them into Eq. (7.85) and numerically integrate the equation to get the current. For this calculation, I modified the Fortran code provided from Averin for the symmetrical MAR effect case (see Appendix D).

Figure 7.7 shows an example of the dc $I-V$ characteristics of an asymmetrical S-I-S junction calculated using Eq. (7.85) for different values of D and for $T = 0$. Here I set the ratio of the two superconducting gaps to $\Delta_R/\Delta_L = 2$ so that the sum of the gaps is $\Delta_L + \Delta_R = 1.5\Delta_R$. As expected, the $I-V$ shows a sudden rise at $V = 1.5\Delta_R/e$. For $D = 0.4$, for example, we see clear subgap current steps at $V = \Delta_R/e$ and $V = \Delta_L/e$.

I also used Eq. (7.85) to examine what happens to the I(V) characteristics when the temperature is not at $T = 0$ K. Figure 7.8 shows examples of the dc $I-V$ characteristics calculated using Eq. (7.85) at different temperatures. In this case, I set the transparency parameter to D=0.25 and used a superconducting gap ratio Δ_R/Δ_L=1/0.47. Notice that when the temperature is higher, the current increases in the subgap region. This happens because there are more quasiparticles present to generate MAR. Examining Fig. 7.8, one also sees that the subgap steps become more rounded for higher temperatures.

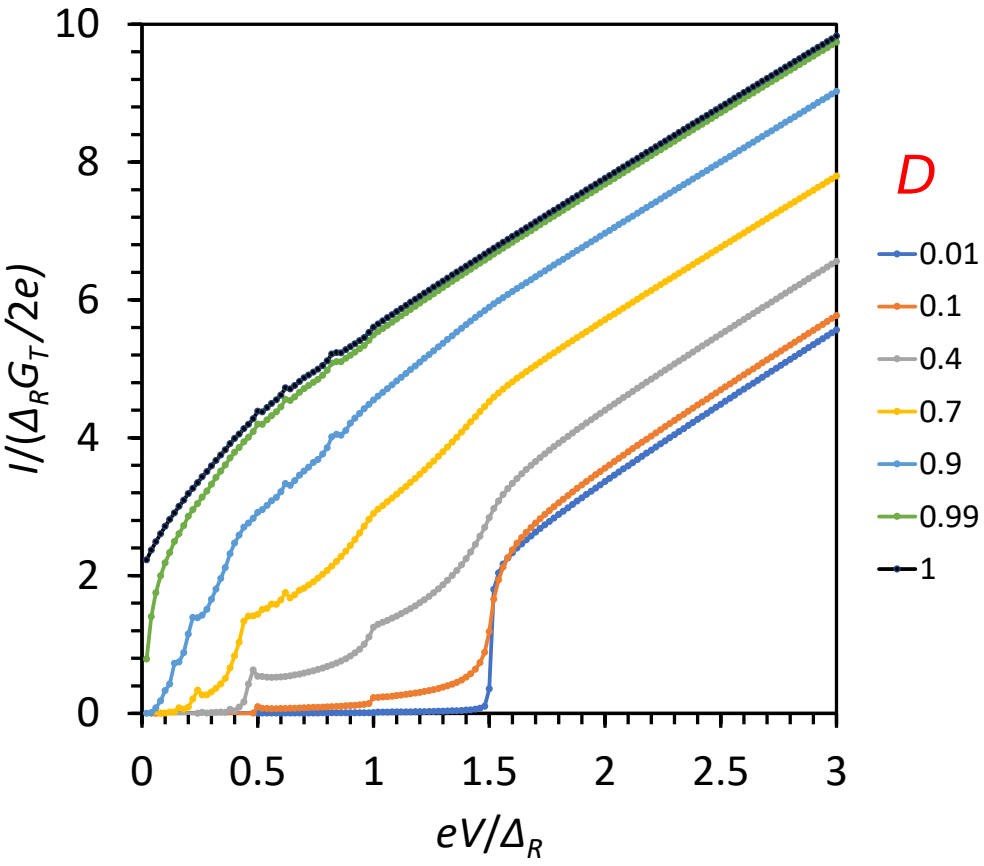

Figure 7.7: Calculated $I-V$ characteristics of an asymmetrical S-I-S junction with MAR at $T=0$. The ratio of the two superconducting gaps is $\Delta_R/\Delta_L=2$ and the different curves correspond to D value of 1, 0.99, 0.9, 0.7, 0.4, 0.1. and 0.01 from top to bottom.

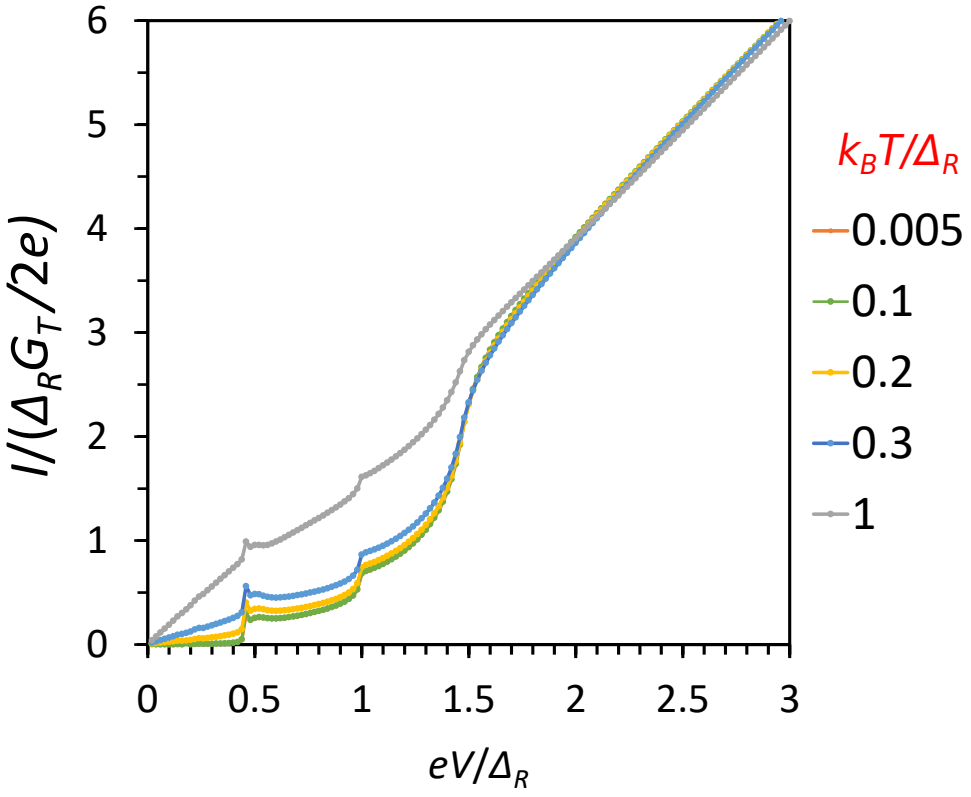

Figure 7.8: Calculated $I-V$ characteristics for transparency $D=0.25$ and $\Delta_R/\Delta_L = 1/0.47$. The different curves correspond to k_BT/Δ_R values of 1, 0.3, 0.2, 0.1 and 0.005 from top to bottom.

Another interesting effect that we can examine by a trivial modification of Eq. (7.85) is what happens to the I(V) curves when the big gap superconductor and the small gap superconductor have different temperatures. Asymmetric junctions have been used as electronic refrigerators [128–130] and thermal transport and heating effects can be important in small junctions. For example, in the superconducting STM, since the STM tip sits on the end of a long thin superconducting wire, it may have more difficulty dissipating heat and reach a higher temperature than a superconducting sample when the junction is biased at a non-zero voltage. I also show in Chapter 5 how local heating effects seamed to be important.

Figure 7.9 shows four $I-V$ characteristics for four different scenarios. For all the curves I set the superconducting gap ratio to Δ_R/Δ_L=1/0.47, the transparency to $D = 0.1$ and $\Delta_R = 1$ meV. The red points are for $T_L = T_R = 0.06$ K. The black points are $T_L = 0.06$ K and $T_R = 2.3$ K. The blue points are for $T_L = T_R = 2.3$ K and green diamonds are for $T_L = 2.3$ K and $T_R = 0.06$ K. Comparing the red and the black curves, we see that the characteristics seem not to be affected. This is not surprising because $\Delta_R \gg k_B T$ and $\Delta_L \gg k_B T$. In contrast, comparing the green curve to red or the black curve in Fig. 7.9, we see the current is somewhat higher in the subgap region for the green curve, causing the $I-V$ characteristic curve to be shifted upwards. This suggests that the characteristics are more sensitive to the temperature of the electrode with a smaller superconducting gap, which is what we would have expected since more quasiparticles will be excited in this case. Finally, comparing the blue and green curves, we see the $I-V$ characteristics are essentially the same, even though the temperature of the high gap side is different. Again, this

is consistent with the characteristics being less sensitive to the temperature of the electrode with the larger superconducting gap. In principle this behavior can be used to determine the temperature of each electrode in the junction.

7.5 The Josephson effect

Electrons in a superconductor form Cooper pairs with charge 2e below the transition temperature T_c. The ground state of a superconductor system can be described by a single macroscopic wave function $\Phi = |\sqrt{N}| \exp(i\phi)$ where the phase ϕ is well defined and N is the number density of pairs. A Josephson junction is formed when two superconducting pieces are separated by a thin insulating layer. Ignoring quasiparticles and assuming that the barrier is sufficiently high so that we can ignore MAR, many of the electrical properties of such a junction can be understood by using simple quantum mechanics [131].

Following a discussion in Feynman's Lecture on Physics, we can write the wavefunction of the pair as

$$\Psi = \sum_{\alpha=1}^{2} C_\alpha \psi_\alpha \tag{7.90}$$

where ψ_1 is non-zero only in superconductor 1 and ψ_2 is non-zero only in superconductor 2. If the two superconductors are uncoupled, then we can write Schrödinger's equation for each superconductor as:

$$i\hbar \frac{\partial \psi_\alpha}{\partial t} = E_\alpha \psi_\alpha \tag{7.91}$$

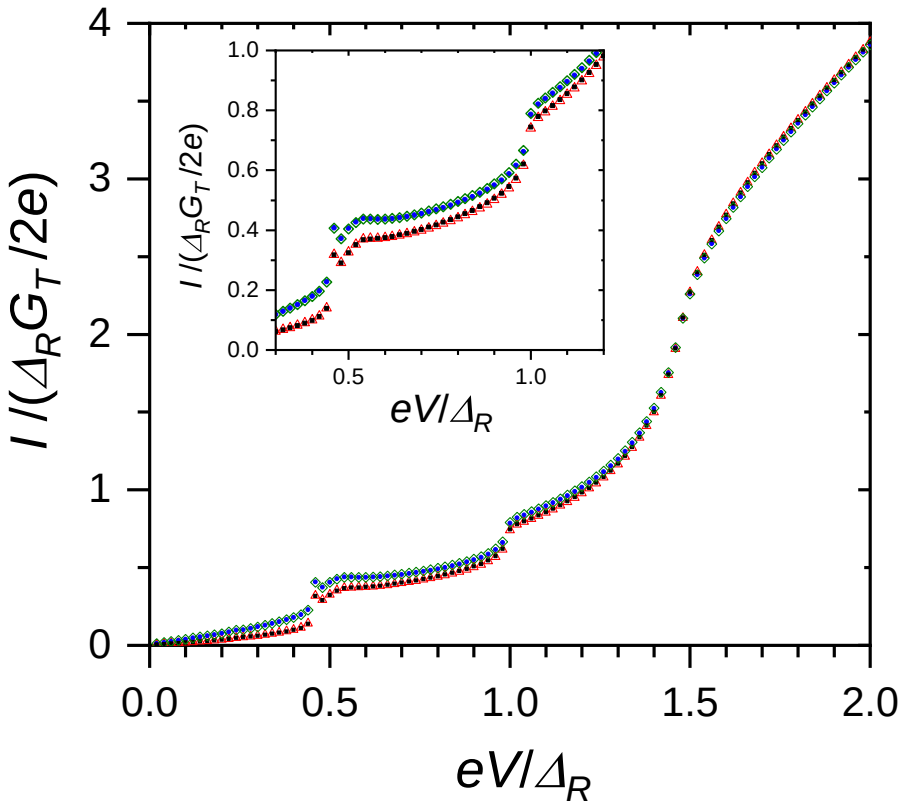

Figure 7.9: Calculated $I-V$ characteristics for different electrode temperatures with transparency D =0.1, $\Delta_R = 1$ meV and $\Delta_L = 0.47$ meV. The open red triangles have $T_L = T_R = 0.06$ K. The solid black squares lie on the red points but have $T_L = 0.06$ K and $T_R = 2.3$ K. The open green diamonds have $T_R = 0.06$ K and $T_L = 2.3$ K. The blue points have $T_L = T_R = 2.3$ K and lie on top of the green diamonds.

Here E_α (for $\alpha = 1, 2$) are the energies of the uncoupled superconductor 1 and 2.

If the superconductors are now joined by a thin insulating region and the insulator thickness is small enough, the wavefunctions from the two superconductors can overlap with each other, and the wavefunction of the coupled superconductors should satisfy the Schrödinger equation

$$i\hbar\frac{\partial\Psi_\alpha}{\partial t} = \hat{H}\Psi_\alpha \tag{7.92}$$

where

$$H = \begin{pmatrix} E_1 + e^*V/2 & -K \\ -K & E_2 - e^*V/2 \end{pmatrix} \tag{7.93}$$

is the total Hamiltonian. The diagonal elements $H_{11} = E_1 + e^*V/2$ and $H_2 = E_2 - e^*V/2$ correspond to the energies of state 1 and 2, where $e^* = -2e$ is the charge of a Cooper pair. The off-diagonal elements $H_{12} = H_{21} = -K$ describe couplings between the two superconductors. Substituting Eq. (7.90) and Eq. (7.93) into Eq. (7.92), we have

$$\begin{cases} i\hbar\dfrac{\partial C_1}{\partial t} = eVC_1(t) - KC_2(t) \\ i\hbar\dfrac{\partial C_2}{\partial t} = -KC_1(t) - eVC_2(t) \end{cases} \tag{7.94}$$

I now let $C_1 = \sqrt{N_1}e^{i\phi_1}$, $C_2 = \sqrt{N_2}e^{i\phi_2}$ where N_1 and N_2 are the number density of Cooper pairs in superconductor 1 and 2. Separating the real and imaginary parts, we find equations for the N_1 part,

$$\hbar \frac{dN_1}{dt} = -2K\sqrt{N_1 N_2}\sin(\phi_2 - \phi_1) \tag{7.95}$$

or:

$$\hbar N_1 \frac{d\phi_1}{dt} = -eVN_1 + K\sqrt{N_1 N_2}\cos(\phi_2 - \phi_1). \tag{7.96}$$

Similarly we have for the N_2 part,

$$\hbar \frac{dN_2}{dt} = 2K\sqrt{N_1 N_2}\sin(\phi_2 - \phi_1) \tag{7.97}$$

or:

$$\hbar N_2 \frac{d\phi_2}{dt} = eVN_2 + K\sqrt{N_1 N_2}\cos(\phi_2 - \phi_1) \tag{7.98}$$

Adding Eq. (7.95) and Eq. (7.97) we find $d(N_1 + N_2)/dt$=0 and $N_1 + N_2$ must be constant, as required by charge conservation. If we multiply Eq. (7.95) and Eq. (7.97) by the charge $-2e$, I find

$$-2e\frac{dN_1}{dt} = 4e\frac{K}{\hbar}\sqrt{N_1 N_2}\sin(\phi_2 - \phi_1) \tag{7.99}$$

$$2e\frac{dN_2}{dt} = 4e\frac{K}{\hbar}\sqrt{N_1 N_2}\sin(\phi_2 - \phi_1) \tag{7.100}$$

Examining Eq. (7.99) and Eq. (7.100) we see that they have the same form as the dc Josephson equation [30, 31],

$$I_s = I_c \sin\phi \tag{7.101}$$

where $\phi = \phi_1 - \phi_2$ is the phase difference between the two electrodes, $I_s = dQ/dt =$

$2e(dN_2/dt) = -2e(dN_1/dt)$ is the supercurrent that flows between the two superconductors and the critical current of the junction $I_c = 4eK\sqrt{N_1 N_2}/\hbar$.

Next consider Eq. (7.96) and Eq. (7.98). Since the individual phases should play no physical role, we can set $\phi_2 = \phi/2$. $\phi_1 = -\phi/2$. Equation (7.96) and Eq. (7.98) becomes,

$$\begin{cases} \hbar N_1 \dfrac{d\phi}{dt} = eVN_1 - K\sqrt{N_1 N_2}\cos(\phi_2 - \phi_1) \\ \hbar N_2 \dfrac{d\phi}{dt} = eVN_2 + K\sqrt{N_1 N_2}\cos(\phi_2 - \phi_1). \end{cases} \tag{7.102}$$

Adding these two equations, we get the ac Josephson equation [30, 31],

$$\frac{\hbar(N_1 + N_2)}{2}\frac{d\phi}{dt} = eV(N_1 + N_2), \tag{7.103}$$

which reduces to

$$\frac{d\phi}{dt} = \frac{2eV}{\hbar} \tag{7.104}$$

Thus the voltage drop V across the junction is related to the rate at which the phase difference ϕ changes.

7.6 Critical current in Asymmetrical junctions with MAR

In the previous section, I presented a simple discussion of the critical current of a Josephson junction in the limit of small barrier transparency. However, it is not obvious from that discussion exactly how the critical current is related to the superconducting gap. In the next chapter I discuss my STM setup with a superconducting Nb tip and a superconducting Nb sample, which formed a Josephson tunnel junction. In most cases, the superconducting tip did not show a full gap and thus we need to understand how this affects the critical current.

Van Duzer in "Principles of Superconducting, Devices and Circuits" [132] pointed out that when one electrode has gap Δ_1 and the other gap Δ_2, the quasiparticle current rise I_{ss} at voltage $(\Delta_1+\Delta_2)$/e is given by:

$$I_{ss} = \frac{G_n \pi \sqrt{\Delta_1 \Delta_2}}{2e} \tag{7.105}$$

In the experiment described in the next chapter, I show that Δ_1 and Δ_2 can be extracted from the voltage at which Andreev steps are observed. We also can measure the point where the quasiparticle current rises and the resistance $R_n = 1/G_n$ of the I(V) characteristics for $V \gg (\Delta_1 + \Delta_2)/e$. Thus we can compare the theoretical I_{ss} value to the measured value I_{qp}. Of course these results are not for the junction critical current but are for the quasiparticle current in a low-transparency barrier.

I can also measure the critical current of a junction and compare it to the theoretical prediction of Ambegaokar and Baratoff [133, 134]. In this paper they

used thermodynamic Green's functions to find an expression for the critical current of a junction with arbitrarily low transparency (i.e. MAR effects are not included). They found:

$$I_0 = R_n^{-1}\Delta_1(T)\Delta_2(T)\frac{\pi}{\beta e}\sum_{l=0,\pm1,\pm2...}[(\omega_l^2+\Delta_1^2(T))(\omega_l^2+\Delta_2^2(T))]^{-1/2} \tag{7.106}$$

where $\omega_l{=}\pi(2l+1)/\beta$, $\beta = 1/k_BT$. In the limit $T \to 0$, the sum can be replaced by an integral and they found:

$$I_0 = \frac{1}{e}R_n^{-1}\Delta_1(T)K([1-\Delta_1^2(T)/\Delta_2^2(T)]^{1/2}) \tag{7.107}$$

where Δ_1 is the smaller of the two energy gaps and K is the modified Bessel function [135]. For a symmetrical junction Eq. (7.107) can be analytically simplified to:

$$I_0 = \frac{\pi}{2e}R_n^{-1}\Delta(T)\tanh\big(\frac{1}{2}\beta\Delta(T)\big) \tag{7.108}$$

which agrees with the well-known Ambegaokar-Baratoff formula [133, 134] for the critical current of a Josephson junction.

Of interest here is that the critical current can also be obtained from the MAR theory discussed in the previous parts of this chapter. In particular, Averin's [122] calculation of the ac current terms can be used to extract the critical current of a junction with a single channel at different transparency parameters D, while my analysis of the case of different gaps allows me to obtain I_0 for different gaps at arbitrary transparency. In particular, the critical current is simply related to the

first Fourier component.

Figure 7.10 (a) shows examples of the real part and the imaginary part of the first Fourier component of the current $I_1(t)$=$I_1 e^{2ieVt/\hbar}$ from Eq. (7.85) with $k = 1$. Note Re(I_1)=0 when the transparency $D < 1$. Therefore the only contribution to the critical current is from Im(I_1). Notice in Fig. 7.10 (b), when the voltage V approaches zero, the current approaches a finite value. This "a.c. current at zero volts" is due to the critical current of the junction.

To find an approximate expression for the critical current, we know from Eq. (7.85) with $k = 1$ that we can write:

$$I_1 = |\operatorname{Im}(I_1)| e^{-i\frac{\pi}{2}} e^{\frac{2ieVt}{\hbar}} \tag{7.109}$$

$$I_{-1} = |\operatorname{Im}(I_{-1})| e^{i\frac{\pi}{2}} e^{-\frac{2ieVt}{\hbar}} \tag{7.110}$$

where $|\operatorname{Im}(I_{-1})| = |\operatorname{Im}(I_1)|$. We will assume the critical current can be approximated as the sum of the first Fourier component term (i.e. I_2, I_3...are small) and write:

$$\begin{aligned} I_0 = I_1 + I_{-1} &= |\operatorname{Im}(I_1)|(e^{-i(\frac{\pi}{2}-\frac{2eVt}{\hbar})} + e^{i(\frac{\pi}{2}-\frac{2eVt}{\hbar})}) \\ &= 2|\operatorname{Im}(I_1)| \cos\left(\frac{\pi}{2} - \frac{2eVt}{\hbar}\right) = 2|\operatorname{Im}(I_1)| \sin\left(\frac{2eVt}{\hbar}\right) \end{aligned} \tag{7.111}$$

Equation (7.111) is the same form as expected for the Josephson supercurrent.

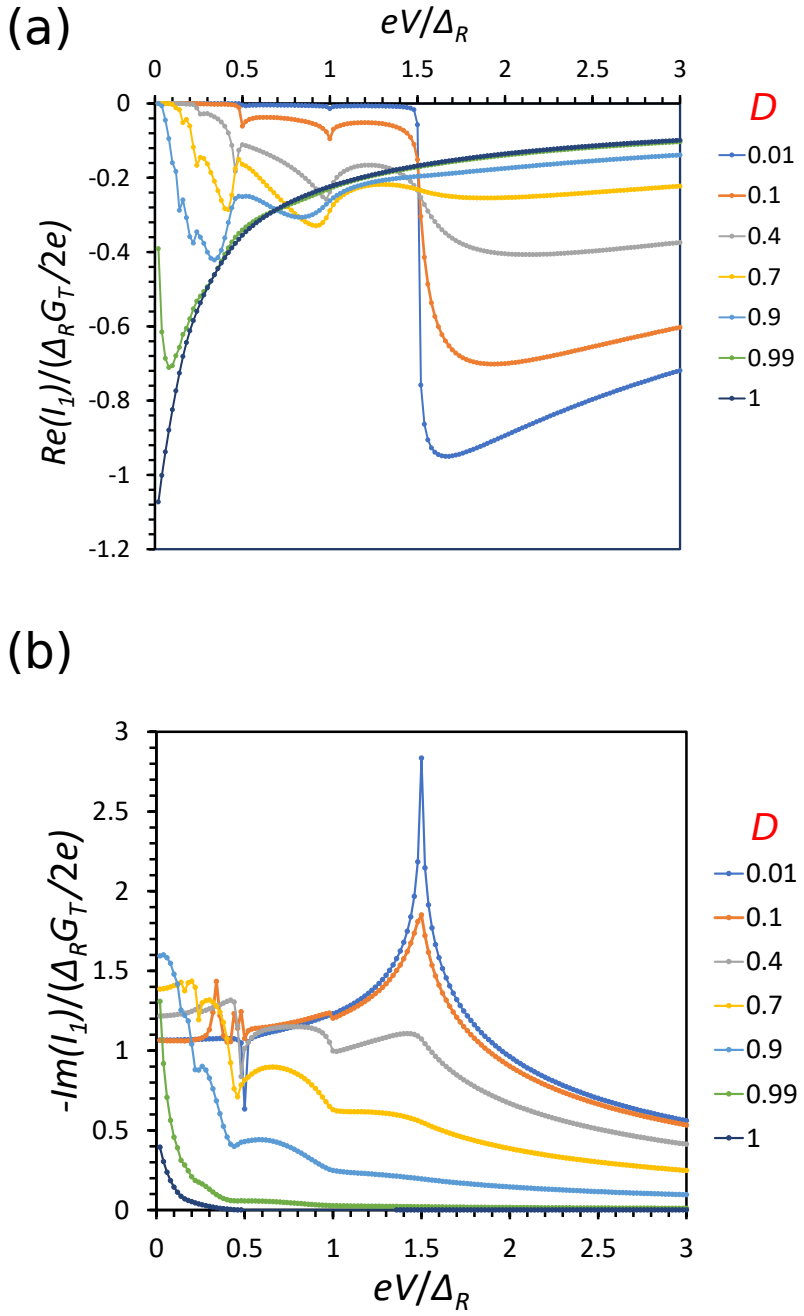

Figure 7.10: (a) Normalized real part and (b) imaginary part of the AC current (first Fourier component) versus normalized voltage for different transparency D and for Δ_R/Δ_L=1/0.5 at T=0.

To see this, note that Eq. (7.101) and Eq. (7.104) can be combined to yield

$$I_s = I_c \sin\left(\frac{2eVt}{\hbar}\right) \tag{7.112}$$

Comparing equations Eq. (7.111) and Eq. (7.112), we find the critical current of the asymmetrical junction is:

$$I_c = 2|\,\mathrm{Im}(I_1)| \tag{7.113}$$

where I_1 can be obtained numerically from Eq. (7.85) for arbitrary D, Δ_1, Δ_2 and T.

As mentioned in Ref. [136], Haberkorn *et al.* obtained results for the critical current for a junction with arbitrary transparency and electrodes with the same gap. In fact, Averin *et al.* note in their paper that they obtained the same form as [136] by using the ac current expression [122]. However the expression Haberkorn *et al.* [136] found was only for a symmetrical junction. Here I have obtained results for the critical current of an arbitrary transparency asymmetrical junction. In practice, Eq. (7.85), Eq. (7.86) and Eq. (7.87) can be evaluated numerically to calculate the value $I_0 = 2|\mathrm{Im}(I_1)|$ in the limit of $V = 0$.

Finally, in Fig. 7.11 I plot the normalized critical current as a function of the temperature T by evaluating Eq. (7.85) for $\Delta_R = 1$ meV, $k = 1$, Δ_R/Δ_L=2 and D=0.5. Note that the critical current reaches a maximum value of about $0.62(2\Delta/eR_n)$ at $T = 0$ and decreases rapidly above about 2 K. For the blue curve,

I assumed that Δ_R and Δ_L are independent of temperature, which is why the plot still shows a critical current at relatively high temperature. For the orange curve I assumed a BCS temperature dependence for the gaps with $\Delta_R(0) = 1$ meV and $\Delta_L(0) = 0.5$ meV. I then used BCS theory to calculate the corresponding gap at specific temperatures and with these gap values, obtained the critical current by evaluating Eq. (7.85). Note that this critical current decreases much more rapidly above 2 K and goes to zero at 3.5 K, when the left electrode goes normal.

7.7 Conclusion

In conclusion, I first discussed Averin and Bardas's derivation of a theoretical model of the I(V) of symmetrical S-I-S junctions with MAR [122]. Once I understood their Eq. (6) for the current [122], I moved on to generalize the theory to the asymmetrical S-I-S junction with MAR. I showed that this generalization essentially yields the same result for the I(V) as in Ref. [126], which used a Green's function approach.

Using the generalized theory, I also obtained an expression for the critical current of an asymmetrical S-I-S junction and its dependence on the transparency D. In Chapter 8, I will show the experimental results from STM of an asymmetrical S-I-S junction with a Nb tip and a Nb sample. Although both the tip and the sample are nominally the same material, the tip does not show a full Nb gap, hence our junction is essentially an asymmetrical junction with different superconducting

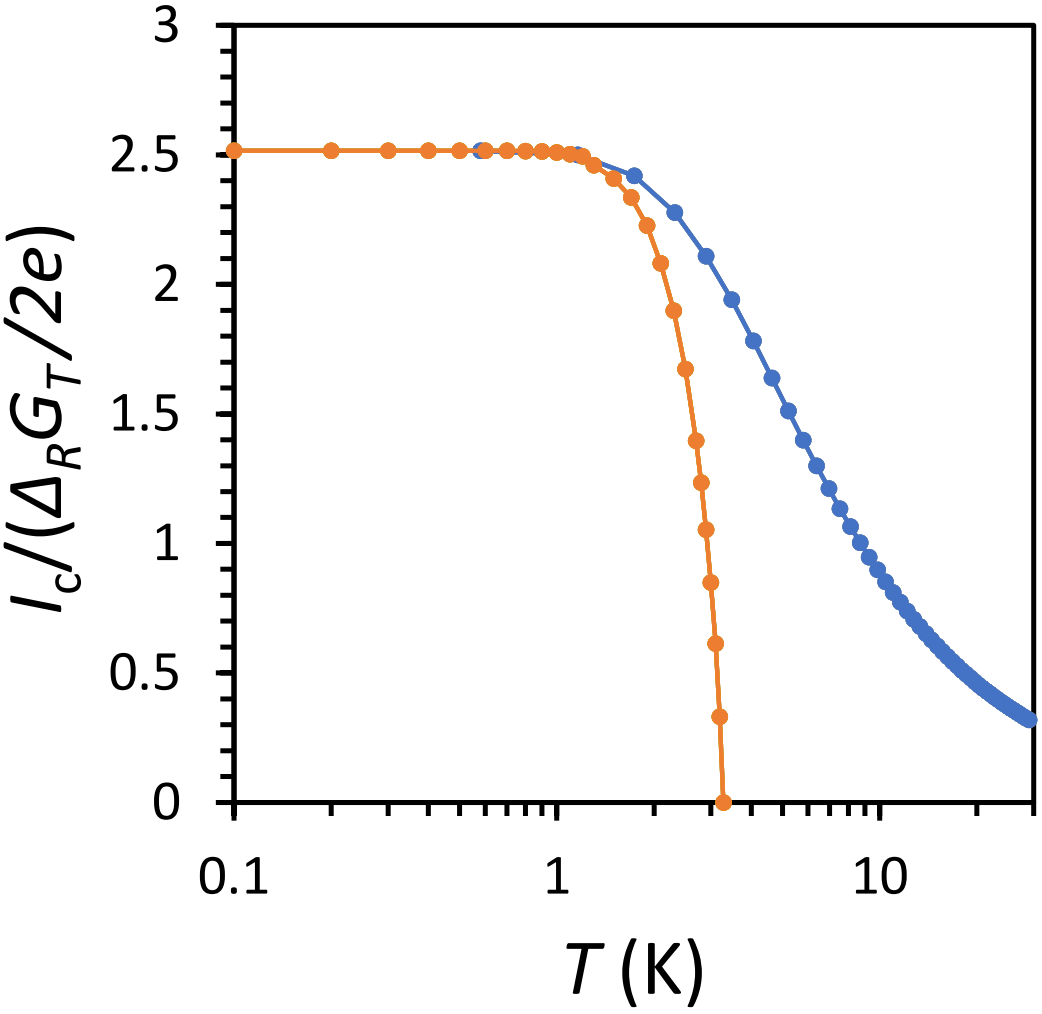

Figure 7.11: Semi-log plot of normalized critical current $I_c/(\Delta_R G_T/2e)$ *vs.* logarithmic scale of temperature T calculated from Eq. (7.85), Eq. (7.86) and Eq. (7.87) for transparency $D = 0.5$. The blue curve uses fixed $\Delta_R = 1$ meV, Δ_R/Δ_L=2 while the orange curve uses temperature dependent gap from BCS theory $\Delta_R(T)$ and $\Delta_L(T)$ with $\Delta_R(0) = 1$ meV and $\Delta_L(0) = 0.5$ meV.

gaps. I also discuss the critical current of our STM formed Josephson junction using the MAR theory of the critical current that I described in Section 7.6. Finally, I note that a critical current is a signature of a phase coherent response of the tunnel junction and it is essential for constructing a SQUID STM.

CHAPTER 8

Ultra-small Josephson Junction Formed Using a Nb STM Tip and Nb Sample

8.1 Introduction

Multiple Andreev Reflection (MAR) effects [137–141] become important when two superconductors are connected through a weak link that has a non-negligible transparency. As I discussed in Chapter 7, MAR causes current to flow at subgap voltage $V = \Delta/ne$, where n is a positive integer. The current-voltage charasteristics for a single superconducting channel with MAR and arbitrary transmission has been calculated theoretically [122–125] and my own analysis for the case of different gaps is presented in Chapter 7. Numerous previous experiments have demonstrated MAR effects in mechanically controllable break-junctions [137, 138, 141, 142] and scanning tunneling microscopy (STM) [71, 139, 140, 143]. However, investigations of MAR effects in Josephson junctions that have electrodes with different superconducting gaps is apparently relatively rare, not only experimentally but also theoretically [71, 126]. Recent interest in Josephson STMs [32, 36, 144–146] has been driven

by the need for better understanding of the physics of small Josephson junctions [147–154] and the behavior of high T_c superconductors.

In this chapter, I describe my use of a scanning tunneling microscope (STM) [20] to look at atomic-scale superconducting tunnel junctions formed between a Nb tip and a Nb sample. In Section 8.2, I discuss the sample preparation and the experimental setup. In Section 8.3, I show the $I-V$ characteristics obtained at 50 mK and 1.5 K for junction tunnel resistance R_n from 10 MΩ to 300 Ω. I analyzed the $I-V$ characteristics by fitting to the MAR theory of Chapter 7. Depending on the temperature T and distance z between the tip and the sample, which determines the tunneling resistance R_n and the junction capacitance C, the junction can be in the phase-diffusion regime [34–36, 38, 71], the underdamped small junction limit [64] or the point contact regime [143, 155]. Next, in Section 8.4 I discuss some important parameters extracted from the fits and some other phenomena, including early switching current and finite resistance on the supercurrent branch. Finally, I conclude in Section 8.5 with a summary and discussion of some implications.

8.2 Sample preparation and experimental setup

Each tip in the millikelvin dual-tip STM [41, 42] (see Fig. 8.1) was made from 250 μm diameter Nb wire etched in an SF_6 reactive ion etcher for about 90 minutes [94]. Each tip was mounted on the STM and was usually cleaned by performing high voltage field emission on an Au(100) or Au(111) single crystal under vacuum

conditions. To perform field emission on a tip, I turn off the z-feedback, pull the tip a few nanometers away from the sample, and then ramp the sample bias to 80-100 V. The current is monitored during the ramp until we see a sudden drop of the current to zero, indicating that the front part of the tip has been ripped of. After cleaning, the quality of the tip is checked by taking $I - V$ spectroscopy on the Au sample to see if the tip is metallic (or superconducting) and by taking images to see if the tip is atomically sharp. Once the quality of the tip is good, I use the sample transfer system to take out the Au sample and put in the sample that I would like to examine next.

I used a 4.5 mm x 4.5 mm x 1 mm Nb (100) single crystal as our sample [156]. The sample was prepared by Ar ion sputtering with a kinetic energy of 2 keV at an Ar pressure of 2.0×10^{-5} mbar for 3-4 hours followed by annealing to 900°C in UHV for 20 minutes. This cycle was repeated two or three times and the sample was then transferred to the STM mounted at the mixing chamber without breaking vacuum [41]. Figure 8.2 shows topographic images taken from the Nb(100) surface at 1.5 K and 50 mK. Atomically flat terraces are clearly visible.

To measure I(V) characteristics I used a relay box to switch from a standard voltage-biased mode to a current-biased mode (See Fig. 8.1). In voltage-biased mode, I acquired topographic images, I(V) and $\mathrm{d}I/\mathrm{d}V - V$ curves. In the current-biased mode, I used either a 1 MΩ, 10 MΩ or 100 MΩ resistor in series with the voltage source to set the current I and then measured the voltage V across the junction using an SR560 voltage amplifier. See Section 2.4 for a detailed description of the current-bias mode.

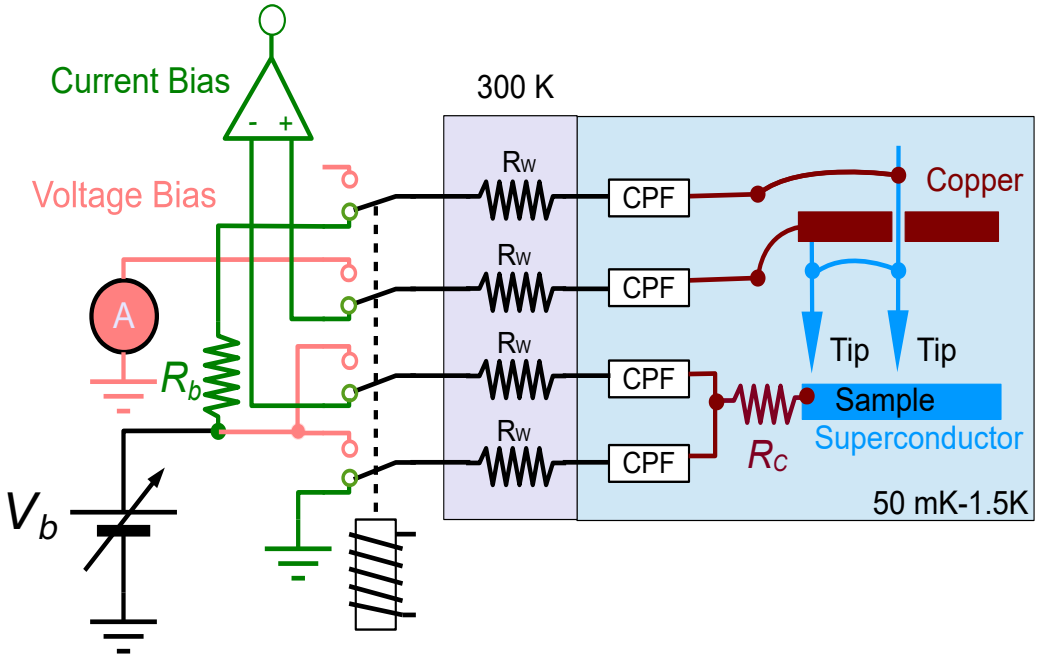

Figure 8.1: Relay box used to switch from STM topographic mode to current bias mode. R_b is set to 1 MΩ, 10 MΩ or 100 MΩ, depending on the tunnel junction resistance. $R_w \approx 220\ \Omega$ is the resistance of each wire and R_c is the contact resistance between the sample mounting stud and the measurement wires.

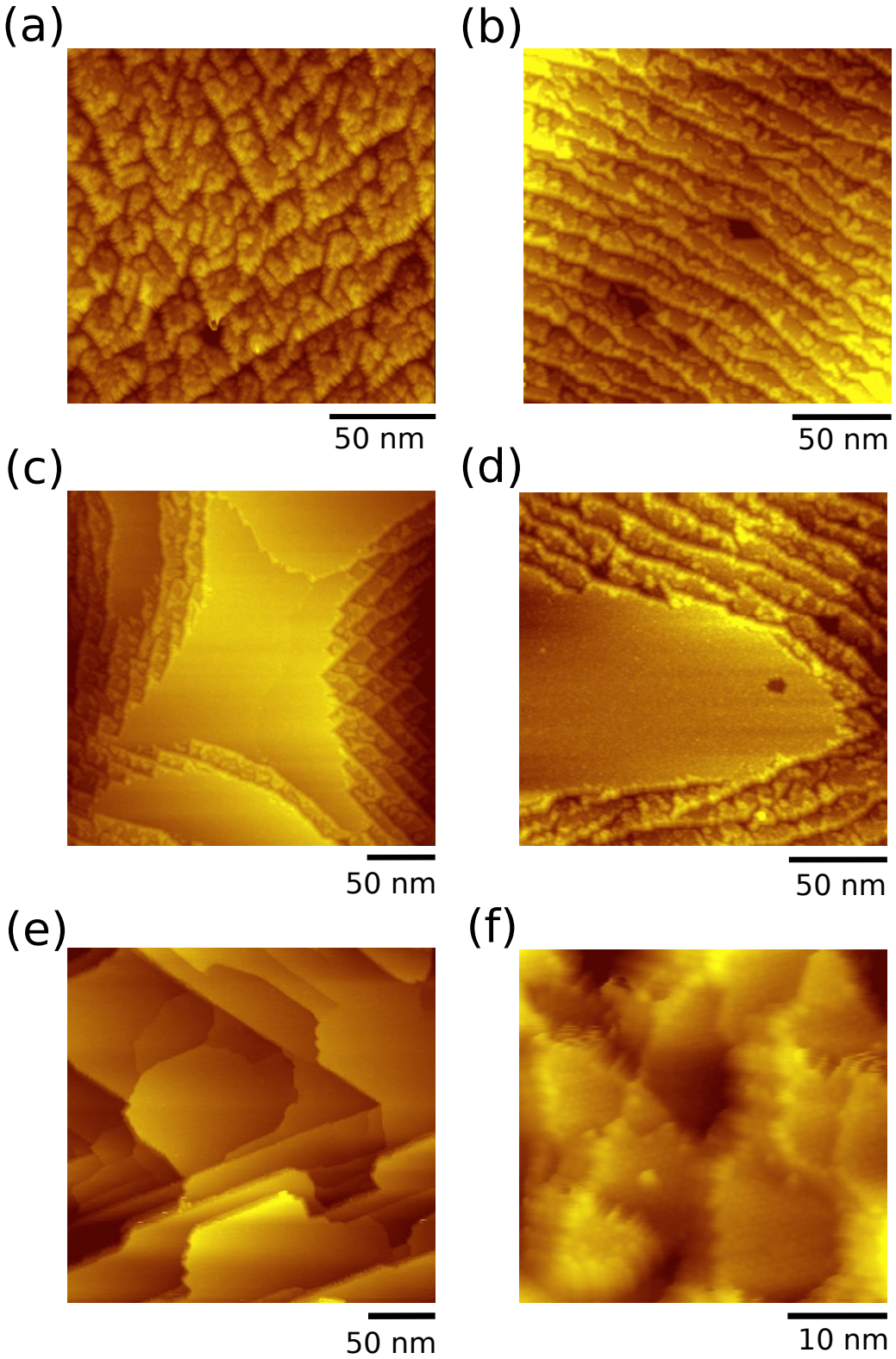

Figure 8.2: Topography of different regions on the Nb crystal surface obtained using the STM at (a)-(d) 1.5 K and (e)-(f) 50 mK.

8.3 $I-V$ characteristics from a Nb tip and a Nb sample

Figure 8.3 shows three $I-V$ characteristics for junction tunnel resistances of R_n =72 kΩ, 7.9 kΩ and 460 Ω. This data was acquired using the current-biased mode at 1.5 K. The blue points are from the backward sweeps (from positive current to negative current) and the black points are from the forward sweeps (from negative current to positive current). Before plotting, the data was processed by subtracting the effect of a contact resistance $R_c \approx 173$ Ω between the sample mounting stud and the measurement wires (see Fig. 8.1).

Examining Fig. 8.3 (a), which shows I(V) when $R_n = 72$ kΩ, we see that the curve looks somewhat like a standard S-I-S tunneling junction with a well defined current rise at voltage $V = (\Delta_{\rm tip} + \Delta_{\rm sample})/e \approx 2.1$ mV. The quasiparticle current rise at $V = 2.1$ mV is $I_{qp} = 23$ nA. The main discrepancies between this I(V) and standard S-I-S tunneling characteristics are the apparent absence of a supercurrent and the significant subgap current steps at about 0.67 mV and 1.4 mV. The current steps are more easily seen in the detailed plot of the sub-gap current shown in Fig. 8.4 (a), which also reveals a supercurrent of about 450 pA. The current steps are what one expects from MAR and the voltages at which they occur provide a direct measure of the gap in the electrodes. Moreover, Fig. 8.3 (b) and (c) show that the steps and supercurrent increase rapidly as the tunnel junction resistance decreases.

The red curves in Fig. 8.3 and Fig. 8.4 show my fits to the MAR theory, with $T = 0$ and the other parameters given in Table 8.1. The theory replicates the clear

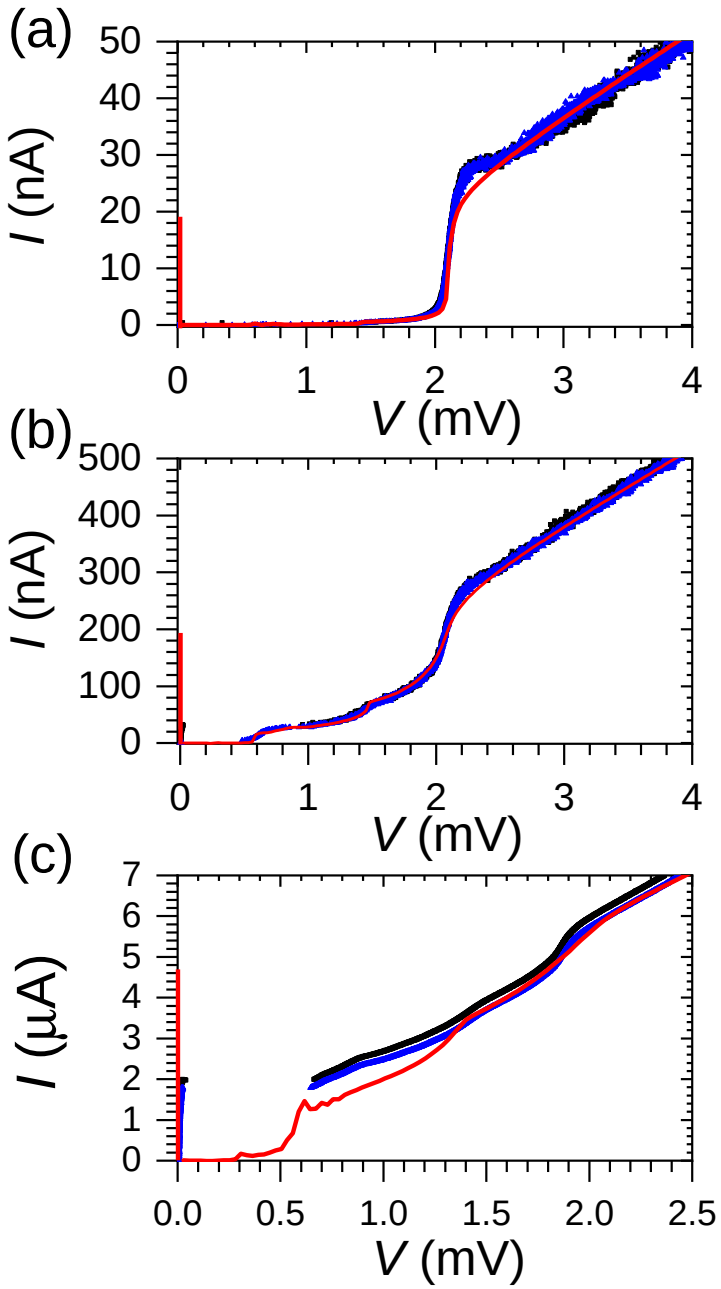

Figure 8.3: $I-V$ characteristics for junction tunneling resistance measured at T =1.5 K of (a) R_n = 72 kΩ, (b) 7.9 kΩ and (c) 0.46 kΩ. In each, the blue curve is a forward sweep, the black curve is a backward sweep, and the red curve is a fit to the asymmetrical MAR theory of Chapter 7. Note the red line at zero voltage is the ideal critical current I_0 predicted from the MAR theory at 1.5 K. See Table 8.1 for fit parameters.

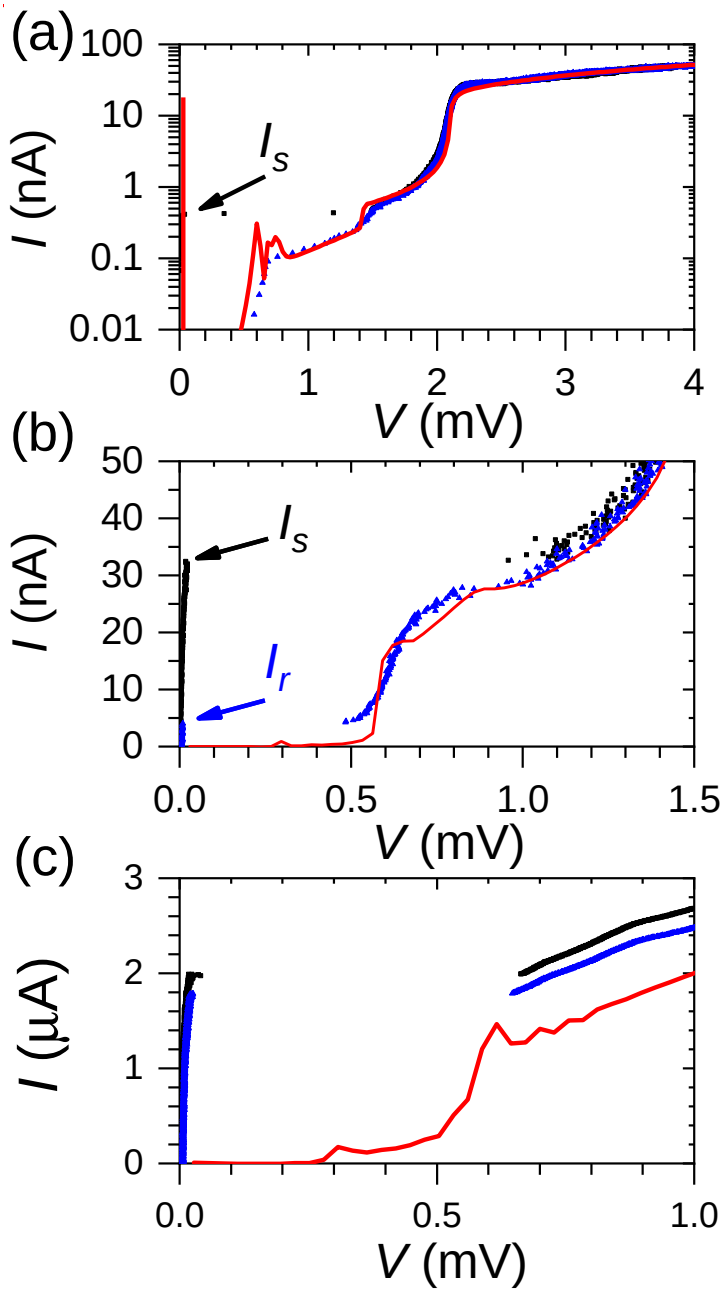

Figure 8.4: (a) Semi-log plot of $I-V$ characteristics from Fig. 8.3 (a). (b) and (c) show detailed view of low voltage section of $I-V$ characteristics from Fig. 8.3 (b) and (c). The ideal critical current is off-scale and not shown.

Table 8.1: Extracted parameters $R_n, \Delta_{\text{tip}}, \Delta_{\text{sample}}, \Delta_{\text{sum}}, D, Z$ from fitting the $I-V$ characteristics in Fig. 8.3 (a)-(c) to the asymmetrical MAR model at $T=0$. Z is the barrier height parameter and D is the transparency parameter.

	R_n (kΩ)	Δ_{sample} (meV)	Δ_{tip} (meV)	Δ_{sum} (meV)	D	Z
Fig. 8.3 (a)	72 kΩ	1.43	0.668	2.098	0.035	4.25
Fig. 8.3 (b)	7.9 kΩ	1.48	0.592	2.072	0.27	1.644
Fig. 8.3 (c)	0.46 kΩ	1.4	0.56	1.96	0.6	0.816

sudden rise at the sum of the superconducting gaps, and the subgap steps. The subgap structure is very sensitive to the transparency value D, with a best fit value of 0.035 for the $R_n = 72$ kΩ curve in Fig. 8.3 (a) and Fig. 8.4 (a). Fitting this curve also gave two gaps with $\Delta_{\text{sample}} = 1.43$ meV and $\Delta_{\text{tip}} = 0.67$ meV.

Figure 8.3 (b) shows the corresponding $I-V$ characteristics for $R_n = 7.9$ kΩ, again with the red curve being the fit to the MAR theory. At $V = \Delta_{\text{sum}}/e \approx 2.1$ mV, the quasiparticle current $I_{qp} \approx 250$ nA. Fitting this curve to the MAR theory with $T = 0$ gives $D = 0.27$. Thus the junction characteristics in Fig. 8.3 (b) correspond to a much more transparent tunnel barrier than that of Fig. 8.3 (a). The subgap currents are also much larger in Fig. 8.3 (b) than Fig. 8.3 (a). Moreover, in Fig. 8.4

(b), the switching current is $I_s \approx 32$ nA, which is about 80 times larger than the switching current in Fig. 8.4 (a), even though R_n differs by less than a factor of 10. Note however that the switching current is not a true super-current because this part of the I(V) curve has a non-zero resistance $R_0 \approx 373\ \Omega$. Fig. 8.4 (b) also shows hysteretic behavior with a retrapping current I_r (the current when switching from a finite voltage state to the zero voltage state) of 4.6 nA.

If we keep lowering the junction resistance, the I(V) curve continues to evolve. Figure 8.3 (c) shows the situation for $R_n = 460\ \Omega$. The characteristics are very rounded and very unlike a traditional S-I-S tunneling characteristic. Note that I_{qp} has increased to nearly 5.1 μA while the switching current has increased to nearly 2 μA. In this regime, unlike the hysteretic behavior in Fig. 8.3 (b), the switching current I_s is nearly equal to the retrapping current I_r. Fitting the MAR theory to this data at $T = 0$, I found $D = 0.6$ and gaps of 0.56 meV and 1.4 meV.

Here is a good place to comment on the identification of the gap of the sample and tip. I typically saw that one of the gaps was close to the value expected for bulk Nb (1.52 meV) while the second gap was typically smaller and varied with the tip cleaning. For this reason, I identified the larger gap as being due to the sample and the smaller gap as being due to the tip. As Table 8.1 shows, Δ_{tip} is significantly smaller at $R_n = 460\ \Omega$ compared its value at $R_n = 72$ kΩ. I also note that the red fit curve in Fig. 8.3 (c) disagrees noticeably with the data below 1.5 mV, but overall the fit does a remarkably good job of fitting the data. One possible explanation is that our single channel MAR theory does not apply to the situation of low junction resistance, and one needs to consider multiple channels with different transparencies

[137–141].

Since we expect a single conductance channel can at most contribute a conductance of $2 \times 2e^2/h \simeq (6.5\ \mathrm{k\Omega})^{-1}$, it is not surprising that the single channel MAR theory may fail for $R_n \leq R_q = 12.9\ \mathrm{k\Omega}$. To better understand this limit I measured how the tunneling current at fixed voltage varied with the distance from the surface. For these measurements, I set the sample voltage at 3 meV, which is above the gap, and adjusted z to set R_n. I then recorded the current I while retracting the tip a distance $\Delta z = 1.5$ nm. Figure 8.5 shows the conductance $G = I/V$, normalized by the quantum conductance $(2e^2/h)$ *vs.* the retraction distance Δz. The different colors represent curves with different starting resistances R_n. This also means that the initial point of each curve has a different distance between the tip and the sample. I note that at $V \gg (\Delta_1 + \Delta_2)/e$, the junction resistance in the STM is set by the bias voltage V and the set current I, with $R_n \approx V/I$. Here I actually set the current, and since $I \propto e^{-\alpha z}$ this requires a smaller tip-sample separation for a lower junction resistance. The curves shown in the plot are not in chronological order.

Examining Fig. 8.5, one sees two orange curves starting at $R_n = 7.5\ \mathrm{k\Omega}$. One curve shows a fairly smooth exponential-like dependence while the other curve just shows some small sudden jumps in conductance. This second orange curve was taken after a scan in which the tip had made contact with the sample surface. Evidently a slight deformation of the tip or sample occurred during the previous scan. The red curves show the behavior when I set the initial resistance to 3 kΩ. Many large random jumps appear as the tip is withdrawn. We can safely conclude that at 3 kΩ, the tip is making physical contact with the sample, causing deformation of the

tip or sample, or causing the transfer of material between the tip and sample. As the tip moves away from the sample, different parts of the tip leave the sample at random times causing this irregular behavior in the I-Δz curve.

As observed in break junctions, the typical variations in conductance are of the order of the quantum conductance [137, 138, 140, 141]. Since the tip makes solid contact with the sample for $R \leq 3.9$ kΩ, and a single channel would have a conductance of 6.5 kΩ (considering quasiparticles with both up and down spin), at least two channels must be contributing. If these channels have different barrier transparency, then my single channel asymmetrical MAR theory will not fit.

Another small but significant discrepancy between the MAR theory and the measured characteristics is visible in Fig. 8.3 (a) and Fig. 8.3 (b) at $V = 2.1$ mV; the theory systematically predicts less current or, we could say, the current rises above the theory at the sum of the gaps.

To illustrate what might be going on, Fig. 8.6 shows the measured $I-V$ characteristics (blue) for a junction resistance of $R_n = 13.5$ kΩ. A detailed view of the subgap region of this curve is shown in Fig. 8.7. One sees a clear hysteretic behavior with a switching current $I_s = 12$ nA and a retrapping current $I_r = 1$ nA. The green, pink, purple and red curves in Fig. 8.6 were calculated using MAR theory for temperatures of 13.3 K, 8.3 K, 5 K and 0 K, respectively. Notice that the 13.3 K curve (green) has more current at all voltages and in particular it follows the data quite nicely for $V > 2.1$ mV. Of course $T < 13.3$ K and the curve does not follow the data for $V < 2.1$ mV. Nevertheless this suggests that the junction may be self-heating to a rather high temperature when biased at voltages above the sum

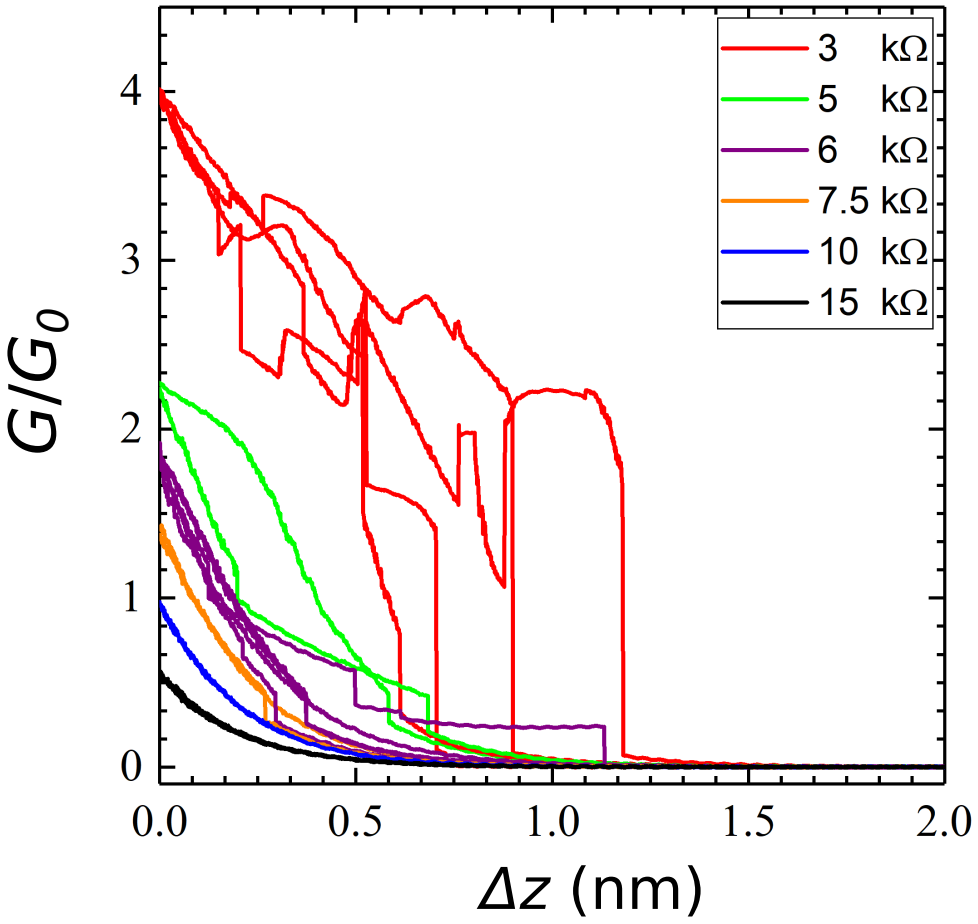

Figure 8.5: Normalized conductance (G/G_0) *vs* distance Δz for different starting normal resistance R_n, where $G_0 = 2e^2/h$ is the conductance quantum and Δz is the distance from the original tip position where we set R_n. All measurements were made at $V = 3$ mV and $T = 1.5$ K. Around $G = G_0$, the curves have occasional sudden jumps, suggesting the tip is forming a point contact with the surface. For $G > 3\ G_0$, the tip probably makes solid contact with the sample and the large variation in conductance is probably due to different parts of the tip leaving the surface at slightly different times.

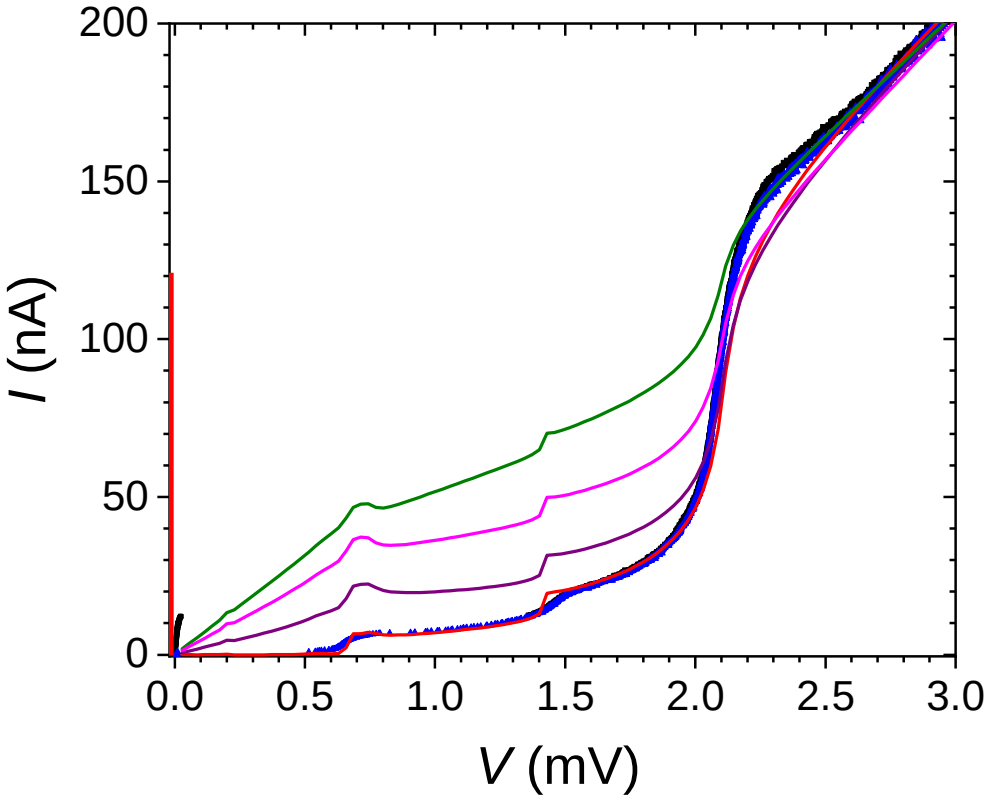

Figure 8.6: Blue and black points show measured $I - V$ characteristics at $T = 1.5$ K for $R_n = 13.5$ kΩ. Green, pink, purple and red curves correspond to calculated MAR theory curves for T =13.3 K, 8.3 K, 5 K, 0 K, respectively. Here I used $\Delta_{\text{sample}} = 1.43$, $\Delta_{\text{tip}} = 0.667$ and $D = 0.15$ for all curves.

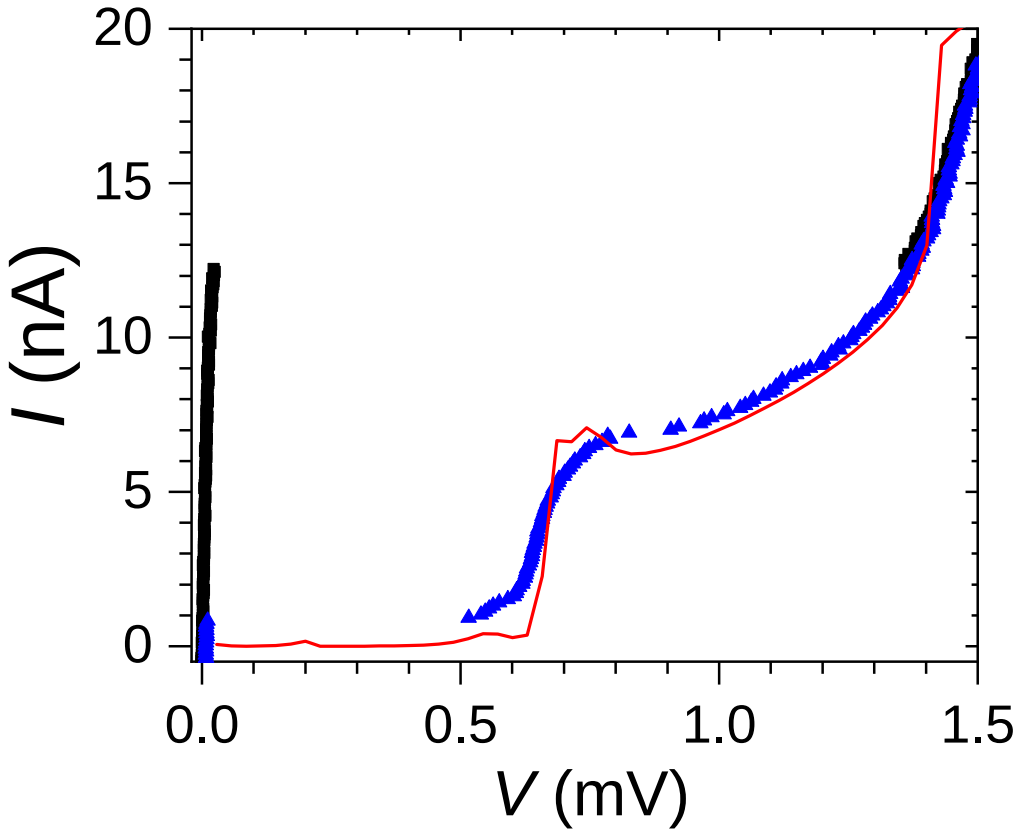

Figure 8.7: Detailed view of subgap current behavior shown in Fig. 8.6. The blue points show the measured forward sweep (large current to small current), the black points show the measured backward sweep and the red curve is a simulation at $T = 0$ K. Note that the zero voltage supercurrent branch has a non-zero resistance. For this simulation $\Delta_{\text{sample}} = 1.43$, $\Delta_{\text{tip}} = 0.667$, $D = 0.15$, $T = 0$ K and $R_n = 13.5$ kΩ.

of the gaps. Note that this heating effect cannot be as significant in the sub-gap region, but of course the dissipated power $I \times V$ is also much less in the subgap region.

Figure 8.8 (a) shows $\Delta_{\text{tip}} + \Delta_{\text{sample}}$ (black squares), Δ_{tip} (red circles), and Δ_{sample} (blue triangles) versus R_n, extracted from fitting the MAR theory to the measured I(V) curves. Note that $\Delta_{\text{tip}} + \Delta_{\text{sample}}$ is constant at about 2.2 mV for $R_n > 10$ kΩ, but for $R_n < 10$ kΩ, it drops steadily. The red dots show $\Delta_{\text{sample}} \approx 1.48$ meV which are nearly constant, this is close to the full superconducting gap of bulk Nb sample (1.5 mV). The blue triangles show the smaller gap value Δ_{tip}, which is only ~ 0.7 meV: since the Nb tip was exposed to air and Nb with O dissolved in it has a lower T_c, it is perhaps not too surprising to see a reduced gap value. A gap of $\Delta_{\text{tip}} = 0.7$ meV; suggests $T_c \sim 4.5$ K, which is consistent with 5 % oxygen in Nb [157]. This is below the solubility limit of 9% [158]. It may also be note that the end of the tip was contaminated in some other way, producing a superconducting gap that is less than the bulk Nb gap.

From Figure 8.8 (a), we see that the gap of the Nb sample Δ_{sample} stays almost constant over the full range of R_n, actually there is a drop of about 0.03 meV at small R_n values, which is barely visible on the plot. In contrast, Δ_{tip} decreases as R_n decreases below 5 kΩ. I note that this decrease is consistent with the decreasing in the sum of the superconducting gaps, which was measured separately from the I(V) characteristics. One possible explanation is that when the junction resistance is below 5 kΩ, the tip starts to make contact with the sample. This applies pressure to the material at the tip, reducing its T_c. In contrast, the sample T_c decreases

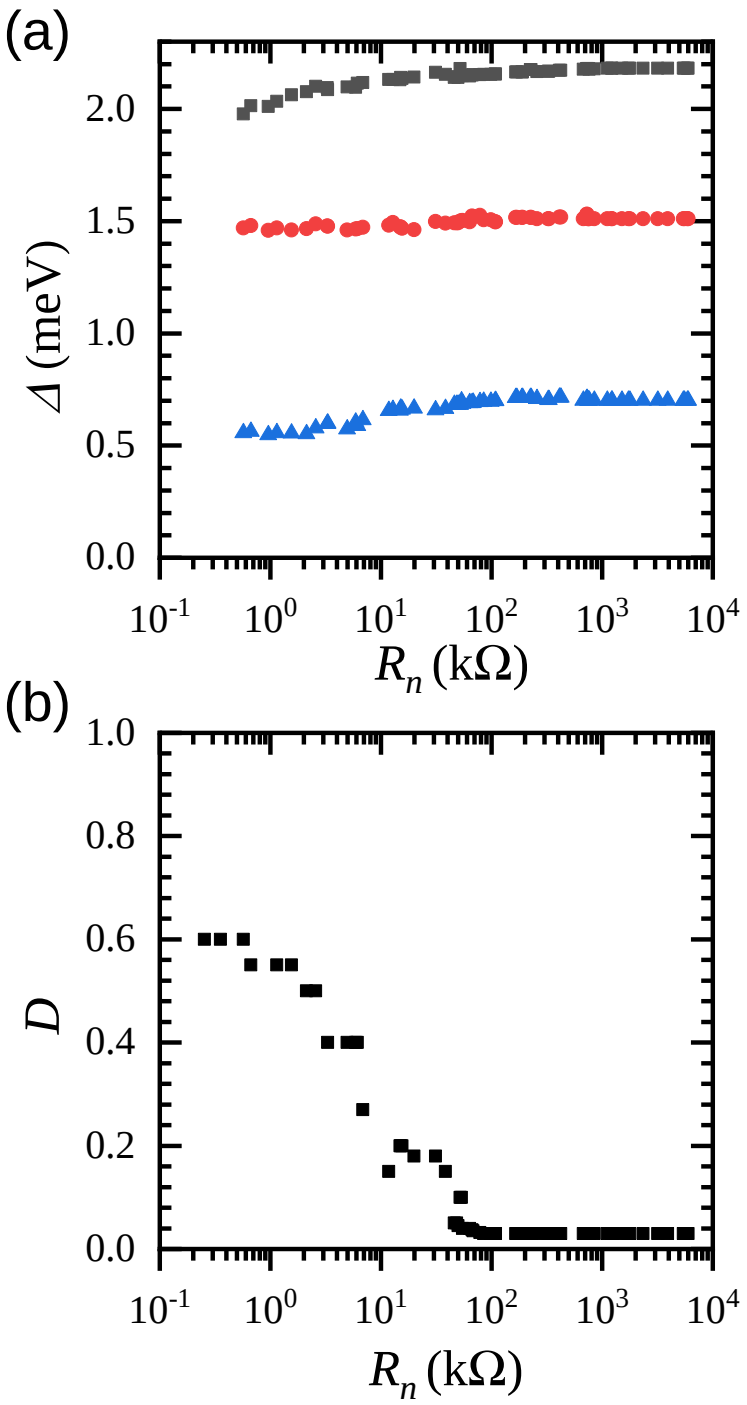

Figure 8.8: (a) Superconducting gap of the Nb sample (red), Nb tip (blue) and the sum of the gaps of the Nb sample and the tip (black) as a function of tunneling resistance R_n of the junction. (b) Transparency parameter D as a function of R_n.

relatively little, perhaps because pure Nb is less sensitive to pressure than oxygen-doped Nb, or perhaps because the spindly tip compresses more than the sample. Another possible explanation is that the large current running through the junction causes heating. The small tip not only has a harder time dissipating heat than the sample, but it has a smaller T_c due to contaminants compared to the sample, leading to a larger decrease in the superconducting gap.

Figure 8.8 (b) shows the corresponding plot of transparency D $vs.$ R_n from fitting the asymmetrical MAR theory to the I(V) data at 1.5 K. As expected, $D \ll 1$ when the junction resistance R_n is high, indicating very low transparency and the junction is in the standard S-I-S tunneling limit [64]. As the tip and sample get closer, R_n decreases and the transparency D becomes larger. Interestingly, D did not reach 1 as $R_n \to 0$ but saturated at around 0.6.

Figure 8.9 shows plots of I_{qp}, I_s and I_r $vs.$ the junction tunneling resistance R_n. I_{qp} is the largest current value around the voltage of the sum of the superconducting gap where it has the sudden rise in current. I_s is the current where it switches out to the finite voltage state from the supercurrent branch, while I_r is the current where the junction is retrapped back to the supercurrent branch from the finite voltage state. The filled points (squares, circles, triangles) were taken at 1.5 K and the open points (squares, circles, triangles) were taken at 50 mK. The cyan stars are the theoretical prediction of the critical current I_0 from the asymmetric MAR theory at 1.5 K and the red hexagons are the theoretical prediction of the quasiparticle current I_{qp} from the asymmetrical MAR theory. The behavior can be divided into three regimes. For 10 kΩ $< R_n >$ 100 kΩ, no hysteresis and no switching current

is observed, consistent with thermal fluctuations destroying phase coherence [34–36, 38, 71]. For $R_n < 100$ kΩ, a small supercurrent branch and a switching current I_s are observed (triangles). In this regime, the switching current I_s is only 1 % to 10 % of the ideal critical current I_0 (cyan stars). The retrapping current I_r (green circles) is relatively large, indicating significant damping in the junction. As R_n decreases, the retrapping current I_r increases much more rapidly than the switching current I_s. For $R_n < 3$ kΩ, where the tip and the sample make contact, $I_r \approx I_s$.

I note that although there was a strong dependence of the junction behavior on R_n, there was very little difference between the data at 1.5 K (filled symbols) and 50 mK (open symbols). Although the thermal energy of the junction at 50 mK was nominally 30 times smaller than at 1.5 K, I_s was not significantly larger at 50 mK, nor was I_r substantially smaller at 50 mK. This suggests that the value of the switching current in our STM junction is not being limited to the thermal energy of the bath. One alternative is macroscopic quantum tunneling [64, 159, 160] of the phase, which becomes important because of the small critical current and small capacitance between the sample and the tip. Another possibility is external noise driving the system to switch into the non-zero voltage state. A third possibility is that with an applied bias current, heating in the leads is creating temperatures well-above the bath temperature. This last two alternatives are unlikely, as principle measurements in our system have shown relatively low noise [40].

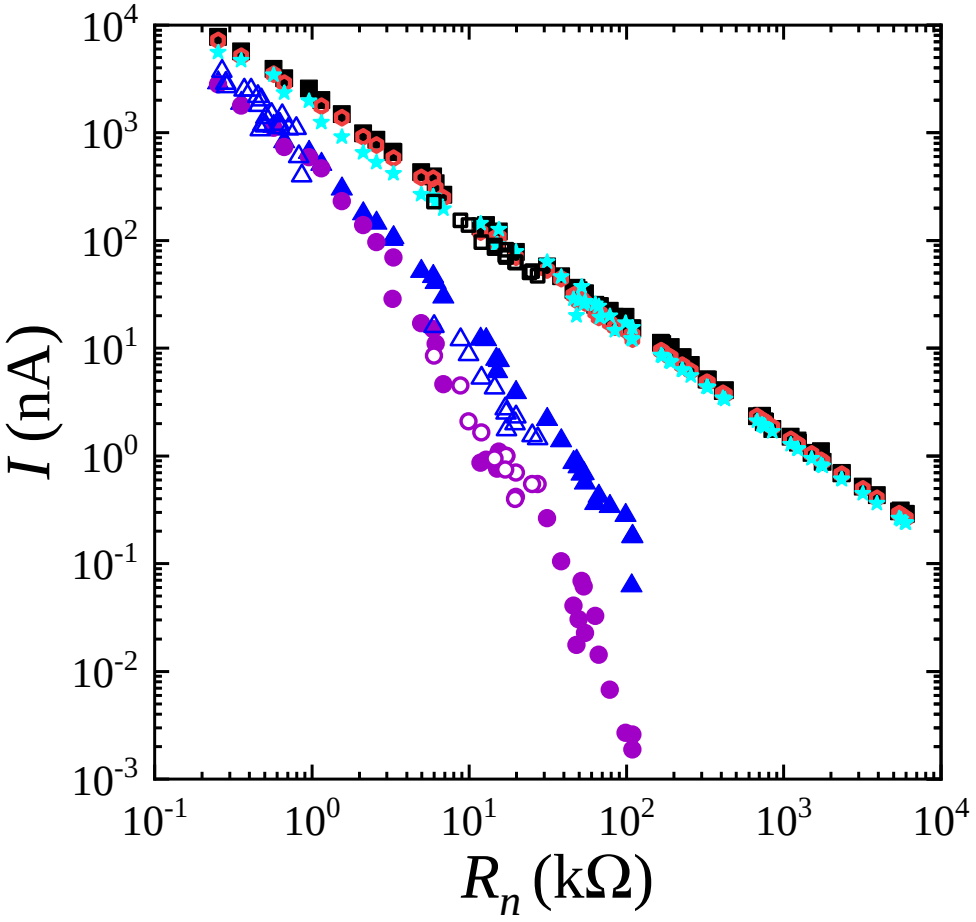

Figure 8.9: Nb-Nb junction parameters including extracted quasiparticle current I_{qp} (black squares), switching current I_s (blue triangles), and retrapping current I_r (purple circles) plotted *vs.* R_n. The filled symbols were taken at 1.5 K whereas the open points were taken at 50 mK. The cyan stars are the critical current values obtained by fitting the I(V) data to the asymmetric MAR theory of Chapter 7 at 1.5 K. Red hexagons are the quasiparticle current values obtained by fitting to the asymmetric MAR theory at 1.5 K. Above 0.1 MΩ, there was no observed supercurrent branch and therefore I_s and I_r were zero. Below 3 kΩ, the STM tip makes contact with the sample and hysteretic behavior disappeared. For R_n between 0.1 MΩ and 3 kΩ, the junction showed hysteretic behavior.

8.4 Dissipation analysis from the retrapping current

So far, I have shown that I could obtain reasonable fitting of the MAR $I-V$ characteristics to my data. However, my observation of a relatively and large retrapping current indicate that the junction is subject to significant dissipation. In this section, I compare my results to the standard RCSJ model [64] to extract some additional important junction parameters.

In the RCSJ model, the Stewart-McCumber [161, 162] hysteresis parameter β_c can be extracted from a hysteretic I(V) characteristics by using [64, 163]:

$$\beta_c = (I_{qp}/I_r)^2 \tag{8.1}$$

where I_r is the retrapping current and I_{qp} is the quasiparticle current at $V = (\Delta_1 + \Delta_2)/e$. For $\beta_c > 1$, the system is underdamped, while for $\beta_c < 1$, the system is overdamped. For small disturbance of the phase, the phase will oscillate at the plasma frequency $\omega_p = \sqrt{2\pi I_0/\Phi_0 C}$ with a quality factor $Q = \sqrt{\beta_c}$.

Figure 8.10 shows extracted values of β_c as a function of R_n (black squares). Note that for all R_n values I found $\beta_c > 1$. If we look carefully at Fig. 8.3 (c), this I(V) curve at $R_n = 490\ \Omega$ and $\beta_c \approx 10$ does not look like a conventional S-I-S overdamped I(V) curve because of MAR effects. Nevertheless, we see that hysteresis is present, I_r is about 90 % of the switching current I_s, and $I_s \sim \frac{1}{3} I_{qp}$.

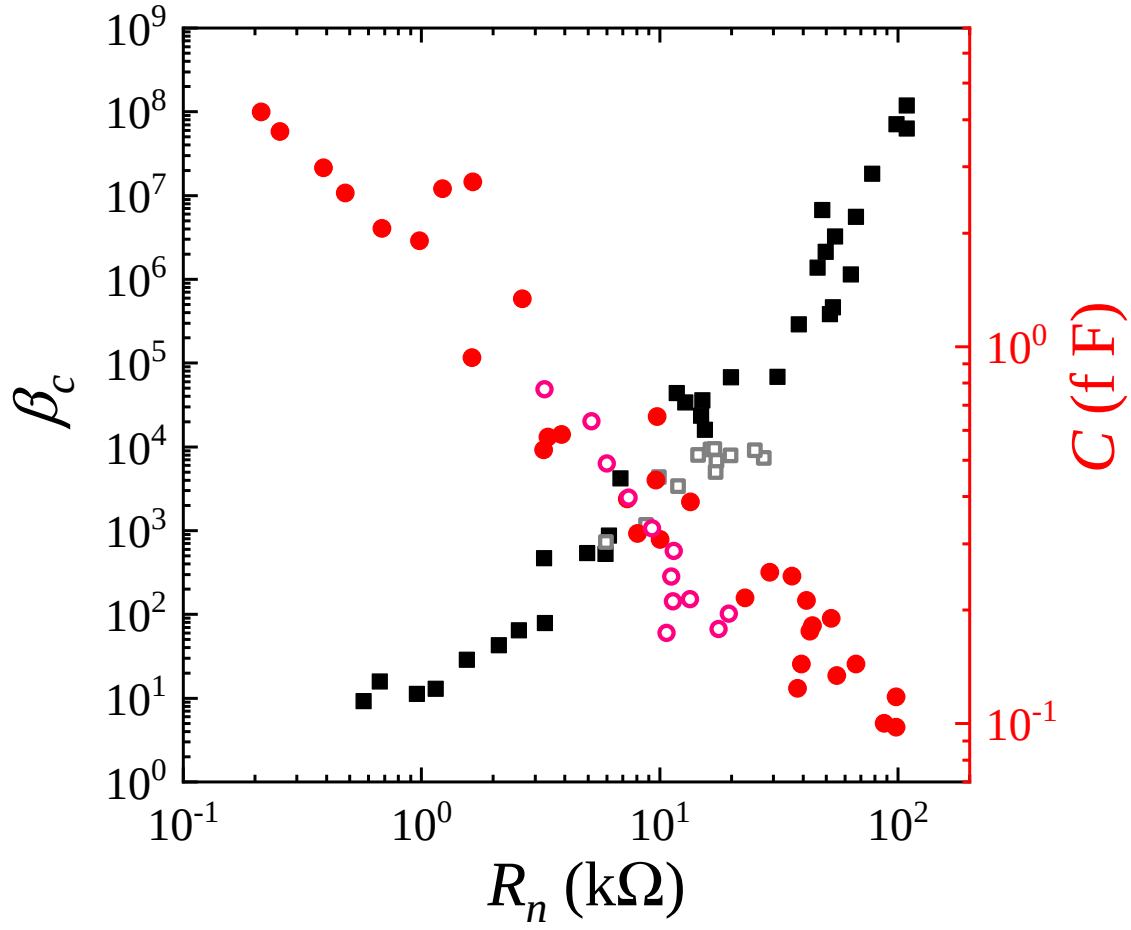

Figure 8.10: Extracted values of Stewart-McCumber parameter β_c (black) and total effective capacitance C (red) of the junction versus tunneling resistance R_n. $\beta_c \gg 1$ indicates the junction is strongly underdamped. The capacitance is roughly consistent with expected STM junction capacitance in the range of fF to aF. Filled symbols represent data taken at 1.5 K while open symbols represent data taken at 50 mK.

The Stewart-McCumber parameter [161, 162] can also be written as:

$$\beta_c = 2\pi I_0 R^2 C/\Phi_0 \tag{8.2}$$

where I_0 is the true critical current of the junction (as opposed to the measured switching current I_s), R is the total effective resistance shunting the Josephson junction and C is the total effective capacitance across the junction. Using the extracted values of β_c and assuming $I_0 = \pi I_{qp}/4$, I can use Eq. (8.2) to obtain:

$$C = 4\beta_c \hbar/2eI_{qp}R^2\pi. \tag{8.3}$$

where the effective resistance at the retrapping voltage is simply:

$$R = V_r/I_r \tag{8.4}$$

and V_r is the corresponding voltage at the retrapping current I_r.

Figure 8.10 shows a plot of the resulting capacitance C as a function of R_n (red points) at 50 mK (open circles) and 1.5 K (filled circles). This method yields a capacitance value that appears to be in a reasonable agreement with one would expect for an STM tip that is near to a conducting surface [164–166], which is on the order of fF to aF. As expected, C increases as R_n becomes smaller, because the distance between the tip and the sample becomes smaller, resulting in a larger capacitance value. For $R_n \geq 100$ kΩ, I could not use this approach to determine C because the retrapping current was too small to measure.

Although I used the RCSJ model to estimate β_c and C, the $I-V$ characteristics show some features that cannot be explained with just this simple model, including MAR, early switching out of the supercurrent state and finite resistance of the supercurrent branch. Although MAR explains much of the behavior for a non-zero voltage, small Josephson junction physics is needed to explain the behavior near $V = 0$. This behavior of Josephson junction [64] is governed by the level of dissipation and the relative size of four different energies: the Coulomb charging energy $E_C = e^2/2C$, the Josephson energy $E_J = I_0\Phi_0/2\pi$, the thermal energy k_BT and the plasma energy $\omega_p \times \hbar$, which is approximately the energy required to excite the junction out of its lowest energy quantum state. Since $\beta_c > 1$ for all R_n (see Fig. 8.10), the junctions are in the relatively low dissipation limit. Figure 8.11 shows Josephson energy, Coulomb energy and plasma energy as a function of the tunneling resistance R_n. As Fig. 8.11 shows, $E_J > \hbar\omega_p > E_c > k_BT$ for $R_n < 10$ kΩ. This is the phase qubit limit, where phase is well-defined but quantum tunneling effects [64, 159, 160] can be important and produce early switching of the super-current.

Also shown in Fig. 8.11 is the escape temperature T_{ESC} and the thermal energy k_BT. From the plot, $T_{ESC} \approx 1$ K which suggests macroscopic quantum tunneling is important. For R_n greater than about 100 kΩ, E_c dominates. In this limit charging effects, phase diffusion and the impedance of the bias leads become important in determining the I(V) characteristics, including in particular the size of the observed phase-coherent supercurrent and the resistance of the supercurrent branch. As far as we know, a full theory, including MAR, charging effects, and circuit impedance has yet to be developed.

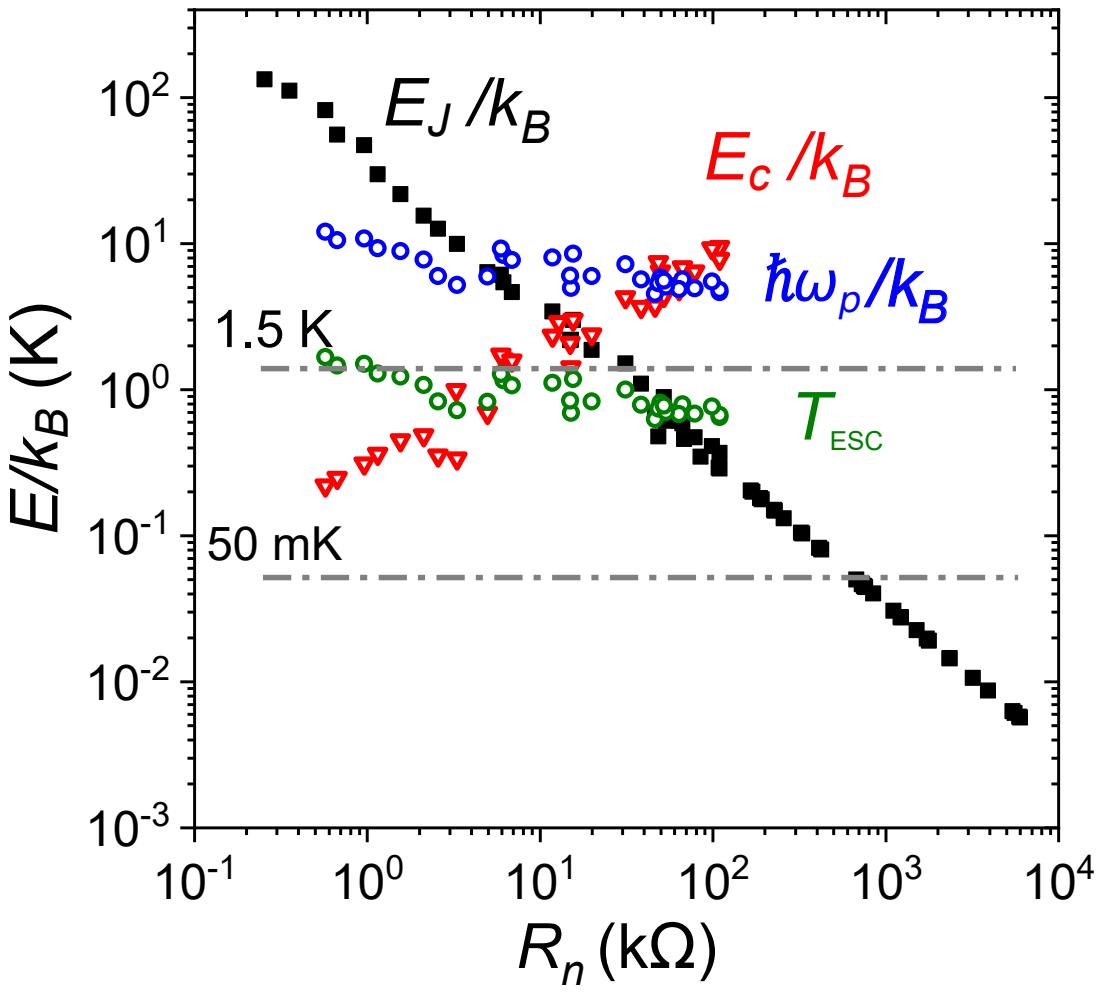

Figure 8.11: Josephson energy E_J (black), charging energy E_C (red) and plasma energy $\hbar\omega_p$ (blue circles) of the Nb-Nb STM junction versus normal resistance R_n of the junction. Dashed dark gray lines show temperature of 1.5 K and 50 mK. Green circles show the MQT escape temperature *vs.* R_n. Note that $T_{EQC} \sim 1$K for a wide range of R_n.

An important part of the small Josephson junction theory is understanding effects produced by the lead impedance [73]. The plasma frequency $\omega_p = \sqrt{2eI_0/\hbar C}$ of a small junction is typically around 10^{10} Hz to 10^{11} Hz and at such frequencies the shunting impedance Z_1 of the bias leads has non-zero real and imaginary parts that typically are of order 50 Ω. Thus Z_1 is typically orders of magnitude smaller than the quasiparticle resistance. Our output leads act like a mismatched transmission line and give high-frequency damping which produces the retrapping current and a measurable non-zero resistance on the supercurrent branch due to the inelastic tunneling of Cooper pairs [64, 159, 160, 167].

The high frequency damping effect also produces noise which causes phase diffusion [74, 152, 153] and an average voltage in the supercurrent branch. For thermally generated noise and $E_J \ll k_B T$, one finds a resistance of [64, 74]:

$$R_0 = 2Z_1(k_B T/E_J)^2 \tag{8.5}$$

In our system there can also be a contact resistance R_c between the Nb sample output leads and the sample bias lines (see Fig. 8.1). Equation (8.5) can then be written as:

$$R_0 = 2Z_1\left[\frac{4e^2 k_B T R_n}{\hbar\pi\Delta}\right]^2 + R_c(T) \tag{8.6}$$

Thus we expect that $R_0 - R_c$ is proportional to the square of the normal resistance, at least in the limit $E_J \ll k_B T$.

Figure 8.12 shows a plot of $R_0 - R_c$ as a function of R_n. The black squares

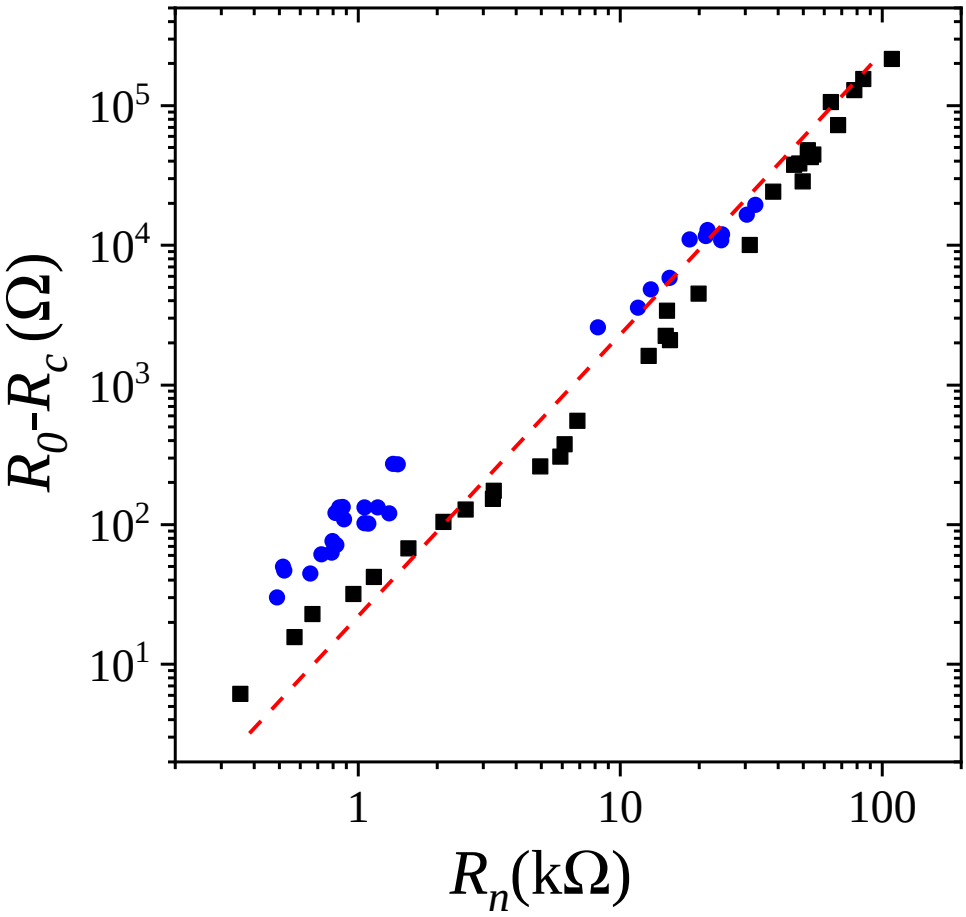

Figure 8.12: Plot of resistance $R_0 - R_c$ of the supercurrent branch versus normal tunnel resistance R_n of the junction. Blue circles are data obtained at 50 mK, black squares show data obtained at 1.5 K and red dashed line is a guide line showing $R_0 - R_c$ is proportional to R_n^2.

were taken at 1.5 K while the blue circles were taken at 50 mK. The red dashed line is a guide line showing $R_0 - R_c$ scales as R_n^2. I estimated the contact resistance $R_c = 173\ \Omega$ at 1.5 K and $R_c = 15\ \Omega$ at 50 mK. Although the data does not scale exactly as R_n^2, it is remarkably close, suggesting that the critical current is being suppressed by phase diffusion, as expected.

8.5 Conclusion

In conclusion, by varying the distance between a Nb STM tip and a Nb sample at 1.5 K, I varied the normal junction resistance R_n and observed $I - V$ characteristics that ranged from the low-transparency S-I-S tunnel limit to the high transparency S-I-S limit with prominent MAR effects. The junction resistance varied from $R_n = 5\ \text{M}\Omega$ to 500 Ω, with standard S-I-S low-transparency behavior above 100 kΩ. For R_n between 3 kΩ and 100 kΩ, the junction behaved like a hysteretic small Josephson junction with an early (premature) switching current I_s and a small but non-zero resistance R_0 on the "supercurrent" branch. Below 3 kΩ, the STM junction acts like a point contact and multiple channel MAR theory needs to be taken into consideration. I also found that the superconducting gap of the tip was significantly lower (70%) in this limit.

Using the retrapping current, I extracted estimates for the Stewart-McCumber hysteresis parameter β_c and the capacitance C of the junction. I also observed a small, non-zero resistance of the supercurrent branch and found that this scaled as

R_n^2, as expected for phase diffusion. I note that early switching of the supercurrent could be suppressed and the phase could be stabalized by using a SQUID-STM configuration [39, 42, 43] in which two superconducting junctions can form a SQUID. One tip could be pushed into the sample to achieve a relatively latge and stable critical current while the other tip is scanned. One then picks up the coherent phase signal detected by applying a small magnetic flux to the loop and then measuring the switching current [39, 42, 43, 168, 169].

CHAPTER 9

Conclusions

9.1 Summary of main results

In this thesis, I described results from my research on three main topics: (i) work towards developing a dual-tip STM that can image the gauge-invariant phase difference on a superconducting surface, (ii) STM imaging of Andreev reflection effects on the surface of TiN which allowed mapping of local variations in the gap, transparency and temperature, and (iii) the development of a theory of multiple Andreev reflection and its application to the analysis of STM Nb-Nb S-I-S tunneling characteristics. After an overview of the thesis in Chapter 1 and a brief review of tunneling in Chapter 2, I described the millikelvin dual-tip STM system that I used for all my research in Chapter 3.

In Chapter 4, I described how I modified the dual-tip STM to connect two tips using a short flexible link made of Nb foil. I then described a new technique to control both tips using $\mathrm{d}I/\mathrm{d}z$and showed results from simultaneous imaging with both tips at room temperature and discussed the potential application of the system

to imaging superconducting phase differences.

In Chapter 5, I reviewed the BTK theory of Andreev reflection effects in S-N tunneling. In Chapter 6, I then showed STM images and tunneling spectroscopy on 50 nm and 25 nm thick TiN film at 500 mK. For the 50 nm thick TiN film I used a vanadium tip while for the 25 nm thick TiN film I used a Nb tip. I observed prominent Andreev effects in the tunneling characteristics and used the BTK theory to analyze the I(V) and $\mathrm{d}I/\mathrm{d}V(\mathrm{V})$ data that I acquired. From the BTK analysis I was able to extract maps of the gap, temperature and barrier transparency, which showed large, correlated local variations. I presented a model that may explain the correlated variation as well as differences between the thick and thin films.

In Chapter 7, I generalized the Averin and Bardas theory of MAR to describe an S-I-S junction with electrodes with different superconducting gaps. Using this theory I obtained an expression for the I(V) characteristics and a prediction of the critical current as a function of the barrier transparency, gaps, and temperature. In Chapter 8, I described my measurement of I(V) characteristics obtained at 50 mK and 1.5 K using an STM with a Nb tip and a Nb sample. I then applied the theory developed in Chapter 7 to analyze the I(V) characteristics and concluded that the asymmetrical MAR theory worked remarkably well at describing the characteristics over the full range of R_n values. The main discrepancies occurred for $R_n < 5$ kΩ, where the tip began to make contact with the sample. I also examined the switching current and retrapping current and identified three regimes: the phase diffusion regime (for $R_n > 100$ kΩ), the underdamped regime (for 3 kΩ $< R_n <$ 100 kΩ) and the point contact regime (for $R_n < 3$ kΩ).

One may well ask, since you succeeded in connecting two Nb STM tips together and simultaneously scanning both tips, you should have been able to form an STM-SQUID, measure flux sensitivity and image the gauge invariant phase difference. In addition, was the observed supercurrent from the single S-I-S Josephson junctions discussed in Chapter 8 phase coherent or incoherent tunneling of Cooper pairs?

Figure 9.1 shows the configuration of the STM controllers and read out electronics for running the SQUID setup. To operate the dual-point system as a SQUID, I first stabilize the two STM tips at the desired junction tunneling resistance R_n, turn the z feedback off and switch the relay to the current bias mode. I then use the function generator to output the current to the junctions and start the counter. The counter waits for a signal from the relay box; once the voltage across the SQUID reaches the threshold (because the SQUID switching out from the supercurrent branch), the counter stops. I repeat this switching measurement many times and for different flux applied to the loop. I can plot the applied flux Φ *vs.* the switching current I_s (converted from the time for the supercurrent state to switch out to the voltage state). Once all the measurements are done, the relay box switched the STM electronics back to the voltage bias mode, and the STM feedback is turned back on.

I actually spent a total of about 6 months attempting to run the STM-SQUID at 30 mK before the refrigerator was damaged and then at 1.5 K after the refrigerator was temporarily fixed. However, I did not observe an obvious critical current modulation when the flux was applied to the SQUID loop [42]. Below I discuss several possible reasons and suggest some possible improvements for the future.

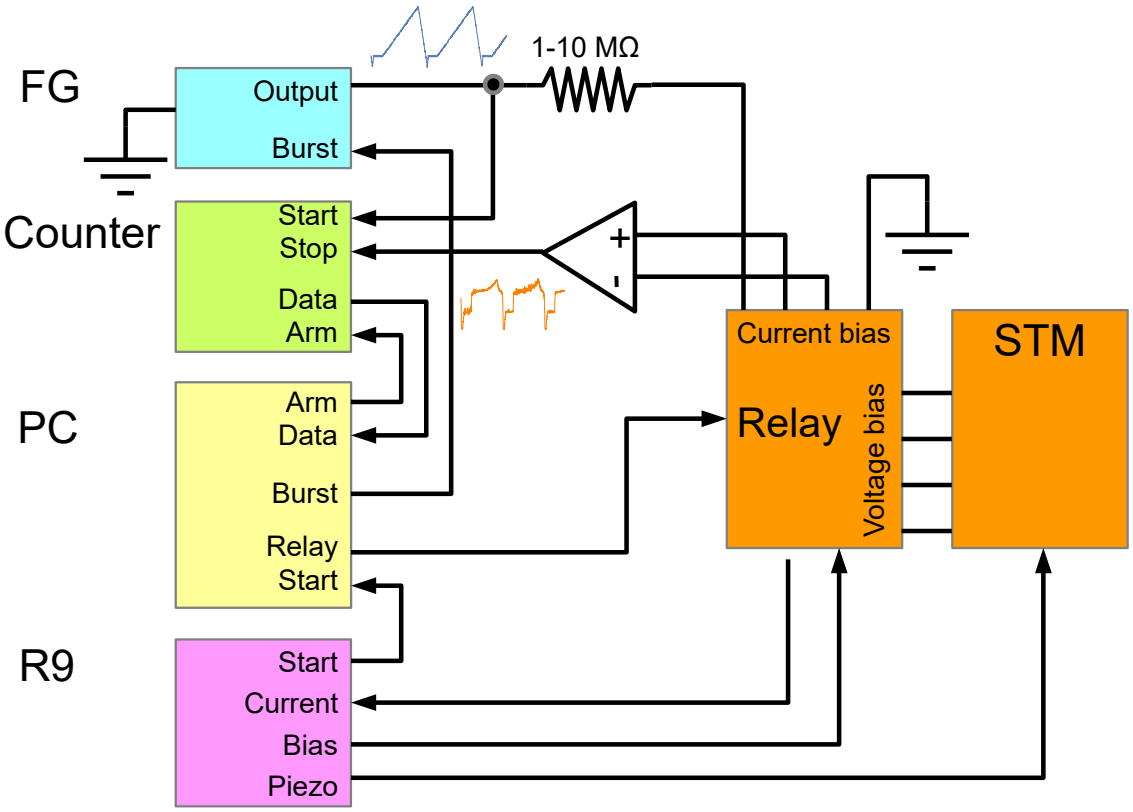

Figure 9.1: Configuration of the STM controllers and read out electronics for running the SQUID setup.

9.2 Some suggestions for further research

9.2.1 Low temperature requirement

Previously most of the reports on Josephson STMs were conducted in the phase diffusive regime [34–36, 38, 71] where the critical current is highly suppressed. For a symmetric superconducting junctions (with electrodes that have the same superconducting gap), the Ambegaokar-Baratoff formula [133, 134] gives a critical current

$$I_0 = \frac{\pi\Delta}{2eR_N}\tanh\left(\frac{\Delta}{2k_BT}\right) \tag{9.1}$$

where R_N is the tunneling resistance of the junction in the normal state [64]. For the critical current I_0 to be close to the measured switching current I_s, the Josephson coupling energy $E_J = \frac{\hbar I_0}{2e}$ must be much greater than the thermal energy $E_T = k_BT$. As we saw in Fig. 8.11, the Josephson energy E_J (black), charging energy E_C (red), and thermal energy k_BT (blue) can be relatively close to each other, and for phase coherent operation for typical parameters we need to use a mK setup. Unfortunately, as I described in Section 3.5, after the accident which damaged the step heat exchanger, we found the refrigerator was stable down to about 0.5 K and could not cool below 0.3 K. I tried to run the SQUID measurement at 0.5 K but it was quite possible that the thermal energy was too big and the phase coherence was not present for the range of junction parameters I tried. Clearly it would be

interesting to replace the refrigerator with a working mK unit and try again at 50 mK.

9.2.2 Smaller SQUID loop

As Roychowdhury *et al*. showed theoretically [40], it is better to have a smaller inductance SQUID loop to observe a phase coherent response if one of the junctions has a small critical current. Unfortunately, the STM tip length was relatively large ($\sim$ 2 mm) (see Fig. 4.2). This also meant that the SQUID had a large pickup area, which makes it very sensitive to magnetic field noise. A total RMS field noise as small as 1 nT would have destroyed the SQUID modulation with applied flux. It clearly would be interesting to try again with a smaller loop formed from shorter STM tips and holders. One could also bend the tips toward each other so that when the tips approached the sample, they would form a smaller SQUID loop.

9.2.3 Better shielding

Currently the IVC can is enclosed in an Amuneal Manufacturing Amumetal 4K shield [170] to reduce the strength of low-frequency magnetic fields and electrical noise in the system. I note that this level of shielding may not be adequate given the relatively large pickup area of the SQUID. With a pickup area of $\sim$ 2 mm^2, a field change of 1 nT would produce a flux change of 1 Φ_0 in the SQUID. Fluctuations of this size would completely obscure measurements of the SQUID critical current.

Since background 60 Hz fields alone are typically 100 nT, we should shield by at least a factor of 1000. In the future, adding one or two more Amumetal shields or a superconducting shield would be a priority. It would also be advisable to add additional radiation shields at the plate or still to reduce black-body radiation at the STM which can produce excess quasiparticle at mK temperature.

9.2.4 Intrinsic system constraint

Dan Sullivan's proof of principle experiment [42] demonstrated the feasibility of using a highly asymmetric SQUID to make phase sensitive measurements. He used e-beam lithography to pattern thin film junctions that mimicked actual STM conditions. In particular, the SQUID had ~ 1 nA of critical current modulation on top of ~ 1 μA critical current. To satisfy this requirement in a dual-point STM, that means one tip would have ~ 1 μA critical current, which is in the point contact regime. The other tip can be in the nA range, which is in the underdamped regime, just as Dan's experiment.

During my data acquisition of the $I-V$ characteristics, I often noticed that it was hard to stabilize the tip with a fixed switching current in the nA range. When I turned off the feedback to make SQUID measurements, the tip typically ended up drifting and within a short time the junction's switching current would change significantly. Although I did not try to make the system run with a large and a small junction, I did try to operate at 0.5 K with both tips having a large switching current. It was stable enough to run the SQUID measurements. Unfortunately, I did not see

any modulation of the device critical current when I varied the flux. Although this was in the point contact regime, I still should have observed a modulation. It is possible that there was too much flux noise, or something was wrong with the coil I was using to apply flux. In the future, it would be interesting to check these possible problems by testing a conventional thin-film lithographically defined SQUID in the apparatus. Another critical test of both the SQUID configuration and the single STM point is to check the response to applied microwaves. As Roychowdhury *et al*. showed, this can be used to distinguish phase coherent tunneling of pairs from incoherent tunneling of pairs [40].

APPENDIX A

χ^2 fit for the TiN film

In Chapter 6 I showed several maps of the gap in TiN films. These superconducting gap maps had gray points which indicated points where I got a bad fit to the BTK theory. Each conductance curve had 115 points and the uncertainty of each measurement of conductivity was estimated to be 5 nS for $V > \Delta/e$ and 1 nS for $V < \Delta/e$. I used $\chi^2 \geq 5000$ as the threshold for a truly bad fit in the image, in Fig. 6.6 (b) and Fig. 6.8 (b), which had 28928 and 25856 pixels. Note that a good fit should yield $\chi^2 \approx 115$. Points with $\chi^2 > 5000$ were colored gray in the maps in Chapter 6. For Fig. 6.6 of the 50 nm film, there were 6617 points that gave bad fits to the Dynes model in Fig. A.1 (a) (22.87 %), while 6748 points had bad fits to the BTK model in Fig. A.1 (b) (23.32 %). For the 25 nm film, there are 6258 points with bad fits to the Dynes model in Fig. A.1 (c) (24.20 %), while 4939 points had bad fits to the BTK model in Fig. A.1 (d) (19.1 %). In the 50 nm film, the quality of the fits to the BTK model and to the Dynes model are not so different. In the 25 nm film, the BTK model gave significantly better fits.

Figure A.1 shows gap maps without using gray to indicate poor fits. Most of

the formally gray points are now red, which suggests that the gap is high. However, examination of these fits shows that this is misleading, as these fit curves have a very poor correspondence with the data. Figure A.1 also shows histograms of the corresponding χ^2 values, which display a long tail.

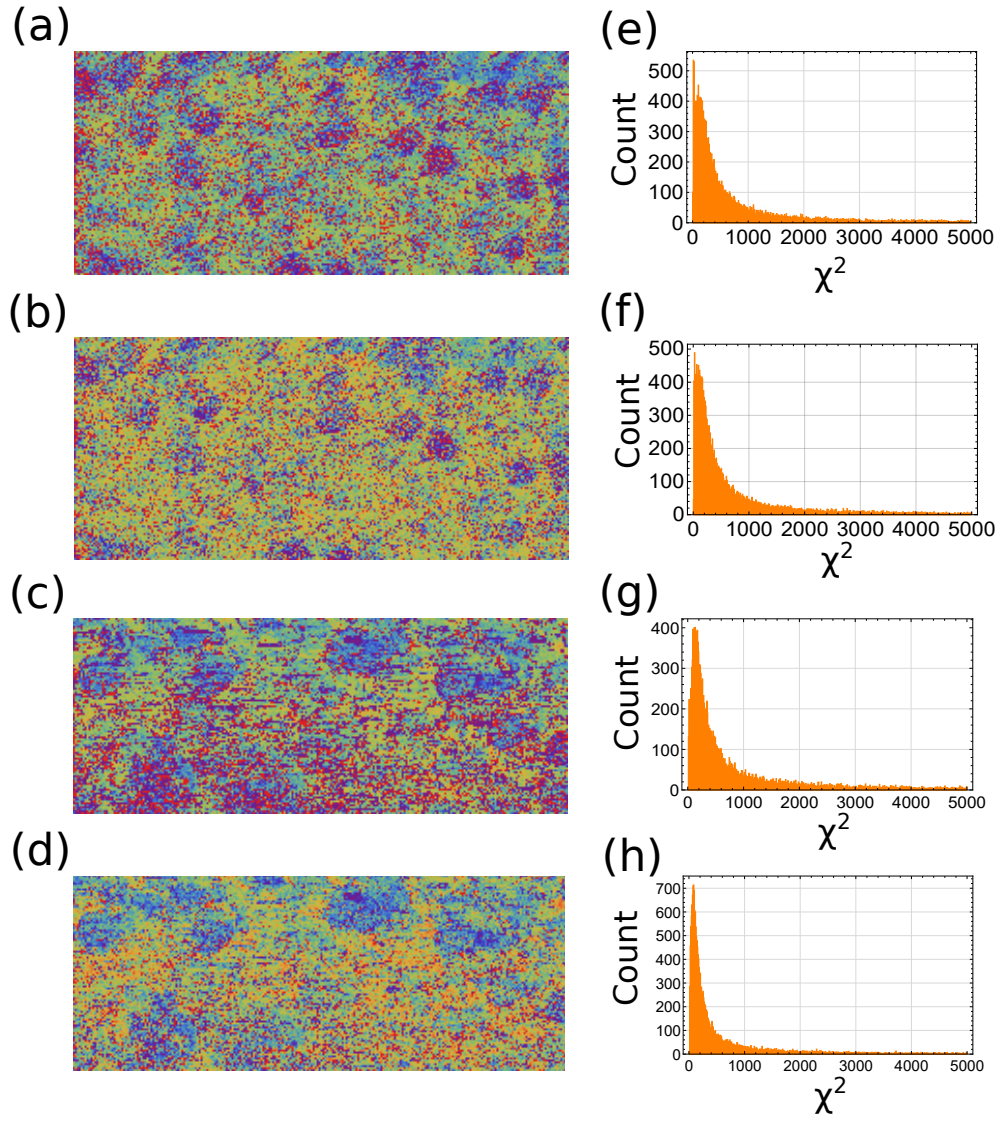

Figure A.1: (a) Gap Δ map of the 50 nm thick TiN film from fitting to the Dynes model and (b) the BTK model. (c) Δ map of the 25 nm thick TiN film from fitting to the Dynes model and (d) the BTK model. (e) χ^2 histograms of the 50 nm thick TiN film by fitting to the Dynes model and (f) the BTK model. (g) χ^2 histograms of the 25 nm thick TiN film by fitting to the Dynes model (h) and the BTK model.

APPENDIX B

50 nm TiN film showing S-I-S junction with a vanadium tip

In the thesis, I mentioned that the superconducting tip did not show superconducting behavior due to it easily picking up debris from the surface. Here I show that I successfully acquired one data set which shows the S-I-S junction on the TiN surface.

Figure B.1 (a) shows a topographic image of a 70 nm $\times$ 33 nm region on the 50 nm thick TiN film. The image was acquired at 0.5 K using a vanadium tip and there are 256 $\times$ 122 pixels. The sample bias was set at 5 mV while the tunneling current was set at 100 pA. Figure B.1 (b) shows the corresponding map of Δ obtained from fitting the conductance curves at each point to the Dynes model. Although in this case I did not use the BTK model to do the fitting (it is very time consuming), from the map we can see that in general the values of the gap are larger than the S-I-N data shown in Chapter 6. Figure B.1 (c) shows a histogram of the superconducting gap using the Dynes fit. Compared to Fig. 6.10 where the maximum of the superconducting gap value lies around 0.6 meV for the 50 nm film,

in this case the peak of the superconducting gap is around 1.5 meV. This suggests that the junction is S-I-S like, instead of S-I-N like.

Figure B.1 (d) shows a $\mathrm{d}I/\mathrm{d}V vs.\ V$ curve taken from one location in Fig. B.1 (a). Qualitatively we see that the coherence peaks are much sharper and the spacing of the coherence peaks is much wider, corresponding to the sum of gaps, $2(\Delta_{\mathrm{tip}} + \Delta_{\mathrm{sample}})$. Moreover, the conductance curve bottoms out at 0 for $V < \Delta_{\mathrm{tip}} + \Delta_{\mathrm{sample}}$. This suggest that there is no current flow inside the superconducting gap, which is expected for a standard S-I-S curve. The red curve in Fig. B.1 (d) shows the fit to the Dynes model. As we can see here, the fit is not very good, and it tends to underestimate the gap. In this case the fit yields the superconducting gap of $\Delta_{\mathrm{tip}} + \Delta_{\mathrm{sample}} = 1.44$ meV. In principle, a better fit could be obtained from the Tinkham formula which involves the numerical integration of the expression Eq. (2.27).

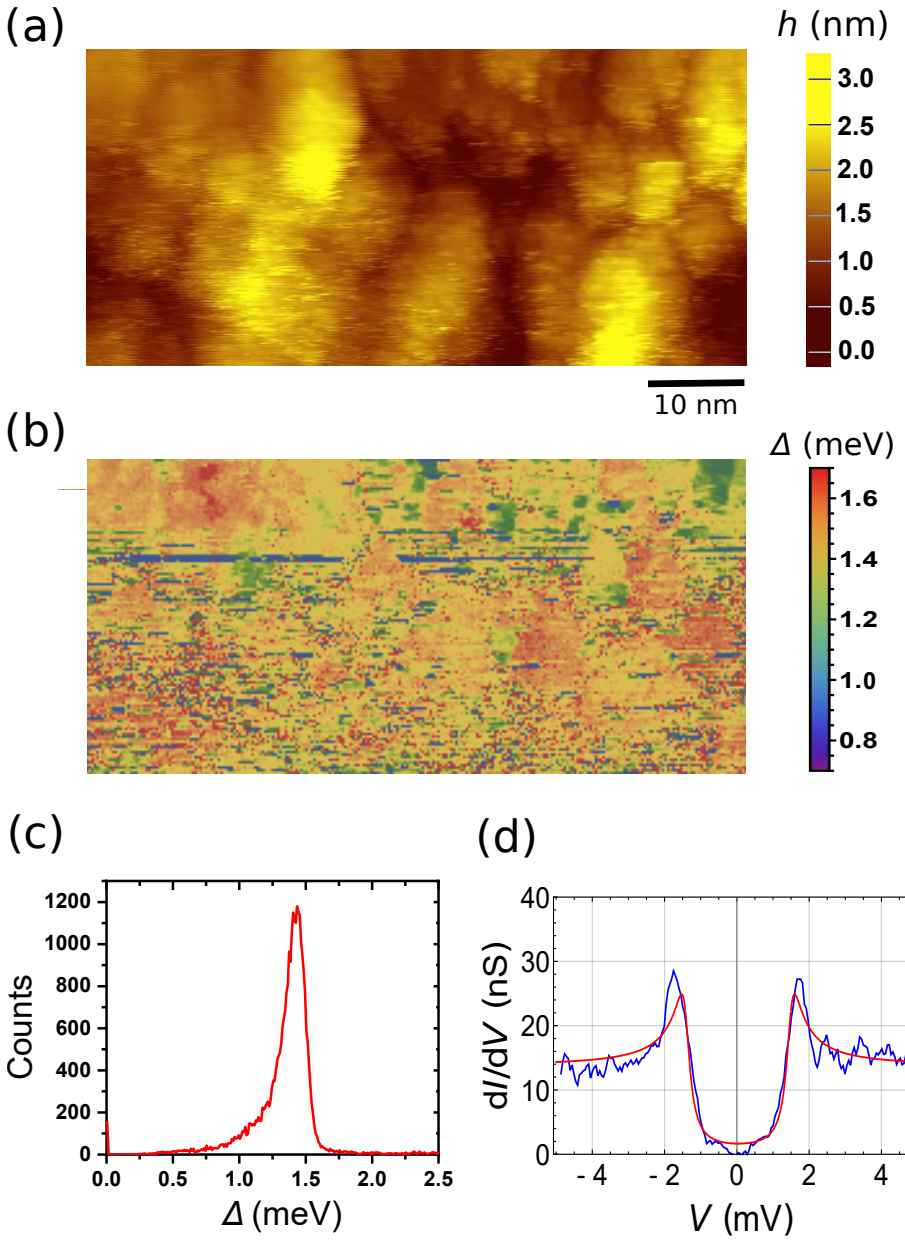

Figure B.1: (a) Topography of 50 nm thick TiN film taken at 100 pA and 5 mV bias.(b) Superconducting gap Δ map of the 50 nm thick TiN film from fitting to the Dynes model. (c) Histogram of superconducting gap from gap map in Fig. B.1 (b) using the Dynes fit. (d) Measured conductance $\mathrm{d}I/\mathrm{d}V vs.\ V$ (blue curve) as well as fit to the Dynes model (red curve).

APPENDIX C

Fortran code for symmetrical S-I-S junction with MAR effect

In the symmetrical S-I-S junction code with MAR effect that I present below, t is the transparency which is D in the Chapter 7, r is the reflection probability which is R in the Chapter 7 and th is the temperature in kelvin. ne is the largest integration upper limit ε_0, e is the integration variable ε, v is the voltage V while ai is the current I.

I use function scat(t,r,n,e,v) to calculate A_n and B_n defined in Chapter 7, and it yields a(k) and b(k), respectively. The Andreev reflection amplitude is defined as an(x) in the code. The Source $J(\varepsilon)$ in this code is used as so(x). ft(x,th) gives the $\tanh\left(\varepsilon/2k_BT\right)$ function.

Finally, I would like to thank Prof. Averin again for providing the Fortran code for the symmetrical S-I-S junction case. I then modified the code and generalized it to the asymmetrical S-I-S junction case (see Appendix C).

```
1         program main
2         double complex a(-1000:1000),b(-1000:1000),w(-2000:2000)
3         double complex y,yy,sa,ai,an
4         double precision e,ft,so
5
6         common/amp/a,b,w
7
8         open(1,file='tmp1.dat')
9         open(2,file='tmp2.dat')
10        open(3,file='tmp3.dat')
11        open(4,file='tmp4.dat')
12
13 !!  This is the transparency parameter defined as D in the theory
14        write(*,*)'input barrier transparency t'
15        read(*,*)t
16
17 !!  This is the temperature, normalized
18        th=0.005
19
20
21 !!  R+T=1
22        r=1.0-t
23
24 !!  jj is the Fourier component of the current term
25        jj=0.
26
27 !!  v is the voltage
28        do 2 kv=1,150
29        v=0.02*kv
30
31 !!  h is the integration interval
32        h=.001
33
34
35 !!  n is how many terms of a(k) and b(k) have
36        n=int(2./v)
37        if(n.LT.20) n=20
38
39 !!  ne is the maximum energy where the integration of the energy
       goes up to
40        ne=int(20./h)
41        if(v.GT.1)ne=int((18.+2.*v)/h)
42
43
44 !!  je is just to alternate the integration terms, one term is 4
       one terms is 2, in the end it divides by 3
45 !!  "do 3" command sums up the current sa at each energy ke
46        sa=0.0
47        je=-1
48        do 3 ke=0,ne
49        je=-je
50
51        do 33 jth=1,2
52
53 !!  both positive energy side and negative energy side have to be
       summed up
54        e=((-1)**jth)*(h*ke+1.0005)
```

```
55
56  !!  y is to calculate the current at certain energy e
57          call scat(t,r,n,e,v)
58          y=(w(2*jj)*a(jj)+conjg(w(-2*jj)*a(-jj)))*so(e)
59          do 4 k=-n,n
60          kk=2*k
61          kj=k-jj
62          yy=1.+w(kk)*conjg(w(kk-2*jj))
63          y=y+yy*(a(k)*conjg(a(kj))-b(k)*conjg(b(kj)))
64  4       continue
65
66  !!  sa is the summed current at specefic voltage v with fermi
        distribution ft
67          sa=sa+(3.+je)*y*ft(e,th)
68  33      continue
69
70  3       continue
71
72  !!  the final current needs to multiply the interval of the
        integration energy
73          ai=sa*h/(3.*t)
74
75          write(*,*)v,ai
76          write(3,*)v,real(ai)
77          write(4,*)v,-imag(ai)
78
79  2       continue
80
81          stop
82          end
83
84
85
86          subroutine scat(t,r,n,e,v)
87          double complex a(-1000:1000),b(-1000:1000),w(-2000:2000)
88          double complex an,s,x,q,u,p,f
89          double precision e,so
90
91          common/amp/a,b,w
92
93          rr=sqrt(r)
94
95          do 1 k=-n-2,n+2
96          a(k)=cmplx(0.,0.)
97  1       b(k)=cmplx(0.,0.)
98
99          do 2 k=-2*n-4,2*n+4
100         w(k)=an(e+k*v)
101 2       continue
102
103         s=(0.,0.)
104         do 3 k=n,1,-1
105         j=2*k
106         j1=j-1
107         i1=j+1
108         u=t*w(j)/((1.,0)-w(j1)**2)
109         f=t*w(i1)/((1.,0)-w(i1)**2)
```

```
         q=f*w(j+2)
         x=u*w(j1)
         p=u*w(j)+f*w(i1)+(1.,0.)-w(j)**2
         s=x/(p-q*s)
3        b(k)=s


         s=(0.,0.)
         do 4 k=-n,-1
         j=2*k
         j1=j-1
         i1=j+1
         u=t*w(j)/((1.,0.)-w(j1)**2)
         f=t*w(i1)/((1.,0.)-w(i1)**2)
         q=f*w(j+2)
         x=u*w(j1)
         p=u*w(j)+f*w(i1)+(1.,0.)-w(j)**2
         s=q/(p-x*s)
4        b(k)=s


         u=t*w(0)/((1.,0.)-w(-1)**2)
         f=t*w(1)/((1.,0.)-w(1)**2)
         q=f*w(2)
         x=u*w(-1)
         p=u*w(0)+f*w(1)+(1.,0.)-w(0)**2
         b(0)=rr*so(e)/(p-b(1)*q-b(-1)*x)



!!  calculation of b(k)
         b(1)=b(0)*b(1)
         b(-1)=b(0)*b(-1)
         do 5 k=2,n
         b(k)=b(k-1)*b(k)
         b(-k)=b(-k+1)*b(-k)
5        continue


!!  calculation of a(k)
         do 6 k=-n,-1
         j=2*k
         j1=j+1
         k1=k+1
         u=a(k)*w(j)*w(j1)
         f=rr*(b(k1)*w(j+2)-b(k)*w(j1))
         a(k1)=u+f
6        continue

         u=a(0)*w(0)*w(1)
         f=rr*(b(1)*w(2)-b(0)*w(1))
         a(1)=u+f+w(1)*so(e)



         do 7 k=1,n
         j=2*k
```

```
        j1=j+1
        k1=k+1
        u=a(k)*w(j)*w(j1)
        f=rr*(b(k1)*w(j+2)-b(k)*w(j1))
        a(k1)=u+f
7       continue



        return
        end

!!  calculation of Andreev reflection amplitude
        double complex function an(x)
        double precision x,g
        g=x**2
        if(g.GE.1.)goto 2
        an=cmplx(x,dsqrt(1.-g))
        goto 1
2       t=x*(1.-dsqrt(g-1.)/abs(x))
        an=cmplx(t,0.)
1       continue
        return
        end

!!  calculation of incoming current source J(e)
        double precision function so(x)
        double precision x,z
        double complex an
        z=Real(an(x))
        so=dsqrt(1.-z**2)
        return
        end

        function sig(x)
        double precision x
        sig=x/abs(x)
        return
        end

!!  ft corresponds to -tanh(e/2T)
        double precision function ft(x,th)
        double precision x,xx
        xx=x/th
        if(xx.LT.0.)goto 1
        if(xx.GT.40)goto 2
        z=dexp(-xx)
        ft=(z-1.)/(1.+z)
        goto 3
2       ft=-1.
        goto 3
1       if(xx.LT.-40.)goto 4
        z=dexp(xx)
        ft=(1.-z)/(z+1.)
        goto 3
4       ft=1.
3       continue
```

```
224         return
225         end
```

APPENDIX D

Fortran code for Asymmetrical S-I-S junction with MAR effect

In this Fortran code, I calculated the ac part of the tunneling current, i.e. jj=1, which is different from the dc part calculated in the previous Appendix C. As I mentioned in Chapter 7, the main difference between the symmetrical junction and the asymmetrical junction is that one has to be careful whether the quasiparticle is reflected off the left electrode or the right electrode. For the case where the current I_L is produced from the left incident quasiparticle L_{AC}, the left electrode Andreev reflection amplitude is an(x), while for the right electrode the Andreev reflection amplitude is bn(x). In contrast, for the case where the current I_R is produced from the right incident quasiparticle R_{AC}, the left electrode is defined as bn(x) in the code while an(x) is for the right electrode.

Finally, the total current from the asymmetrical S-I-S junction is calculated using $I = I_L - I_R$. In my calculation here, the ratio of the gap of the left electrode to the gap of the right electrode is $\Delta_L/\Delta_R = 1/0.5 = 2$.

L_{AC} :

```
      program main
      double complex a(-1000:1000),b(-1000:1000),w(-2000:2000)
      double complex y,yy,sa,ai,an,bn
      double precision e,ft,so

      common a,b,w

      open(3,file='tmp3.dat')
      open(4,file='tmp4.dat')


      jj=1.

      do 2 kt=1,50
      th=0.05*kt
      t=0.5
      v=0.01

      h=.001
      r=1.-t


      n=int(2./v)
      if(n.LT.20) n=20

      ne=int(20./h)
      if(v.GT.1)ne=int((18.+2.*v)/h)

      sa=0.0
      je=-1
      do 3 ke=0,ne
      je=-je

      do 33 jth=1,2

      e=((-1)**jth)*(h*ke+1.0005)


      call scat(t,r,n,e,v)
      y=(w(2*jj)*a(jj)+conjg(w(-2*jj)*a(-jj)))*so(e)
      do 4 k=-n,n
      kk=2*k
      kj=k-jj
      yy=1.+w(kk)*conjg(w(kk-2*jj))
      y=y+yy*(a(k)*conjg(a(kj))-b(k)*conjg(b(kj)))
4     continue

      sa=sa+(3.+je)*y*ft(e,th)
33    continue
3     continue

      ai=sa*h/(3.*t)

      write(*,*)th,ai
```

```
55          write(3,*)th,real(ai)
56          write(4,*)th,-imag(ai)
57
58
59  2       continue
60
61          stop
62          end
63
64          subroutine scat(t,r,n,e,v)
65          double complex a(-1000:1000),b(-1000:1000),w(-2000:2000)
66          double complex an,bn,s,x,q,u,p,f
67          double precision e,so
68
69          common a,b,w
70
71          rr=sqrt(r)
72
73          do 1 k=-n-2,n+2
74          a(k)=cmplx(0.,0.)
75  1       b(k)=cmplx(0.,0.)
76
77          do 2 k=-2*n-4,2*n+4,2
78          w(k)=an(e+k*v)
79  2       continue
80
81          do 3 k=-2*n-3,2*n+3,2
82          w(k)=bn(e+k*v)
83  3       continue
84
85          s=(0.,0.)
86          do 4 k=n,1,-1
87          j=2*k
88          j1=j-1
89          i1=j+1
90          u=t*w(j)/((1.,0)-w(j1)**2)
91          f=t*w(i1)/((1.,0)-w(i1)**2)
92          q=f*w(j+2)
93          x=u*w(j1)
94          p=u*w(j)+f*w(i1)+(1.,0.)-w(j)**2
95          s=x/(p-q*s)
96  4       b(k)=s
97
98
99          s=(0.,0.)
100         do 5 k=-n,-1
101         j=2*k
102         j1=j-1
103         i1=j+1
104         u=t*w(j)/((1.,0.)-w(j1)**2)
105         f=t*w(i1)/((1.,0.)-w(i1)**2)
106         q=f*w(j+2)
107         x=u*w(j1)
108         p=u*w(j)+f*w(i1)+(1.,0.)-w(j)**2
109         s=q/(p-x*s)
110 5       b(k)=s
111
```

```
112
113           u=t*w(0)/((1.,0.)-w(-1)**2)
114           f=t*w(1)/((1.,0.)-w(1)**2)
115           q=f*w(2)
116           x=u*w(-1)
117           p=u*w(0)+f*w(1)+(1.,0.)-w(0)**2
118           b(0)=rr*so(e)/(p-b(1)*q-b(-1)*x)
119
120
121           b(1)=b(0)*b(1)
122           b(-1)=b(0)*b(-1)
123           do 6 k=2,n
124           b(k)=b(k-1)*b(k)
125           b(-k)=b(-k+1)*b(-k)
126   6       continue
127
128
129           do 7 k=-n,-1
130           j=2*k
131           j1=j+1
132           k1=k+1
133           u=a(k)*w(j)*w(j1)
134           f=rr*(b(k1)*w(j+2)-b(k)*w(j1))
135           a(k1)=u+f
136   7       continue
137
138           u=a(0)*w(0)*w(1)
139           f=rr*(b(1)*w(2)-b(0)*w(1))
140           a(1)=u+f+w(1)*so(e)
141
142
143           do 8 k=1,n
144           j=2*k
145           j1=j+1
146           k1=k+1
147           u=a(k)*w(j)*w(j1)
148           f=rr*(b(k1)*w(j+2)-b(k)*w(j1))
149           a(k1)=u+f
150   8       continue
151
152
153           return
154           end
155
156
157           double complex function an(x)
158           double precision x,g
159           g=x**2
160           if(g.GE.1.)goto 2
161           an=cmplx(x,dsqrt(1.-g))
162           goto 1
163   2       t=x*(1.-dsqrt(g-1.)/abs(x))
164           an=cmplx(t,0.)
165   1       continue
166           return
167           end
168
```

```
      double complex function bn(x)
      double precision x,g
      g=x**2
      if(g.GE..25)goto 3
      bn=cmplx(2.*x,dsqrt(1.-4.*g))
      goto 4
3     t=x*(2.-dsqrt(4.*g-1.)/abs(x))
      bn=cmplx(t,0.)
4     continue
      return
      end


      double precision function so(x)
      double precision x,z
      double complex an
      g=x**2
      if(g.LT.1.)goto 2
      z=Real(an(x))
      so=dsqrt(1.-z**2)
      goto 1
2     so=0.0
1     continue
      return
      end


      double precision function ft(x,th)
      double precision x,xx
      xx=x/th
      if(xx.LT.0.)goto 1
      if(xx.GT.40)goto 2
      z=dexp(-xx)
      ft=(z-1.)/(1.+z)
      goto 3
2     ft=-1.
      goto 3
1     if(xx.LT.-40.)goto 4
      z=dexp(xx)
      ft=(1.-z)/(z+1.)
      goto 3
4     ft=1.
3     continue
      return
      end
```

R_{AC} :

```
      program main
      double complex a(-1000:1000),b(-1000:1000),w(-2000:2000)
      double complex y,yy,sa,ai,an,bn
      double precision e,ft,so

      common a,b,w

      open(3,file='tmp3.dat')
      open(4,file='tmp4.dat')

!!  calculate the AC part first Fourier component
      jj=1.

      do 2 kt=1,50
      th=0.05*kt
      t=0.5
      v=0.01
      h=.001


      r=1.-t
      n=int(2./v)
      if(n.LT.20) n=20


!!  now the ne goes a little bit further due to e only starts from
    0.5005 instead of 1.005
      ne=int(20.5/h)
      if(v.GT.1)ne=int((18.5+2.*v)/h)

      sa=0.0
      je=-1
      do 3 ke=0,ne
      je=-je

      do 33 jth=1,2

!!  the energy e where it starts to contribute some current is
    outside the superconducting gap which is 0.5
      e=((-1)**jth)*(h*ke+0.5005)


      call scat(t,r,n,e,v)
      y=(w(-2*jj)*a(-jj)+conjg(w(2*jj)*a(jj)))*so(e)
      do 4 k=-n,n
      kk=2*k
      kj=k-jj
      yy=1.+conjg(w(kk))*w(kk-2*jj)
      y=y+yy*(conjg(a(k))*a(kj)-conjg(b(k))*b(kj))
4     continue

      sa=sa+(3.+je)*y*ft(e,th)
33    continue
3     continue
```

```
53
54          ai=sa*h/(3.*t)
55
56          write(*,*)th,ai
57          write(3,*)th,real(ai)
58          write(4,*)th,-imag(ai)
59
60
61  2       continue
62
63          stop
64          end
65
66
67          subroutine scat(t,r,n,e,v)
68          double complex a(-1000:1000),b(-1000:1000),w(-2000:2000)
69          double complex bn,an,s,x,q,u,p,f
70          double precision e,so
71
72          common a,b,w
73
74          rr=sqrt(r)
75
76          do 1 k=-n-2,n+2
77          a(k)=cmplx(0.,0.)
78  1       b(k)=cmplx(0.,0.)
79
80
81  !!  for the odd term it sees bn(x) function, even term it sees an(x
        ) function
82          do 2 k=-2*n-4,2*n+4,2
83          w(k)=an(e-k*v)
84  2       continue
85
86          do 3 k=-2*n-3,2*n+3,2
87          w(k)=bn(e-k*v)
88  3       continue
89
90          s=(0.,0.)
91          do 4 k=n,1,-1
92          j=2*k
93          j1=j-1
94          i1=j+1
95          u=t*w(j)/((1.,0)-w(j1)**2)
96          f=t*w(i1)/((1.,0)-w(i1)**2)
97          q=f*w(j+2)
98          x=u*w(j1)
99          p=u*w(j)+f*w(i1)+(1.,0.)-w(j)**2
100         s=x/(p-q*s)
101 4       b(k)=s
102
103
104         s=(0.,0.)
105         do 5 k=-n,-1
106         j=2*k
107         j1=j-1
108         i1=j+1
```

```
          u=t*w(j)/((1.,0.)-w(j1)**2)
          f=t*w(i1)/((1.,0.)-w(i1)**2)
          q=f*w(j+2)
          x=u*w(j1)
          p=u*w(j)+f*w(i1)+(1.,0.)-w(j)**2
          s=q/(p-x*s)
5         b(k)=s


          u=t*w(0)/((1.,0.)-w(-1)**2)
          f=t*w(1)/((1.,0.)-w(1)**2)
          q=f*w(2)
          x=u*w(-1)
          p=u*w(0)+f*w(1)+(1.,0.)-w(0)**2
          b(0)=rr*so(e)/(p-b(1)*q-b(-1)*x)


          b(1)=b(0)*b(1)
          b(-1)=b(0)*b(-1)
          do 6 k=2,n
          b(k)=b(k-1)*b(k)
          b(-k)=b(-k+1)*b(-k)
6         continue


          do 7 k=-n,-1
          j=2*k
          j1=j+1
          k1=k+1
          u=a(k)*w(j)*w(j1)
          f=rr*(b(k1)*w(j+2)-b(k)*w(j1))
          a(k1)=u+f
7         continue

          u=a(0)*w(0)*w(1)
          f=rr*(b(1)*w(2)-b(0)*w(1))
          a(1)=u+f+w(1)*so(e)


          do 8 k=1,n
          j=2*k
          j1=j+1
          k1=k+1
          u=a(k)*w(j)*w(j1)
          f=rr*(b(k1)*w(j+2)-b(k)*w(j1))
          a(k1)=u+f
8         continue


          return
          end

!!  bn(x) function represents the full superconducting gap
          double complex function bn(x)
          double precision x,g
          g=x**2
          if(g.GE.1.)goto 2
```

```
166         bn=cmplx(x,dsqrt(1.-g))
167         goto 1
168 2       t=x*(1.-dsqrt(g-1.)/abs(x))
169         bn=cmplx(t,0.)
170 1       continue
171         return
172         end
173
174 !!  an(x) function represents the half superconducting gap (0.5)
175         double complex function an(x)
176         double precision x,g
177         g=x**2
178         if(g.GE..25)goto 3
179         an=cmplx(2.*x,dsqrt(1.-4.*g))
180         goto 4
181 3       t=x*(2.-dsqrt(4.*g-1.)/abs(x))
182         an=cmplx(t,0.)
183 4       continue
184         return
185         end
186
187 !!  so(x) function function starts from gap 0f 0.5 (see codition g.
    LT..25)
188         double precision function so(x)
189         double precision x,z
190         double complex an
191         g=x**2
192         if(g.LT..25)goto 2
193         z=Real(an(x))
194         so=dsqrt(1.-z**2)
195         goto 1
196 2       so=0.0
197 1       continue
198         return
199         end
200
201
202         double precision function ft(x,th)
203         double precision x,xx
204         xx=x/th
205         if(xx.LT.0.)goto 1
206         if(xx.GT.40)goto 2
207         z=dexp(-xx)
208         ft=(z-1.)/(1.+z)
209         goto 3
210 2       ft=-1.
211         goto 3
212 1       if(xx.LT.-40.)goto 4
213         z=dexp(xx)
214         ft=(1.-z)/(z+1.)
215         goto 3
216 4       ft=1.
217 3       continue
218         return
219         end
```

Bibliography

[1] Z. Z. Sheng, A. M. Hermann, A. El Ali, C. Almasan, J. Estrada, T. Datta, and R. J. Matson, "Superconductivity at 90 K in the Tl-Ba-Cu-O system," *Phys. Rev. Lett.* **60**, 937 (1988).

[2] A. Schilling, M. Cantoni, J. D. Guo, and H. R. Ott, "Superconductivity above 130 K in the Hg-Ba-Ca-Cu-O system," *Nature* **363**, 56 (1993).

[3] M. Rotter, M. Tegel, and D. Johrendt, "Superconductivity at 38 K in the iron arsenide $(Ba_{1-x}K_x)Fe_2As_2$," *Phys. Rev. Lett.* **101**, 107006 (2008).

[4] K. Sasmal, B. Lv, B. Lorenz, A. M. Guloy, F. Chen, Y.-Y. Xue, and C.-W. Chu, "Superconducting Fe-based compounds $(A_{1-x}Sr_x)Fe_2As_2$ with A = K and Cs with transition temperatures up to 37 K," *Phys. Rev. Lett.* **101**, 107007 (2008).

[5] S. N. Putilin, E. V. Antipov, O. Chmaissem, M. Marezio, and H. R. Ott, "Superconductivity at 94 K in $HgBa_2CuO_{4+\delta}$," *Nature* **362**, 226 (1993).

[6] A. P. Drozdov, M. I. Eremets, V. Troyan, I. A.an Ksenofontov, and S. I. Shylin, "Conventional superconductivity at 203 kelvin at high pressures in the sulfur hydride system," *Nature* **525**, 73 (2015).

[7] C. W. Chu, L. Gao, F. Chen, Z. J. Huang, R. L. Meng, and Y. Y. Xue, "Superconductivity above 150 K in $HgBa_2Ca_2Cu_3O_{8+\delta}$ at high pressures," *Nature* **365**, 323 (1993).

[8] J. R. Kirtley, C. C. Tsuei, J. Z. Sun, C. C. Chi, L. S. Yu-Jahnes, A. Gupta, M. Rupp, and M. B. Ketchen, "Symmetry of the order parameter in the high-T_c superconductor $YBa_2Cu_3O_{7-\delta}$," *Nature* **373**, 225 (1995).

[9] C. C. Tsuei and J. R. Kirtley, "Pairing symmetry in cuprate superconductors," *Rev. Mod. Phys.* **72**, 969 (2000).

[10] V. B. Geshkenbein, A. I. Larkin, and A. Barone, "Vortices with half magnetic flux quanta in "heavy-fermion" superconductors," *Phys. Rev. B* **36**, 235 (1987).

[11] Y. Zhang, E. Demler, and S. Sachdev, "Competing orders in a magnetic field: Spin and charge order in the cuprate superconductors," *Phys. Rev. B* **66**, 094501 (2002).

[12] J. Chang, E. Blackburn, A. T. Holmes, N. B. Christensen, J. Larsen, J. Mesot, R. Liang, D. A. Bonn, W. N. Hardy, A. Watenphul, M. v. Zimmermann, E. M. Forgan, and S. M. Hayden, "Direct observation of competition between superconductivity and charge density wave order in $YBa_2Cu_3O_{6.67}$," *Nat. Phys.* **8**, 871 (2012).

[13] D. A. Wollman, D. J. Van Harlingen, W. C. Lee, D. M. Ginsberg, and A. J. Leggett, "Experimental determination of the superconducting pairing state in YBCO from the phase coherence of YBCO-Pb dc SQUIDs," *Phys. Rev. Lett.* **71**, 2134 (1993).

[14] C. C. Tsuei, J. R. Kirtley, C. C. Chi, L. S. Yu-Jahnes, A. Gupta, T. Shaw, J. Z. Sun, and M. B. Ketchen, "Pairing symmetry and flux quantization in a tricrystal superconducting ring of $YBa_2Cu_3O_{7-\delta}$," *Phys. Rev. Lett.* **73**, 593 (1994).

[15] Z.-X. Shen, D. S. Dessau, B. O. Wells, D. M. King, W. E. Spicer, A. J. Arko, D. Marshall, L. W. Lombardo, A. Kapitulnik, P. Dickinson, S. Doniach, J. DiCarlo, T. Loeser, and C. H. Park, "Anomalously large gap anisotropy in the a-b plane of $Bi_2Sr_2CaCu_2O_{8+\delta}$," *Phys. Rev. Lett.* **70**, 1553 (1993).

[16] J. Xia, Y. Maeno, P. T. Beyersdorf, M. M. Fejer, and A. Kapitulnik, "High resolution polar Kerr effect measurements of Sr_2RuO_4: Evidence for broken time-reversal symmetry in the superconducting state," *Phys. Rev. Lett.* **97**, 167002 (2006).

[17] A. P. Mackenzie and Y. Maeno, "The superconductivity of Sr_2RuO_4 and the physics of spin-triplet pairing," *Rev. Mod. Phys.* **75**, 657 (2003).

[18] J. Slezak, J. Lee, M. Wang, K. McElroy, K. Fujita, B. Andersen, P. Hirschfeld, H. Eisaki, S. Uchida, and J. Davis, "Imaging the impact on cuprate superconductivity of varying the interatomic distances within individual crystal unit cells," *Proc. of the Nat. Acad. of Sci.* **105**, 3203 (2008).

[19] M. H. Hamidian, I. A. Firmo, K. Fujita, S. Mukhopadhyay, J. W. Orenstein, H. Eisaki, S. Uchida, M. J. Lawler, E.-A. Kim, and J. Davis, "Picometer registration of zinc impurity states in $Bi_2Sr_2CaCu_2O_{8+\delta}$ for phase determination in intra-unit-cell Fourier transform stm," *New J. of Phys.* **14**, 053017 (2012).

[20] G. Binnig and H. Rohrer, "Scanning tunneling microscopy," *Surf. Sci.* **126**, 236 (1983).

[21] H. F. Hess, R. B. Robinson, and J. V. Waszczak, "Vortex-core structure observed with a scanning tunneling microscope," *Phys. Rev. Lett.* **64**, 2711 (1990).

[22] F. Giubileo, D. Roditchev, W. Sacks, R. Lamy, D. X. Thanh, J. Klein, S. Miraglia, D. Fruchart, J. Marcus, and P. Monod, "Two-gap state density in

MgB_2: A true bulk property or a proximity effect?" *Phys. Rev. Lett.* **87**, 177008 (2001).

[23] G. Karapetrov, M. Iavarone, W. K. Kwok, G. W. Crabtree, and D. G. Hinks, "Scanning tunneling spectroscopy in MgB_2," *Phys. Rev. Lett.* **86**, 4374 (2001).

[24] G. Rubio-Bollinger, H. Suderow, and S. Vieira, "Tunneling spectroscopy in small grains of superconducting MgB_2," *Phys. Rev. Lett.* **86**, 5582 (2001).

[25] H. Murakami and R. Aoki, "Observation of multi-stage superconducting gap states in $Bi_2Sr_2CaCu_2O_x$ crystal surface by LT-STM/STS," *J. of the Phys. Soc. of Japan* **64**, 1287 (1995).

[26] S. Pan, E. Hudson, K. Lang, H. Eisaki, S. Uchida, and J. Davis, "Imaging the effects of individual zinc impurity atoms on superconductivity in $Bi_2Sr_2CaCu_2O_{8+\delta}$," *Nature* **403**, 746 (2000).

[27] S. H. Pan, J. O'neal, R. Badzey, C. Chamon, H. Ding, J. Engelbrecht, Z. Wang, H. Eisaki, S. Uchida, A. Gupta, K.-W. Ng, E. Hudson, K. Lang, and J. Davis, "Microscopic electronic inhomogeneity in the high-Tc superconductor $Bi_2Sr_2CaCu_2O_{8+\delta}$," *Nature* **413**, 282 (2001).

[28] A. Yazdani, B. Jones, C. Lutz, M. Crommie, and D. Eigler, "Probing the local effects of magnetic impurities on superconductivity," *Science* **275**, 1767 (1997).

[29] A. Yazdani, C. M. Howald, C. P. Lutz, A. Kapitulnik, and D. M. Eigler, "Impurity-induced bound excitations on the surface of $Bi_2Sr_2CaCu_2O_8$," *Phys. Rev. Lett.* **83**, 176 (1999).

[30] B. D. Josephson, "Possible new effects in superconductive tunnelling," *Phys. Lett.* **1**, 251 (1962).

[31] B. D. Josephson, "The discovery of tunnelling supercurrents," *Rev. Mod. Phys.* **46**, 251 (1974).

[32] M. Hamidian, S. Edkins, S. H. Joo, A. Kostin, H. Eisaki, S. Uchida, M. Lawler, E.-A. Kim, A. Mackenzie, K. Fujita, and J. C. S. Davis, "Detection of a Cooper-pair density wave in $Bi_2Sr_2CaCu_2O_{8+\delta}$," *Nature* **532**, 343 (2016).

[33] O. Naaman, W. Teizer, and R. Dynes, "Fluctuation dominated Josephson tunneling with a scanning tunneling microscope," *Phys. Rev. Lett.* **87**, 097004 (2001).

[34] Y. Noat, T. Cren, V. Dubost, S. Lange, F. Debontridder, P. Toulemonde, J. Marcus, A. Sulpice, W. Sacks, and D. Roditchev, "Disorder effects in pnictides: a tunneling spectroscopy study," *J. of Phys.: Cond. Matter* **22**, 465701 (2010).

[35] N. Bergeal, Y. Noat, T. Cren, T. Proslier, V. Dubost, F. Debontridder, A. Zimmers, D. Roditchev, W. Sacks, and J. Marcus, "Mapping the superconducting condensate surrounding a vortex in superconducting V_3Si using a superconducting MgB_2 tip in a scanning tunneling microscope," *Phys. Rev. B* **78**, 140507 (2008).

[36] H. Kimura, R. P. Barber, S. Ono, Y. Ando, and R. C. Dynes, "Scanning Josephson tunneling microscopy of single-crystal $Bi_2Sr_2CaCu_2O_{8+\delta}$ with a conventional superconducting tip," *Phys. Rev. Lett.* **101**, 037002 (2008).

[37] J. Rodrigo, V. Crespo, and S. Vieira, "Josephson current at atomic scale: Tunneling and nanocontacts using a STM," *Physica C: Supercond.* **437**, 270 (2006).

[38] T. Proslier, A. Kohen, Y. Noat, T. Cren, D. Roditchev, and W. Sacks, "Probing the superconducting condensate on a nanometer scale," *Europhys. Lett.* **73**, 962 (2006).

[39] A. Roychowdhury, M. Dreyer, J. R. Anderson, C. J. Lobb, and F. C. Wellstood, "Microwave photon-assisted incoherent Cooper-pair tunneling in a Josephson STM," *Phys. Rev. Appl.* **4**, 034011 (2015).

[40] A. Roychowdhury, "Development of a dual-tip millikelvin Josephson scanning tunneling microscope," *Ph.D. Dissertation* (2014).

[41] A. Roychowdhury, M. Gubrud, R. Dana, J. Anderson, C. Lobb, F. Wellstood, and M. Dreyer, "A 30 mK, 13.5 T scanning tunneling microscope with two independent tips," *Rev. of Sci. Instru.* **85**, 043706 (2014).

[42] D. F. Sullivan, S. K. Dutta, M. Dreyer, M. A. Gubrud, A. Roychowdhury, J. R. Anderson, C. J. Lobb, and F. C. Wellstood, "Asymmetric superconducting quantum interference devices for suppression of phase diffusion in small Josephson junctions," *J. of Appl. Phys.* **113**, 183905 (2013).

[43] W.-T. Liao, C. Lobb, F. Wellstood, and M. Dreyer, "Simultaneously scanning two connected tips in a scanning tunneling microscope," *J. of Appl. Phys.* **121**, 214501 (2017).

[44] A. Andreev, "The thermal conductivity of the intermediate state in superconductors," *Sov. Phys. JETP* **19**, 1228 (1964).

[45] G. E. Blonder, M. Tinkham, and T. M. Klapwijk, "Transition from metallic to tunneling regimes in superconducting microconstrictions: Excess current, charge imbalance, and supercurrent conversion," *Phys. Rev. B* **25**, 4515 (1982).

[46] B. Foxen, J. Y. Mutus, E. Lucero, Graff, *et al.*, "Qubit compatible superconducting interconnects," *Quant. Sci. and Techn.* **3**, 014005 (2017).

[47] J. B. Chang, M. R. Vissers, A. D. Crcoles, M. Sandberg, J. Gao, D. W. Abraham, J. M. Chow, J. M. Gambetta, M. B. Rothwell, G. A. Keefe, M. Steffen, and D. P. Pappas, "Improved superconducting qubit coherence using titanium nitride," *Appl. Phys. Lett.* **103**, 012602 (2013).

[48] M. R. Vissers, J. S. Kline, J. Gao, D. S. Wisbey, and D. P. Pappas, "Reduced microwave loss in trenched superconducting coplanar waveguides," *Appl. Phys. Lett.* **100**, 082602 (2012).

[49] M. R. Vissers, J. Gao, D. S. Wisbey, D. A. Hite, C. C. Tsuei, A. D. Corcoles, M. Steffen, and D. P. Pappas, "Low loss superconducting titanium nitride coplanar waveguide resonators," *Appl. Phys. Lett.* **97**, 232509 (2010).

[50] J. M. Sage, V. Bolkhovsky, W. D. Oliver, B. Turek, and P. B. Welander, "Study of loss in superconducting coplanar waveguide resonators," *J. of Appl. Phys.* **109**, 063915 (2011).

[51] J. Gao, M. R. Vissers, M. Sandberg, D. Li, H. M. Cho, C. Bockstiegel, B. A. Mazin, H. G. Leduc, S. Chaudhuri, D. P. Pappas, and K. D. Irwin, "Properties of TiN for detector and amplifier applications," *J. of Low Temp. Phys.* **176**, 136 (2014).

[52] H. G. Leduc, B. Bumble, P. K. Day, *et al.*, "Titanium nitride films for ultrasensitive microresonator detectors," *Appl. Phys. Lett.* **97**, 102509 (2010).

[53] P. Diener, H. G. Leduc, S. J. C. Yates, Y. J. Y. Lankwarden, and J. J. A. Baselmans, "Design and testing of kinetic inductance detectors made of titanium nitride," *J. of Low Temp. Phys.* **167**, 305 (2012).

[54] T. Cecil, A. Miceli, L. Gades, A. Datesman, O. Quaranta, V. Yefremenko, V. Novosad, and B. Mazin, "Kinetic inductance detectors for x-ray spectroscopy," *Physics Procedia* **37**, 697 (2012), Proc. of the 2nd Int. Conf. on Techn. and Instrum. in Part. Phys. (TIPP 2011).

[55] O. Noroozian, P. K. Day, B. H. Eom, H. G. Leduc, and J. Zmuidzinas, "Crosstalk reduction for superconducting microwave resonator arrays," *IEEE Trans. on Microwave Theory and Techn.* **60**, 1235 (2012).

[56] G. Binnig, H. Rohrer, C. Gerber, and E. Weibel, "Tunneling through a controllable vacuum gap," *Appl. Phys. Lett.* **40**, 178 (1982).

[57] G. Binnig, H. Rohrer, C. Gerber, and E. Weibel, "Surface studies by scanning tunneling microscopy," *Phys. Rev. Lett.* **49**, 57 (1982).

[58] G. Binnig, H. Rohrer, C. Gerber, and E. Weibel, "7 $\times$ 7 reconstruction on si(111) resolved in real space," *Phys. Rev. Lett.* **50**, 120 (1983).

[59] J. Bardeen, "Tunnelling from a many-particle point of view," *Phys. Rev. Lett.* **6**, 57 (1961).

[60] J. Tersoff and D. R. Hamann, "Theory and application for the scanning tunneling microscope," *Phys. Rev. Lett.* **50**, 1998 (1983).

[61] J. Tersoff and D. R. Hamann, "Theory of the scanning tunneling microscope," *Phys. Rev. B* **31**, 805 (1985).

[62] R. Wiesendanger, *Scanning preobe microscopy and spectroscopy: methods and applications* (Cambridge university press, 1994).

[63] S. Pan, E. Hudson, and J. Davis, "^{3}He refrigerator based very low temperature scanning tunneling microscope," *Rev. of Sci. Inst.* **70**, 1459 (1999).

[64] M. Tinkham, *Introduction to superconductivity* (Courier Dover Publications, 2012).

[65] I. Giaever and K. Megerle, "Study of superconductors by electron tunneling," *Phys. Rev.* **122**, 1101 (1961).

[66] R. C. Dynes, V. Narayanamurti, and J. P. Garno, "Direct measurement of quasiparticle-lifetime broadening in a strong-coupled superconductor," *Phys. Rev. Lett.* **41**, 1509 (1978).

[67] J. Šmakov, I. Martin, and A. V. Balatsky, "Josephson scanning tunneling microscopy," *Phys. Rev. B* **64**, 212506 (2001).

[68] H. Kimura, R. Barber Jr, S. Ono, Y. Ando, and R. Dynes, "Josephson scanning tunneling microscopy: A local and direct probe of the superconducting order parameter," *Phys. Rev. B* **80**, 144506 (2009).

[69] A. V. Balatsky, J. Smakov, and I. Martin, "Potential applications of a scanning tunnelling microscope with a superconducting tip," *Supercond. Sci. and Tech.* **15**, 446 (2002).

[70] R. F. Voss and R. A. Webb, "Macroscopic quantum tunneling in 1-μm Nb Josephson junctions," *Phys. Rev. Lett.* **47**, 265 (1981).

[71] M. Ternes, W.-D. Schneider, J.-C. Cuevas, C. P. Lutz, C. F. Hirjibehedin, and A. J. Heinrich, "Subgap structure in asymmetric superconducting tunnel junctions," *Phys. Rev. B* **74**, 132501 (2006).

[72] L. Kuzmin, Y. V. Nazarov, D. Haviland, P. Delsing, and T. Claeson, "Coulomb blockade and incoherent tunneling of Cooper pairs in ultrasmall junctions affected by strong quantum fluctuations," *Phys. Rev. Lett.* **67**, 1161 (1991).

[73] Y. Anchenko and L. ZilBerman, "The Josephson effect in small tunnel contacts," *Sov. Phys. JETP* **28**, 113 (1969).

[74] G.-L. Ingold, H. Grabert, and U. Eberhardt, "Cooper-pair current through ultrasmall Josephson junctions," *Phys. Rev. B* **50**, 395 (1994).

[75] F. Pobell, *Matter and Methods at Low Temperatures*, 3rd ed. (Springer-Verlag Berlin Heidelberg, 2007).

[76] J. Annett, *Superconductivity, Superfluids and Condensates*, Oxford Master Series in Physics (OUP Oxford, 2004).

[77] Kadel Engineering, Danville IN.

[78] Model AH 2700A, Andeen-Hagerling Inc.

[79] M. A. Gubrud, "Scanning tunneling microscopy at millikelvin temperatures: Design and construction," *Ph.D. Dissertation* (2010).

[80] Britannia House, Cambridge, UK.

[81] EutecRod 157, Eutectic Corporation, USA.

[82] Models Starcell 75 and 300, Varian.

[83] Model ST2 and Varian Model 929-022, Vacuum Generators.

[84] Model VIG18/Arun Microelectronics Ltd. PGC1, VG Scienta.

[85] TModel V551 Navigator/VT 1000HT, Varian.

[86] Model TriScroll600, Varian.

[87] Model XT200, Extorr.

[88] Model EFM3/EVC 100, Omicron.

[89] Model IQE 10, Specs.

[90] Model HPT, VG Scienta.

[91] SPM 1000 Scanning Probe Microscope Control System, RHK.

[92] R9 Scanning Probe Microscope Control System, RHK.

[93] Model 1211 current amplifier, DL instruments.

[94] A. Roychowdhury, R. Dana, M. Dreyer, J. Anderson, C. Lobb, and F. Wellstood, "Plasma etching of superconducting niobium tips for scanning tunneling microscopy," *J. of Appl. Phys.* **116**, 014308 (2014).

[95] Plasmatherm 790 RIE, Plasma-Therm, Saint Petersburg, Fl.

[96] T. A. Fulton, L. N. Dunkleberger, and R. C. Dynes, "Quantum interference properties of double Josephson junctions," *Phys. Rev. B* **6**, 855 (1972).

[97] K. Mitra, F. W. Strauch, C. J. Lobb, J. R. Anderson, F. C. Wellstood, and E. Tiesinga, "Quantum behavior of a dc squid phase qubit," *Phys. Rev. B* **77**, 214512 (2008).

[98] D. J. Van Harlingen, "Phase-sensitive tests of the symmetry of the pairing state in the high-temperature superconductors–Evidence for $d_{x^2-y^2}$ symmetry," *Rev. Mod. Phys.* **67**, 515 (1995).

[99] Dual pulse 125, Unitek Equipment.

[100] Topometrix ECU+ (ECU: Electronic control unit) , ThermoMicroscopes, 1171 Borregas Ave., Sunnyvale, Ca 94089 (does not exist anymore).

[101] J. Bardeen, L. N. Cooper, and J. R. Schrieffer, "Microscopic theory of superconductivity," *Phys. Rev.* **106**, 162 (1957).

[102] J. Bardeen, L. N. Cooper, and J. R. Schrieffer, "Theory of superconductivity," *Phys. Rev.* **108**, 1175 (1957).

[103] L. N. Cooper, "Bound electron pairs in a degenerate Fermi gas," *Phys. Rev.* **104**, 1189 (1956).

[104] N. N. Bogoljubov, "On a new method in the theory of superconductivity," *Il Nuovo Cimento (1955-1965)* **7**, 794 (1958).

[105] N. N. Bogoliubov, "A new method in the theory of superconductivity. i," *Sov. Phys. JETP* **34** (1958).

[106] R. Shankar, "Renormalization-group approach to interacting fermions," *Rev. Mod. Phys.* **66**, 129 (1994).

[107] W. Kohn and J. M. Luttinger, "New mechanism for superconductivity," *Phys. Rev. Lett.* **15**, 524 (1965).

[108] V. L. Ginzburg, "On superconductivity and superfluidity (what i have and have not managed to do), as well as on the physical minimumat the beginning of the 21st century," *ChemPhysChem* **5**, 930 (2004).

[109] V. L. Ginzburg and L. D. Landau, "On the theory of superconductivity," *Sov. Phys. JETP* **20**, 1064 (1950).

[110] A. Mackenzie and Y. Maeno, "p-wave superconductivity," *Physica B: Condensed Matter* **280**, 148 (2000).

[111] K. Maki, "Introduction to d-wave superconductivity," *AIP Conference Proceedings*, **438**, 83 (1998).

[112] J. Valatin, "Comments on the theory of superconductivity," *Nuovo cimento* **7**, 843 (1958).

[113] C. Kittel, *Introduction to Solid State Physics*, 8th ed. (Wiley, 2004).

[114] N. B. Kopnin, "Theory of superconductivity," *http://ltl.tkk.fi/opetus/supertheory/tfy-3.491/TheorySC06.pdf* (2006).

[115] T. I. Baturina, A. Y. Mironov, V. M. Vinokur, M. R. Baklanov, and C. Strunk, "Localized superconductivity in the quantum-critical region of the disorder-driven superconductor-insulator transition in TiN thin films," *Phys. Rev. Lett.* **99**, 257003 (2007).

[116] B. Sacépé, T. Dubouchet, C. Chapelier, M. Sanquer, M. Ovadia, D. Shahar, M. Feigelman, and L. Ioffe, "Localization of preformed Cooper pairs in disordered superconductors," *Nature Phys.* **7**, 239 (2011).

[117] W. Escoffier, C. Chapelier, N. Hadacek, and J.-C. Villégier, "Anomalous proximity effect in an inhomogeneous disordered superconductor," *Phys. Rev. Lett.* **93**, 217005 (2004).

[118] I. Giaever, "Energy gap in superconductors measured by electron tunneling," *Phys. Rev. Lett.* **5**, 147 (1960).

[119] H. I. Jaim, J. Aguilar, B. Sarabi, Y. Rosen, A. Ramanayaka, E. Lock, C. Richardson, and K. Osborn, "Superconducting TiN films sputtered over a large range of substrate dc bias," *IEEE Transactions on Applied Superconductivity* **25**, 1 (2015).

[120] M. Gurvitch, "Ioffe-Regel criterion and resistivity of metals," *Phys. Rev. B* **24**, 7404 (1981).

[121] R. Machunze and G. Janssen, "Stress and strain in titanium nitride thin films," *Thin Solid Films* **517**, 5888 (2009).

[122] D. Averin and A. Bardas, "ac Josephson effect in a single quantum channel," *Phys. Rev. lett.* **75**, 1831 (1995).

[123] E. Bratus, V. Shumeiko, and G. Wendin, "Theory of subharmonic gap structure in superconducting mesoscopic tunnel contacts," *Phys. Rev. lett.* **74**, 2110 (1995).

[124] J. Cuevas, A. Martin-Rodero, and A. L. Yeyati, "Hamiltonian approach to the transport properties of superconducting quantum point contacts," *Phys. Rev. B* **54**, 7366 (1996).

[125] G. B. Arnold, "Superconducting tunneling without the tunneling Hamiltonian. ii. Subgap harmonic structure," *J. of Low Temp. Phys.* **68**, 1 (1987).

[126] S.-T. Wu and S. Yip, "ac Josephson effect in asymmetric superconducting quantum point contacts," *Phys. Rev. B* **70**, 104511 (2004).

[127] A. Bardas and D. V. Averin, "Electron transport in mesoscopic disordered superconductor–normal-metal–superconductor junctions," *Phys. Rev. B* **56**, R8518 (1997).

[128] J. P. Pekola, J. V. Koski, and D. V. Averin, "Refrigerator based on the Coulomb barrier for single-electron tunneling," *Phys. Rev. B* **89**, 081309 (2014).

[129] J. T. Muhonen, M. Meschke, and J. P. Pekola, "Micrometre-scale refrigerators," *Reports on Progress in Physics* **75**, 046501 (2012).

[130] F. Giazotto, T. T. Heikkilä, A. Luukanen, A. M. Savin, and J. P. Pekola, "Opportunities for mesoscopics in thermometry and refrigeration: Physics and applications," *Rev. Mod. Phys.* **78**, 217 (2006).

[131] R. Feynman, R. Leighton, and M. Sands, *The Feynman Lectures on Physics, Vol. III: The New Millennium Edition: Quantum Mechanics*, The Feynman Lectures on Physics (Basic Books, 2011).

[132] T. Van Duzer and C. W. Turner, "Principles of superconductive devices and circuits," (1981).

[133] V. Ambegaokar and A. Baratoff, "Tunneling between superconductors," *Phys. Rev. Lett.* **10**, 486 (1963).

[134] V. Ambegaokar and A. Baratoff, "Tunneling between superconductors-errata," *Phys. Rev. Lett.* **11**, 104 (1963).

[135] J. D. Jackson, *Classical electrodynamics*, 3rd ed. (Wiley, 1999).

[136] A. A. Golubov, M. Y. Kupriyanov, and E. Ilichev, "The current-phase relation in Josephson junctions," *Rev. of Mod. Phys.* **76**, 411 (2004).

[137] E. Scheer, W. Belzig, Y. Naveh, M. H. Devoret, D. Esteve, and C. Urbina, "Proximity effect and multiple Andreev reflections in gold atomic contacts," *Phys. Rev. Lett* **86**, 284 (2001).

[138] B. Ludoph, N. Van der Post, E. Bratus, E. Bezuglyi, V. Shumeiko, G. Wendin, and J. Van Ruitenbeek, "Multiple Andreev reflection in single-atom niobium junctions," *Phys. Rev. B* **61**, 8561 (2000).

[139] R. Hiraoka, R. Arafune, N. Tsukahara, M. Kawai, and N. Takagi, "Transport characteristics of a single C_{60}-molecule junction revealed by multiple Andreev reflections," *Phys. Rev. B* **90**, 241405 (2014).

[140] E. Scheer, N. Agraït, J. C. Cuevas, A. L. Yeyati, B. Ludoph, A. Martín-Rodero, G. R. Bollinger, J. M. van Ruitenbeek, and C. Urbina, "The signature of chemical valence in the electrical conduction through a single-atom contact," *Nature* **394**, 154 (1998).

[141] E. Scheer, P. Joyez, D. Esteve, C. Urbina, and M. H. Devoret, "Conduction channel transmissions of atomic-size aluminum contacts," *Phys. Rev. Lett.* **78**, 3535 (1997).

[142] N. Van der Post, E. Peters, I. Yanson, and J. Van Ruitenbeek, "Subgap structure as function of the barrier in atom-size superconducting tunnel junctions," *Phys. Rev. Lett.* **73**, 2611 (1994).

[143] J. Rodrigo, H. Suderow, S. Vieira, E. Bascones, and F. Guinea, "Superconducting nanostructures fabricated with the scanning tunnelling microscope," *J. of Phys.: Condensed Matter* **16**, R1151 (2004).

[144] M. T. Randeria, B. E. Feldman, I. K. Drozdov, and A. Yazdani, "Scanning Josephson spectroscopy on the atomic scale," *Phys. Rev. B* **93**, 161115 (2016).

[145] B. Jäck, M. Eltschka, M. Assig, M. Etzkorn, C. R. Ast, and K. Kern, "Critical Josephson current in the dynamical Coulomb blockade regime," *Phys. Rev. B* **93**, 020504 (2016).

[146] B. Jäck, J. Senkpiel, M. Etzkorn, J. Ankerhold, C. R. Ast, and K. Kern, "Quantum brownian motion at strong dissipation probed by superconducting tunnel junctions," *Phys. Rev. Lett.* **119**, 147702 (2017).

[147] C. Muller, J. van Ruitenbeek, and L. de Jongh, "Experimental observation of the transition from weak link to tunnel junction," *Physica C: Supercond.* **191**, 485 (1992).

[148] A. Steinbach, P. Joyez, A. Cottet, D. Esteve, M. Devoret, M. Huber, and J. M. Martinis, "Direct measurement of the Josephson supercurrent in an ultrasmall Josephson junction," *Phys. Rev. Lett.* **87**, 137003 (2001).

[149] M. Watanabe and D. B. Haviland, "Quantum effects in small-capacitance single Josephson junctions," *Phys. Rev. B* **67**, 094505 (2003).

[150] L. S. Kuzmin, Y. V. Nazarov, D. B. Haviland, P. Delsing, and T. Claeson, "Coulomb blockade and incoherent tunneling of Cooper pairs in ultrasmall junctions affected by strong quantum fluctuations," *Phys. Rev. Lett.* **67**, 1161 (1991).

[151] Y. Harada, H. Takayanagi, and A. A. Odintsov, "Cooper-pair tunneling in small junctions with tunable Josephson coupling," *Phys. Rev. B* **54**, 6608 (1996).

[152] J. M. Martinis and R. L. Kautz, "Classical phase diffusion in small hysteretic Josephson junctions," *Phys. Rev. Lett.* **63**, 1507 (1989).

[153] R. L. Kautz and J. M. Martinis, "Noise-affected I-V curves in small hysteretic Josephson junctions," *Phys. Rev. B* **42**, 9903 (1990).

[154] P. Joyez, D. Vion, M. Götz, M. Devoret, and D. Esteve, "The Josephson effect in nanoscale tunnel junctions," *J. of Supercond.* **12**, 757 (1999).

[155] N. Agrait, J. Rodrigo, and S. Vieira, "Transition from the tunneling regime to point contact and proximity-induced Josephson effect in lead–normal-metal nanojunctions," *Phys. Rev. B* **46**, 5814 (1992).

[156] Nb (100) single crystal, Accument Materials, USA.

[157] C. C. Koch, J. O. Scarbrough, and D. M. Kroeger, "Effects of interstitial oxygen on the superconductivity of niobium," *Phys. Rev. B* **9**, 888 (1974).

[158] T. Kárník, "Niobium oxide for capacitor manufacturing," *Metal 2008* (2008).

[159] M. Iansiti, M. Tinkham, A. T. Johnson, W. F. Smith, and C. J. Lobb, "Charging effects and quantum properties of small superconducting tunnel junctions," *Phys. Rev. B* **39**, 6465 (1989).

[160] J. M. Martinis, M. H. Devoret, and J. Clarke, "Experimental tests for the quantum behavior of a macroscopic degree of freedom: The phase difference across a Josephson junction," *Phys. Rev. B* **35**, 4682 (1987).

[161] W. Stewart, "Current-voltage characteristics of Josephson junctions," *Appl. Phys. Lett.* **12**, 277 (1968).

[162] D. McCumber, "Effect of ac impedance on dc voltage-current characteristics of superconductor weak-link junctions," *J. of Appl. Phys.* **39**, 3113 (1968).

[163] Y. Chen, M. P. Fisher, and A. Leggett, "The return of a hysteretic Josephson junction to the zero-voltage state: I-V characteristic and quantum retrapping," *J. of Appl. Phys.* **64**, 3119 (1988).

[164] S. Kurokawa, A. Sakai, *et al.*, "Tip-sample capacitance in STM (STM-BEEM interfaces)," *Science reports of the Research Institutes, Tohoku University. Ser. A, Physics, Chemistry and Metallurgy* **44**, 173 (1997).

[165] J. de Voogd, M. van Spronsen, F. Kalff, B. Bryant, O. Ostojić, A. den Haan, I. Groot, T. Oosterkamp, A. Otte, and M. Rost, "Fast and reliable preapproach for scanning probe microscopes based on tip-sample capacitance," *Ultramicroscopy* **181**, 61 (2017).

[166] S. Kurokawa and A. Sakai, "Gap dependence of the tip-sample capacitance," *J. of Appl. Phys.* **83**, 7416 (1998).

[167] M. H. Devoret, J. M. Martinis, D. Esteve, and J. Clarke, "Resonant activation from the zero-voltage state of a current-biased Josephson junction," *Phys. Rev. Lett.* **53**, 1260 (1984).

[168] D. J. Van Harlingen, "Probing the symmetry of the pairing state of unconventional superconductors by SQUID interferometer measurements," *Physica C: Supercond.* **282**, 128 (1997).

[169] D. van Harlingen, J. Hilliard, B. Plourde, and B. Yanoff, "Extending SQUID interferometry beyond the cuprates and beyond d-wave symmetry," *Physica C: Supercond.* **317-318**, 410 (1999).

[170] Amuneal, Magnetic Shielding Materials.